Direct Measurement of Electrostatic Forces between Colloids

by

Franceska Waggett

A dissertation submitted to the University of Bristol
in accordance with the requirements for award
of the degree of Doctor of Philosophy in the

Faculty of Science

2019

Word count: 46000

Declaration of Authorship

I declare that the work in this dissertation was carried out in accordance with the requirements of the University's Regulations and Code of Practice for Research Degree Programmes and that it has not been submitted for any other academic award. Except where indicated by specific reference in the text, the work is the candidate's own work. Work done in collaboration with, or with the assistance of, others, is indicated as such. Any views expressed in the dissertation are those of the author.

Signed: ..... Date: .....

UNIVERSITY OF BRISTOL

Abstract

Faculty of Science
School of Chemistry

Doctor of Philosophy

Direct Measurement of Electrostatic Forces between Colloids

by Franceska Waggett

Many applications, such as printing inks and engine oils, are based on dispersions of solid particles in nonpolar solvents. In such systems, electrostatics dominate over other interactions between the particles at large separations, thus controlling their behaviour. Derjaguin–Landau–Verwey–Overbeek (DLVO) theory remains the cornerstone in describing the stability of colloids in dilute, univalent electrolytes. This thesis aims to investigate the electrostatic interactions between charged poly(methyl methacrylate) (PMMA) particles suspended in a nonpolar solvent, dodecane. By probing the double layer surrounding these particles, and testing the stability of the suspensions under various conditions, unexpected observations were made that contradict DLVO theory.

Firstly, the electrostatic repulsions between the particles were directly measured using blinking optical tweezers. The first significant deviation from expected behaviour was observed in the trend of the decay of these repulsions with the electrolyte concentration. By simultaneously measuring the conductivity of the solutions, the Debye-Hückel (DH) length could also be measured. According to the DLVO theory, the decay length of the pair interactions should equate with the bulk determined DH length, however our measurements have shown that this is not the case at high electrolyte concentrations. Not only this, but we have measured a nonmonotonic relationship of the decay length of the interactions with the electrolyte concentration, despite the system remaining in the limits of mean-field theories. The second unusual observation made in this system was the formation of aggregates, even at low electrolyte concentrations where the electrostatic repulsions are still strong. Furthermore, the attraction clearly present in the system is strong enough to overcome the steric stability inferred to the particles by a polymer brush layer on their surface. This attraction is not believed to be due to van der Waals interactions, which are too weak and short ranged to overcome the steric stability. By observing the behaviour of the aggregates in an electric field, it strongly suggests that they have a dipole moment, indicating that a dipole interaction could be the origin of attraction.

These observations both provide evidence that the surface of the particles can charge regulate. By deriving a model to describe the interaction between two charge regulating surfaces, both the unexpected form of the repulsions, and the presence of a dipolar attraction are explained.

Acknowledgements

I would firstly like to thank those involved with this research. Primarily my thanks go to my supervisor, Paul Bartlett, with whom I have had many interesting discussions over the last few years. His enthusiasm in this subject was always contagious and our meetings inspired me to learn more. Next I would like to thank my fellow group member, Danial Shafiq, for his collaborative efforts. I could always rely on his consistency and willingness. Other students I have worked with and who have been invaluable to my progress are Dr Sam Finlayson for showing me how to use the optical tweezers, and all the undergraduate project students who conducted experiments alongside me (Isaac Charlton, Charlotte Pugsley & Kristian Beckers). Finally, my thanks go to those who have made suggestions to improve and further this investigation, including the rest of the soft matter group, the other academics in the Bristol colloid group, and those academics who I have met during conferences.

Secondly, I would like to thank the financial support of the EPSRC and Unilever.

Finally, I would like to thank those who gave me support alongside my studies. My Dad, Mum and brother, Hugh, all have a strong love for learning which has always been inspirational. I'd like to thank them for their support and advice which has never faltered throughout my life. Just as important to me are my friends, especially Fay, Sam, Eleanor and Sally, and my housemates Charlie and Charlotte, who have given me constant encouragement to do my best and to enjoy what I do.

I am so grateful for the support from everyone mentioned above, thank you.

List of Publications

Publications during this PhD:

- F. Waggett, M. Shafiq and P. Bartlett, 'Failure of Debye-Hückel Screening in Low-Charge Colloidal Suspensions', *Colloids and Interfaces*, **2**, 51-59, (2018)
- I. Muntz, F. Waggett, M. Hunter, A. Schofield, P. Bartlett, D. Marenduzzo and J. Thijssen, 'Interaction between Nearly Hard Colloidal Spheres at an Oil-Water Interface', arXiv preprint: *arXiv:1812.10299*, 2018

Prior publications from the author:

- J. Bonham, F. Waggett, M. Faers and J. van Duijneveldt, 'The role of initiator on the dispersibility of polystyrene microgels in non-aqueous solvents', *Colloid and Polymer Science*, **295**, 479-486, 2017

Contents

List of Figures

List of Symbols

ε	Permittivity	F m^{-1}
ε_r	Dielectric constant	
$\mathcal{F}$	free energy	J
U	Potential energy	J
S	Entropy	J K^{-1}
ψ	Potential	V
T	Absolute temperature	K
η	Solvent viscosity	Pa s
$k_B T$	Thermal energy	J
λ	Wavelength	m
ν	Frequency	s^{-1}
n	Refractive index	
P	Power	W
P^*	Critical power	W
E	Electric field	V m^{-1}
I	Intensity	W m^{-2}
SCS	Scattering cross section	m^2
p	Momentum	kg m s^{-1}
α	Polarisibility	C m^2 V^{-1}
μ	Chemical potential	J mol^{-1}
δ	Dipole moment	C m
Σ	Conductivity	S m^{-1}
C	Capacitance	F
ℓ_B	Bjerrum length	m
κ^{-1}	Screening length in DLVO theory	m
κ	Inverse screening length in DLVO theory	m^{-1}
λ_D	DH length	m
κ_D	Inverse DH length	m^{-1}
κ_{meas}^{-1}	Measured screening length from BOT	m
κ_{meas}	Measured inverse screening length from BOT	m^{-1}
b	Gouy-Chapman length	m
r	Centre−centre particle separation	m
h	Surface−surface particle separation	m
L	Flat plate separation	m
a	Radius of colloidal particle	m
R_{salt}	Physical size of salt	m
$R_\pm$	Radius of ion	m
c	Concentration	M
CAC	Critical aggregation concentration	M
ϕ_v	Volume fraction	
ϕ_s	Surface fraction	
SA	Surface area	m^2

μ_e	Electrophoretic mobility	$m^2\ V^{-1}\ s^{-1}$
z	Valency of charge	
q	Particle charge	C
Z	Particle charge number	e
Z_{eff}	Effective particle charge $= Z\ell_B/a$	e
ψ_s	Surface potential	V
σ	Surface charge density	$e\ m^{-2}$
ρ	Charge density	$C\ m^{-3}$
ρ_{ion}	Charge density of ions	$C\ m^{-3}$
n_{ion}	Ion number density	m^{-3}
Π	Osmotic pressure	Pa
P	Pressure	Pa
F	Force between particles	N
v	Particle pair velocity	$m\ s^{-1}$
t	Time	s
D	Particle pair diffusion coefficient	$m^2\ s^{-1}$
f_0	Stoke's drag coefficient	$kg\ s^{-1}$
ℓ_g	Gravitational length	m
Pe	Péclet number	
H	Hamaker constant	J
ξ	Manning parameter	
Ξ	Coulomb coupling parameter	
R^2_{adj}	'R-squared' fit statistic	
φ	Order parameter in the Landau model	
γ	Surface tension	$N\ m^{-1}$

Physical Constants

c_0	Speed of light in a vacuum	$2.9979246 \times 10^8\ m\ s^{-1}$
k_B	Boltzmann's constant	$1.3806485 \times 10^{-23}\ J\ K^{-1}$
N_A	Avogadro's constant	$6.0221409 \times 10^{23}\ mol^{-1}$
e	Elementary charge	$1.6021766 \times 10^{-19}\ C$
ε_0	Permittivity of free space	$8.8541878 \times 10^{-12}\ F\ m^{-1}$
h_P	Planck's constant	$6.6260700 \times 10^{-34}\ m^2\ kg\ s^{-1}$

Abbreviations

PB	**P**oisson-**B**oltzmann
DH	**D**ebye-**H**ückel
GC	**G**ouy-**C**hapman
DLVO	**D**erjaguin-**L**andau-**V**erwey-**O**verbeek
DL	**D**ouble-**L**ayer
CR	**C**harge **R**egulation
vdW	**v**an **d**er **W**aals
BOT	**B**linking **O**ptical **T**weezers

Chapter 1

Introduction

The introduction to this investigation is separated into two main sections, the first being the theories of electrostatics, and the second being the system used to investigate them, namely charged colloidal suspensions. This research focusses on the electrostatics governing the behaviour of a colloid suspension in a nonpolar solvent. This system, and the techniques used to observe it, are detailed in the experimental chapter. The results of this study are divided into the different observations made, namely the repulsions and the attractions, each detailing the current literature that has observed similar or contradictory behaviour to that found in this investigation. Finally, a probable explanation that can account for all the observations made is discussed within one theoretical framework in the final chapter.

1.1 Electrostatics

Being one of the four fundamental forces that govern the entire universe, electromagnetic interactions are clearly very important to study. Specifically in this investigation is the interaction between electrically charged objects - those which have either an excess (or deficiency) of electrons or protons. When this excess is over an entire object, monopolar interactions are considered. An excess can also arise more locally due to thermal fluctuations, or inhomogeneity across a surface, in which case correlation interactions and dipolar interactions must also be considered.

1.1.1 Charged Systems

There are many systems that function due to the electrostatic force, including biological processes, natural phenomena, and man-made applications, because they contain electrically charged components. One naturally occurring and extremely abundant state of matter in the universe is plasma, an ionised gas. Formed by heating a gas to high temperatures, or applying strong electric fields, plasma is present within stars and in the Earth's atmosphere, being responsible for natural phenomena such as lightening, flames and the aurora (*1*). Being either partially or totally ionised, the components of a plasma interact via electromagnetic forces. Charging matter does not always require high temperatures or strong electric fields however. When in solution for example, chemical groups can dissociate solely from thermal fluctuations; the driving force for this dissociation is the entropic gain of

the system when the ions can occupy any volume in the sample rather than being confined to the volume next to the counterion. Many biological processes rely on this charging process in solution, for example the infamous double helix shape of DNA molecules; a fine balance between electrostatic repulsion and attraction exists that keeps the DNA strands together whilst preventing it from collapsing (2–4).

Sometimes, surfaces will become electrically charged due to charge transfer when in contact with other surfaces. This is termed static electricity and is again important for many applications. Static charging of the surface of a bee's body as it flies through the air is believed to increase the amount of pollen it can collect due to electrostatic attraction to the slightly negatively charged pollen particles (5–7). The static charge of dust and soot particles is also utilised when attempting to filter them out of exhaust emissions from burning fossil fuels (8), or when vacuuming a floor (9). This is achieved by passing the exhaust gases through a series of filters and electrodes that slowly collect such particles due to electrostatic attraction. The opposite issue is found for spacecraft visiting other planets or the Moon, where dust particles are attracted to the walls of the vehicle and will collect there. Some attempts have been made to hinder this effect by inducing oscillating electric fields across the surface of the spacecraft such that the dust particles are 'bounced' along the surface rather than sticking to it (10).

Being of most interest for this study are *liquid* systems containing charges, specifically those with no water present. Most commonly these arise in the form of salt solutions or ionic liquids which have received a lot of attention recently (11, 12). An ionic liquid is defined as a salt which is in the liquid state below 100 °C (13). An immediate benefit of such compounds is that you effectively reach maximum ion density, i.e. the system is totally made of ions with no solvent present. Measurements can therefore be done at higher ion concentrations which were previously limited by the solubility of solid salts. The molarity of the ionic liquid can then be decreased by the addition of a miscible solvent. A few phrases that turned many heads towards the topic of ionic liquids were '*designer solvents*' (14, 15) or '*green solvents*' (16). The term 'designer' referring to the vast number of combinations of cations and anions that would form an ionic liquid, and the term 'green' referring to their potential in replacing toxic and expensive solvents in certain syntheses (17). As such, suggested applications for ionic liquids span from being used as a media for liquid-liquid extraction (18, 19), CO_2 capture (20–22), catalysis (23) and supercapacitors (24, 25). In some cases, ionic liquids have been incorporated into the synthesis of polymeric particles to increase their charging in less polar solvents (26). With apparently numerous applications, many publications then emerged to ascertain if and how the electrostatics of such concentrated ionic systems differ from those for dilute electrolytes (27).

1.1.2 Laws of Electrostatics

Every electrically charged object will interact with another charged object via the electrostatic force. According to Coulomb's law, every point charge induces a radial electric field that decreases in magnitude with the inverse square of the distance from the point charge, hence extending to an infinite distance. The force of interaction between two point charges hence also follows the same inverse square relationship on the separation r of the point charges. When molecules, such as water, are located between the two point charges, they will align according to the electric field induced from the point charges. As a consequence, the average electric field strength between the two point charges is weakened, with more polar molecules resulting in a stronger effect. How strongly a molecule will oppose an electric field in this way is quantified by its *permittivity* ε, often stated as its relative permittivity with that of a vacuum ε_0, also called its *dielectric constant* ε_r, i.e. $\varepsilon = \varepsilon_r\varepsilon_0$. Materials that act in this way are called dielectric materials. Physically, the permittivity describes the polarity of a dielectric medium, so water, being a very polar molecule, has a large permittivity $\varepsilon_r \approx 80$, whereas for air $\varepsilon_r \approx 1.0006$, so the electrostatic force between two point charges q_1 & q_2 is significantly weaker when the two are submerged in water than in air as the force of interaction F follows

$$F = \frac{q_1 q_2}{4\pi\varepsilon_r\varepsilon_0 r^2}. \tag{1.1}$$

The permittivity of a material is also dependent on temperature and the frequency of the applied electric field. The temperature dependence is due to different orientations of the molecules and volume expansion at different temperatures (*28*–*30*), with large changes often accompanying phase boundaries (*31*, *32*). The frequency dependence is due to the fact that the molecules will orientate with the field, so when it oscillates, they will also rotate to realign. With a very high frequency electric field, the molecules cannot realign fast enough, and hence the frequency dependence becomes zero. The permittivity at intermediate frequencies generally decreases with increasing frequency, sometimes accompanied by resonance peaks (*30*). The static dielectric constant is the most commonly used value to compare different solvents (ε_r), which is the value at zero-frequency.

The permittivity of a medium defines its electrical properties, and from it, other physical parameters can be calculated. One such parameter is a length scale which describes the comparative strength of the electrostatic and thermal energy in a medium, and is called the Bjerrum length ℓ_B. By equating the thermal energy $k_B T$ with the electrostatic energy (integral of eq. (1.1)), this length scale is defined as

$$\ell_B = \frac{e^2}{4\pi\varepsilon_r\varepsilon_0 k_B T}, \tag{1.2}$$

where k_B is Boltzmann's constant, T is the absolute temperature, and e is the elementary charge. Effectively it is a measure of when the entropic gain from

dissociating a pair of opposite point charges is large enough to overcome the energetic cost, hence its dependence on temperature. So, using water as an example again, $\ell_B \approx 0.7$ nm which is significantly less than in a hydrocarbon solvent where $\ell_B \approx 30$ nm ($\varepsilon_r \approx 2$). This means that in order to dissolve a salt in a solvent, the size of the ions in solution must be of order ℓ_B or greater to ensure they separate far enough for dissociation to occur. Often this is achieved by dissolving much larger salts into less polar (smaller ε_r) solvents. The Bjerrum length also provides an estimate for the maximum ion density possible in different solvents. If the assumption is made that only one ion can reside in a volume ℓ_B^3, then each ion would occupy a cubic volume (≈ 0.7 nm)^3 in water, or (≈ 30 nm)^3 in a hydrocarbon solvent. Describing the electrostatics for systems beyond just two point charges can be complicated, one example of such a system is an electrolyte solution, and the electrostatics that govern them was described by Debye & Hückel in 1923 (33).

1.1.3 Debye-Hückel (DH) Theory

The electrostatic behaviour of complex systems can be derived by considering the fundamental laws that govern electrostatics (34). Two such laws are Gauss' law (eq. (1.3a)) and Poisson's equation (eq. (1.3b)):

$$\int \vec{E} \cdot \mathrm{d}\,\vec{\mathrm{SA}} = \frac{q}{\varepsilon_r \varepsilon_0}, \tag{1.3a}$$

$$\nabla^2 \psi = -\frac{\rho}{\varepsilon_r \varepsilon_0}. \tag{1.3b}$$

Gauss' law gives the magnitude of the electric field $\vec{E}$ induced from a point charge q by evaluating the electric field flux through a Gaussian surface (which for a point charge in three-dimensional space is spherical). From Gauss' law comes Coulomb's law (eq. (1.1)) as the integral gives the surface area of a sphere (SA $= 4\pi r^2$). Poisson's equation (which is directly derivable from Gauss' law as $E = -\mathrm{d}\psi/\mathrm{d}r$) describes the magnitude of the electric potential ψ due to a volume of uniform charge density ρ. This equation is derived by a summation of the potentials from all constituent point charges, or equivalently an integration over a volume of uniform charge density, then applying the Laplacian ∇^2 to both sides of the equation.

From these fundamentals of electrostatics, Debye & Hückel (DH) derived a theory that describes the electrostatics of electrolyte solutions by ignoring the discrete nature of each ion, and treating the solution as one of uniform charge density (33). Solvated ions are free to diffuse and will arrange themselves such that their free energy is minimised; electrostatic energy is minimised when all ions are neutralised by their counterion, however the entropy of the system is increased when the ions dissociate and mix in solution, hence a dissociation equilibrium exists for every pair of ions. The DH theory describes the distribution of the ions by calculating the ensemble average of the potential due to each ion. The distribution

of the ions is assumed to follow Boltzmann statistics, which gives for the number density of ions i at the location r,

$$n_i(r) = n_{i,0} \exp\left(-\beta w_i(r)\right), \tag{1.4}$$

where $n_{i,0}$ is the number density of ions i in the bulk of the system, $w_i(r)$ is the potential of mean force on ion i at the location r, and $\beta = 1/k_B T$.

Poisson's equation then becomes (35–37)

$$\nabla^2\langle\psi\rangle = -\frac{1}{\varepsilon_r\varepsilon_0}\sum_i z_i e n_{i,0} \exp(-\beta w_i), \tag{1.5}$$

where z_i is the valency of the ion i, and $\rho_{i,0} = z_i e n_{i,0}$ is the total charge density due to ions i in the bulk of the system. The first assumption made in DH theory is that $w_i = z_i e\langle\psi_i\rangle$ which for a $z_+ = z_- = z$ electrolyte of total charge density $\rho_{ion} = \rho_{+,0} + \rho_{-,0}$, reduces equation (1.5) to the Poisson-Boltzmann (PB) equation,

$$\nabla^2\psi = \frac{z e n_{ion}}{\varepsilon_r\varepsilon_0} \sinh\left(\beta z e \psi\right). \tag{1.6}$$

The PB equation is the foundation of most of the discussion in line with this work. Being a mean-field theory, where taking the ensemble average simplifies a many-body system, the PB equation has its limitations as will be discussed later. However, it has been proven rigorously that for strong, dilute electrolytes, PB theory describes electrostatics very accurately (38).

Being a difficult, non-linear differential equation to solve, DH linearised the PB equation by assuming a small potential ($\beta z e \psi << 1$) to give the DH equation,

$$\nabla^2\psi = \kappa_D^2\psi, \tag{1.7}$$

where

$$\kappa_D^2 = \frac{\beta e^2}{\varepsilon_r\varepsilon_0}\sum_i z_i^2 n_i. \tag{1.8}$$

This linear differential equation is now easier to solve. The boundary conditions for the system are set within a restricted primitive model, for which an outline is given in figure 1.1, where each ion in the system is assumed to have a radius of $R/2$, such that the distance of closest approach of two ions is R. These boundary conditions then give that for the region of space contained between $R/2 < r < R$, there is no charge density, $\rho_{ion} = 0$, i.e. equation (1.7) is only true for $r > R$. This assumption highlights that the DH theory assumes a dilute concentration of ions where no ion is in contact and hence the charge of the ions do not overlap, otherwise there would be some charge within the region $R/2 < r < R$. First, equation (1.7) is rewritten in spherical coordinates to better represent the situation in figure 1.1:

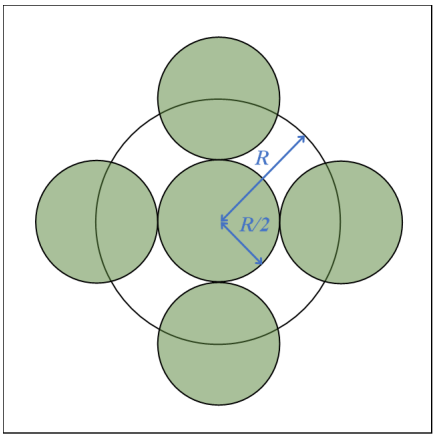

FIGURE 1.1: A diagram of the boundary conditions within the restricted primitive model.

$$\frac{1}{r^2}\frac{\mathrm{d}}{\mathrm{d}r}\left(r^2\frac{\mathrm{d}\psi}{\mathrm{d}r}\right) = \kappa_D^2\psi, \tag{1.9}$$

for which a solution is:

$$\psi = A_1\frac{\exp\left(-\kappa_D r\right)}{r} + B_1\frac{\exp\left(\kappa_D r\right)}{r}. \tag{1.10}$$

To satisfy the condition that $\psi(r \to \infty) \to 0$, $B_1 = 0$. To determine A_1 we solve at the boundary $r = R$, where following Poisson's equation when $\rho_{\text{ion}} = 0$ (Laplace's equation),

$$\frac{1}{r^2}\frac{\mathrm{d}}{\mathrm{d}r}\left(r^2\frac{\mathrm{d}\psi}{\mathrm{d}r}\right) = 0, \tag{1.11}$$

for which a solution is

$$\psi = \frac{A_2}{r} + B_2. \tag{1.12}$$

Then, applying Gauss' law where $E = -\mathrm{d}\psi/\mathrm{d}r$, we find that $A_2 = q/4\pi\varepsilon_r\varepsilon_0$. Finding A_1 and B_2 requires another boundary condition in electrostatics to be applied that across a charge boundary, ψ & $\varepsilon_r\varepsilon_0(\mathrm{d}\psi/\mathrm{d}r)$ must be continuous, i.e. at $r = R$,

$$\frac{A_1}{R}\exp\left(-\kappa_D R\right) = \frac{q}{4\pi\varepsilon_r\varepsilon_0 R} + B_2, \tag{1.13a}$$

$$\frac{A_1}{R^2}\exp\left(-\kappa_D R\right) + \frac{\kappa_D A_1}{R}\exp\left(-\kappa_D R\right) = \frac{q}{4\pi\varepsilon_r\varepsilon_0 R^2}, \tag{1.13b}$$

which gives:

$$A_1 = \frac{q\exp\left(\kappa_D R\right)}{4\pi\varepsilon_r\varepsilon_0(1+\kappa_D R)}, \tag{1.14a}$$

$$B_2 = -\frac{q\kappa_D}{4\pi\varepsilon_r\varepsilon_0(1+\kappa_D R)}. \tag{1.14b}$$

The final form of the DH theory is then

$$\psi = \frac{q}{4\pi\varepsilon_r\varepsilon_0}\frac{\exp(-\kappa_D(r-R))}{r(1+\kappa_D R)} \qquad r > R \tag{1.15}$$

$$= \frac{q}{4\pi\varepsilon_r\varepsilon_0 r} - \frac{q\kappa_D}{\varepsilon_r\varepsilon_0(1+\kappa_D R)} \qquad R/2 < r < R, \tag{1.16}$$

which for $r > R$ reduces for simplicity to

$$\psi = \frac{q\Theta}{4\pi\varepsilon_r\varepsilon_0}\frac{\exp(-\kappa_D r)}{r}, \tag{1.17}$$

where $\Theta = \exp(\kappa_D R)/(1+\kappa_D R)$ is the correction factor due to the exclusion of ions from the region $R/2 < r < R$. So, the potential from a point charge in a medium containing a dilute amount of additional point charges follows a screened coulomb potential, often termed a Yukawa potential, when $r > \kappa_D^{-1}$. At closer separations, the potential approximates to a Coulombic ($\psi \propto r^{-1}$) dependence. This is the major result of the DH theory, where the parameter $\lambda_D = \kappa_D^{-1}$ is the DH length, an extremely useful length scale in describing the electrostatics of electrolytes. This can be written more simply by inputting the definition of the Bjerrum length (eq. (1.2)) into equation (1.8) such that the DH length becomes, for univalent ($z = 1$) electrolytes,

$$\lambda_D = (4\pi\ell_B n_{ion})^{-1/2}. \tag{1.18}$$

A few sanity checks from this theory are to analyse Poisson's equation again by inputting the DH result for $\nabla^2\psi$, and this shows that the total charge that surrounds a single ion equals the charge of that ion, i.e. the ionic atmosphere that surrounds a point charge in solution completely neutralises it, so when outside that ionic atmosphere, that point charge is completely *screened*. The DH length λ_D hence gives an indication of the width of the ionic atmosphere. As the interaction between two charged species is in fact due to the overlap of these ionic atmospheres, λ_D also gives an indication of the range for electrostatic interactions between charged objects in solution. Equation (1.18) may initially indicate that the range of electrostatics is smaller in less polar solvents where ℓ_B is longer. However, n_{ion} is usually much smaller in such solvents due to less dissociation, and as previously mentioned the maximum $n_{ion} \sim \ell_B^{-3}$, so in fact the scaling can be thought of as $\lambda_D \sim \ell_B$. Thus, longer ranging electrostatic interactions are predicted in less polar solvents due to the weaker screening.

1.1.4 Charged Surfaces

Chemical groups on the surface of materials will also dissociate when immersed into a solvent. Indeed it is difficult for any surface to remain completely neutral when in solution. The driving force again is the entropy gain of the counterion no longer

being confined to the surface. Charging can also occur by adsorption of ions from the solution onto a surface.

The simplest system is one where a surface is immersed in a de-ionised solvent such that it becomes charged and only the counterions exist in solution, i.e. the salt-free limit, or equivalently the *counterion-only* limit. Such systems are likely to arise when either two surfaces are very close together such that all coions are expelled between them or near highly charged surfaces. Such systems that invoke this approximation are between liquid crystal bilayers (39–42), charged membranes (43) and in the swelling of clays (44–46). This is also assumed to be the case in nonpolar solvents where, unlike water, the solvent molecules themselves remain uncharged and nonpolar and hence do not act as either a coion or counterion (47). Despite the general assumption that charges should not exist in nonpolar solvents due to the large Bjerrum length, evidence of electrostatic interactions, and hence surface charging, have been observed in the literature (48, 49). Most commonly, charging in nonpolar solvents is achieved by the addition of surfactants which provides stabilisation to the ions by increasing their effective size closer to ℓ_B (50–53). The subtleties of electrostatics with regard to nonpolar systems is described in more detail in section 1.2.7.

Counterion-only limit

For a system containing just a surface of charge density σ and univalent counterions (e.g. $z_+ = 0, z_- = 1$), the PB equation becomes a more simple equation to solve,

$$\frac{d^2\psi}{dx^2} = -\frac{\rho_{ion}}{\varepsilon_r\varepsilon_0}\exp\left(-\beta e\psi\right), \tag{1.19}$$

for which a solution is (43, 54)

$$\psi = \frac{2}{\beta e}\ln\left(x+b\right) + \psi_s, \tag{1.20}$$

where b is the Gouy-Chapman length,

$$b = \frac{2\varepsilon_r\varepsilon_0}{\beta e|\sigma|} = \frac{e}{2\pi\ell_B|\sigma|}. \tag{1.21}$$

This length provides an identical physical meaning to the Bjerrum length ℓ_B, but rather than the interaction being between two point charges, it is between a point charge and a charged surface; b is the distance from a charged surface where half the counterions reside.

Inputting this result for ψ back into the Boltzmann equation (eq. (1.4)) we arrive for the profile of the density of ions from the surface,

$$\rho(x) = \frac{1}{2\pi\ell_B}\frac{1}{(x+b)^2}. \tag{1.22}$$

The main point to note from the counterion-only case is that the ion profile decays algebraically from the surface.

Charged Surfaces in Electrolyte Solutions

A different profile of ions exists when both counterions and coions are present. Just as they do in the bulk, ions will arrange themselves due to the same principles near a charged surface to reduce the free energy. This arrangement was first proposed by Helmholtz to consist of a bound layer of counterions that completely neutralises the surface charge (*55*), with the rest of the ions in the bulk. However, due to thermal motion, a more probable arrangement was thought by Gouy & Chapman to be a diffuse arrangement of ions above the surface (*56*, *57*). What is currently accepted is that both these arrangements are partly present and form a *double layer* of ions, an inner bound layer, and an outer diffuse layer (*58*). Often called the Stern layer, the inner bound layer of ions is thought to be of molecular thickness, whereas the diffuse layer was derived by Gouy & Chapman to have a thickness equivalent to the DH length λ_D (eq. (1.18)). The Gouy-Chapman (GC) theory was in fact published before the DH theory, and again utilises the PB equation (eq. (1.6)) to describe the arrangement of ions above, in this case, a surface of charge density σ and surface potential ψ_s. The system is considered one-dimensional, with the x-axis directed perpendicular to the charged surface. The derivation of this result is given in appendix B, where the final form reduces to an exponential decay,

$$Y = Y_s \exp(-\kappa_D x), \tag{1.23}$$

where $Y = \tanh(\beta z e \psi/4)$ & $Y_s = \tanh(\beta z e \psi_s/4)$, which for small potentials reduces to $\psi = \psi_s \exp(-\kappa_D x)$. A diagram of the form of the potential in the double layer is shown in figure 1.2, where the exponential profile exists in the outer, diffuse layer of ions, but decreases linearly across the inner, bound (Stern) layer.

The surface charge density σ according to Gauss' law is then proportional to the derivative of the potential at the surface $\psi_{x\to 0}$,

$$\left.\frac{d\psi}{dx}\right|_{x=0} = -\frac{\sigma}{\varepsilon_r \varepsilon_0}. \tag{1.24}$$

Interestingly this equation means that although a surface potential may be positive, the charge may not always also be positive. This would occur, for example, if a positive potential initially increased in magnitude away from the surface. Within the PB framework, σ can be reached by an integration of equation (1.6) in this one-dimensional analysis which gives (see appendix A)

$$\sigma = \sqrt{\frac{4\rho_{ion}}{\beta z e}} \sinh(\beta z e \psi_s/2). \tag{1.25}$$

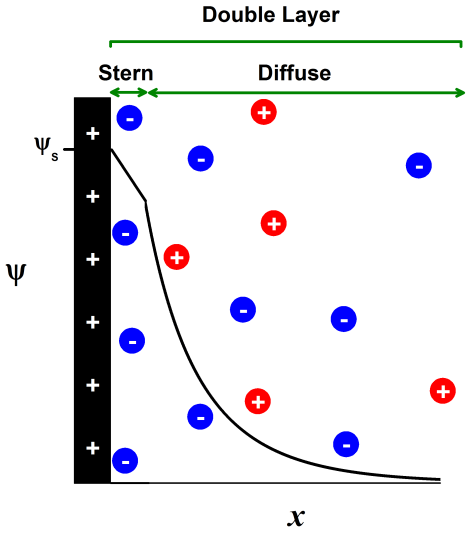

FIGURE 1.2: Diagram of the double layer of counterions and coions near a charged surface in an electrolyte solution. The inner bound layer of counterions is called the Stern layer, and the outer layer is the diffuse layer. The potential drops linearly cross the Stern layer, but follows the exponential decay derived in GC theory ($\psi = \psi_s \exp(-\kappa_D x)$) in the diffuse layer. The two plots for the potentials are not to scale in this diagram.

This is known as the Grahame equation and relates the surface charge density with the potential at the surface due to the electrical double layer.

1.1.5 Interaction Between Charged Surfaces

The electrostatic interaction between two charged objects in solution arises due to the overlap of the double layers of ions near the surfaces. This interaction is purely entropic, but is called an electrostatic (or double layer) interaction due to it being a consequence of the charge of the surfaces. Because the ionic atmosphere extends away from the surface, the electrostatic interaction is often the longest ranging between two surfaces unless sufficient charge screening (compaction of the double layer) is induced. This means that the electrostatic interaction is hugely important in governing the overall interaction between particles in suspension.

The interaction between two charged surfaces can be described by the pressure (force per unit area) exerted on the surfaces due to the confined ions. This is often calculated to be an osmotic pressure Π which is the difference between this pressure between the plates, and the pressure due to the bulk ions. The pressure P due to the ions is approximated by the ideal gas pressure of the ions between the two plates ($P = nk_BT$), so that the osmotic pressure, often called the disjoining pressure, is $\Pi = k_BT(n_{i,\text{in}} - n_{i,0})$. Where $n_{i,\text{in}}$ and $n_{i,0}$ are the number density of ions i between the plates and in the bulk respectively. An additional, attractive electrostatic pressure also acts on the two surfaces which is the Maxwell stress tensor, and this is given to

be $\Pi_{el} = -\varepsilon_r\varepsilon_0 E^2/2$. So the total osmotic pressure between two charged plates in solution due to their overlapping double layers is

$$\Pi = -\frac{\varepsilon_r\varepsilon_0}{2}\left(\frac{d\psi}{dx}\right)^2 + k_B T\left[\sum_i n_{i,in} - \sum_i n_{i,0}\right], \tag{1.26}$$

where $\sum_i n_{i,0} = n_{ion}$, and $\sum_i n_{i,in} = n_{i,0}\cosh(\beta e\psi)$ from Boltzmann's equation (eq. (1.4)) and thus,

$$\Pi = -\frac{\varepsilon_r\varepsilon_0}{2}\left(\frac{d\psi}{dx}\right)^2 + k_B T n_{ion}\left[\cosh(\beta e\psi) - 1\right]. \tag{1.27}$$

The first term from this shows the attractive electrostatic term between the two plates (negative contribution) and the second term gives the entropic repulsion between the plates due to the confinement of the ions.

For two surfaces at a separation L, where one plate is at $x = 0$ and the other is at $x = L$, Π can be evaluated at the mid-plane between the two surfaces (at $x = L/2$). Here the potential goes through a minimum for two identical surfaces (same surface potential), i.e. $\psi' = 0$ and therefore the pressure between the two plates is simply dependent on the potential at the mid-plane $\psi_m = \psi(x = L/2)$, which for small potentials approximates equation (1.27) to

$$\Pi(L) \approx n_{ion}\beta e^2\psi_m^2. \tag{1.28}$$

Therefore, within the PB framework, the interaction between two identically charged surfaces is always repulsive due to the intervening ions in solution. ψ_m can be calculated from the superposition of the two potential profiles from both surfaces that follow GC theory (Appendix B), so for large separations where $\psi \to (4/\beta e)Y_s\exp(-\kappa_D x)$,

$$\psi_m \approx \psi_1 + \psi_2 \approx 2\frac{4k_B T}{e}Y_s\exp(-\kappa_D L/2), \tag{1.29}$$

where $Y_s = \tanh(\beta ze\psi_s/4)$. A diagram of the form of this potential between two surfaces is given in figure 1.3. The pressure between two charged plates is then, for weakly overlapping double layers (large L),

$$\Pi(L) = 64Y_s^2 n_{ion}k_B T\exp(-\kappa_D L), \tag{1.30}$$

where again for small potentials as in the DH approximation, $Y_s \to \beta ze\psi_s/4$. The validity of this final approximate form has been shown for large plate separations and weakly charged surfaces ($L > b > \lambda_D$) where DH theory (linear PB) is predicted to hold (54).

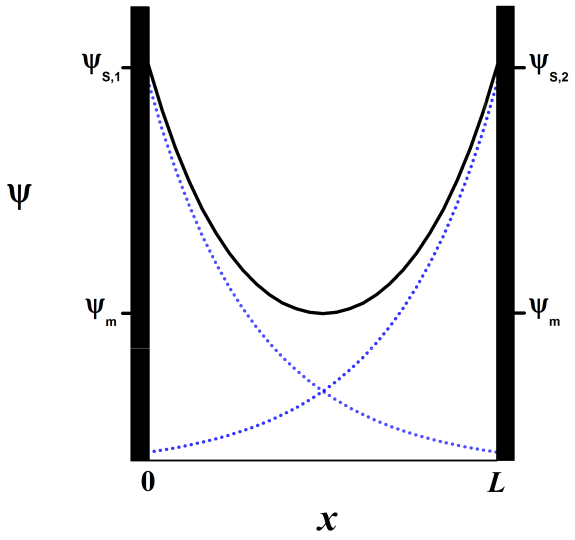

FIGURE 1.3: Solid line is the total potential, and the dashed lines are the potentials from the two charged surfaces, according to equation (1.29).

Counterions-only

In the case of just univalent counterions between the two charged surfaces, the PB equation can be solved to give the interaction potential (*54*),

$$\psi(x) = \frac{k_B T}{e} \ln(\cos^2(Kx)), \tag{1.31}$$

where here, the inverse length scale $K = \sqrt{2\pi\ell_B n_m}$ and the counterion density at the mid-plane is n_m. Using that $\psi'_m = -\sigma/\varepsilon_r\varepsilon_0$, and the definition for the GC length b (eq. (1.21)), the inverse length scale becomes

$$KL\tan(KL/2) = \frac{L}{b}. \tag{1.32}$$

Using equation (1.26), the osmotic pressure then becomes

$$\Pi = k_B T n_m = \frac{k_B T}{2\pi\ell_B} K^2. \tag{1.33}$$

For weakly charged surfaces ($L/b << 1$), the osmotic pressure can be approximated by

$$\Pi = \frac{k_B T}{\pi\ell_B b}\frac{1}{L}, \tag{1.34}$$

and for strongly charged surfaces ($L/b >> 1$), the approximation becomes

$$\Pi = \frac{\pi k_B T}{2\ell_B}\frac{1}{L^2}. \tag{1.35}$$

So again, in the case where only counterions are present, the interaction becomes algebraic in the surface separation rather than exponential.

Boundary Conditions

The above discussion into the theory of electrostatic interactions between charged surfaces has been done so under the assumption that the two surfaces remain at a constant surface charge density (CC), i.e. σ is independent of L. This assumption is valid while L is large, but at smaller surface separations, this assumption is not always true in real systems. In the opposite limit, some surfaces are far better described by having a constant surface potential (CP) instead, where charge groups can dissociate and associate to modify the surface charge density, but the surface potential remains a fixed value. This is appropriate with metallic surfaces for example. At large L, both these boundary conditions will produce the same asymptotic value for the osmotic pressure, but at small L, usually around the thickness of the double layer (λ_D) or less, these boundary conditions will give different results.

Physically, these two boundary conditions can be explained with the presence of the counterions in the double layers. As explained above, a repulsion exists between two identically charged surfaces due to the confinement of the double layers, with a stronger repulsion felt between more highly charged surfaces due to the increased number of ions in the double layers. For plates of opposite charge, the overlap of the double layers results in ejection of ions between the two surfaces. As the surfaces begin to mutually neutralise each other, the ions are no longer needed to neutralise the surface charge. This expulsion of counterions results in an osmotic attraction between the plates to fill the now empty solvent between them. If the plates are of precisely equal and opposite charge, they will totally neutralise each other and will attract until contact. However, if one plate has a different charge density than the other, however slight, some counterions will remain between the two plates to neutralise this excess surface charge, thus a repulsion arises at close separations. The larger the difference in charge magnitude, the more counterions will reside between the plates, and the longer ranged the repulsion will be. This is the case if both surfaces are kept to be a constant charge density.

Applying either a CC ($\psi'_m = -\sigma/\varepsilon_r\varepsilon_0 = \text{constant}$) or CP ($\psi_s = \text{constant}$, $\sigma \sim L$) condition before evaluating the osmotic pressure derived in equation (1.27), it can be shown (see reference (*59*) for a fuller explanation) that at small L this gives two different limiting results:

$$\Pi_{CC} \to L^{-1}, \tag{1.36a}$$

$$\Pi_{CP} \to \Pi_{L=0}. \tag{1.36b}$$

So in the CC case, the repulsion diverges at small L because there is a finite number of counterions between the surfaces, whereas for the CP case, the repulsion

tends to a fixed value because $\sigma \to 0$. It is not just the limiting value of the repulsive pressure that is different when applying either of these boundary conditions. What is also different and extremely important to note, is that for non-identically charged surfaces, repulsions can turn into attractions at small surface separations (*60*).

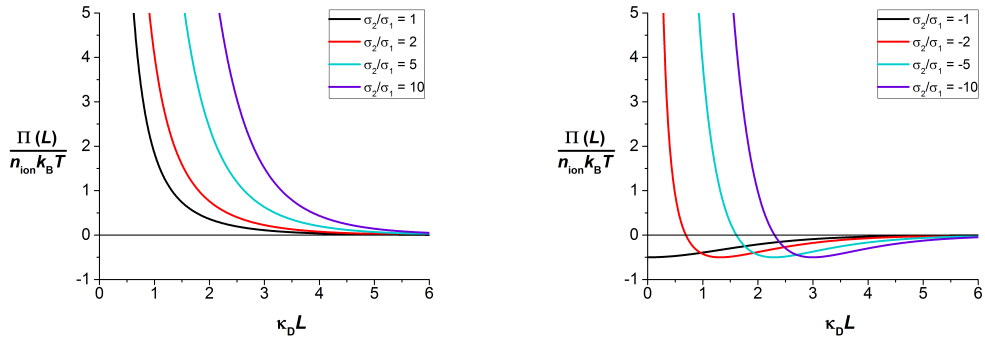

(a) Like-charge (b) Opposite-charge

FIGURE 1.4: Constant charge boundary conditions applied to calculate the osmotic pressure between two charged surfaces with different ratios of their surface charge density σ_2/σ_1 as a function of their reduced separation $\kappa_D L$.

The interaction between two charged surfaces will always be repulsive at small L when held under CC boundary conditions, unless $\sigma_1 = -\sigma_2$ in which case the interaction is purely attractive. This is because there will always be counterions present between the two surfaces to neutralise the more strongly charged surface, and this results in a repulsive osmotic pressure. For two oppositely-charged surfaces, the interaction will change from attractive to repulsive at small L if $\sigma_1 \neq -\sigma_2$. The crossover point from attractive to repulsive interactions depends on the ratio σ_1/σ_2, and are plotted in figure 1.4. The plots for this case follow on from reference (*60*) where they derived for the CC boundary condition within the DH theory (eq. (1.7)) the osmotic pressure between two surfaces of surface charge density σ_1 & σ_2 to be

$$\frac{\Pi(L)}{n_{\text{ion}} k_B T} = \frac{2\sigma_1\sigma_2 \cosh L + \sigma_1^2 + \sigma_2^2}{2\sinh^2 L}. \tag{1.37}$$

The converse behaviour is observed for the CP case, where attractions between two surfaces will always occur at small L even if they are of like-charge. The only case where the interaction remains repulsive until contact is when $\psi_1 = \psi_2$, where $\psi_1 = \psi_s(1)$ & $\psi_2 = \psi_s(2)$. With a constant value of ψ_s, the local ion density near a surface will remain fixed, but the surface charge density will diverge at small separations, hence resulting in an attraction at small L. For the case of like-charged surfaces, this modification of the surface charge density results in a switch in sign of the charge of one of the surfaces. Although slightly difficult to envisage, this is because the effective surface charge density is defined as the derivative of the surface potential, which can switch in sign if the surfaces are close enough. Again, the

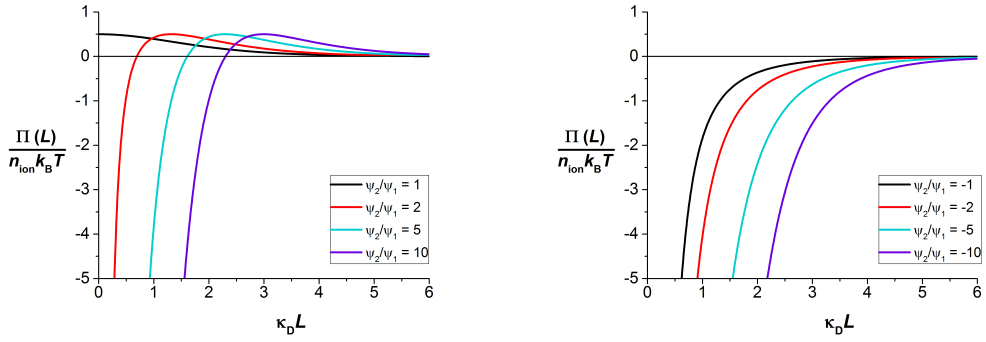

(a) Like-charge (b) Opposite-charge

FIGURE 1.5: Constant potential boundary conditions applied to calculate the osmotic pressure between two charged surfaces as a function of their reduced separation $\kappa_D L$.

crossover from repulsion to attraction depends on the ratio ψ_1/ψ_2, and are plotted in figure 1.5. The plots for this case again follow on from reference (*60*) where they derived for the CP boundary condition within the DH theory (eq. (1.7)) the osmotic pressure between two surfaces of surface potential ψ_1 & ψ_2 to be

$$\frac{\Pi(L)}{n_{\text{ion}} k_B T} = \frac{2\psi_1\psi_2 \cosh L - \psi_1^2 - \psi_2^2}{2\sinh^2 L}. \tag{1.38}$$

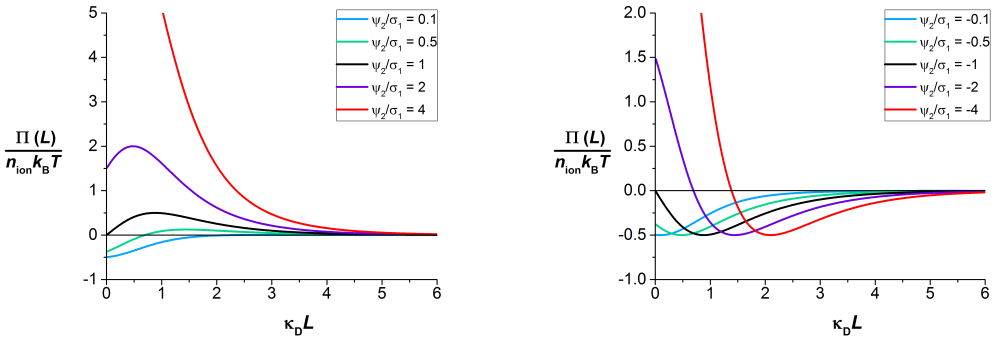

(a) Like-charge (b) Opposite-charge

FIGURE 1.6: Mixed CC and CP boundary conditions as a function of their reduced separation $\kappa_D L$, where in the figures, $\psi_2 = \psi_s(2)$.

What Ben-Yaakov & Andelman also derived was the osmotic pressure in the case where the two surfaces are so different that they can be held under different boundary conditions, i.e. one as CC and one as CP (*60*). This results in very unusual trends in the osmotic pressure, where energy minima (zero osmotic pressure) are located at specific surface separations. This suggests that in such cases the equilibrium separations between the surfaces is at a finite distance apart, depending on the ratio ψ_1/σ_2, which governs which boundary condition will dominate at the

smaller separations. These plots are plotted in figure 1.6, and from (*60*), the osmotic pressure is derived to be

$$\frac{\Pi(L)}{n_{\text{ion}} k_{\text{B}} T} = \frac{2\psi_1 \sigma_2 \sinh L + \psi_1^2 - \sigma_2^2}{2\cosh^2 L}. \tag{1.39}$$

Although this study focuses on interactions between two of the same particles, where each surface being under a different boundary condition is unlikely, this exotic behaviour predicted due to differences between the two interacting surfaces is very suggestive that the surface has a pivotal role in determining whether interactions between charged objects are repulsive or attractive over different length scales.

1.1.6 Charge Regulation Boundary Condition

Most systems are not in fact well described by either a constant potential or a constant charge boundary condition, but reside somewhere between these two extremes. This regime has come to be called the *charge regulation* (CR) boundary condition, and as its name suggests, describes how the surface charge adapts to the local electrostatic field. This therefore better describes surfaces with ionisable surface groups that are in equilibrium with the bulk ions, where the charge groups on the surface can associate or dissociate (changing σ), and the local ion density above the surface is not fixed (changing ψ_s). The two pioneers of the CR boundary condition were Ninham and Parsegian in the 1970s, who derived a mean-field surface dissociation model to show how the interaction between two cell surfaces changes the pH at the surface, and thus the charge density through proton association/dissociation (*61*).

The model they used considered the charging equilibrium on the surface, where a surface group AB can dissociate into a charged surface group A^+ and a counterion B^- (*59*). The equilibrium constant for this process is

$$K_{\text{d}} = \frac{[\text{A}^+][\text{B}^-]_{\text{s}}}{[\text{AB}]}, \tag{1.40}$$

where $[\text{B}^-]_{\text{s}}$ is the surface concentration of B^- that can be determined with the Boltzmann relation (eq. (1.4)) to be $[\text{B}^-]_{\text{s}} = c_{\text{B}} \exp(\beta e \psi_{\text{s}})$, where c_{B} is the bulk concentration of the counterion. The surface fraction of A^+, $\phi_{\text{s}} = \sigma R_+^2 / e$, can be approximated as $\phi_{\text{s}} \sim [\text{A}^+]$, where R_+^2 is the surface area per A^+ charge, because the charge density of the surface σ is purely due to the concentration of A^+, so $[\text{AB}] \sim 1 - \phi_{\text{s}}$. Rearranging equation (1.40) then becomes

$$\phi_{\text{s}} = \frac{K_{\text{d}}}{K_{\text{d}} + c_{\text{B}} \exp(\beta e \psi_{\text{s}})}, \tag{1.41}$$

so the number of charged groups on the surface reduces as the bulk concentration of ions (c_{B}) or potential at the surface (ψ_{s}) increases. For the example where the surface

contains acidic groups, such that $HA \rightleftharpoons A^- + H^+$, this shows how the number of charged groups on the surface reduces as the pH at the surface is reduced. What can also increase the surface potential is the proximity to another charged surface, and therefore it has been shown that the charge density decreases with the surface separation (62–67). This is generally the major result when considering the CR boundary condition. Because counterions can associate with the surface groups and reduce the charge density, the magnitude of the repulsion is therefore reduced below that of the CC case (eq. (1.37)). The exact form of the osmotic pressure between two CR surfaces is shown to depend on the charging process of a particular surface, i.e. if it can adsorb/dissociate just cations/anions or both (59). For a surface that can adsorb just cations or anions, the repulsion is shown to diverge, as in the CC case, at close separations as $\Pi \sim L^{-1/2}$. However, for a surface that can adsorb both cations and anions, the repulsion is shown to tend to a constant value Π_0, as in the CP case, with a gradient $-\Pi_1$ at close separations, i.e. $\Pi \sim \Pi_0 - \Pi_1 L$.

When implementing the CR boundary condition, it has been shown that complex interactions arise between surfaces, including attractions between like-charged surfaces. Unlike the cases outlined for the CC and CP boundary conditions, where attractions only arose between surfaces with an initial asymmetry, the CR boundary condition has been shown to predict attractions between initially identical surfaces due to their ability to modify their surface charge densities (68, 69). Details of this behaviour will be discussed throughout this investigation.

The interaction between point charges and charged surfaces discussed thus far are the foundations for describing the electrostatics between any charged objects in solution. From these theories, the interaction between charged spheres can be approximated, and these interactions govern the stability and function of many colloids.

1.2 Colloids

The term 'colloid' was first used by Thomas Graham in 1861, taken from the Greek word for glue, *kólla*, due to his studies on the differences in diffusion through a membrane of glue and gelatin to salts and acids (70). This classification introduces the size range of a colloid which is from nanometres to tens of microns. Such objects can be dispersed within a solid, liquid, or gaseous phase. For example, liquid droplets or solid particles can be dispersed in the air (aerosols) or in another liquid (emulsion), or air bubbles can can be dispersed to form foams in either a liquid or a solid phase. Colloids remain dispersed for long periods of time, sometimes indefinitely. Some clay suspensions made by Langmuir remained stable for $\sim$ 30 years, and some gold suspensions of Faraday's remain stable even after $\sim$ 150 years (71, 72). Colloidal suspensions are in fact not thermodynamically stable, however, in the case of some gels and glasses, they are kinetically trapped and as such remain

metastable for long periods of time. Many applications of colloids rely on their stability, or controlling their instability, and hence understanding their interactions is crucial. The gospel for colloid stability is DLVO theory, named after its founders Boris Derjaguin and Lev Landau in the USSR in 1941 (73), and Evert Verwey and Theodor Overbeek independently in the Netherlands in 1948 (74). This theory describes the interplay between the van der Waals (vdW) force and the double layer force and how this determines the overall stability of a colloid. Measuring the interactions between charged particles is thus a direct probe to investigate the double layer structure, and thus test current electrostatic theories.

The title of the book '*The colloidal domain: where physics, chemistry, biology, and technology meet*' (75) sums up the numerous applications that can benefit from research into colloids. Given the wide size range that defines them, colloids encompass an enormous number of systems. Many such systems are biological, such as proteins, DNA, viruses, lipids, surfactants, cells, bacteria, mitochondria, etc. This makes colloid science central to understanding interactions between such objects and thus their function, or in designing new medicines. A lot of research for example focuses on synthesising synthetic particles or surfaces that mimic biological systems which they can then study the behaviour of. Many foods are also colloidal dispersions, such as jelly, ice-cream, mayonnaise, and gravy. Then there are basically all cosmetics: shampoos, soaps, moisturisers, deodorants, and make-up, again a very profitable industry. Colloids are also central to the formulations used in the agrochemical, fire-fighting foam, adhesive, and mining industries. The umbrella of colloids also encompasses many natural processes, such as clouds, fog, pearls, rubber, and milk. Despite all these systems being different in their chemical and physical properties, they share several physical attributes and their stability in suspension, and thus their function, can be described by the same general theories.

1.2.1 Scattering

Given the size of colloidal particles, they often exhibit several common physical behaviours. For example, colloids scatter radiation. This phenomenon was first noticed by Faraday in 1857, where solutions of gold nanoparticles appeared red in colour but that a blue colour emerged when a light was passed through it (76). The colour of the solutions he also noted depended on the size of the gold particles. The blueish colour was again observed by Tyndall in 1869, where he documented that this was a feature of samples consisting of particulate gases or solutions (77). This scattering of visible light he suggested is the reason why the sky is also blue, as it contains particles comparable in size or smaller than the wavelength of light. A few years later, Rayleigh derived that the scattered light intensity is proportional to the wavelength of the light to the power of four (78). Blue light, having the largest wavelength, is then the most dominant colour in the scattered light, and hence why suspensions such a flour in water have a blue hue. This phenomenon is now known as the Tyndall effect, and can explain the blue colour of the sky due to scattering

by molecules, the red colour of sunsets when there is dust in the air (without the dust it appears a more yellow colour) and even blue eyes (there is no blue pigment in the eye, it is the scattering through a layer above the eye that determines eye colour. The more pigment in this layer, the more brown the eye colour). Indigo and violet, having longer wavelengths than blue, are seemingly less dominant than blue because our eyes cannot detect them as strongly. This colouration effect is due to the scattering of objects smaller than the wavelength of the light. Scattering also occurs from particles of similar size to the wavelength of light, but this results in no difference in scattering between different wavelengths, and hence it simply results in colloids appearing white, just like milk or clouds, and this phenomenon is called Mie scattering (*79*). The appearance of colloids can therefore directly indicate their stability. For solutions of particulates around the micron size, stability is inferred by a white solution, but for solutions of smaller particles, a cloudy appearance can suggest instability as any aggregates formed become the right size to be a Mie scatterer. One obvious application of colloids because of this ability to scatter light is in paints and inks.

1.2.2 Diffusion

Being in solution, the motion of a colloid is disturbed by interactions with the solvent (or air) molecules. The motion induced by such interactions is random and is known as *Brownian motion*, after Brown's studies on the movement of pollen grains in 1828 (*80*). At the time, the reason for this random movement was not understood, but now it is known to be due to the constant collisions of the solvent or air molecules with the surface of the particles. Although one collision is negligible given their relative sizes, the combined effect over the entire colloid surface is enough to displace it. In 1906, Einstein derived a theory that explains Brownian motion within a random-walk framework, and related this motion to the diffusion of the particles towards an evenly distributed suspension (*81*). The diffusion process is analogous to that of molecules described by Fick $\sim$ 50 years previously (*82*), where the process is encompassed within a parameter called the diffusion coefficient D, with units of $\mathrm{m}^2\ \mathrm{s}^{-1}$.

The definition of D comes from Fick's laws of diffusion (*82*):

$$J = -D\,\frac{\partial c}{\partial x}, \tag{1.42a}$$

$$\frac{\partial c}{\partial t} = D\,\frac{\partial^2 C}{\partial x^2}. \tag{1.42b}$$

The first law describes the flux J of a material across a boundary due to a concentration gradient $\partial c/\partial x$, and the second law describes the time-dependence

of the diffusion of particles. A solution to this differential equation is, for a system confined to one-dimension (x only),

$$c(x,t) = \frac{1}{\sqrt{4\pi Dt}} \exp\left(-\frac{x^2}{4Dt}\right). \tag{1.43}$$

This is a normal distribution with a mean displacement $\langle x \rangle = 0$ and a mean square displacement (equivalently the variance in the separation) $\left\langle \left(x - \langle x \rangle\right)^2 \right\rangle = \langle x^2 \rangle = 2Dt$. Then when confined in n-dimensions, this becomes

$$\langle r^2 \rangle = 2nDt, \tag{1.44}$$

where $r = (x,y)$ in $n = 2$ dimensions and $r = (x,y,z)$ in $n = 3$ dimensions. So, after an infinite amount of time, the probability of finding a particle at any point in a sample should be the same as any other location. This diffusion process is equivalent to the diffusion of a particle in Brownian motion, as the statistics of a random walk also produces a normal distribution, but instead of starting with a specific number of particles, a single particle is located at the origin, then diffuses about this location over time. The same diffusion process occurs even for a particle in an external force, whose average location may also vary with time, $\langle x \rangle = vt$, where v is the particle's velocity. Examples of the probability distribution P(x,t) for the location of a particle undergoing Brownian motion is given in figure 1.7, where in 1.7(a), the particle has no net velocity, but in 1.7(b) it does.

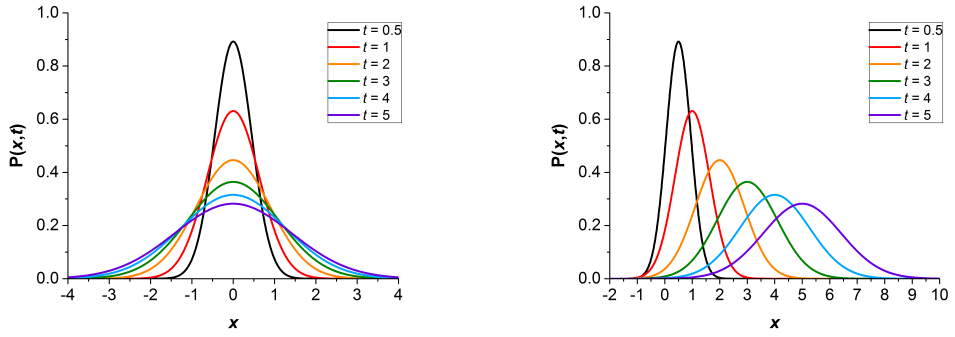

(a) $v = 0$ (b) $v = 1$

FIGURE 1.7: The probability distribution P(x,t) for a particle originally at $x = 0$ to be located at x at a time t. This distribution follows a normal distribution with a mean displacement $\langle x \rangle = vt$ and mean square displacement $\left\langle \left(x - \langle x \rangle\right)^2 \right\rangle = 2Dt$, where in this example $D = 0.2$, and in (a) $v = 0$ and in (b) $v = 1$, taking all parameters to be unitless.

The driving force for diffusion is the difference in chemical potential μ between areas of differing concentrations of particles, so $F_{\text{diff}} = -(1/N_A)\partial\mu/\partial x$, where $\mu = \mu_0 + RT \ln(\gamma c)$, and γ is unity in a dilute system (83). Therefore,

$$F_{\text{diff}} = k_{\text{B}}T\frac{\partial \ln c}{\partial x} = -\frac{k_{\text{B}}T}{c}\frac{\partial c}{\partial x}, \tag{1.45}$$

so for a single particle diffusing under Brownian motion with no external field acting, the opposing force to this motion is the viscous drag force of the solvent molecules, i.e. $F_{\text{diff}} = -F_{\text{drag}}$. The drag force is often termed the Stokes' force, and it is the force exerted on a sphere due to the obstruction of the medium it is moving through. Drag is a force that depends on the velocity of the object moving through a medium, examples of which are air resistance, or in the case relevant here, fluid resistance. For slow moving particles, where the Reynolds number is small (signalling that the inertial forces of the particle are much weaker than the viscous forces from the solvent), the drag force is proportional to the object's velocity v. The coefficient of friction is termed the Stokes' drag coefficient which is found to be $f_0 = 6\pi\eta a$, i.e.

$$F_{\text{drag}} = 6\pi\eta a v, \tag{1.46}$$

where η is the viscosity of the suspending medium, and a is the particle's radius. So as expected, there is more resistance to movement for a larger particle in a more viscous solvent when moving faster. So now equating $F_{\text{diff}} = -F_{\text{drag}}$, with the flux of the particles $J = cv$, and using Fick's first law gives the Stokes-Einstein relation,

$$D_0 = \frac{k_{\text{B}}T}{6\pi\eta a}, \tag{1.47}$$

where we term $D = D_0$ for a freely diffusing particle, also termed the diffusion coefficient at infinite dilution. For a particle with a 1 μm radius (at 298 K) in water, $D_0 \approx 0.24$ μm^2 s^{-1}, or in oil this is reduced to ≈ 0.15 μm^2 s^{-1} due to the higher viscosity.

Although a very useful parameter, the self-diffusion coefficient is only valid for a single sphere. The presence of other particles or walls will cause a deviation in the diffusion coefficient from D_0 due to hydrodynamic coupling. A second body, be it a wall or particle, will alter the fluid flow and distribution near the first body. If one of the bodies moves, this will cause a movement in the fluid surrounding that object and the other object if it is nearby. This fluid movement will then affect the hydrodynamics of the other body and in this way the two bodies are said to be hydrodynamically coupled. The extent of the deviation in the diffusion coefficient from D_0 will then depend on how close those two bodies are, as this coupling effect will be more significant the closer the bodies are. Simply put, if one body moves away from another nearby body, the fluid surrounding it cannot redistribute as fast due to the obstruction of the second body and hence it will diffuse less than expected. Measuring the diffusion coefficient D as a function of particle separation r can be done through the variance in the particle displacement (eq. (1.44)). Batchelor & Green derived the form of the diffusion coefficient for varying separations between

two spheres in a suspension by defining the mobility tensor of the two spheres (*84*, *85*). This tensor describes the coupling effect, and results in the separation dependence of the diffusion coefficient to be

$$D(r) = D_0\left(1 - \frac{3}{2}\frac{a}{r}\right), \tag{1.48}$$

so as the separation between two bodies is decreased, the diffusion coefficient is decreased below that of the self-diffusion coefficient due to hydrodynamic coupling.

1.2.3 Stability: DLVO Theory

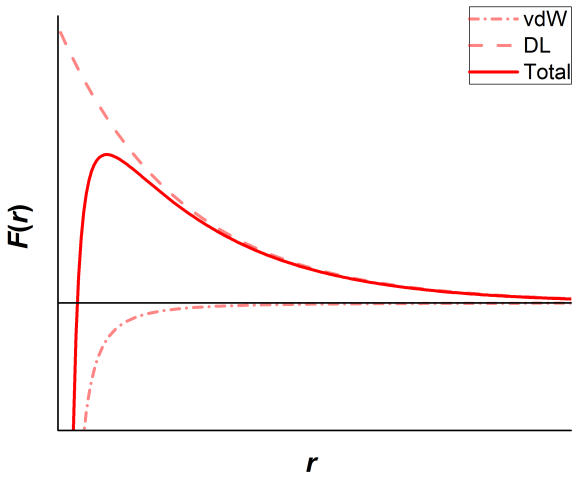

FIGURE 1.8: The force of interaction between two charged spheres according to DLVO theory, the attraction comes from a vdW interaction, and the repulsion from the double layer (DL) interaction. The total interaction force is the addition of these two contributions and governs the overall stability of the colloid.

The DLVO theory describes the stability of a colloid from a summation of the interactions acting between two spheres. The two interactions considered in the DLVO theory are due to the double layer overlap and the vdW force. Combining these contributions produces interaction profiles like those presented in figure 1.8. This shows how the total interaction profile between two identical particles depends on the comparative strength of the electrostatic repulsion and the vdW attraction. Either decreasing the surface charge density or increasing the charge screening, for example by increasing the electrolyte concentration, results in the vdW force becoming more dominant, and an unstable colloid results.

Double Layer Repulsion

The electrostatic force between two charged particles was derived in DLVO theory by first determining the double layer (DL) structure, and hence potential, around a

charged sphere. One method to do this is to invoke the theory of Debye & Hückel by stating that each particle is effectively a point charge surrounded by an excluded area with the radius of the particle a. This method was implemented initially by Levine & Dube (*86*), but perfected in the DLVO theory to give the potential profile from a sphere of charge $q = Ze$ (equivalent to eq. (1.17)),

$$\psi_{DL}(r) = \frac{q\Theta}{4\pi\varepsilon_r\varepsilon_0}\frac{\exp(-\kappa r)}{r}, \tag{1.49}$$

where the point charge correction factor is now $\Theta = \exp(\kappa a)/(1+\kappa a)$, and $\kappa = \kappa_D$. So again, the potential has a screened Coulomb (Yukawa) form. The force of interaction between two identical spheres is then (and inputting the definition of the Bjerrum length (eq. (1.2))),

$$F_{DL}(r) = q\Theta\frac{d\psi(r)}{dr} = Z^2\Theta^2\ell_B k_B T\exp(-\kappa r)\frac{1+\kappa r}{r^2}. \tag{1.50}$$

Derjaguin's Approximation

The electrostatic force between two spheres can also be approximated from the equivalent interaction between two flat plates, but this is only valid in the case of thin double layers ($\kappa_D a >> 1$). This simple relationship is called Derjaguin's approximation, and relates the energy per unit surface area of interaction between two charged plates $U(L)$ and the force $F(h)$ between two charged spheres of radii a_1 & a_2 (*87*) according to

$$F(h) \approx 2\pi\left(\frac{a_1 a_2}{a_1+a_2}\right)U(L). \tag{1.51}$$

Here we note the difference in the symbols used to define separation. L is the separation of two flat plates, h is the separation between the nearest surfaces of two spheres, and r is the separation between the centres of two spheres (i.e. $r = h + 2a$). The energy (per unit surface area) of interaction between two plates is calculable from the pressure between them via

$$U(L) = -\int_{\infty}^{L}\Pi(L)dL. \tag{1.52}$$

The electrostatic contribution to DLVO theory comes from the osmotic pressure derived in GC theory (eq. (1.30)), which gives for the energy (per unit surface area),

$$U_{DL}(L) = \frac{64Y_s^2 n_{ion}k_B T}{\kappa}\exp(-\kappa L), \tag{1.53}$$

so the force of interaction between two charged spheres of radii a_1 & a_2 is then

$$F_{DL}(h) = \frac{128\pi Y_s^2 n_{ion}k_B T}{\kappa}\frac{a_1 a_2}{a_1+a_2}\exp(-\kappa h), \tag{1.54}$$

where for two identical particles of radius a, the factor $a_1a_2/(a_1+a_2) = a/2$. This approximation also derives the interaction between a sphere and a flat plate by using that $a_1a_2/(a_1+a_2) \rightarrow a_2$ for $a_1 >> a_2$.

The DH derivation for $F(r)$ (eq. (1.50)) is a better approximation for thicker double layers, as is more likely the situation in the nonpolar colloids of interest in this study.

vdW Attraction

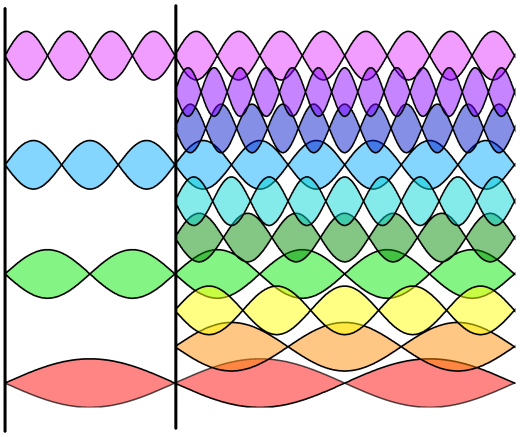

FIGURE 1.9: Diagram to explain the Casimir effect whereby there is an energy difference within the cavity to outside as less modes are allowed and hence there is an attractive force between the plates to reduce the size of the cavity.

The vdW interaction is responsible for the fact that two overall neutral species can attract each other because of the dynamic nature of charges, including electrons, protons, dipoles, charged molecules, etc (*88*). Charges fluctuate in position due to thermal agitation or due to quantum uncertainty, and as they do so they emit electromagnetic (EM) radiation. Those charges also react to absorbed EM radiation as the local electric field is altered. So, when a charge is placed near a mirror, its fluctuation will emit an EM wave, which when reflected back to it by the mirror, will alter the fluctuation of that same charge. This is called a correlation as the movement of the charge is affected by the incoming wave and hence alters its next outgoing wave and so on. When scaled up to two identical molecules next to each other, every charged species in that molecule will emit EM waves that will affect the dynamics of the neighbouring molecule. This change in dynamics will be sent back to the original molecule in a modified wave thus creating a constant *coupling* between the two molecules. This is made more complicated by the fact that different charged species will oscillate at different frequencies (e.g. electron translation at high frequencies, dipole rotations at low frequencies). This coupling results in an interaction force between those molecules which, when summed over all the components of both molecules at all frequencies passing between them, gives the vdW force. Although it is a quantum effect between two parallel conducting

plates, the 'Casimir effect' provides a nice explanation of this force for a colloid scientist by stating that it is a depletion force with the depletant being the EM field; between two parallel plates, only a certain number of EM waves (frequencies) are allowed within that space, whereas outside that space an infinite number of frequencies can exist (*89*). Therefore to increase the space where all frequencies can exist, the plates must push together (see figure 1.9). This effect is seen easily with two plates in a sonicator bath (*90*), or two boats in the ocean (*91*). Obviously for large molecules or even larger objects such as particles, the summation over every charge is cumbersome. Using a continuum approximation, this interaction was derived in full by Lifshitz by assuming the bodies have a continuous, frequency dependent dielectric constant (*92*, *93*). Before this approach was taken, Hamaker assumed a pairwise additivity of the interactions of all the constituents of a large body and devised a way to give every material a physical constant (Hamaker constant) that can tell you the magnitude of the vdW forces between two spherical particles of that material (*94*). For two different materials A & B interacting across a medium m, the Hamaker constant can be approximated from the individual Hamaker constants by $H \approx (\sqrt{H_{\mathrm{A}}} - \sqrt{H_{\mathrm{m}}})(\sqrt{H_{\mathrm{B}}} - \sqrt{H_{\mathrm{m}}})$. For two particles interacting across a medium with Hamaker constant H, the interaction energy between them due to the vdW attraction is (*94*)

$$U_{\mathrm{vdW}}(h) = -\frac{H}{6}\left(\frac{2}{s^2-4} + \frac{2}{s^2} + \ln\frac{s^2-4}{s^2}\right), \tag{1.55}$$

where $s = r/a$. For close separations (small $s = 2 + h/a$), which is a valid approximation as this interaction is short ranged, and at large separations it decays even faster, this becomes

$$U_{\mathrm{vdW}}(h) = -\frac{Ha}{12h}, \tag{1.56}$$

so the force of interaction is then the derivative of this which gives

$$F_{\mathrm{vdW}}(h) = -\frac{Ha}{12h^2}. \tag{1.57}$$

As an example, for polystyrene (PS) interacting across water, $H \sim 10$ zJ (where 1 zJ = 1 $\times 10^{-21}$ J), and across a vacuum this is greatly increased to $H \sim 66$ zJ (*95*). As with most things, using a Hamaker *constant* is an oversimplification, as the value in fact changes with separation between materials, so instead we should use a Hamaker *coefficient* $H_{\mathrm{coef}}(h)$. This coefficient is a summation over every frequency possible ν between the two materials A & B at a given surface separation h, of the difference in the dielectric response ε of both materials and the suspending medium m at those frequencies (the dielectric response of a material depends on the incoming frequency and can be experimentally determined from a material's absorption spectrum as the charges absorb radiation at the wavelengths that correspond to its physical movements (resonance)):

$$H_{\text{coef}}(h) = \frac{3k_{\text{B}}T}{2}\sum_{\nu}\left(\frac{\varepsilon_{\text{A}}(\nu)-\varepsilon_{\text{m}}(\nu)}{\varepsilon_{\text{A}}(\nu)+\varepsilon_{\text{m}}(\nu)}\right)\left(\frac{\varepsilon_{\text{B}}(\nu)-\varepsilon_{\text{m}}(\nu)}{\varepsilon_{\text{B}}(\nu)+\varepsilon_{\text{m}}(\nu)}\right)R(h,\nu), \tag{1.58}$$

where $R(h,\nu)$ includes the terms changing in separation and frequency. So for identical materials A=B, the interaction is always attractive, but for different materials A≠B it depends on the values of ε_{A}, ε_{B} & ε_{m}, which are all a function of ν. This definition immediately shows that the vdW attraction is strongest between two particles when immersed in a medium whose permittivity is different, thus explaining the factor of 6 difference in the Hamaker constant for PS in water and in a vacuum.

The absorption spectra, which gives the frequencies for the summation, consists of maxima with energy of multiples of the thermal energy and hence there are far more high frequency contributions than low (the spectra is over a log scale) and therefore is usually dominated in the UV range. Usually, ε decreases with increasing frequency, but because of the much larger number of high frequency terms, the summation becomes dominated by them. The low frequency contributions are hence excitable by thermal fluctuations such as the rotation of dipolar molecules. The '*zero-frequency term*' is the contribution from the translation of ionic groups as they move so slowly comparatively to the speed of light. The movement of electrons however is much faster and contributes to frequencies in the UV and higher spectral range, and their movement is due to quantum uncertainties rather than thermal agitations. Because of their dominance, equation (1.58) is often approximated to the integral over the highest frequency terms, where the spectrum of allowed frequencies becomes almost continuous.

However, under certain circumstances, the lowest frequency terms become the dominant ones, such as for water where the molecules are dipolar and hence their rotations (low frequency contribution) dominate, or associating and dissociating surface groups (zero frequency contribution) can dominate. In short, the response of the permittivity of a material to frequency depends on the charge constituents of that material; it is the relative difference in those dielectrics of the material and medium, at each frequency in the summation, that gives the total Hamaker coefficient, and hence the strength of the vdW interaction.

The function $R(h,\nu)$ explains how the lower frequency contributions are longer ranging and hence dominate at large separations. This function is called the 'relativistic retardation correction factor' and is a consequence of the speed of light being a constant value c_0. Simply put, because the time taken for any wave to travel from point A to B (a distance h) and back again across the medium takes a finite time ($\propto h/c_0$), higher frequency oscillations have already completed several oscillations in that time and hence will not exhibit a correlation. However, low frequency oscillations may not have completed an oscillation in that time and therefore will correlate with the reflected wave. Effectively, $R(h,\nu)$ decreases with frequency approximating to 1 at low frequencies, and to 0 at high frequencies.

Mathematically this is seen in the following equations, where the relative time scale for oscillation is τ and wave travel is t:

$$r_t(h,\nu) = \frac{t}{\tau} = \frac{2h\varepsilon_m^{1/2}/c_0}{1/\nu} \propto h\nu, \tag{1.59}$$

where the refractive index $n \approx \varepsilon_m^{1/2}$. So $r_t(h,\nu)$ is small for low frequencies and small separations. $R(h,\nu)$ is then given as a function of $r_t(h,\nu)$,

$$R(h,\nu) = \left[1 + r_t(h,\nu)\right] \exp(-r_t(h,\nu)) \approx \left[1 + h\nu\right] \exp(-h\nu), \tag{1.60}$$

so for a significant contribution to the Hamaker coefficient ($R(h,\nu) \to 1$), $r_t(h,\nu)$ needs to be small to reduce the exponential damping term, which at large h is only achieved with low ν. So in our system where long range interactions are being measured, the significant contribution from vdW forces is the lowest frequency terms.

As with the coulomb interaction, the low frequency interaction is also electrostatically screened by the double layer of counterions and coions surrounding the two surfaces. What is different with this interaction is that because it relies on the 'to and fro' of the wave, the interaction is effectively doubly screened, i.e. from A to B the interaction is screened by the factor e^{-h/λ_D}, then on its return to A it is again screened by the factor e^{-h/λ_D}, where λ_D is the Debye screening length (eq. (1.18)). So, for this specific case, the factor $R(h,\nu)$ in equation (1.58) becomes

$$R(h,\nu \to 0) = \left[1 + 2h/\lambda_D\right] \exp(-2h/\lambda_D). \tag{1.61}$$

What this section has shown, is that often, only the high frequency terms are considered when discussing vdW interactions. This however is not a suitable approximation to make in systems where long-range interactions are being measured, such as in nonpolar systems, as at these distances, it is the lower-frequency contributions that become dominant.

DLVO

The DLVO theory then sums the contributions of the vdW and double layer interactions to give the final form for the total interaction between two charged particles in suspension. Ignoring for now the additional complexity discussed above for the vdW interactions, when the simplified Hamaker constant H is considered, the DLVO interaction is given by

$$F_{Tot} = Z^2\Theta^2\ell_B k_B T \exp(-\kappa r)\frac{1+\kappa r}{r^2} - \frac{Ha}{12(r-2a)^2}. \tag{1.62}$$

The stability of a colloid suspension can therefore be modified by altering the electrostatics through the solvent (varying ℓ_B), the charge screening (varying κa) or the attraction (varying H). The effect of changing κa (and therefore Θ) and H are

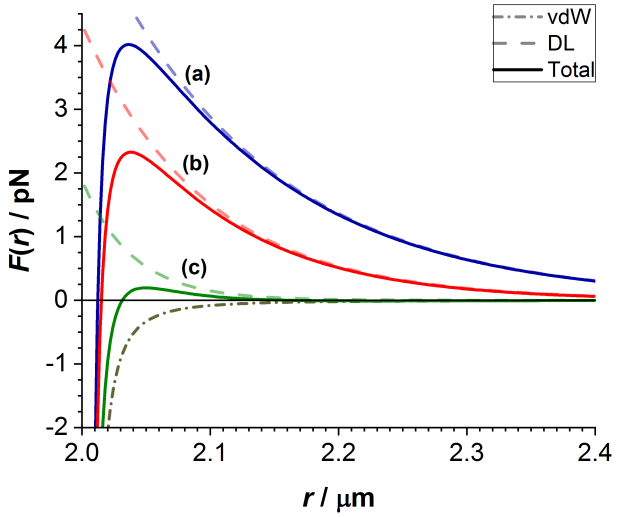

FIGURE 1.10: The effect on the total interaction force profiles by increasing the charge screening from (a) $\kappa a = 7$ to (b) $\kappa a = 10$ to (c) $\kappa a = 25$. The other parameters are kept the same at $a = 1$ μm, $\ell_B = 1$ nm, $H = 10$ zJ, $Z\ell_B/a = 5$, and $T = 298$ K.

shown in figures 1.10 & 1.11 respectively. Increasing either the amount of charge screening, or increasing the Hamaker constant, both result in an interaction that is dominated by the attraction rather than the repulsion.

The effect of changing ℓ_B is shown by comparing two different systems altogether, one representing typical values for PS in water, and the other poly(methyl methacrylate) (PMMA) in dodecane. These two systems therefore have different values of ℓ_B, H and κa, each modifying the total interaction force and hence their stability. This comparison is presented in figure 1.12. The most obvious effect of increasing ℓ_B is that the electrostatic repulsion becomes significantly longer ranged (as it results in a smaller κa), and much weaker at smaller separations. Despite this, the total interaction remains stable until very close particle separations because of the weak vdW interaction in the system. The profiles in figure 1.12 shows how the double layer force can be probed in nonpolar solvents at much larger particle separations, making it a useful system to explore experimentally.

1.2.4 Beyond DLVO (non-electrostatically)

Due to the wide variety of colloidal suspensions, there are more features that can cause either attraction or repulsion between two particles. These can be due to either surface features, or additional objects in the solution, and can result in complex arrangements of the particles, such as a gel.

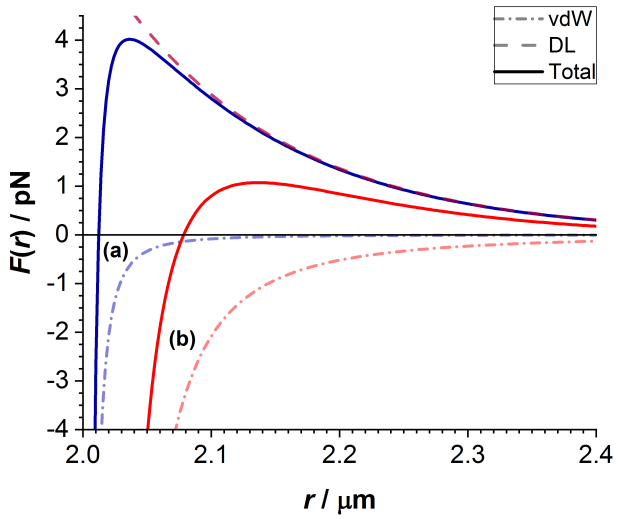

FIGURE 1.11: The effect on the total interaction force profiles of increasing the Hamaker constant from a value typical for (a) PS in water ($H = 10$ zJ (95)) to (b) gold in water ($H = 250$ zJ (96)). The other parameters are kept the same at $a = 1$ μm, $\ell_B = 1$ nm, $Z\ell_B/a = 5$, $T = 298$ K, and $\kappa a = 7$. It is likely that Z would be different for gold and PS in water, but for an easier comparison of just a change in H it is assumed the same here.

Steric/Bridging

The addition of polymer chains to the surface of a particle can result in either a repulsion or an attraction between the particles depending on their density on the surface. At low densities, the polymers tend to adsorb the free end to a nearby particle, bridging them together. To increase the entropy of the polymer, it contracts and hence results in an attraction between the particles. This is termed bridging flocculation (97, 98). However at high densities, polymers fixed to the surface can induce a repulsion between two particles due to the confinement of the brush layers when two particles approach (99). This entropic repulsion is known as steric repulsion, and such polymer layers are often added to particles to maintain stabilisation of the particles by not letting them approach close enough for vdW attractions to dominate. A diagram of the effects of bridging flocculation and steric stabilisation are given in figures 1.13(a) & 1.13(b) respectively. Using this method to stabilise a colloid can have several benefits over just having charged surfaces. Firstly, the steric stability is not affected by the amount of salt in the solution, unless the quality of the solvent is decreased for the polymer, causing them to collapse (100, 101). Secondly, stability will remain even at higher colloid volume fractions because the steric repulsion prevents particles from coming close enough to attract through the vdW attraction. Thirdly, stability can be ensured in systems that are difficult to charge, such as nonpolar ones. The conformation of such chains on the surface was described by de Gennes, which leads to the repulsive osmotic pressure due to

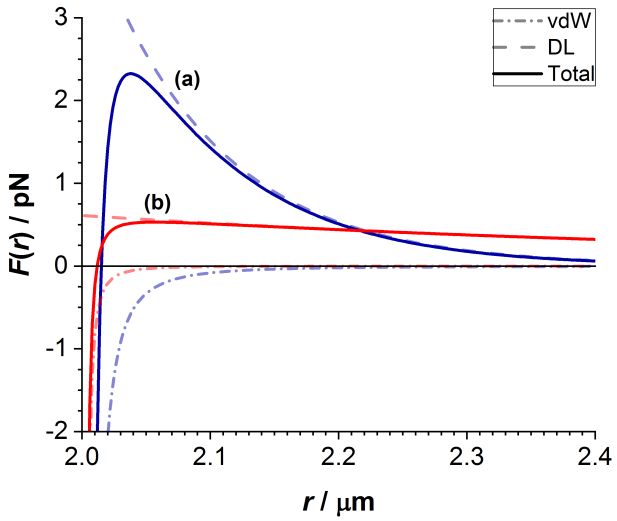

FIGURE 1.12: The different interaction force profiles expected when comparing two different systems: (a) PS in water ($\ell_B = 1$ nm, $\kappa a = 10$, $H = 10$ zJ), and (b) PMMA in dodecane ($\ell_B = 30$ nm, $\kappa a = 1$, $H = 1$ zJ). Typical values for ℓ_B, H and κa in each case are stated, but the other parameters are kept the same for both systems: $a = 1$ μm, $Z\ell_B/a = 5$, and $T = 298$ K.

contraction of the chains to be (*102*, *103*)

$$\Pi_{\text{steric}}(L) \approx \frac{k_B T}{\Delta^3}\left[\left(\frac{2L_0}{L}\right)^{9/4} - \left(\frac{L}{2L_0}\right)^{3/4}\right], \tag{1.63}$$

where L_0 is the unperturbed thickness of the polymer brush layer, and Δ is the distance between each chain adsorbed at the surface. This is the repulsion when the separation of the surfaces is $L < 2L_0$, i.e. when the chains start to inter-penetrate. For separations larger than this, the chains do not touch and hence no pressure is exerted.

Depletion

If polymers are added that do no adsorb to the surface of the particles, a totally different outcome can result. Each polymer chain in the solution has an effective size, usually defined by their radius of gyration R_G. Each chain is free to diffuse just like the particles, and can exist in any volume not occupied by another chain or a particle. Around each particle however, there is a volume of space that the centres of each chain cannot enter, and this volume has a height R_G above the surface. This volume is therefore *depleted* of any polymer, and is thus called a depletion zone. To maximise the entropy of the system, the total volume of all the depletion volumes must be minimised, and this is done so by overlapping them, i.e. bringing the particles into proximity. Of course, when a polymer chain does occupy the space between two particles, the interaction will be repulsive as the chain is in the way, but

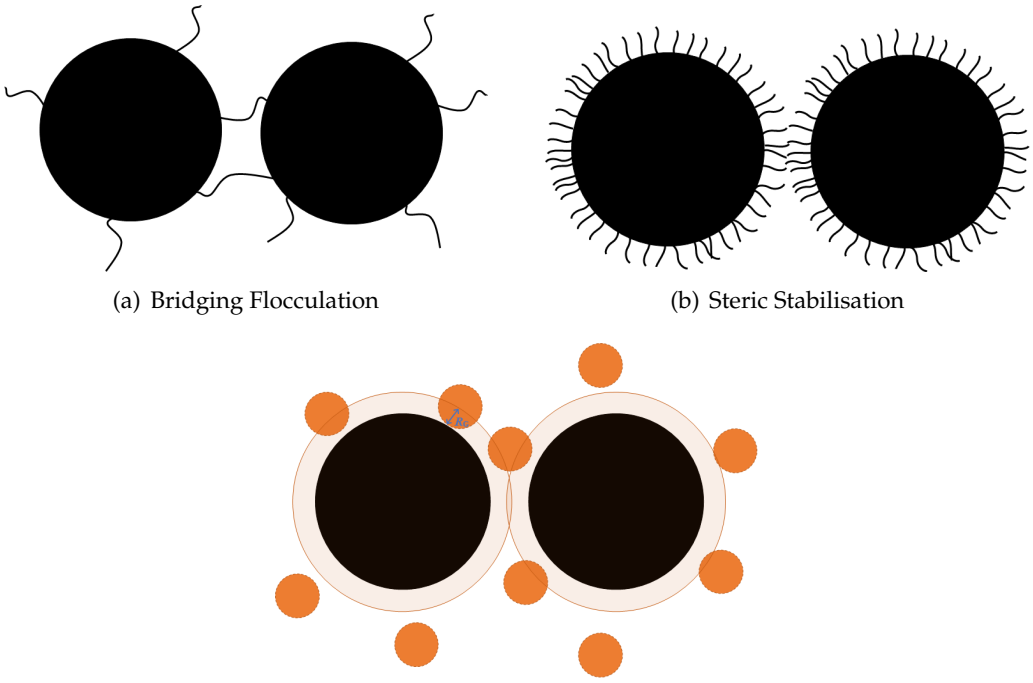

(a) Bridging Flocculation

(b) Steric Stabilisation

(c) Depletion Attraction

FIGURE 1.13: Some non-DLVO interactions due to adsorbed or non-adsorbed polymer that can cause interactions such as (a) flocculation due to the bridging of a few polymer chains adsorbed to the surface of both particles, (b) stabilisation due to a dense covering of polymer chains on the particle surface preventing the particles from coming into contact, and (c) an entropic attraction between two particles induced by the presence of depletants.

taking the average interaction over the entire system results in an overall entropic attraction between particles. This phenomenon is called a *depletion interaction*. It is not just polymer chains that will induce this attraction, but any non-adsorbing additive will do it. The *depletant*, as these objects are called, must be large enough to cause a depletion zone of significant size comparative to any double layers or steric hindrance to cause an overall attraction. A diagram of this effect is given in figure 1.13(c). The model used to describe this interaction was pioneered by Asakura and Oosawa in the 1950s, where the osmotic pressure between two particles of radius a is (*104*, *105*)

$$\Pi_{\text{dep}}(L) \approx \pi c_{\text{dep}} k_{\text{B}} T a \left(2R_{\text{G}} - h\right), \tag{1.64}$$

where c_{dep} is the concentration of the depletant, and the radius of the depletant is R_{G}. Again, this interaction is zero when the separation of the particle surfaces $h > 2R_{\text{G}}$, as there is no overlap of the depletion volumes. This interaction is therefore stronger if more depletant particles are added or if the size of the particles are increased. The range of the interaction is completely governed by the size of the depletants as they determine the overlap volume.

Steric and depletion interactions are of most interest in this study, but they are

not the only 'non-DLVO' forces that can be present between colloidal particles. A few other interactions that can affect the stability of a colloid are capillary forces, the hydrophobic effect and hydrodynamic interactions. Due to the difference in polarity between some molecules and water, a motion will occur to reduce the number of interactions between polar and nonpolar species. This is generally referred to as the 'hydrophobic effect'. What results is that hydrophobic species will aggregate in water to reduce their contact area with water molecules, and water will 'bead-up' on hydrophobic surfaces. This effect, for example, is the reason that surfactant molecules will aggregate into spherical micelles in solution, to reduce the contact of either their hydrophobic tails with water, or their hydrophilic head groups with an oil solvent. A good analogy of the capillary force is given by Butt & Kappl in their book on surface forces (see (106)): "*It is impossible to shape dry sand. To build a sand castle, the sand has to be wet. Wet sand can be shaped because particles adhere to each other*". Physically, this is because water can flow into small gaps without an external force pushing it in. A small enough gap can be formed between two particles in close proximity. At the edge of the gap, the liquid will form a meniscus due to the competition of gravity and the interaction of the liquid and the substrate. The curvature of this meniscus causes an attractive osmotic pressure between the two surfaces. Within a capillary, this has the effect of drawing the liquid up the capillary, hence why it is called a capillary force. The forces considered already have been static effects, but sometimes dynamic effects must be considered. A force can be felt by a particles close to an interface due to the fact that the medium it is suspended in no longer acts as it would in the bulk. The fluid near the edge of a beaker, for example, will flow differently due to the physical barrier of the glass wall than it would in the bulk. This difference in flow will then affect the dynamics of the particles suspended near the boundary. An analogy would be to think how different it feels to swim in the open ocean, than it is right next to the beach, and partly why it is preferable to swim in the middle lanes in a swimming race. This means that one must be careful when measuring forces between particles in suspension to ensure that any hydrodynamic effects are considered, or that the experiment is undertaken far from any boundaries.

1.2.5 Beyond DLVO (electrostatically) / Limitations of DH Theory

The DLVO theory describes the electrostatic interaction between two charged particles in line with the mean-field, PB theory. The major assumptions made in the DLVO theory are that the concentration of particles and electrolyte is low, and that the surface potential of the particle is low. This means that far-field and weak interactions between charged particles are well described by the DH theory, which by making certain assumptions, the PB equation can be simplified and thus solvable analytically. These assumptions are made by stating that some considerations can be assumed negligible, including the finite size and discrete nature of every ion, correlations between neighbouring ions, ion specific effects such as the hydration of

ions due to water molecules, and the inhomogeneity of the solution's permittivity near charged surfaces. Thinking of the overall effect each of these additional considerations has on the double layer structure, it can be approximated that they will cancel each other out; with some effects increasing or decreasing the thickness of the double layer or the surface potential, PB theory has been shown to predict very well the electrostatic interaction between two charged particles (*50*, *107*). In some specific systems where such assumptions cannot be made, certain additional electrostatic effects can have a significant effect on the double layer, and therefore the interaction profile. A few such interactions are discussed and include strong correlations between ions, specifically between multivalent ions; interactions between particles with a permanent dipole or 'patchy' surface charges; and interactions due to fluctuating charges on the surface of particles. Considering these phenomena can result in behaviour not predicted within the PB framework, such as charge reversal of surfaces and attractive interactions between like-charged particles.

Strong Coupling

The limits that define the PB theory (low surface potential/surface charge density and univalent counterions at high temperature (this can be encompassed into the definition of the Bjerrum length to mean systems with small Bjerrum lengths)) can be said to describe a *weak coupling* regime. The opposite, *strong coupling* regime, is then one in which there are high surface charge densities and/or the ions are multivalent and/or the Bjerrum length is large. In such systems, the electrostatic interactions between ions in solution and ions and the surface are much stronger. The pioneers in explaining the electrostatics in the strong coupling limit were Rouzina & Bloomfield (*108*) who focussed on explaining the onset of attraction between DNA strands upon addition of multivalent electrolytes (*109*–*112*). The work continued, using mostly a counterion-only description as these are the important ions here, by Shklovski (*113*), Levin (*114*) and then finally formalised by Netz (*115*–*119*) (and their coworkers). Moreira & Netz introduced a *coupling parameter* to define the two opposite regimes, encompassing the different limits mentioned (*115*, *116*),

$$\Xi = \frac{z\ell_{\mathrm{B}}}{b}, \tag{1.65}$$

where the coupling parameter $\Xi < 1$ in the weak coupling regime, when the valency z of the counterions is small, the temperature is high (small ℓ_{B} (eq. (1.2))), and the surface charge density is small (large Gouy Chapman length b (eq. (1.21))). Thus, the strong coupling regime is defined when $\Xi > 1$. Physically, in the weak coupling regime, the ions near the surface are in a three-dimensional diffuse arrangement where the thickness of the counterion layer ($\sim b$) is larger than the average distance between the counterions d. In the strong coupling regime however, the counterions form an almost two-dimensional arrangement above the surface, as their average

spacing becomes larger than the thickness of the layer. A diagram of the counterion profile in the opposite limits of strong and weak coupling are given in figure 1.14. Without a diffuse arrangement of ions, it is therefore obvious that PB theory will break down. This two-dimensional arrangement of ions is due to strong ion-ion and ion-surface correlations, and the consequence is that the counterion profile from the surface is no longer algebraic (eq. (1.22)), but instead becomes exponential (see (*116*)). Therefore the interaction profile deviates substantially from that derived within the PB framework for weakly coupled systems.

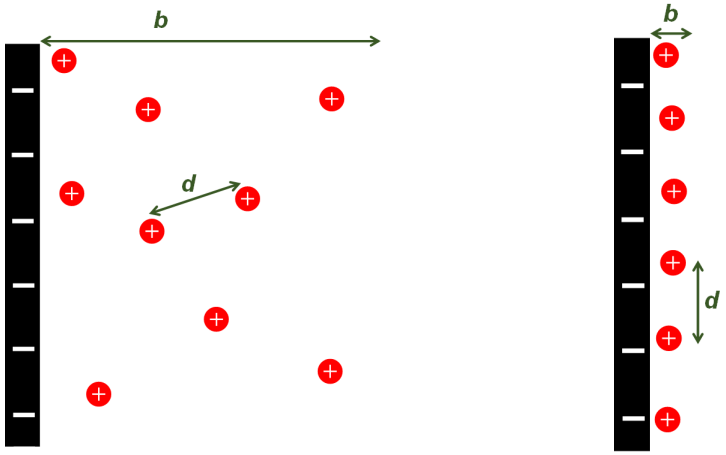

(a) $\Xi < 1$ (b) $\Xi > 1$

FIGURE 1.14: The counterion profile near a charged surface in the (a) weak coupling and (b) strong coupling regimes.

One such deviation from PB theory is the observed attractions between like-charged macroions (particles and biological species) due to the addition of multivalent ions (see for example refs (*120*–*134*)). In PB theory, repulsion is always predicted when counterions reside between the two surfaces. This is explained within the strong coupling regime where the multivalent ions result in $\Xi > 1$. This attraction is described in detail by Netz (*116*) and is due to the strong attraction between the counterions and the surface that becomes dominant over the entropic repulsion due to the confined counterions, thus leading to an overall attraction between the two surfaces. Another consequence of this strong coupling of counterions to the surface is observations of a charge reversal of the surface (*124*, *135*–*142*). This occurs when the counterions are multivalent, such that when enough condense on the charged surface, they outnumber the charge of the surface, causing the effective charge of the surface to reverse. This charge reversal has been used to explain the attractions seen in strongly coupled systems (*143*). However it has been shown that attractions occur before the onset of charge reversal and so is not the sole source of attraction in the strong coupling limit (*144*). The reason for the attraction is due to counterion condensation on the surfaces when the coupling between counterion and the surface is strong (large Ξ). Because of the dependence on counterion condensation, this effect is also determined by the curvature of the surfaces involved. The Manning

parameter is often used to define the relative curvature a with the Gouy Chapman length b ($\xi = a/b$) and as such defines the regime where counterion condensation will occur. This limit also depends on the particle concentration (145). If ξ is too small (small radii), counterion condensation will not occur as the attraction between the surface and counterion is not strong enough. So, the attraction between two particles can be predicted in the strong coupling limit, if the Manning parameter is large enough, or if the surface separation is sufficiently close (146).

Image Charges

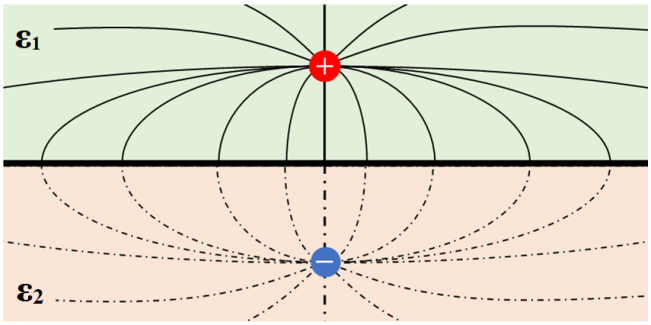

FIGURE 1.15: The image charge ($-$) produced at an interface between two dielectrics due to a point charge ($+$) located near the interface with a dielectric of larger permittivity ($\varepsilon_2 > \varepsilon_1$). The image charge would also be ($+$) if $\varepsilon_2 < \varepsilon_1$. The solid and dashed lines show the electric field lines induced from the point charge and image charge respectively.

A dielectric material is an electrical insulator, however, the molecules that make it up become polarised in an applied electric field. Some examples include ceramics, plastics, oil and deionised water. How easily polarised the material is is quantified by the material's permittivity ε. What results from this polarisation is that the effective electric field in the primary medium is modified. The simplest case to describe this effect is with a point charge in a medium with permittivity ε_1 near the interface with a medium with permittivity ε_2. The electric field emitted radially from the point charge will induce an electric field within medium 2 because both media are dielectrics. The form of this induced electric field in medium 2 is identical to that if another point charge was located in the mirror image location of the initial point charge, as shown in figure 1.15. This imaginary point charge is therefore called an *image charge*. For a conductive boundary, i.e. if medium 2 was a metal, this image charge would have an equal charge magnitude to the point charge. However, between two dielectric media, the charge is lessened to a magnitude of $q(\varepsilon_1 - \varepsilon_2)/(\varepsilon_1 + \varepsilon_2)$, where q is the charge of the point charge. So if $\varepsilon_1 < \varepsilon_2$, the image charge will be oppositely charged, and the interaction of the point charge with the boundary will be attractive, but if $\varepsilon_1 > \varepsilon_2$, the image charge will be of like charge, and the point charge will be repelled from the interface. So, charges will be repelled from media of lower permittivity. This phenomenon was used by Wagner (147) and

Onsager & Samaras (148) to explain why electrolyte ions were depleted from the air-water interface, thus causing the measured increase in the surface tension upon addition of electrolyte (149–152). This same effect occurs between the ions in the double layer and the surface of a charged particle, altering the double layer structure from that predicted within the PB theory, and consequently the interactions between them (153). It has been shown, for example, that because of the depletion of ions near the surface of two neutral plates in polar solvents, a short-ranged attraction and long-range repulsion can result (154). The attraction arising due to the depletion of ions, and the enhanced repulsion due to the decreased screening. For highly charged particles however, the consequences of image charges has been found to be negligible, but may still be important in nonpolar systems, where the particles are expected to be more weakly charged (155, 156).

Patchy Charged Surfaces

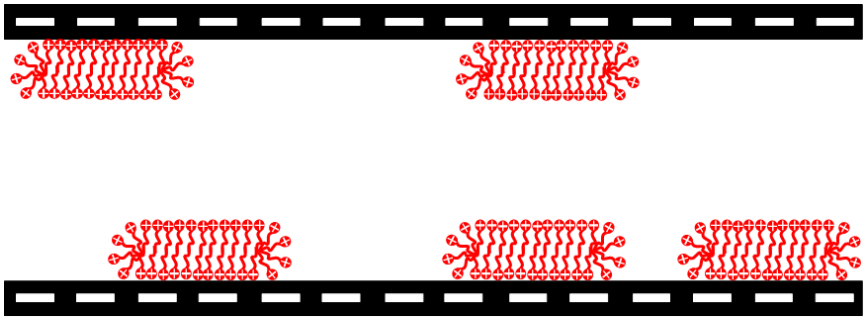

FIGURE 1.16: Cationic surfactant deposited onto a negatively charged surfaces via the Langmuir-Blodgett method and then left submerged in water leads to a surface with patches of charge.

The surface of the particles has thus far been assumed to be homogeneous. However, this may not be the case, especially when considering that in nonpolar systems, the charge of a particle can be due to randomly adsorbed impurities, or dissociation of a few groups on the surface. At large separations, particles can be assumed to be a point charge, but at close separations, any heterogeneity on the surface cannot be ignored. The interaction between two surfaces can be very different depending on the landscape of the surfaces, and interesting structures are expected depending on the 'patchiness' (157–159). Such patchy surfaces have been produced on mica surfaces (useful for SFA measurements) by first depositing surfactant films onto the surfaces, then allowing the surface to be submerged in water (160, 161). The result produces a surface with randomly positioned patches of charge, like that shown in figure 1.16. The interactions between such surfaces has been observed by a few groups, with many concluding that the origin is electrostatic due to its dependence on the ionic strength of the intervening solution (162, 163). Similar, surfactant covered surfaces have been used to produce hydrophobic surfaces to probe what is called the 'hydrophobic attraction' (164–168). The interactions measured in

these studies could however be an indirect consequence of their hydrophobicity; Israelachvili and co workers have suggested that the patchy-charge interaction could in fact be the cause (169).

An explanation of the attraction between two patchy surfaces is that a correlation arises between them to align the oppositely charged patches, possible if the patches are allowed some mobility on the surface (170). This explanation would however predict no interaction between surfaces that could not correlate in this way. Taking this idea, one study measured the interaction between two patchy-charged surfaces *whilst* applying a lateral movement to one of the surfaces (171). The amplitude of the lateral movement was set such that it would frustrate any correlation effects between the two surfaces. Despite this, they measured no difference between the attraction of the two surfaces when moving laterally or not, suggesting that a correlation attraction was not the origin. What the group proposed to explain these findings was that the interaction between two oppositely charged patches is not of equal magnitude to the interaction between two like charged patches. Considering the Coulomb force between point charges in a vacuum this is clearly not the case as they are always equal and opposite, but within the PB framework, applying CC or CP boundary conditions results in unequal, averaged interactions where the attraction between oppositely charged patches is stronger than the repulsion between like-charged patches. Thus, an overall attraction arises between patchy surfaces, even if they are neutrally charged overall (172, 173).

Dipolar Particles

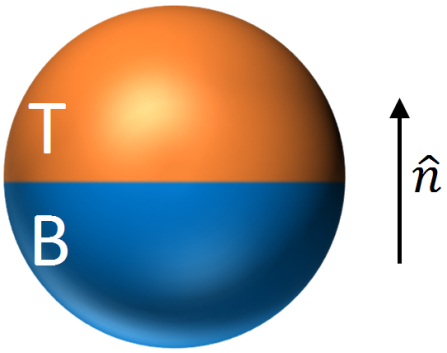

FIGURE 1.17: A dipolar particle with a different charge density on the top (T) and bottom (B) of the particle. The director $\hat{n}$ indicates the unit vector from the bottom to the top of the particle, and is thus the same direction as the dipole moment of the particle $\vec{\delta}$.

The surface of a particle can be less randomly heterogeneous by having two hemispheres of differing surface charge. Such a particle is then dipolar, and the interactions between two such particles will no longer be monopolar, but will contain a dipolar contribution. Particles like this are often termed Janus particles, after the Roman god with two faces (174–176). Such particles are useful due to the different structures they form (177–180), and because of their aligning behaviour

in electric or magnetic fields and at interfaces (181). Their synthesis has therefore seen a lot of attention in the literature, and particles of differing shapes have been synthesised to be dipolar in their charge, hydrophobicity and chemical functionality (182–188). We focus here on particles which are dipolar due to two hemispheres having different charge densities, which results in a particle with a dipole moment $\vec{\delta}$.

The total interaction between two dipolar particles at a separation r is the sum of the monopole-monopole, monopole-dipole and dipole-dipole interaction. The monopole-monopole (MM) is the same as in DLVO theory (eq. (1.50)). The monopole-dipole (MD) and dipole-dipole (DD) interaction potentials are given by de Graaf et al. (189), which when differentiated gives the forces:

$$F_{\mathrm{MD}}(\vec{r}) = \ell_{\mathrm{B}} k_{\mathrm{B}} T \frac{\exp\left(-\kappa_{\mathrm{D}} r\right)}{r^2}\left(\frac{2}{r} + \kappa_{\mathrm{D}}\right)\left[(\vec{\delta}_i \cdot \hat{r})Z_j - (\vec{\delta}_j \cdot \hat{r})Z_i\right], \tag{1.66}$$

$$F_{\mathrm{DD}}(\vec{r}) = \ell_{\mathrm{B}} k_{\mathrm{B}} T \frac{\exp\left(-\kappa_{\mathrm{D}} r\right)}{r}\left[\left(A\vec{\delta}_i \cdot \vec{\delta}_j\right) - \left((B+C)(\vec{\delta}_i \cdot \vec{r})(\vec{\delta}_j \cdot \vec{r})\right)\right], \tag{1.67}$$

where:

$$A = \kappa_{\mathrm{D}}\left(r^{-3} + r^{-2}\right) + \left(3 + 2\kappa_{\mathrm{D}}\right)r^{-4}, \tag{1.68a}$$

$$B = \kappa_{\mathrm{D}}\left(3r^{-3} + 3\kappa_{\mathrm{D}} r^{-2} + \kappa_{\mathrm{D}}^2 r^{-1}\right), \tag{1.68b}$$

$$C = 4.5r^{-4} + 6\kappa_{\mathrm{D}} r^{-3} + \kappa_{\mathrm{D}} r^{-2}. \tag{1.68c}$$

In this case, the dipole moment is given by the difference in the charge of the top (T) and bottom (B) of the particle, separated by the director $\hat{n}$ as indicated in figure 1.17 via

$$\vec{\delta} = \left(q_{\mathrm{T}} - q_{\mathrm{B}}\right)\frac{3a\exp\left(\kappa_{\mathrm{D}} a\right)}{12\left(1 + \kappa_{\mathrm{D}} a\right) + \left(\kappa_{\mathrm{D}} a\right)^2}\hat{n}, \tag{1.69}$$

and the charge of the particle Z is

$$Z = \left(q_{\mathrm{T}} + q_{\mathrm{B}}\right)\frac{\exp\left(\kappa_{\mathrm{D}} a\right)}{1 + \kappa_{\mathrm{D}} a}. \tag{1.70}$$

Considering the combination of these forces, certain cluster phases are more favourable over the expected phases from hard-sphere colloids (190–193). A lot of the studies to determine such structures have been done with magnetic particles, with either permanent magnetic moments or under applied fields, but the principles of their dipolar interactions are comparable. For example, chains and loops are favoured over closed structures as aligning the dipoles is energetically favourable (194–198). The structures of charged, dipolar particles depends on the relative length of the DH length with the particle radius $\kappa_{\mathrm{D}} a$. This determines the relative strength

of the monopolar and dipolar forces and hence the structures of the clusters formed, and the phase behaviour (*199*).

Kirkwood-Shumaker Interactions

The interaction that arises due to fluctuations in the location of charged groups or dipoles is described by the vdW interaction. This attractive force (eq. (1.57)) is due to correlations between such fluctuations, but commonly, only high-frequency terms are included when the vdW interaction is discussed. The seminal work of Kirkwood & Shumaker (KS) (*200*, *201*) described the attraction between charged proteins due to the protonation/deprotonation of the amino acid groups resulting in a fluctuation in the charge state of the protein and is therefore sometimes referred to as '*proton fluctuations*' or '*monopole fluctuations*' (*68*). Since their work, the general term of '*KS interactions*' is often used to describe macroion fluctuations (*202*, *203*). KS interactions are equivalent to (and sometimes referred to as) '*zero-frequency vdWs*' and is termed '*ionic fluctuations*' by Parsegian (*204*). As described in equation (1.61), the retardation factor that defines the strength of the Hamaker constant (eq. (1.58)) is electrically screened in the case of the low frequency contributions, thus the KS interaction is doubly screened with a magnitude dependent on the variance in the charge (*203*),

$$F_{\mathrm{KS}} \approx \langle \Delta Z^2 \rangle^2 \, \ell_{\mathrm{B}}^2 \, \frac{\exp\left(-2\kappa_{\mathrm{D}} r\right)}{r^2}, \tag{1.71}$$

where $\langle \Delta Z^2 \rangle = \langle (Z - \langle Z \rangle)^2 \rangle$ is the variance in the dimensionless particle charge $Z = q/e$. $\langle \Delta Z^2 \rangle / Z$ must therefore be large to overcome the charge repulsion. For a highly charged particle, for example, a small fluctuation in charge will not lead to an attraction strong enough to overcome the charge repulsion. Again, in nonpolar systems, the small value of Z expected could result in fluctuations of just a few charged groups to be significant enough to cause an attraction between two charged particles.

1.2.6 Measuring Electrostatics

Probing the electrostatics of colloidal systems can be done by observing behaviour in applied electric fields or by measuring the interaction strengths of overlapping double layers. There are several ways by which to measure the force of interaction between charged objects, and some of the most commonly used techniques in colloid science are the surface force apparatus (SFA), colloidal probe-atomic force microscope (CP-AFM) and optical tweezers. In all cases, they measure the repulsion or attraction due to the overlap of the double layers of two interacting objects. The profile of such an interaction can therefore give a strong indication if/how a surface is charged, and describe the intervening solution properties too. Some instruments instead measure the movement of charged particles (phase analysis light scattering (PALS)) or ions (conductivity) in solution to determine surface charge densities or

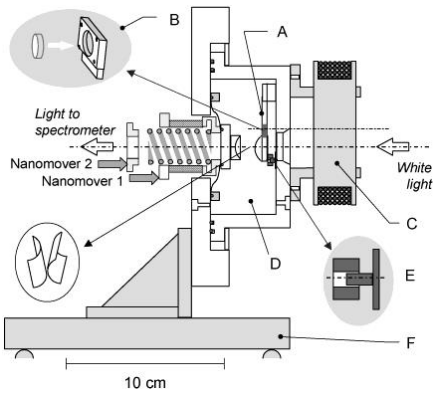

(a) SFA

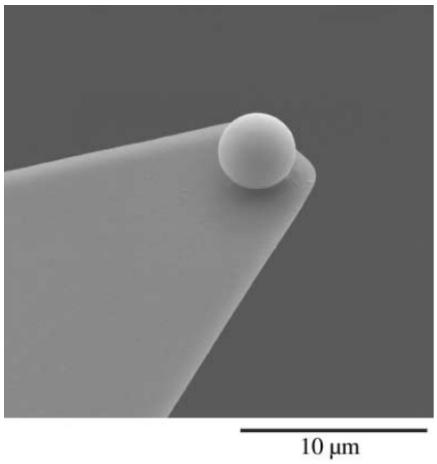

(b) CP-AFM

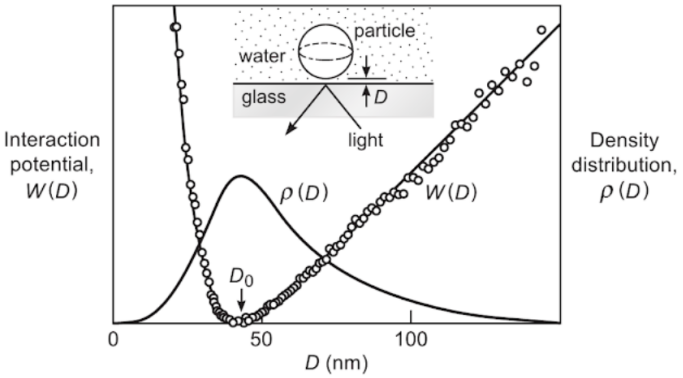

(c) TIRM

FIGURE 1.18: Commonly used techniques for measuring the interactions between particles and/or surfaces include the (a) the surface force apparatus (SFA) (47), (b) colloidal probe-atomic force microscope (CP-AFM) (205), and (c) total internal reflection microscopy (TIRM) (206).

ionic strengths respectively. With all techniques, each presents a different benefit for using it in an investigation, but equally they each have their limitations on the systems being investigated. These methods are briefly outlined here, with the methods used in this study being further discussed in the methodology sections.

Surface Force Apparatus (SFA)

The SFA is a technique developed in the 1970s by Jacob Israelachvili and Gerald Adams (207) that measures the force of interaction between two mica surfaces in a crossed-cylindrical arrangement in solution. A typical setup is shown in figure 1.18(a). The technique can measure down to plate separations $L > 1.5$ nm with Å precision, making it ideal for systems where interactions are very short-ranged. The crossed cylindrical geometry presents the equivalent of a sphere-flat plate interaction. The separation of the plates is measured by multiple-beam interferometry, whereby interference of a light source reflected several times

between the two plates results in the wavelength of the emerging beam being characteristic of the plate separation. There are a few different versions of the SFA which can measure different length scales and different magnitudes of force, but generally it has been used to measure electrostatic (208–210), vdW (211), hydration (212), friction/lubrication (213–215), hydrophobic (216), and structural (217) forces (to name a few). These studies were achieved by either modifying the surfaces of the mica with, for example, adsorbed polymer brushes (103, 218, 219) or lipid bilayers (220, 221), or by modifying the intervening solution to probe non-polar solvents (47, 222) or changes in solvent structure upon confinement (223–226). The SFA is extremely useful in measuring surface forces, however it is limited on the substrates that can be used; mostly, the SFA works with mica surfaces, as they are optically transparent and can be made molecularly smooth.

Colloidal Probe - Atomic Force Microscopy (CP-AFM)

The atomic force microscope (AFM) was modified to investigate colloidal interactions by Pashley and coworkers (227) and Butt (228, 229). They named it colloidal probe-atomic force microscopy (CP-AFM) as it consists of sticking a colloidal particle onto the end of the cantilever tip in the conventional AFM setup, as shown in figure 1.18(b). The deflection in the cantilever is then due to interactions between the particle and the surface. This method takes away the benefits of the sharp tip for determining the topography of the surface, but offers an alternative means of measuring particle-surface forces. A variety of particles have been used, with the most popular being silica (227) or glass (228). CP-AFM has been utilised to measure interactions in a multitude of systems, where the interaction due to adhesion (205), electrostatics (230–233), vdW (234) and friction (235) forces have been measured. The CP-AFM has also been useful in determining if species adsorb onto surfaces (236) and in quantifying the elasticity of polymer layers (237). CP-AFM is also limited on the substrates/particles that can be used due to the fact that some materials are difficult to manufacture in a smooth, spherical geometry, and small spheres are difficult to attach to the cantilever. The glue used, and other solvents or agents used to transfer the probe to the cantilever can also introduce contaminants into the system. Another important step before measuring forces with the CP-AFM is calibrating the stiffness of the cantilever. This has been done by a variety of methods, including applying a known gravitational (238), electrostatic (239) or hydrodynamic drag (240, 241) force to the cantilever to find its spring constant. Not only does the spring constant need to be known, but it also needs to be optimised; too large and the force resolution becomes small, but too small and thermal fluctuations can cause irreproducible data.

Total Internal Reflection Microscopy (TIRM)

The technique known as total internal reflection microscopy (TIRM) was first mentioned by Temple in 1981 as a means of observing structures at the surface of a transparent substrate (242). This technique was established by Dennis Prieve et al. to determine the interaction of micrometre size PS spheres above a glass plate (243–245). The theory behind the TIRM technique lies in the understanding of light propagation between materials with different refractive indices n. For rays propagating from media of high to low refractive index, i.e. $n_1 > n_2$, Snell's law gives a critical angle, above which total internal reflection of the incident wave occurs at the interface, and only an imaginary refracted ray exists in the second media. Physically this represents an electric field that, rather than oscillating sinusoidally through space, decays exponentially with distance into the second media and is called an evanescent wave. If a particle with refractive index different to that of the second media is suspended above the interface within range of the evanescent wave, it will scatter it. The scattered intensity is measured by a detector placed above (or below) the interface, where the intensity can be directly translated into information on the particle's height above the interface. Due to Brownian motion, the particle's position will fluctuate about a mean height above the interface, and hence a probability distribution of particle height can be obtained. This can then be directly transferred into the corresponding interaction potential using Boltzmann statistics (eq. (1.4)). In order to directly calculate particle heights from the scattered intensity, the intensity at zero-height is required, and this is measured as the scattering intensity once the particle has been forced to stick onto the surface. An example probability distribution and corresponding interaction potential is given in figure 1.18(c).

From this direct conversion between scattered evanescent wave intensity, particle height above the interface and its total potential energy, TIRM offers a means of determining the potential energy profile of a particle in proximity to a surface within different solutions without interfering with the particle's Brownian motion. It also offers a means to directly compare the profiles of the particle as, for example, the solvent is changed, an external field is applied or additional solutes are introduced. The predominant success of TIRM lies in its high sensitivity of measuring interactions of order $k_B T$ in magnitude between particles and surfaces in close proximity, allowing measurements of vdW (246–248), electrostatic (249) and depletion (250, 251) forces to be made.

Optical Tweezers

Measuring the force between two particles, rather than a particle and a surface, or two surfaces, is obviously more realistic of a colloidal suspension. Optically trapping particles in suspension offers a means to measure their interaction without physically touching them which could introduce impurities or grounding of electric

charges. Instead, the particles are visually tracked to ascertain their interaction strengths. Optical trapping was pioneered by Arthur Ashkin in the 1970s & 1980s, who has since won a Nobel prize for his work. A high numerical aperture objective is used to focus a laser beam such that when it refracts through a particle in suspension, the optical forces keep it trapped in three-dimensions (252). This method has seen use in aerosols (253, 254) and in in vitro studies of, for example, DNA manipulation (255–258). Because it uses light to manipulate matter, optical trapping relies on the refractive index differences of the material and suspension, and as is detailed later, this restricts its use to only certain systems. For example, due to their high reflectivity, metallic objects are difficult to trap as it relies on light refraction through the object. The size of the object to be trapped is also restricted in terms of the width of the optical trap produced. There are 2 primary methods of measuring the force between two optically trapped particles, the first being with *constant traps* where two particles are brought into proximity, and their displacement from the centre of the trap determines the strength of the interaction force. As with the CP-AFM cantilever, this method requires calibration of the trap stiffness to quantify the force. The other method doesn't require this calibration step, as it only tracks the particles during periods of time when the optical traps are turned off. This method is called *blinking optical tweezers* (BOT).

This technique is utilised in this study to directly measure the force between pairs of PMMA particles in nonpolar suspensions. The apparatus used and the concepts behind optical trapping are outlined in section 2.1.1.

Phase Analysis Light Scattering (PALS)

The magnitude of charge on the surface of particles in suspension can be done by measuring how fast they move in applied electric fields. The electrophoretic mobility μ_e of a colloid is its velocity v in an applied electric field of $E = 1$ V m^{-1}, i.e.

$$\vec{v} = \mu_e \vec{E}. \tag{1.72}$$

More highly charged particles move faster in an electric field, and hence have a higher electrophoretic mobility. As will be discussed further in section 2.1.4, the electrophoretic mobility has been found to be a function of the electric field strength in nonpolar solvents, whereas in polar solvents this is assumed a constant (145). In strong electric fields, the thick ionic atmosphere surrounding particles in nonpolar solvents (large λ_D), is 'stripped' from the particle, effectively removing counterions away from the particle surface and hence increasing the particle's effective charge. Because it relies on the scattering of light from the particle to ascertain its velocity, difficulties also arise with this technique if aggregates are present in the solution as this can confuse the data.

Conductivity

Measuring how conductive a solution is can give direct insight into the average number of charge carriers present, i.e. the ionic strength. For example, measuring the conductivity of water supplies can be invaluable for knowing if any impurities are present and therefore if it is safe to drink. Measuring the conductivity also allows for determination of salt concentrations and their degree of dissociation. By applying a current across a solution and measuring the resulting voltage, the ability of the solution to *carry* charge can be determined. Because the current is carried by ionised species in the solution, a solution of higher ionic strength is more conductive. The conductance of pure solvents also varies due to the nature of the solvent molecules.

1.2.7 Nonpolar Systems

There are many applications that use colloids in nonpolar solvents specifically (*259*). These include paints, printing inks, dry cleaning agents, engine oils and additives and are used in electrophoretic displays in, for example, electronic-readers (*260*). Their uses rely on properties such as preventing bacterial growth, low evaporation temperatures making drying after deposition fast, and their low conductivity which is important for electrical insulation (*261*). In terms of electrostatics, nonpolar solvents are distinguished from other solvents by their low dielectric constant, usually $\varepsilon_r < 5$. This means they have large Bjerrum lengths ($\ell_B \sim \varepsilon_r^{-1}$) and hence little or no dissociation of chemical groups into ions is predicted. However, the small number of ions present in the system has a more significant effect as the double layers formed are much thicker ($\lambda_D \sim \ell_B$), this makes the electrostatic nature of such systems very sensitive to impurities or humidity. The earliest work on probing the electrical properties of nonpolar solvents was done by Fuoss & Kraus (*262*–*265*) and La Mer & Downes (*266*, *267*) in the early 1930s by measuring the conductance of salts in benzene ($\varepsilon_r \sim 2$ (*268*)). The major conclusion from both these studies was that ions can exist in nonpolar solvents. Studies on particle charging in nonpolar solvents began by van der Minne & Hermanie in 1952 by measuring the electrophoresis of carbon black suspensions in benzene (*269*, *270*). The stability they observed they inferred to the particles having a surface charge and thus the presence of a double layer despite the low dielectric constant. Koelmanns & Overbeek then looked into the stability of micron sized particles of many different compounds by measuring the settling velocity and electrophoresis (*271*). They came to the same conclusion that only the particles that charged showed stability. Overbeek then went on to explain how the stability in nonpolar solvents can be complicated by particle concentration due to the thick double layers present (*272*, *273*).

The mechanisms for charging a surface in a nonpolar solvent are restricted to either surface group dissociation, or adsorption of micelle aggregates. Adsorption of ions from the solvent, which is likely in aqueous systems, is very unlikely

in a solvent that contains very few ions due to the large Bjerrum length and nonpolar molecules. Despite narrowing these mechanisms down, there were a lot of observations that made it difficult to determine exactly how surfaces charge in nonpolar solvents. Such observations include differences in sign of TiO_2 (274) and α-Fe_2O_3 (275) in different solvents, suggesting that the solvent was in fact determining the charge of the surface, not the surface groups. It was later suggested that the sign and magnitude of the surface charge can be predicted by how electron donating the solvents are (276). Another sensitivity in nonpolar systems is the effect of trace amounts of water; although a weak electrolyte, water is very polar and, just like a charged additive, can result in significant increases in the conductivity (277). It has been suggested that the water molecules will adsorb to the surfaces (278), which could explain observations of Al_2O_3 particles turning from negative to positive upon addition of water (279) and why different systems exhibit different effects when water is added (280), but no effect has been seen in some cases (281). Another important observation made with TiO_2 particles is how long nonpolar systems can take to equilibrate their charge (277). In this study, McGown et al. found that the particle charge did not equilibrate for 24 hours, with the charge even showing a change in sign after 15 hours. All these early observations highlight the sensitivity of charge effects in nonpolar systems, and despite being $>$ 50 years on from the studies of van der Minne & Hermanie (269, 270), the same questions are asked at conferences about equilibration time, water content, and charging mechanisms.

Electrostatic stabilisation of nonpolar colloids is possible, but as stated in (278), this requires sufficient surface charging, and not too many ions in solution that the double layer is completely suppressed, but enough to induce the entropic repulsion between two surfaces. This balance is achievable as observed in some of the early studies already eluded to, but in some systems, additional stability is required by either boosting the electrostatic repulsion, or by sterically stabilising the particles with layers of polymers.

The hindrance to charging in nonpolar solvents is the large Bjerrum length. For hydrocarbon oils this length is $\sim$ 30 nm, so species much less than that in size have a very low probability of dissociating. So, increasing the effective size of the ions should result in a higher number of ions. There have been a few methods to achieve this in the literature such as charging of fullerenes (282), functionalising the surface of particles with large (283) or more ionic groups (284), and using large organic salts (269, 270, 285). Of most interest to us is the charging of polymeric particles, of which there have been two main successes: incorporation of strongly ionic organic monomers into their synthesis (286, 287), or using surfactants to stabilise an ion within its core thus increasing its effective size (288). Dioctyl sulfosuccinate sodium salt, known as Aerosol OT (AOT), has been the most commonly used ionic surfactant in this field since the work of Koelmans and Overbeek (271). The inverse micelles formed in nonpolar solvents have been known to increase the conductivity of nonpolar systems since the work of Nelson & Pink (289). The mechanism for

this is now thought to be due to the exchange of charge during thermal collision between two inverse micelles. The charge group is either due to the ionisation of an ionic surfactant, or in the case of neutral surfactants, this is thought to be a result of a disproportionation process between two neutral micelles (*290*). The micelles in solution are then able to adsorb to the surface of particles, and can result in charging of the surface (*291*). This is due to either promoting the dissociation of surface groups by solvating counterions, or by preferential adsorption of either the negatively or positively charged micelles (*51*).

Although a very useful way to charge particles sufficiently to maintain stability, this study has not used surfactants, but relies on the bare surface charge of PMMA and a polymer brush layer on the surface for steric stability. This bare charge of PMMA has been observed before in cyclohexyl bromide (CHB) (*38*). In that case, the solvent was thought to be the origin of the particle's charge due to self-decomposition of CHB, where protons formed could charge the particle. The heightened conductivity was also thought to be due to some gaseous HBr formed. This study uses only dodecane as a solvent, so the cause of charging may be different, but nonetheless clearly present from the results.

1.3 Structure of Thesis

Colloids offer a means to investigate electrostatics by experimental observations in a multitude of different systems. Measurements of their interactions for example can directly probe the theories outlined in this introduction.

Chapter 2 details the nonpolar colloidal suspensions under investigation in this study, along with the techniques used to observe them.

Chapter 3 presents the data of direct measurements of the interaction force between the colloidal particles, highlighting that the repulsive force between two charged particles is not always well described by the DLVO theory.

Chapter 4 then presents observations made of attractions between like-charge particles, another contradiction to the predictions made in DLVO theory. In order to ascertain the origin for this attraction, the cluster shapes, sizes, and behaviour in applied electric fields are discussed.

Chapter 5 derives a theoretical framework that can be applied to the system studied here in order to explain the unusual observations made in chapters 3 & 4.

Chapter 6 finally concludes the major findings of this investigation, and highlights their impact for better understanding electrostatics in suspensions, and their importance when considering the stability of colloidal suspensions.

Chapter 2

Experimental

This chapter will firstly describe in detail the experimental techniques used in this investigation, with particular emphasis on the use of optical tweezers in measuring inter-particle forces. Secondly, the synthesis of the particles and electrolyte, and the method of sample preparation is detailed.

2.1 Methods

2.1.1 Blinking Optical Tweezers (BOT)

Optical tweezers offer a non-invasive method of manipulating colloidal particles, both in aerosols as well as in solution, and as such have been useful in biological applications (*292*) such as stretching out DNA (*255*, *293*). This study utilises optical traps to manipulate colloidal particles in solution in order to measure their interaction. The method used to do this is called blinking optical tweezers (BOT) and is fully explained below.

Optical Trapping

The two predominant forces that describe the trapping of material by a laser is the radiation pressure, which directs along the direction of the photon propagation, and the gradient force, which directs up the intensity gradient, i.e. towards the point of highest intensity. Radiation pressure can be explained in terms of the transfer of momentum from a photon to an interface. When light is incident at the interface between two materials with different refractive indices, part of its intensity (and hence energy) will transmit through, and part will reflect. The difference in direction of the incident and the reflected or transmitted beam means a change in momentum occurred, resulting in a force acting on that interface (Newton's law of motion).

The momentum p carried by a single photon can be quantified from its wavelength λ due to its simultaneous wave-particle nature, $p = h_P/\lambda$, and hence the change in momentum of a reflected photon is $\Delta p = 2h_P/\lambda$, where h_P is Planck's constant. For a laser of power P at frequency ν, the number of photons incident on a material is $P\Delta t \,/\, h_P\nu$, and hence the total force exerted on a surface that reflects a fraction α of the laser beam is

$$F = \frac{2\alpha P n}{c_0}, \tag{2.1}$$

where $n = c_0/h_P\lambda$ is the refractive index of the primary media, and c_0 is the speed of light in a vacuum. So, forces produced by a laser trap are of order pN for a mW laser power, and is hence a useful technique for investigating the forces involved with colloidal particles as this is $\sim k_B T$ over a nm.

When this principle is applied to a laser interacting with a spherical particle, it is the refraction of the photons at the particle surface that induces the reaction force. If we have a particle of refractive index higher than its surrounding medium, a totally transmitting beam will refract at the circumference as shown in figure 2.1. Ignoring the scattering force due to the reflection of the beam, the rays shown indicate the beam's momentum and the net momentum change of the beam is indicated in both cases. For a beam focussed through the centre of the particle (fig. 2.1(a)), the transmitted beam does not change momentum at the interfaces and hence no force acts on the particle. If the beam is focussed slightly to one side of the particle's centre, the beam does change momentum at the particle's interfaces. As depicted in figure 2.1(b), the net change in momentum of the beam is directed towards the particle's centre. The resultant force acting as a result of this momentum change therefore acts from the particle centre towards the beam focus. This force acting towards the highest intensity of the beam (the focus) is called the gradient force, and is responsible for the lateral trapping of a particle in a laser beam. In a situation where the particle is of lower refractive index than the surrounding medium, the gradient force will act away from the beam focus, and hence no particle trapping will occur. This effect was noted by Ashkin when air bubbles in a glycerol-water mixture in the optical beam were pushed downstream and outwards from the beam focus (*294*). This indicates one of the constrictions on the technique of optical trapping, where the refractive index mismatch between the particle and surrounding medium must be optimised.

As may be apparent from the ray diagrams shown, the resultant force has a component that is directed along the propagation of the laser beam. This component is the radiation pressure, sometimes called the scattering force, and pushes the particle along the direction of the beam's propagation. In order to achieve a 3D trap, the scattering force must be balanced with another force so the particle is not pushed down the laser beam. Ashkin initially proposed two methods to do this: the first was to use two laser beams, directed in opposite directions, both focussed at the trap location (*294*). This way, the scattering force from both beams cancel out, and all that remains is the gradient forces. The second proposal was to balance the scattering force with the gravitational force on a particle that was then '*levitated*' above the laser source (*295*). These two methods showed great promise and were useful for scattering, aerosol and spectroscopic applications.

It was not however until 1986 that Ashkin et al. successfully trapped a particle

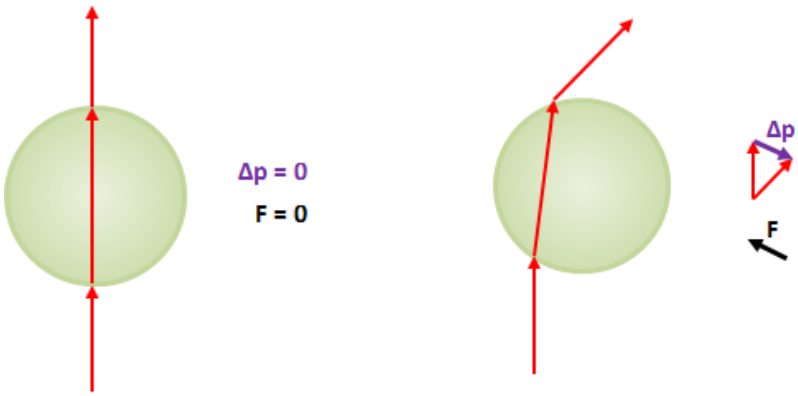

(a) Propagation of a beam focussed at the centre of a particle.

(b) Propagation of a beam focussed to the left of the particle's centre.

FIGURE 2.1: Ray diagrams to show how the change of momentum of a laser beam refracting through a particle imparts a gradient force on that particle such that it moves its centre towards the focus of the laser beam. This observation holds true for particles of higher refractive index than the surrounding medium. This diagram ignores the additional scattering force which acts in the direction of the beam propagation. This ray optics regime is also only applicable where the beam wavelength is less than the particle radius.

with a single beam without the need to balance the scattering force with an external force (252). Ashkin et al. succeeded in producing a '*negative radiation pressure*' which is an 'axial intensity gradient force'. As depicted in figure 2.2, a high numerical aperture objective is used to focus a Gaussian laser beam to a high intensity point such that an axial gradient force arises that opposes the forward scattering force. In a later paper, Ashkin highlights the necessity for a tightly focussed beam above a minimum convergence angle to produce strong enough axial gradient forces to overcome the scattering forces (296). This tightly focussed beam produces an optical potential well that traps colloidal particles in 3D; these are the fundamentals behind optical tweezers. This method of trapping allows for 3D trapping of a wider range of particle sizes, encompassing both the Rayleigh (particle diameter $<<$ wavelength) and Mie (particle diameter $\simeq$ wavelength) regimes.

The explanations by Ashkin as to the fundamentals behind optical tweezers are done so with particles larger than the beam wavelengths. However, for Rayleigh or Mie scattering, this is not the case. Derivations of the scattering and gradient forces in the Rayleigh regime are given by Harada & Asakura (297). The assumptions in this regime are that the particle of radius a and refractive index n_p has a induced dipole δ in the electric field of the beam (E) of magnitude $\delta = \alpha E$. The polarisibility of the particle is given by

$$\alpha = 4\pi n_p^2 \varepsilon_0 a^3 \frac{m^2 - 1}{m^2 + 2}, \tag{2.2}$$

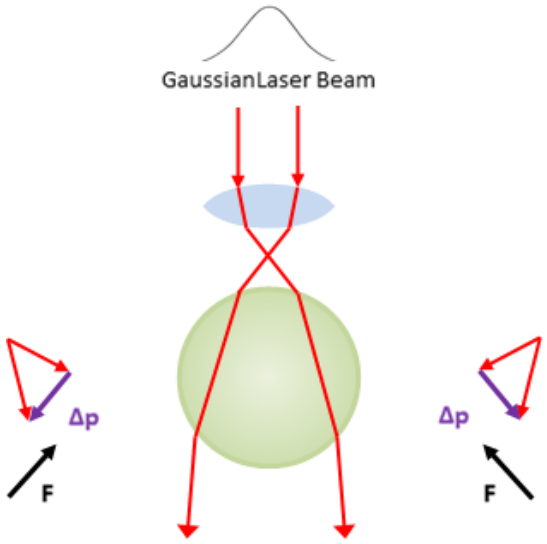

FIGURE 2.2: Ray diagram to depict how a single Gaussian laser beam can be used to trap a particle in 3D without the necessity to counter the scattering force with an external force.

where we use the refractive index ratio $m = n_p/n_s$ for the particle and surrounding media.

The gradient force on this induced dipole is then $\vec{F}_{grad} = \delta\nabla E = \frac{1}{2}\alpha\nabla E^2$, which gives (*298*)

$$\vec{F}_{grad} = \frac{1}{2n_s c_0 \varepsilon_0}\alpha\nabla I. \tag{2.3}$$

This gradient force is directed up the intensity gradient (∇I where ∇ is the differential operator), towards the location of highest beam intensity. In the Rayleigh regime, the scattering cross section of a sphere is given by

$$\text{SCS} = \frac{8}{3}\pi a^6 \left(\frac{m^2-1}{m^2+2}\right)^2 k^4, \tag{2.4}$$

where k is the magnitude of the wavevector of the laser beam and is equal to $2\pi/\lambda$. The scattering force is given by (*298*)

$$\vec{F}_{scat} = \frac{n_s \text{SCS}}{c_0} I\,\hat{k}. \tag{2.5}$$

This force is not affected by the intensity gradient in the beam, but is directed along the propagation direction of the beam as indicated by the wavevector $\hat{k}$.

So, we have two approximations for the scattering and gradient forces (*299*):

$$\vec{F}_{scat} \propto (n_p - n_s)^2\, a^6 I\,\hat{k}, \tag{2.6a}$$

$$\vec{F}_{grad} \propto (n_p - n_s)\, a^3\, \nabla I. \tag{2.6b}$$

With these two equations it is now easier to see what properties of a system

can be modified to optimise optical trapping. For example, if the refractive index difference between the particle and the solvent is too large, the scattering force will dominate over the gradient force and no stable trap will result. Equally, larger particles will also result in an unstable trap.

Holographic Optical Tweezers

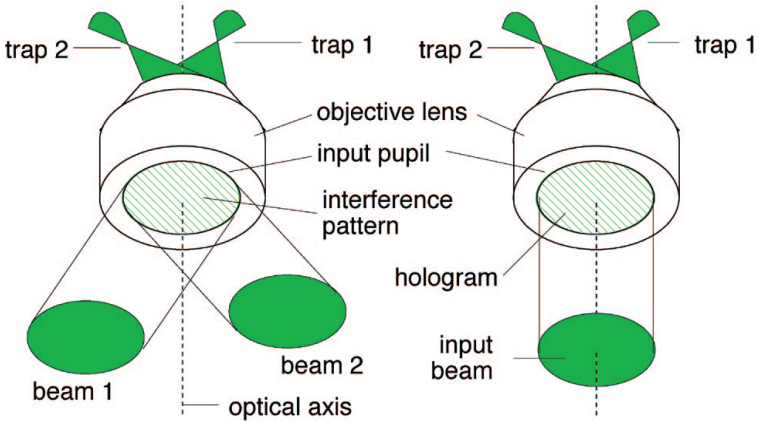

FIGURE 2.3: Left: A diagram of how two laser beams create a diffraction pattern at the input pupil of the objective and result in a characteristic array of tweezers. Right: A diagram to show how an image of the same diffraction pattern (a hologram) at the input pupil, created using only one laser beam, also results in the same array of tweezers. Figure taken from reference (*300*).

Measuring particle-particle interactions requires two particles to be held by separate optical traps, i.e. there needs to be two laser foci. The position of both tweezers also needs to be controlled separately in order to modify their separation. Several methods have been proposed to create multiple tweezers including time sharing one beam (*301*), using multiple lasers, splitting a beam into s and p polarisations (*302*) and scanning-line traps (*303*). All methods offer different benefits and issues, but the one most useful to our investigation is to use holograms to create several traps from a single laser beam.

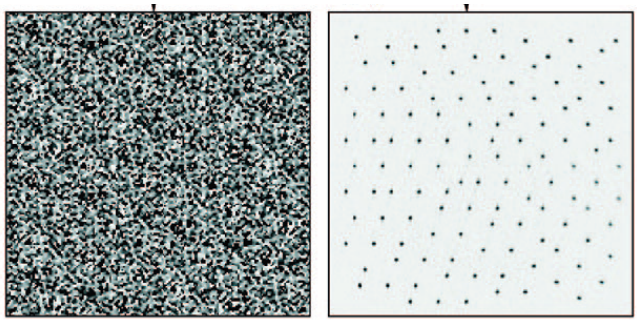

FIGURE 2.4: An image of the diffraction pattern (left) created in order to produce the array of traps shown on the right. Image taken from reference (*300*).

When two separate laser beams are shone through the same objective, their focus and incident propagation direction will determine where their traps will be located. Interference between these two beams will occur at the input pupil as shown in figure 2.3. The diffraction pattern created at this back focal plane of the objective is characteristic of the locations of the resultant traps. In 1998, Dufresne & Grier described how a hologram of these characteristic diffraction patterns can be created from a single laser beam that results in exactly the same array of optical tweezers (*304*). This idea is also shown in figure 2.3.

An example of a diffraction pattern and its resultant tweezer array is given in figure 2.4. In order to form these holograms, Grier & Roichman used a liquid crystal spacial light modulator (SLM). A SLM is an example of a reflective 'diffractive optical element' whereby a laser beam is reflected off the SLM surface where it is transformed into the required diffraction pattern. This is achieved by each pixel of the SLM surface containing a liquid crystal whose orientation can be controlled independently. Each pixel can impart a phase change to the beam reflected from it depending on the liquid crystal's alignment. The reflected beam is hence spatially modified in both phase and amplitude such that it presents a hologram to the input pupil of the objective.

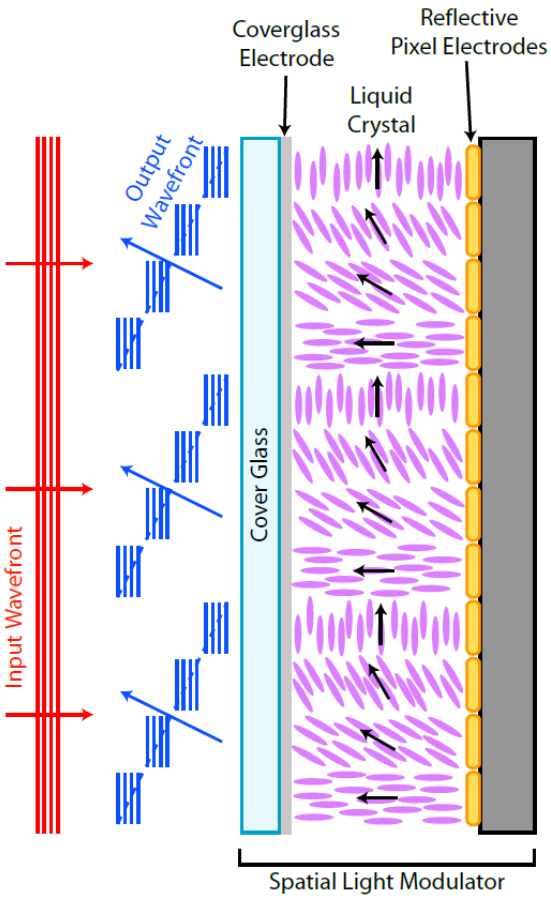

FIGURE 2.5: A diagram of the spacial light modulator (SLM) taken from reference (*305*).

A diagram of the SLM has been taken from reference (305) and is shown in figure 2.5. What this shows is how each pixel on the SLM is separately controlled by an electrode that causes the liquid crystal molecules between it and the coverglass electrode to orientate according to the voltage applied to that pixel. Due to the different orientations of the molecules in each pixel, the output wavefront will contain a specific optical path length. The relative differences in the path lengths between the wavefronts from the different pixels results in the phase difference necessary for a specific combination of optical traps in the sample. Some examples of the diffraction pattern required for different configurations of optical traps are given in figure 2.6. Each pixel in the image shown corresponds to a pixel on the SLM, where the different value of the grey scale corresponds to a different applied voltage. Each pixel for our SLM is 8 μm wide, and the total size is 15.36 × 8.64 mm (305).

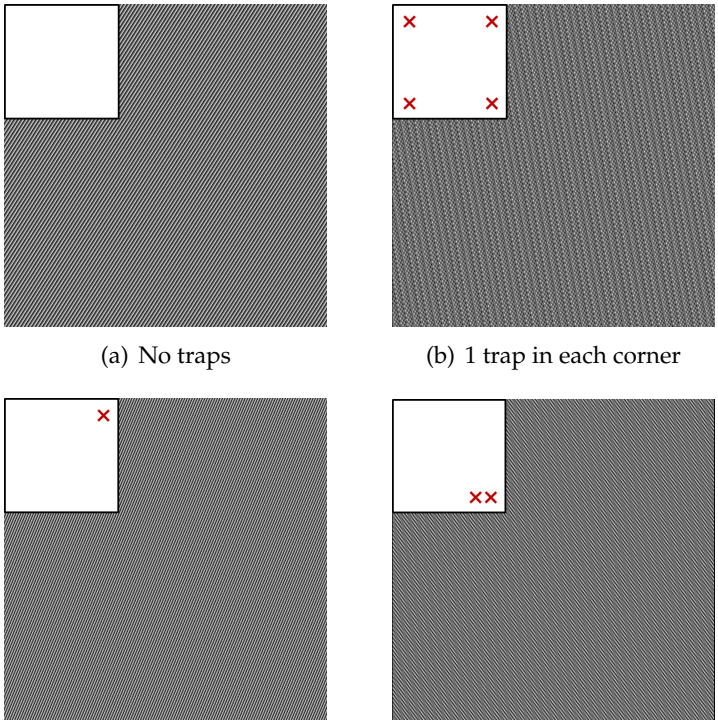

(a) No traps (b) 1 trap in each corner

(c) 1 trap top right (d) 2 traps bottom right

FIGURE 2.6: The diffraction pattern created with the SLM to produce the location and number of traps indicated in the schematic inset onto each image. The scale is unknown for the SLM image, but the traps are roughly 3 μm in width as shown in the real images of traps in figure 2.7.

One issue with this holographic method is that often there is an unwanted trap in the centre of the image. This is due to the undiffracted, zeroth order beam. In several setups, this unwanted central tweezer is removed by the use of a ball-stop; a bead is suspended in the path of the beam before it enters the microscope in an attempt to stop this central beam passing into the objective (306). Although this ball stop may be effective in removing unwanted tweezers, it can affect the diffraction

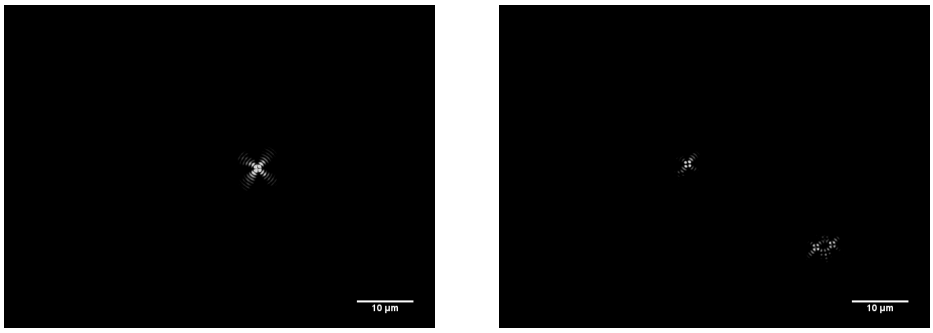

(a) (b)

FIGURE 2.7: Images taken of an empty cell with no back-light illumination from the microscope. The diffracted crosses present are the locations of the laser traps. (a) Centered laser tweezer. (b) Bottom-right double laser traps + undiffracted central tweezer.

pattern entering the objective, and can cause a *dead zone* where no stable traps can be produced in the centre of the image (*305*). The image shown in figure 2.7(b) highlights the presence of this central tweezer. These images were taken in an empty cell with no back-light illumination from the microscope. To avoid any issues with the unwanted centred trap, or with the *dead area*, measurements are taken near the corners of the field of view, as suggested by the tweezers in the bottom-right corner in figure 2.7(b). Another issue with using holograms is that the resulting optical trap is fairly weak, and the more traps produced from the same laser beam, the weaker they all become. Figure 2.7 shows this, where the same laser power is used to produce the single trap in figure 2.7(a) as the three clearly weaker traps in figure 2.7(b).

Experimental Setup

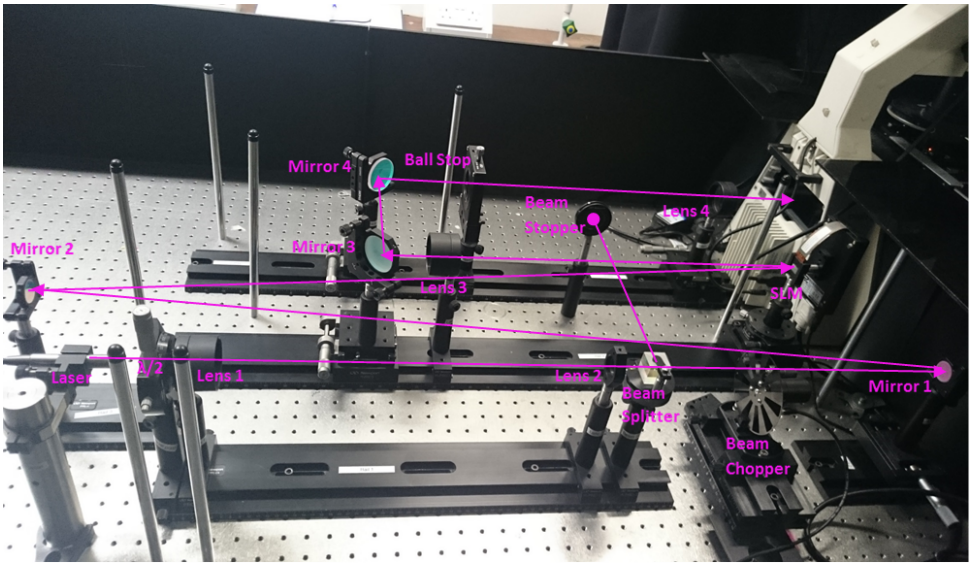

FIGURE 2.8: Optical setup for the BOT.

The optical setup was constructed by Ian Williams, and is detailed thoroughly in his thesis (305). An image is given in figure 2.8 that shows the path of the laser through the optical setup before entering the inverted microscope (Carl Zeiss, Axiovert 200) and being focussed by the objective (Plan Neofluor, 100x, 1.3 NA oil, Carl Zeiss). Briefly, the laser (5W Nd:YAG laser, 1064 nm, IPG photonics) first travels through a half-wave plate ($\lambda/2$) to rotate the polarisation such that when it passes through the beam splitter, only the vertical polarisation is transmitted. Between these elements, the light passes through Lenses 1 & 2 which expands the width of the beam to be the same as the size of the spacial light modulator (SLM). A Beam stopper is added perpendicular to the beam splitting cube to contain the horizontally polarised light that is not utilised. The laser then passes through the beam chopper (Thorlabs MC2000), which was an element added by Samuel Finlayson (307), which periodically turns the laser traps on and off, hence the name *blinking* optical traps. This beam chopping disc is rotated at 20 Hz, and the notches result in the laser turning off for 25 ms, then on for 25 ms continuously. An in-built detector near the disc records the times the laser is turned off, so that the tracking data is only taken when the laser is off.

Once through the beam chopper, the laser is reflected by mirrors 1 & 2 onto the SLM (PLUTO-NIR, HoloEye). The reflected light from the SLM then contains the phase distribution necessary for the required location of the optical traps in the sample. This light is then passed through Lenses 3 & 4 to again change the width of the beam to be just wider than the width of the objective aperture. The ball stop is added to try to remove the undiffracted central trap present from this method, but as stated, this can result in a *dead zone* where the optical traps will not work in the sample. This setup seems to result in both a central optical trap, as shown in figure 2.7, and a dead zone in a '+' shape in the field of view.

The same objective is used to focus the laser and to image the sample. This means that moving the focus of the objective simultaneously moves the focus of the optical traps, i.e. the laser trap is always in focus with the image. The sample is then viewed through a camera (Genie DALSA HM 640, pixel size $\approx$ 118 ($\pm$6) nm), and no eyepiece is connected to avoid the laser entering anybody's eye.

Software

The SLM is controlled by LabView code written by Miles Padgett's group in Glasgow (308). Through this interface, the number and location of the optical traps can be determined by the user. Briefly, the user defines where the traps are to be located, and the program defines the equivalent diffraction pattern required to produce them. This is then sent as a hologram to be projected onto the SLM. A separate program is used to track the particles in the field of view at the camera acquisition rate of 500 frames per second. The tracking method used is detailed in section 2.1.2. One more LabView program is also run alongside the one that is tracking the particles, that records the time at which the laser is off and on. This

means that the tracking data collected can be cross-referenced with these times to ascertain when the particles are trapped or freely moving in the sample.

Force Measurements

The preparation of the samples is outlined in section 2.2.3. Once prepared, the samples were taken up into a capillary (CM scientific, borosilicate, internal dimensions: 0.1 × 2 mm) which was then sealed and simultaneously glued to a microscope slide with UV adhesive (Norland Optical Adhesives, no.81) and cured with a UV lamp. The sample was placed upside down on the inverted microscope stage using a 100× objective with 1.3 N.A. immersion oil. Two optical traps are produced and their locations chosen using the LabView program that controls the SLM. These traps are used to optically trap two stable particles in the sample in a region far from the capillary walls and other particles to ensure only forces between the two trapped particles were measured and no wall effects were present. Since the solvent used is not density matched to the particles, this was often achieved by simply waiting until the rest of the particles sedimented away from the optically trapped pair. Once trapped, the laser was repeatedly blinked on and off with the beam chopper such that both particles are repeatedly held at a specific centre-centre separation r and then released every 50 ms. The particle positions were tracked using the high speed camera at 500 frames per second (every 2 ms).

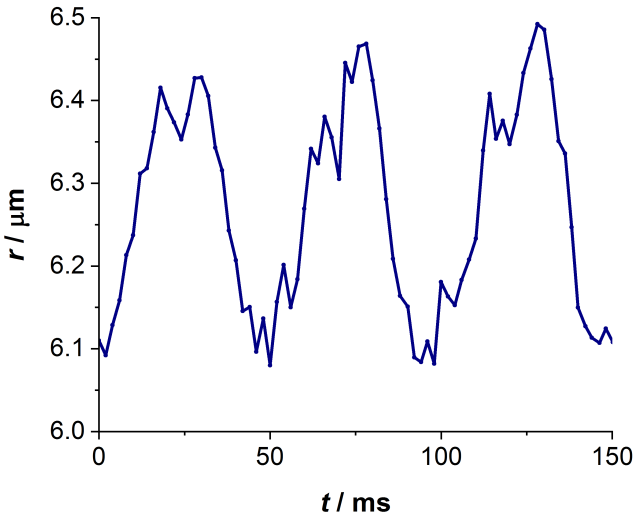

FIGURE 2.9: The raw tracking data for two interacting particles, held at a separation of ~ 6 µm, showing the separation r at time t after the laser is turned off. The plot shows the tracking data over four cycles of the laser turning off and on again every 50 ms, i.e. the laser in the plot is turned off at $t = 0$, 50, 100 & 150 ms, and turned on at $t = 25$, 75 & 125 ms.

An example of the raw tracking data collected is given in figure 2.9, showing the separation r of two particles over 150 ms, during which time the lasers were

blinked off and on 3 times. As the data shows, once the laser is blinked off (at $t = 0$, 50 & 100 ms), the separation of the particles increases over time. Once the laser is turned on again (at $t = 25$, 75 & 125 ms), the particles are brought back to the original separation of the two optical traps. What is clear from the raw data, is that every time the laser is blinked off, the particles move apart with, on average, the same velocity. Also apparent is that there are fluctuations about this trend, indicating the inherent Brownian motion of the two particles, from which the mean square displacement over time can be calculated.

This tracking data was collected for $\sim$ 8000 blinking cycles to produce histograms of the separations of the two particles at time intervals after the optical traps were turned off; the times at which the laser was on and off were separately recorded, allowing for cross referencing with the tracking data. From these histograms, the change in the mean displacement and mean square displacement over time was calculated to give the velocity v and the diffusion coefficient D (eq. (1.44)) respectively. Examples of such histograms are given in the following results section in figure 3.6. The inter-particle force can then be equated with the drag force (eq. (1.46)) for several initial separations r to produce a force profile,

$$F(r) = k_B T \frac{v(r)}{D(r)}. \tag{2.7}$$

2.1.2 Particle Tracking

The particle tracking algorithms embedded in the LabView code (provided by the group in Glasgow (*308*)) used in our setup to control the SLM and the imaging are based on the methods of Crocker & Grier (*309*). The tracking requires images of the particles which are as focussed as possible such that they appear with bright centres and a dark ring at the circumference. An example of such an image is given in figures 2.10(a) & 2.10(b). The system used to develop the tracking methods in this section were not the same as in the rest of the study, but were silica particles in water, with a diameter of 1.86 μm. Each image contains pixels with intensity values between 0 - 255; 0 indicates black, and 255 indicates white, hence a 'gray value' scale is used. So, each image is transformed into an array of 'gray values' with large numbers indicating brightness peaks, and low values indicating dark troughs. The method of tracking that Crocker & Grier used is to locate brightness maxima in the pixel array which are then identified as the centres of particles. By setting some threshold brightness value, typically equalling just above the background intensity, true peaks due to particles can be determined from false peaks due to fluctuations in the background intensity.

An example of a profile plot of the pixel intensities of an imaged particle is given in figure 2.10(c). The profile plot shows a background intensity around 90, then an intensity trough around 40 before a wide peak, maximised at around 170. The plot

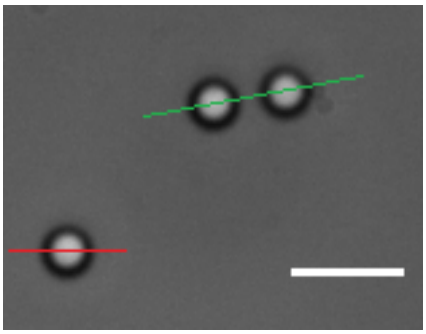

(a)

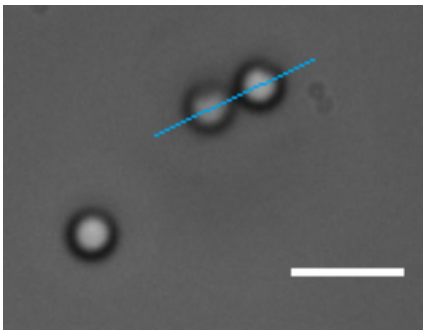

(b)

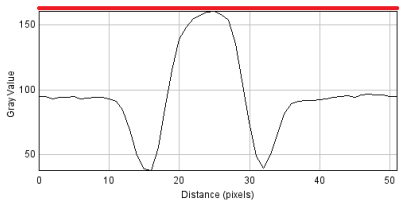

(c) Profile plot of the lone particle in image (a).

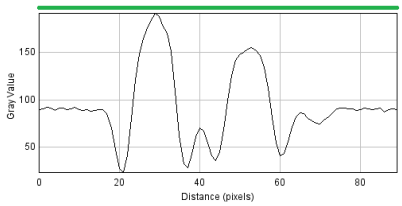

(d) Profile plot of the pair of particles in image (a).

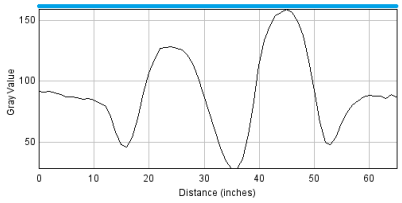

(e) Profile plot of the pair of close particles in image (b).

FIGURE 2.10: Left: Optical micrographs taken of silica particles (diameter = 1.86 μm) in water. Right: The profile plots along the coloured lines indicated showing the difference in the particle plots of a lone and a pair of particles at two different separation distances. The scale bar is 5 μm.

is symmetric about the intensity maximum, typical of a homogeneous, spherical particle.

Particles appear with these peaks and troughs in intensity due to the way images are collected in a microscope. As the scattered light leaves the particle, it passes through an aperture where it diffracts. The image viewed is hence the diffraction pattern created by the light radiated by the sample which, as figure 2.10(c) indicates, results in a bright peak surrounded by a dark ring. When two particles are in the same image, but are sufficiently separated, microscopy can successfully image both as separately resolved particles, each with this trough-peak-trough profile plot. However, when the particles are in proximity, the resolution is not sufficient to determine one particle's diffraction pattern from another's and hence the result is a linear superposition of the two patterns. An example of this effect is given in figures 2.10(d) & 2.10(e). Two major differences can be seen in the profile plots as the particles become progressively closer. First is the disappearance of the background intensity between the particles, indicating that neither particle is fully resolved, but that overlap of their diffraction patterns has occurred (*310*). The second problem

may not be apparent in these profiles, but it is that the overlap causes the peaks to be skewed towards each other, giving a false particle separation distance by the tracking algorithms that rely on the peak intensity location. Simulations have been done to quantify how much these peaks can be skewed due to this effect (311).

We can see that at the closer separation, one of the particles becomes less clearly defined. This could either be due to this diffraction pattern interference causing one peak to be dimmed, or it could be because the particles at this close proximity begin to move vertically. This occurs due to the vertical stiffness of the optical traps being weaker than the horizontal stiffness. This second factor is accounted for in the experiments by ceasing to collect tracking data when this happens, as the tracking methods cannot track in the vertical direction.

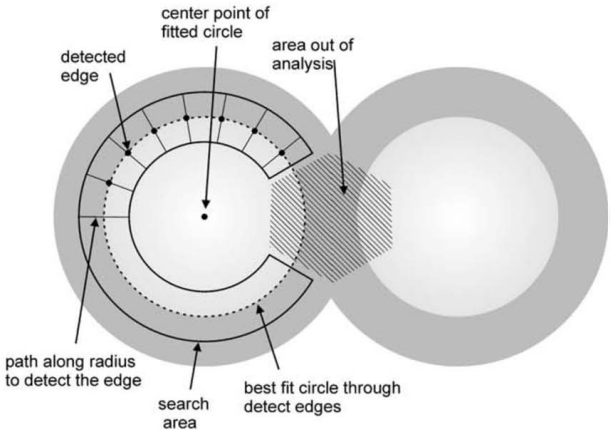

FIGURE 2.11: Diagram of the analysis algorithms used to detect the edge of the ring around the particle. The area that is neglected in the analysis is also shown resulting in a "C-shaped" template. Figure taken from reference (312).

Two ways to improve the tracking at closer separations could be to synthesise particles that contain a fluorescent core, such that only the very centre of the particles are imaged when viewed with a fluorescent camera, hence removing the issue of diffraction pattern overlap (313, 314). This however requires lengthy synthesis, and the requirement for a different camera and possibly laser source. A second method would be to improve the tracking method used. One such method was suggested by Gutsche et al. and is used in several of their group's studies using optical tweezers in aqueous solutions (312, 315). Rather than locating intensity peaks in the image arrays, the edges of the rings around the particles are located to create a circle that follows this edge. The centre of this fitted circle is then determined as the location of the centre of the particle. How this method offers a superior tracking method over locating intensity peaks can be explained with the profile plots in figure 2.10. The part of the image that is most distorted is between the two particles, whereas the outer edges of the particles are far less distorted. Hence, if the tracking algorithms focussed only on the outer edges of the particles, the impact of this diffraction overlap on locating the particle position is much reduced. This

method is described in figure 2.11, showing which section of the edge is detected, and where the corresponding particle centre is determined to be.

This idea was then adopted by a group in Switzerland who produced a MATLAB program that locates particles in an image by this method (*316*). The code was published online (*317*) and we have since adapted it in order for it to use a "C" template for the left-hand particle and a "Ↄ" template for the right-hand particle.

Tracking Error

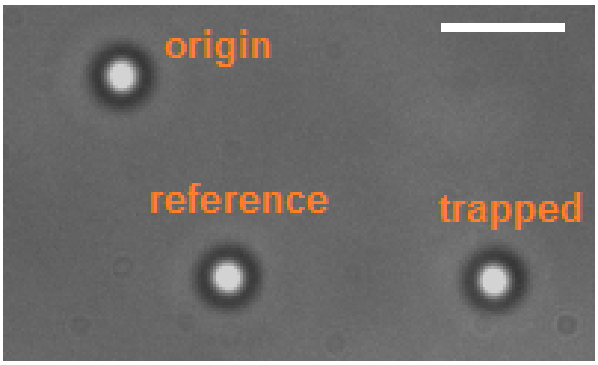

FIGURE 2.12: An optical microscopy image of the setup used to calculate the tracking errors, showing the origin, reference and optically trapped particles. The scale bar is 5 μm.

To ascertain the potential errors from the two different tracking methods, a tracking error was calculated for both at different particle separations. The method to do this follows the paper by Zhang et al. (*316*), whereby two particles are 'stuck' (through adsorption) to the bottom of the cell such that they are stationary in the image. One of these particles is used as the origin, and the other as a reference particle. A third particle is then trapped in a constant laser trap and brought progressively closer to the reference particle. This setup is shown in figure 2.12. Before the optically trapped particle is brought into proximity with the reference particle, their 'true' locations are noted with respect to the origin particle. These locations are then used to calculate the '*true separation*' of the trapped and reference particles. The '*measured separation*' is then taken to be the difference in location of the trapped and reference particle as determined by the tracking method used. The tracking error is then just the difference between the '*measured separation*' and the '*true separation*'.

The tracking error is a gauge of how well the tracking method can locate the centres of two particles, given that when they are in proximity, the two particles become difficult to distinguish. A negative tracking error shows that the tracking method under-calculates the particle separation, and a positive tracking error shows an over-calculation. The standard deviation in the tracking errors gives an indication of the reliability of the tracking method over a range of separations. If the standard deviation remains small, but the average tracking error is non-zero, then this

indicates a systematic error in the tracking method, either it always under- or over-calculates the separation. However, if the standard deviation increases, this would suggest that the tracking method results in a less systematic error in the separation, with sometimes the separation being incorrect by a larger amount than at other times.

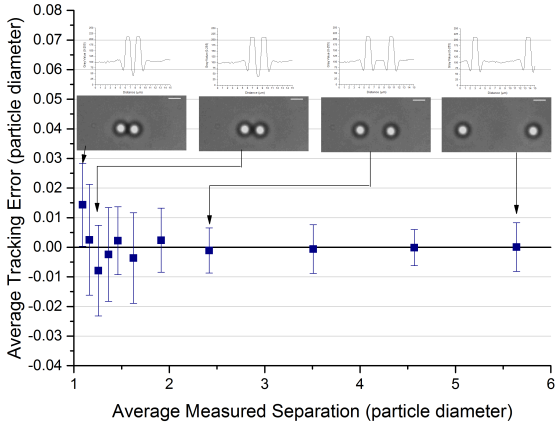

(a) Crocker & Grier tracking method

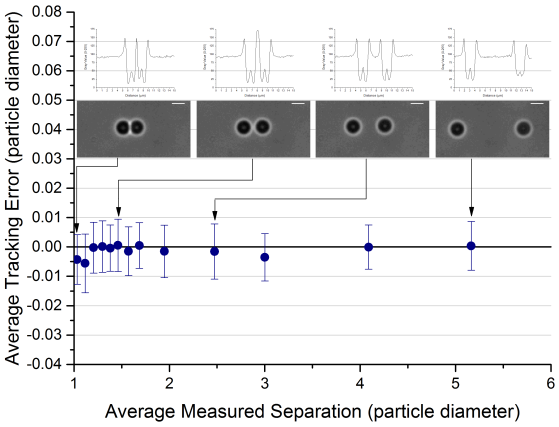

(b) Gutsche et al. tracking method

FIGURE 2.13: The tracking error determined for the (a) Crocker & Grier tracking method of locating the pixel peaks (*309*), and the (b) Gutsche et al. tracking method of locating a 'C'-shaped template of bright pixels (*312*). Both the tracking error and the measured separation are given in units of the particle diameter, which is here 1.86 μm. The error bars plotted are one standard deviation. Inset onto the plots are snapshots of the particles and their profile plots. The axes of the profile plots above the images are distance (μm) along the x-axis and Gray Value (0 - 255) along the y-axis. The scale bar in the images is 2 μm.

Figures 2.13(a) & 2.13(b) give the tracking errors, in units of the particle diameter, calculated for the two tracking methods used in this study, that of Crocker & Grier

and of Gutsche et al. respectively. For the Crocker & Grier method, figure 2.13(a) shows that this method of tracking is very accurate at separations greater than two particle diameters. As the inset images suggest, this is when the particles appear as two separate, well resolved particles with no image overlap. At these distances, the average error in the separation is less than 0.0001 particle diameters ($<$ 0.2 nm) and the standard deviation in this range is consistently less than 0.01 particle diameters ($<$ 19 nm). However, at closer separations than two particle diameters, the trend shows fluctuation in the tracking error to values of 0.015 particle diameters ($\sim$ 30 nm) and standard deviations up to 0.02 particle diameters ($\sim$ 40 nm). These errors are still not huge as the maximum likely tracking error is around 0.04 particle diameters ($\sim$ 70 nm), but the trend does show that an increased uncertainty in the tracking method does arise at close separations. The lack of a trend in the tracking error, and the increase in the standard deviation at these smaller separations suggests that the error at close separation is not systematic, but that it is just more difficult to resolve the two particles at closer proximity. It has been suggested that the Crocker & Grier method consistently under-calculates the separation (negative tracking error) due to this interference (*316*). In contrast, Verma et al. suggest the converse occurs (*318*). However, we have found that it is not so systematic, with the tracking error fluctuating between negative and positive values.

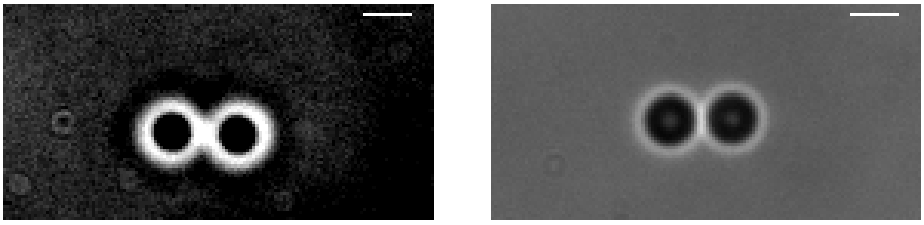

(a) Focussed image, inverted then contrast adjusted.

(b) Unfocussed image.

FIGURE 2.14: Optical microscopy images of two particles, taken with the particles (a) in focus and (b) slightly out of focus. The focussed image was then inverted to provide a bright ring, and the contrast was adjusted to give the image in (a). This is necessary for optimum tracking. The focussed image was not modified at all between image capture and particle tracking. The two images show the particles at the same measured separation of 1.3 particle diameters (2.4 μm). The scale bar in the images is 2 μm.

The first thing to note in comparing the plots in figures 2.13(a) & 2.13(b) is the inset images. The particles are the same, and are held at the same separations in both cases. The difference is that to achieve two particles that have two bright rings, the z-position is changed such that the particles sit slightly above the focus of the image. Because of this, the particles also appear larger than in the focussed case. This is true for the central circle, but the outer circumference of the rings is the same in both images. This method is chosen by us rather than taking focussed images then inverting them to have bright rings as the ring in this method is much better

defined. When unfocused, the bright ring has a uniform thickness around the whole particle (except between the particles when in close proximity). The difference in their appearances is shown in figure 2.14. As is apparent in the two figures, the edge of the bright ring in the unfocused, inverted and adjusted image (fig. 2.14(a)) is far less defined, and varies more in pixel value than the unfocused particles (fig. 2.14(b)). Another major difference in the images is the emergence of a central peak in the unfocused image. This is obvious in the profile plots inset on the tracking error plot in figure 2.13(b) where there is a peak in the centre of the dark pixel minimum. This does not effect the tracking, as it tracks only the periphery of the particles. Finally, using these unfocused images of the particles requires no adjustment of the images before analysing them, which when collecting several thousand images to measure one value of the force profile, considerably reduces the time taken for an experiment. Due to these reasons, images were taken of the particles when slightly unfocused as in figure 2.14(b) rather than focussed as in figure 2.14(a).

Comparing the tracking errors determined when using the Gutsche et al. method (fig. 2.13(b)) rather than the Crocker & Grier method (fig. 2.13(a)) shows that both methods are equally accurate for particle separations greater than $\sim$ two particle diameters. However, the Gutsche et al. method of tracking just the furthest separated regions of the two particles remains accurate at much closer separations. In fact, not until $\sim$ 1.2 particle diameters does any increase in the tracking error occur. This is because the regions where the tracking is occurring are still far apart on the two particles. At the very closest separations, a systematic under-calculation of the particle separation emerges. This error is still very small at -0.005 particle diameters (-10 nm) and is much smaller than that calculated for the Crocker & Grier method. At these small separations there is also the added effect of the proximity of the optical trap on the reference particle. Because the diameter of the optical trap protrudes beyond the size of the particle, the reference particle when in such close proximity will be attracted to the centre of the trap. Although the particle is adsorbed to the bottom of the cell, it may in fact shift slightly towards the reference particle, which would cause such a systematic under-calculation of the particle separation. If this is the origin of the tracking error at close separations, it should not effect the collected data in the BOT experiments, as during those experiments, data is only collected when the laser traps are off, so any deviation in the starting separation should still be tracked correctly.

The tracking errors have highlighted that both tracking methods offer accurate means of tracking two particles at a range of separations. At large separations, the Crocker & Grier method has smaller tracking errors and smaller standard deviations and appears to be the superior tracking method. However, as the particles are brought closer than 2 particle diameters apart, the tracking errors start to fluctuate between positive and negative values. Additionally, the standard deviation in the tracking errors starts to increase indicating its worsening accuracy in determining particle positions at close proximity. The Gutsche et al. method on the other

hand remains very accurate to separations of $\sim$ 1.2 particle diameters. There is however an increased error at very close proximity, but as explained earlier, this could be a systematic error where the laser trap is close enough to interact with both the reference particle and the trapped particle, displacing it slightly from its 'true' position on the glass surface. Also mentioned above, this error would be accounted for in the tracking anyway as the measurements are taken only once the laser trap is turned off.

Direct Comparison of a Single Measurement

	Crocker & Grier's Method	Gutsche et al.'s Template Method
r / μm	12.09 ($\pm$ 0.11)	12.20 ($\pm$ 0.12)
v / μm s^{-1}	1.83 ($\pm$ 0.20)	1.91 ($\pm$ 0.13)
D / μm^2 s^{-1}	0.19 ($\pm$ 0.02)	0.24 ($\pm$ 0.01)
F / fN	39.05 ($\pm$ 5.72)	32.72 ($\pm$ 2.41)

TABLE 2.1: The values of the initial separation r, velocity v and diffusion coefficient D determined from the two tracking methods and their calculated force F. The errors in the brackets indicate one standard deviation in the values measured.

A direct comparison was made for one measurement of the force between two PMMA particles (AC12) in dodecane. The laser was set to an output power of 0.4 W. The results from using the two methods of tracking are presented in table 2.1, which shows the resulting velocity and diffusion coefficients, and the calculated force between the particles at that separation. The standard deviations in each of the values are given which gives an indication of the errors in both methods. As table 2.1 shows, the code used for both tracking methods agree with each other and are therefore both assumed correct.

As the values in table 2.1 suggests, both tracking methods produce data that agrees with each other within their errors.

2.1.3 Conductivity

The conductivity was measured using a Scientifica conductivity meter (model 627) at an operating frequency of 15 Hz. This frequency would be required to be higher in more conductive (polar) solvents, where the larger number of ionic species causes resistivity due to the ions collecting on the electrodes. In nonpolar solvents this is not an issue and the frequency is therefore kept low where the permittivity of the solvent can be better assumed to be in the zero-frequency limit (*319*). A cylindrical, concentric stainless steel probe was immersed in the solution and the reading was recorded once the meter reached a consistent value. Before measurements were

taken, the probe was rinsed thoroughly with dodecane until the reading reached a value for the pure solvent $\Sigma_0 = 3.00 \times 10^{-11}$ S m^{-1}.

The number density of ions n_{ion} in a sample is calculated directly from the measured conductivity Σ via

$$n_{\text{ion}} = 2N_{\text{A}}\frac{\Sigma - \Sigma_0}{\Lambda_+ + \Lambda_-}, \tag{2.8}$$

where the molar conductivity of the z valency ions $\Lambda_\pm$ is calculated from the solvent viscosity η and the radius of the cation or anion $R_\pm$ via

$$\Lambda_\pm = \frac{z^2e^2N_{\text{A}}}{6\pi\eta R_\pm}, \tag{2.9}$$

where N_{A} is Avogadro's number and e is the elementary charge. Accordingly within the classical theory of Debye and Hückel, the screening length of the ions can be directly calculated using equation (1.18). For TDAT, the ion radii R_+ and R_- are 5.85 and 4.40 Å respectively (*26*). For the cation, this value was calculated from the vdW volume (*320*), and for the anions this was determined from X-ray crystallography (*321*).

2.1.4 Phase Analysis Light Scattering (PALS)

The electrophoretic mobility μ_e of the samples was measured using a universal dipcell electrode (Malvern, 2 mm electrode gap) in a square, glass cuvette (3.5 mm internal width, Helma) and a Malvern Zetasizer Nano Z instrument (4mW laser, 633 nm). The PALS method relies on measuring the phase shift of the scattered light from the particle comparative to a reference beam, and is the method used here over measuring the Doppler shift. The Zetasizer measures the velocity of a particle v in an applied electric field of strength E (which can be adjusted), from which the mobility can be calculated via equation (1.72). By measuring the electrophoretic mobility of the particles, the sign of their charge can be determined; negative electrophoretic mobilities indicates negatively charged particles. The fitted value of the particle charge from the BOT data comes from taking the square root of the value Z^2 which will always be positive, hence giving the magnitude of the charge only. So PALS offers a complimentary technique to determine the sign of their charge.

2.1.5 Surface Tension

The interfacial tension between dodecane and air was measured by a Kruss K100 Force Tensiometer, using the pull-off Wilhelmy plate method at 298 K. A roughened platinum plate was brought towards the solvent surface at a force of 0.1 mN and the interfacial force value was recorded through a force sensor attached to the tensiometer.

2.1.6 Karl Fischer Titration

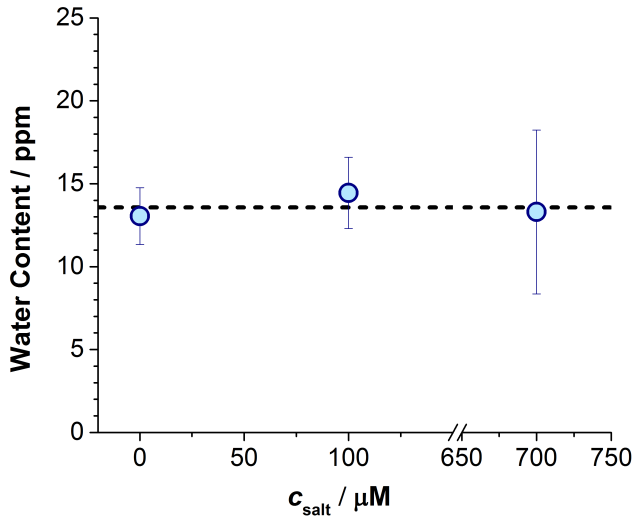

FIGURE 2.15: The water content of the samples in ppm without electrolyte present, and when 100 & 700 μM electrolyte is added.

The water content was measured via a Karl Fischer titration (Metrohm KF Coulometer) to ensure that the water content remained low, and that it did not increase with electrolyte concentration. As figure 2.15 shows, the water content of the samples is low, and there is no notable change in the water content upon addition of electrolyte, even at the highest electrolyte concentration studied in this investigation of 720 μM.

2.1.7 Dynamic Light Scattering (DLS)

The size of a colloidal particle can be determined from measuring light scattered from it, which is commonly detected at 90° for DLS. The dynamic motion of the particles in Brownian motion causes fluctuations in the scattered intensity. The time between the fluctuations are analysed with a correlation function, from which the diffusion coefficient D can be directly obtained from the decay time $\tau \propto D^{-1}$. Then, the size of the particle can be calculated from the diffusion coefficient (eq. (1.47)). The DLS instrument used in this study was the Zetasizer Nano S90 (Malvern).

2.1.8 Small-Angle X-ray Scattering (SAXS)

The samples were also observed using X-ray scattering using the SAXSLAB Ganesha 300 XL. For this, the samples were taken up into 1.5 mm borosilicate glass tubes (Capillary Tube Supplies Ltd.) to a height of 2 cm. The tubes were sealed with UV adhesive glue (Norland Optical Adhesives, no.81).

2.2 Materials

2.2.1 Particle Synthesis

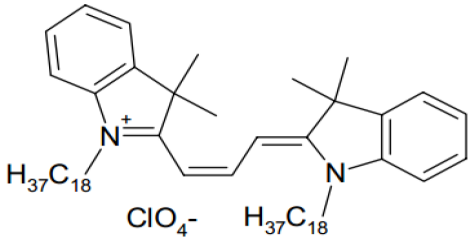

FIGURE 2.16: $DiIC_{18}$

Being widely used in nonpolar colloidal studies, this work also uses poly(methyl methacrylate) (PMMA) particles, sterically stabilised with poly(12-hydroxystearic acid) (PHSA). The majority of this work was conducted with the particles named AC12. These particles were synthesised by Andrew Campbell during his PhD in the same research group, and the full details of the synthesis are found in his thesis (322). The procedure used was first published as a collaborative effort by several people (323, 324), and is effectively a single-pot reaction. The monomers are methyl methacrylate and methacrylic acid, the initiator is azobisisobutyronitrile, the stabiliser is PHSA. These were all mixed together with a thiol which acts as a chain transfer agent in a solvent mixture of dodecane and hexane. This was then heated for around two hours at 80 °C until opalescent. A locking agent was then added to ensure the PHSA is chemically fixed to the surface of the particle, and the mixture was then heated to 120 °C and left overnight. To make the AC12 fluorescent, the dye 1,1'-ioctadecyl-3,3,3',3'- tetramethylindo-carbocyanine percholate ($DiIC_{18}$) was incorporated into the initial reaction mixture, for which the molecular structure is shown in figure 2.16. The same procedure was used to synthesise particles named AC11 also, but without the addition of the fluorescent dye. The other PMMA particles used in this study (IM6) were synthesised slightly differently by Ghulam Hussain with the addition of charged monomer groups (325). The synthesis was identical to the above synthesis, but an ionic monomer (trihexylpropyl ammonium methacrylate ($C_{25}H_{50}O_2N^+$) cations with tetrakis (3,5-bis(trifluoromethyl)phenyl) borate ($C_{32}H_{12}F_{24}B^-$) anions) (IM) was added rather than the methacrylic acid in the initial reaction mixture.

Particle Name	Dye	IM	Radius a ($\pm$) / μm	Reference
AC12	yes	no	0.775 (0.025)	(322)
AC11	no	no	0.645 (0.025)	(322)
IM6	no	yes	1.250 (0.001)	(26, 325)

TABLE 2.2: The names of the particles used in this study, indicating if they contain the dye $DiIC_{18}$, and/or an ionic monomer (IM). The size of the particles is also given, ascertained from DLS, from the references given. The references also provide the details of the synthesis used for each batch of particles.

2.2.2 Electrolyte Synthesis

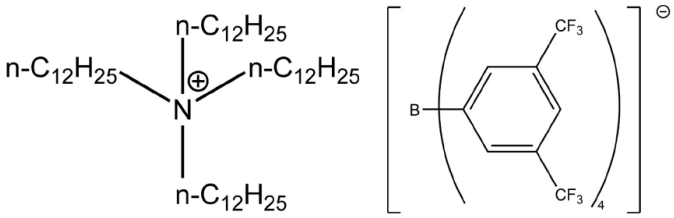

FIGURE 2.17: TDAT

The electrolyte tetradodecylammonium tetrakis (3,5-bis(trifluoromethyl)phenyl) borate, abbreviated to TDAT in this study, was synthesised as follows. Equimolar amounts of tetradodecylammonium bromide ($CH_3(CH_2)_{10}CH_{24}NBr$) and sodium tetrakis (3,5-bis (trifluoromethyl)phenyl)) borate ($C_{32}H_{12}F_{24}BNa$) were separately dissolved in enough methanol to dissolve the solids before combining together. This mixture was left in an oven at $>$ 60 °C to evaporate the methanol, and once dry, diethyl ether was added until the solid dissolved. This was poured into a separating column and water was added to dissolve the NaBr and separate it from the TDAT now dissolved in the diethyl ether. The water phase was removed and the process was repeated until no white solid remained to ensure maximum purity. The solution was finally left to evaporate any remaining water and diethyl ether in an oven at $>$ 100 °C. The final product has an oily appearance that is yellow in colour. Because it is an ionic liquid, TDAT appears almost molten at room temperature and only needs slight heating to turn it into a fluid with a honey-like viscosity. Before dissolving into the solutions, the TDAT was heated to this transparent, low viscosity appearance, as this maximised the amount that dissolved into the dodecane. The molecular structure of TDAT is shown in figure 2.17, and has a molecular mass of 1554.74 g mol^{-1}.

2.2.3 Sample Preparation

In this study, the low dielectric solvent used was dodecane (Alfa Aesar, $\varepsilon_r \sim 2$), which was kept dry using 10 Å molecular sieves. The solvent was not used until the conductivity reduced to $\Sigma_0 = 3.00 \times 10^{-11}$ S m^{-1}. The PMMA particles were repeatedly cleaned via centrifugation until the supernatant measured a conductivity of that of pure dodecane to ensure that they introduced no contaminants to the samples. Each sample was then made up firstly to a particle volume fraction of 3.7×10^{-4} before adding the TDAT to the required molar concentration c_{salt}.

Chapter 3

Results: Inflated Screening Length

This chapter presents the measured screening lengths for the PMMA-TDAT-dodecane system. Firstly, the value of the DH length λ_D is calculated directly from measurements of the conductivity. Secondly, the decay length of the pair interactions κ_{meas}^{-1} is measured using BOT. These values are then compared to ascertain if the assumption of DLVO theory, that $\kappa_{meas}^{-1} = \lambda_D$, is true across a range of electrolyte concentrations $c_{salt} < 1$ mM. Also presented are measurements of the particle charge, both from fitting of the force profiles and by measuring their electrophoretic mobilities.

3.1 Literature Review

The DLVO theory of colloid stability predicts that the electrostatic interaction between two charged spheres will follow a Yukawa interaction potential (eq. (1.50)), where the decay length of the interaction κ^{-1} is identical to the DH screening length λ_D, defined within linear PB theory. This implies that the form of the double layer above a charged surface can be predicted by DH theory and indeed has been calculated in a rigorous dressed-ion approach by Kjellander & Mitchell (*326*). Some, but not many, measurements have been made of the interaction between charged surfaces and/or particles. Possibly the earliest such measurement was by Israelachvili & Adams in 1978 who used the SFA to measure the repulsion between mica surfaces across dilute, aqueous KNO_3 solutions (*327*). At low ($c < 1$ mM) electrolyte concentrations, the measured decay length of the interactions was indeed found to be the DH length, as was measured with the SFA when proteins were bound to the surfaces (*328*), with the CP-AFM (*329*–*331*) or TIRM (*332*) technique at large separations, and using optical tweezers on emulsion droplets (*333*). In a few of these studies, the limitations of their measurement technique was highlighted. For example, in a couple of studies using TIRM, $\kappa^{-1} > \lambda_D$ was measured at higher electrolyte concentrations (*334*, *335*), but what was apparent in repetitions of the work from other groups was that in such concentration regimes, retarded vdW interactions (*246*) become difficult to distinguish from the electrostatic interactions (*248*). A different problem was noted with the optical tweezer measurements made (*333*). At high electrolyte concentrations, λ_D became smaller than the Brownian oscillations of the particle in a constant trap and therefore the results measured an

apparently increased screening length. In fact, the value coincided with the standard deviation in the fluctuations. With the BOT method used in this study, this feature is not an issue in the measurements as the tracking only occurs once the particles are freely diffusing, and Brownian motion is averaged out. In all cases however, these experimentally measured agreements show up the boundaries of validity expected within DH theory. Namely, the electrolyte concentration and the particle surface potential must be low (weakly coupled systems), and the measurement must be done when the separation is large ($h > \lambda_D$) (weakly overlapped double layers).

For the case of multivalent electrolytes (strong coupling regime), the screening length has been calculated (*336*–*338*) and experimentally observed (*339*–*341*) to be smaller than the DH length. The experiments were conducted with the SFA across a solution of cytochrome which resembles a 12:1 electrolyte (*339*) and between adsorbed layers of insulin (*341*), or measured between DNA with the osmotic pressure force measurement method with multivalent ligands (*340*). The reason for this discrepancy is due to the strong coupling present between multivalent ions and the charged surface, compacting the double layer compared with that for a monovalent electrolyte. Another interesting observation was made when measuring the interaction across surfactant solutions. In such systems, $\kappa^{-1} > \lambda_D$ was measured at high surfactant concentrations (*342*) because the micelles (formed above the CMC) did not appear to contribute to the charge screening between the surfaces, despite themselves being charged (*343*). In these cases, the value of λ_D was calculated assuming that the micellar solution is equivalent to a 1:1 electrolyte. Another limitation observed by many is that the DLVO theory describes the interactions measured at large separations only. At shorter separations, Pashley and coworkers measured enhanced repulsions, rather than the expected vdW attraction, beyond the upper limit of a CC boundary condition (*227*, *344*). They, and others since then, have attributed this to 'hydration' forces due to the additional energy required to dehydrate the cations at higher concentrations at the mica surface (*208*, *212*, *345*). Further measurements in the literature began to show that the forces at these separations were oscillatory, with periods of the physical size of the solvent molecules. This type of oscillatory profile has also been seen in other, less polar solvents (*222*, *346*–*348*). Such a force profile suggests the importance of solvent structure near interfaces, difficult to ignore when measuring forces at such close separations or in systems with high volume fractions of particles (*349*).

One very significant experimental observation was made by a group in Oxford, whereby the SFA revealed very large decay lengths in highly concentrated electrolytes and ionic liquids (*350*). At low ion concentrations, the force profiles measured between the mica substrates were well described by the DLVO theory, in agreement with earlier work (*351*). However, once the ionic strength reached a level that results in the DH length equalling the size of the ions, the interactions became longer ranging, showing a nonmonotonic relationship of κ^{-1} with the ionic strength. At this point, the classical way of thinking about charge screening (Debye-Hückel)

becomes difficult, as it requires freedom of the ions to arrange into the diffuse double layer. After analysing the measured force across several different ionic solutions, the group concluded that the measured decay length followed a scaling relationship of $\kappa_{meas}^{-1} \sim \ell_B \rho_{ion} R^3$, where R is the diameter of the ion (*352*, *353*). Initially, the suggested origin of this long-range force at high ionic strengths was due to the confined ions behaving instead as a dilute electrolyte; instead of the ions being the charge carriers, the solvent was now the species with freedom and as such acted as an effective charge carrier. Other suggestions included the effect of the strong correlations between the ions (*354*), massive ion pairing due to confinement (*355*) (previously theorised by Zwanikken & van Roij (*356*)), and non-equilibrium effects such as viscous forces (*357*). The effect of temperature has also been probed. Hjalmarsson et al. found that these long-range interactions were promoted when increasing the temperature (*358*), contrary to previous studies where the increase in temperature caused increased ion pair dissociation and thus decreased the DH length (*359*). As with other SFA measurements made at these close surface separations, the measured interaction shows an oscillatory profile, where a simultaneous switch from having a period of the solvent size, to the size of the ion pairs was observed above the point of the minimum in the measured decay length (*360*, *361*). Also prompted by these puzzling experimental observations of ionic liquids were many theoretical publications. For example, Adar et al. make additional calculations outside the DH theory to account for the excluded volume terms inevitable when the ions are considered with a finite size rather than point charges (*362*). This of course is important once the ions are no longer far from each other (*363*). Incorporation of the finite ion sizes has also been considered more crudely by Rotenberg et al. (*364*). Another suggestion was that the correlation lengths between solvent and ion molecules, and between two ions become distinguishable at high ion concentrations (*365*). This is because charge screening is unphysical when the solvent interactions becomes shorter ranged than the particle interactions (*366*). Contrary to the common theoretical thinking, this study by Coupette et al. suggests that in these regimes, the solvent cannot be ignored, but the specific interactions of the solvent molecules must be considered, in their case, as spheres also.

Although a fascinating and popularly debated topic, this chapter focusses within the limits of the DH theory. For weakly charged, well-separated particles in dilute, monovalent electrolyte solutions, the system should be well described by DLVO theory, where the decay length of pair interactions $\kappa^{-1} = \lambda_D$ (*367*). The method we employ in this chapter follows very closely the work done 10 years ago by Sainis et al., where BOT was used to measure the force between PS or PMMA particles in hexadecane using AOT surfactant as charge carriers (*368*, *369*). The difference with our study is in the charge additive; where they have added AOT surfactant, we are adding a hydrophobic electrolyte, TDAT. Of particular interest to us was their findings that the measured screening length appeared to be different when just changing the particle from PS to PMMA. They attribute this difference to the fact that

the cell had to be lined with a PMMA-MMA coating for the PMMA study to prevent particle adsorption to the glass, possibly modifying the ionic strength of the micellar solutions. Another suggestion was that the experiments were conducted at different times of the year and hence the local humidity was different. This highlights the sensitivity of nonpolar suspensions to impurities, and every care was hence taken to ensure that water content and contamination was kept to a minimum in all samples. This also suggests the possibility that the surface of the particle itself may also be a factor that needs considering when determining the interaction force.

3.2 Data for AC12

The majority of this chapter was conducted with the AC12 particles ($a = 775$ nm). Firstly, the conductivity of the sample was measured in order to calculate the classical DH length λ_D. Then in the same samples, the interaction force between two particles was measured with BOT and fitted to give a measured screening length κ_{meas}^{-1}, and an effective particle charge Z_{eff}. The values from these methods are then compared.

3.2.1 Conductivity

Every ion present in a solution will contribute to the total conductivity due to its mobility μ_e in an electric field (eq. (1.72)). Equating the Stoke's drag force (eq. (1.46)) with the electric force on a point charge ion of radius $R_\pm$ in an electric field, the electrophoretic mobility becomes

$$\mu_e = \frac{e}{6\pi\eta R_\pm}. \tag{3.1}$$

The contribution of a mole of simple ions is termed the limiting molar conductivity and is calculated to be $\Lambda_\pm = N_A e \mu_e$. From equation (3.1), this leads to the conductivity being inversely proportional to the size of the ion $R_\pm$ and the viscosity of the solvent η,

$$\Lambda_\pm = \frac{e^2 N_A}{6\pi\eta R_\pm}. \tag{3.2}$$

Each different type of ion present will then contribute to the total conductivity differently due to its different limiting molar conductivity. In a low dielectric solvent such as dodecane, electrolytes are expected not to fully dissociate into simple ions X^+ or Y^-, but either remain as an associated pair XY, or form a triplet ion $XY_2{}^-$ or X_2Y^+ due to the large Bjerrum length. At higher electrolyte concentrations, higher order ions are expected to predominate, but in these systems, triplets, pairs and single ions are assumed to be the only species present (*370*, *371*). The existence of such species follow these equilibria:

$$XY \rightleftharpoons^{K_p} X^+ + Y^- \tag{R 3.1}$$

$$XY_2^- \rightleftharpoons^{K_{t-}} XY + Y^- \tag{R 3.2}$$

$$X_2Y^+ \rightleftharpoons^{K_{t+}} XY + X^+ \tag{R 3.3}$$

If we assume that the electrolyte will form equal numbers of cations and anions, charge balance means that $[X^+] = [Y^-]$, and $[X_2Y^+] = [XY_2^-]$, then $K_{t-} = K_{t+} = K_t$. Furthermore, for the case where few ions are expected such as this low permittivity one, the approximation that $[XY] \approx c_{salt}$ can be made. The equilibrium constant K_p can be described as a function of the fraction of electrolyte present as a simple ion, X^+ or Y^-, $\alpha = [X^+]/c_{salt} = [Y^-]/c_{salt}$, via

$$K_p = \frac{[X^+][Y^-]}{[XY]} = \alpha^2 c_{salt}, \tag{3.3}$$

so $\alpha = \sqrt{K_p/c_{salt}}$. Similarly for the triplet ion, where the fraction $\alpha_t = [X_2Y^+]/c_{salt} = [XY_2^-]/c_{salt}$,

$$K_t = \frac{[XY][Y^-]}{[XY_2^-]} = \frac{\alpha c_{salt}}{\alpha_t}, \tag{3.4}$$

so $\alpha_t = \alpha c_{salt}/K_t = \sqrt{c_{salt}K_p}/K_t$. Introducing the limiting molar conductivities for the simple ions, and using equation (3.2), $\Lambda_0 = \Lambda_- + \Lambda_+ = 0.0024015$ S m^2 mol^{-1} (equivalent units are $\times 10^{10}$ pS cm^{-1} μM^{-1}) and the triplet ions $\Lambda_t = \Lambda_{t+} + \Lambda_{t-} = 0.001601$ S m^2 mol^{-1} produces for the measured specific conductivity (which is the solvent corrected conductivity $\Sigma - \Sigma_0$),

$$\Sigma - \Sigma_0 = c_{salt}(\alpha\Lambda_0 + \alpha_t\Lambda_t) = C\, c_{salt}^{1/2} + D\, c_{salt}^{3/2}, \tag{3.5}$$

where the fitting parameters $C = \Lambda_0\sqrt{K_p}$ and $D = \dfrac{\Lambda_t\sqrt{K_p}}{K_t}$. The measured values of the conductivity, corrected with the solvent conductivity Σ_0, are plotted in figure 3.1 and fit with equation (3.5). The fitted values of C and D then indicate the relative amounts of triplet and single ions present in the solution.

The residuals from this fit (the difference between the data and the fit) are plotted in figure 3.2 and shows that the deviation from the fit is random. A fit statistic called the adjusted R-Squared value R^2_{adj} can be calculated from these residuals, and is defined in appendix C. The fit in figure 3.1 gives a value $R^2_{adj} = 0.994$, which is close to unity and therefore indicates a good fit. We therefore have taken this fit of the conductivity data to calculate n_{ion} and λ_D to smooth out the trend for a clearer comparison with the screening lengths κ^{-1}_{meas} measured with BOT.

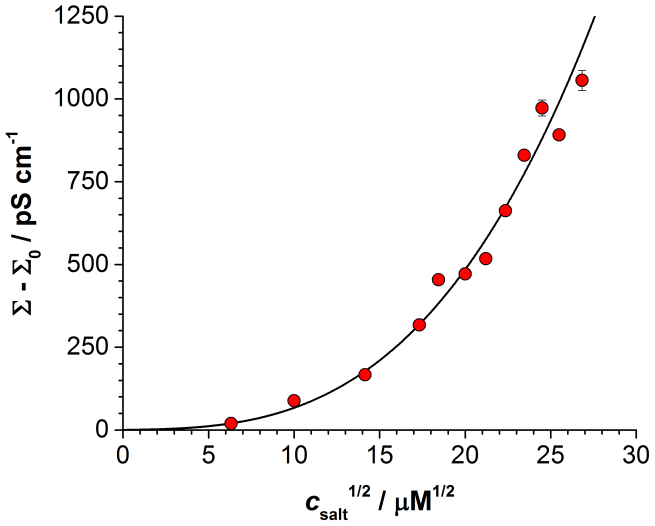

FIGURE 3.1: Specific conductivity $(\Sigma - \Sigma_0)$ as a function of the square-root of the electrolyte concentration $c_{\text{salt}}^{1/2}$. The data is fitted with the cubic form of equation (3.5), for which the fit gives the parameters $C = 0.844 \pm 0.149$ pS cm^{-1} μM$^{-1/2}$ & $D = 0.0585 \pm 0.0016$ pS cm^{-1} μM$^{-3/2}$, and the fit produces an $R^2_{\text{adj}} = 0.994$.

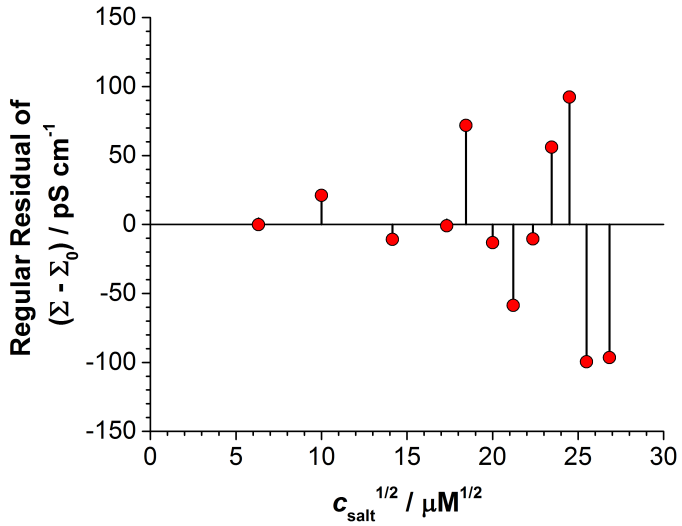

FIGURE 3.2: Residuals for the fit of the specific conductivity in figure 3.1.

The limiting molar conductivity of a triplet ion is related to that of the single ions if you consider that their respective electrostatic energies or radii are proportional. A few different values have been stated (372) since the work of Fuoss and Krauss on conductance of ionic solutions (370, 373–375), but if the assumption that $\Lambda_t \approx (2/3)\Lambda_0$ is made (376, 377), then the number density of single ions $= [X^+] + [Y^-] = 2N_A C\ c_{\text{salt}}^{1/2}/\Lambda_0$, and the number density of triplet ions $= [XY_2{}^-] + [X_2Y^+] = 2N_A D\ c_{\text{salt}}^{3/2}/\Lambda_t$. The total number density of ions is then just the sum of the single

and triplet ions. These quantities are plotted in figure 3.3(a). As the figure shows, the number of triplet ions is significantly larger than the number of single ions, completely dominating the total number of ions. This is not unexpected in a low dielectric solvent such as dodecane due to the large Bjerrum length. This also gives an indication of the amount of salt that formed ions. This fraction is plotted in figure 3.3(b), and shows that even at nearly 1 mM electrolyte, only 0.02 % of the salt molecules ionised as either single ions, or triplet ions. Again, this is not unexpected in this low dielectric solvent, but indicates the effect that just small numbers of ionic species has on the total conductance of a nonpolar solution. This also highlights how low levels of impurities could hugely effect the electrostatic properties of nonpolar colloids.

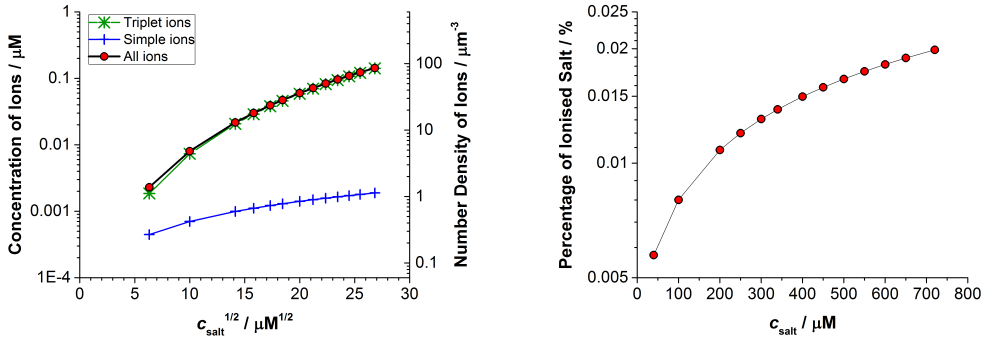

FIGURE 3.3: (a) The concentration and number density of ions n_{ion}, including the number density of the simple (blue plus) and triplet (green star) ions separately, as a function of the electrolyte concentration c_{salt}. (b) The percentage of salt that dissociates into an ionic species, calculated by $(n_{\text{ion}} N_{\text{A}}/c_{\text{salt}}) \times 100\% = 2(\alpha + \alpha_{\text{t}})$.

The equilibrium constants K_{p} and K_{t} for the single and triple ion formation can be calculated from the fitting parameters C and D, $C = \Lambda_0 \sqrt{K_{\text{p}}}$ and $D = \dfrac{\Lambda_{\text{t}} \sqrt{K_{\text{p}}}}{K_{\text{t}}}$. This gives that $K_{\text{p}} = 1.235 \times 10^{-9}$ μM and $K_{\text{t}} = 9.62$ μM. So, at $c_{\text{salt}} = 100$ μM, $\alpha = 3.51 \times 10^{-4}$ % and $\alpha_{\text{t}} = 0.00365$ %, and at $c_{\text{salt}} = 1$ mM, $\alpha = 1.11 \times 10^{-4}$ % and $\alpha_{\text{t}} = 0.0115$ %. The percentage of salt that dissociates into an ion (either triplet or simple, so $2(\alpha + \alpha_{\text{t}})$) is plotted in figure 3.3(b).

Finally, from the values of n_{ion}, the DH length can be calculated by following equation (1.18), and these values are plotted in figure 3.4. The trend shows what is expected within DH theory, with λ_{D} decreasing monotonically with increasing electrolyte concentration. By measuring the conductivity, it also assures us that the additional electrolyte added does dissociate and increase the number of ions in the solution to ensure the monotonic trend. This therefore predicts that the greater number of ions present should result in shorter ranged interactions between the particles in these solutions accordingly.

Now we have measured the DH length for these solutions, we can determine the value $\kappa_{\text{D}} a$, where $\kappa_{\text{D}} = \lambda_{\text{D}}^{-1}$, which is an indication whether the system can be

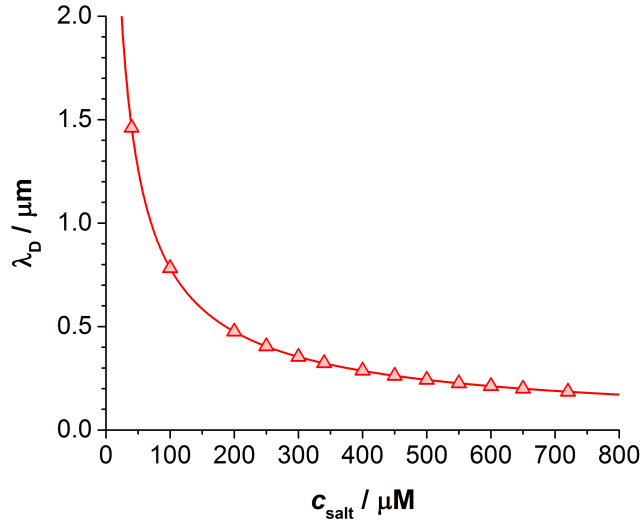

FIGURE 3.4: The DH length λ_D, calculated from equation (1.18), using the smoothed values of n_{ion} from figure 3.3, as a function of the electrolyte concentration c_{salt}.

considered as point charges (small $\kappa_D a$) or flat plates (large $\kappa_D a$). These values are $\approx$ 0.5 at $c_{salt} = 100$ μM, and ≈ 4 at $c_{salt} = 700$ μM, so across the electrolyte concentration studied, the system can not be fully described by either case. However, the limit for the applicability of the GC theory is around $\kappa_D a > 5$ (*378*) and so this system is likely best described by DLVO theory that assumes a system closer to being point charges than to flat plates.

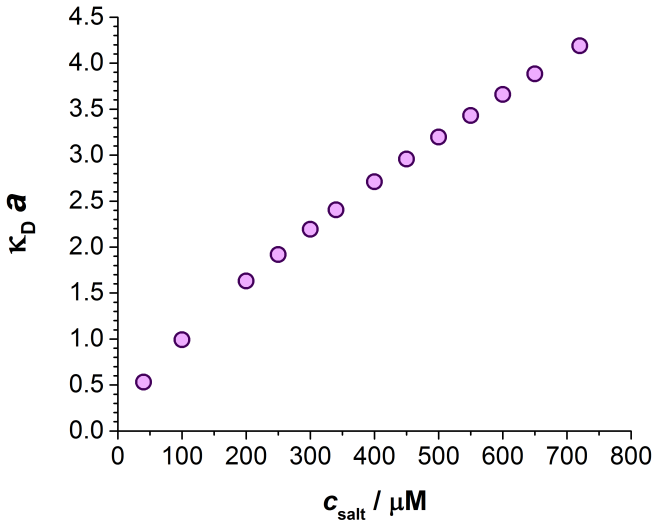

FIGURE 3.5: Values of $a/\lambda_D = \kappa_D a$ as a function of c_{salt}. The system changes from a more point-like particle ($\kappa_D a << 1$) to a more flat-plate ($\kappa_D a >> 1$) description on increasing the electrolyte concentration.

3.2.2 Blinking Optical Tweezers (BOT)

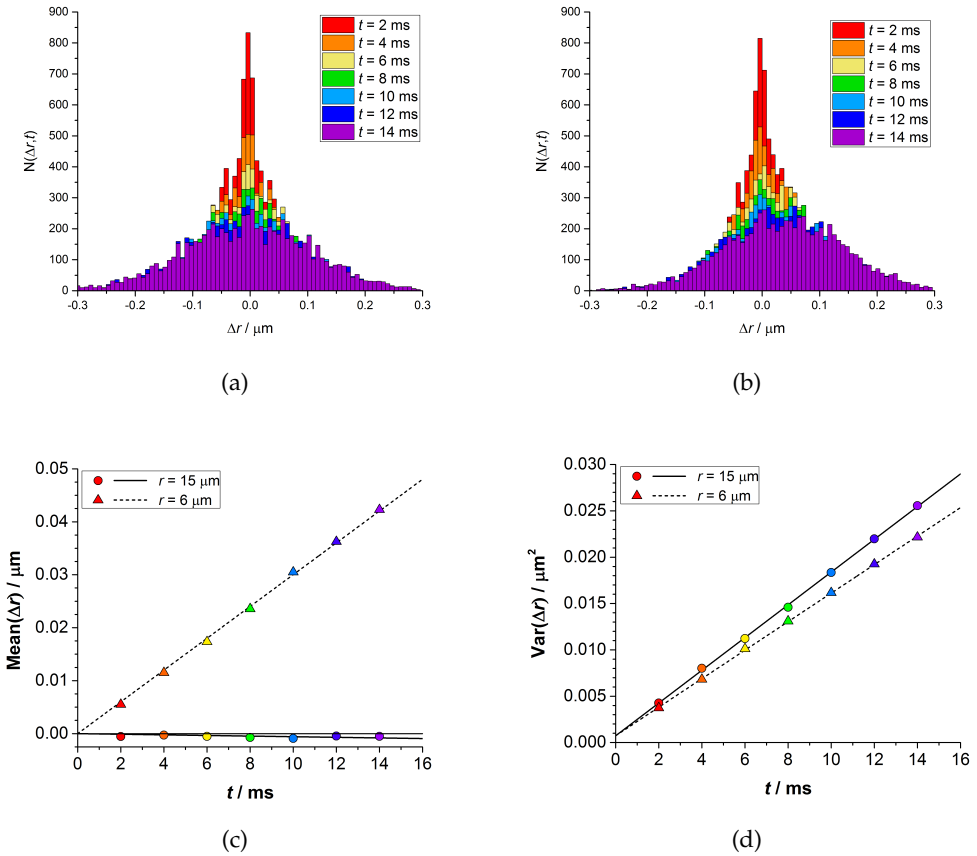

FIGURE 3.6: This figure gives an example of the data collected with BOT for AC12 particles in dodecane with no TDAT added. Top: The histograms indicating the distribution (N(Δr,t)) in the change in particle separation Δr over time t, starting at an initial separation of 15 μm (left) and 6 μm (right). Each colour represents an average of ∼ 8000 repeats of one pair of particles at time t after the laser is blinked off. Bottom: The corresponding values of the mean and variance in Δr over time from the histograms above. The data for an initial separation of 15 μm is shown as circles, and 6 μm as triangles. The gradients of the linear fits are then proportional to the velocity and diffusion coefficient of the particle pair at that initial separation. The errors in Δr are omitted in the plot as they are comparatively large. The standard deviation in Δr can be calculated from $\sqrt{\text{Var}(\Delta r)}$, ∼ 0.1 μm, from the plot in figure 3.6(d).

As explained in the experimental section 2.1.1, the BOT method measures the force between two AC12 particles by calculating simultaneously the particle's velocity and diffusion coefficient at different particle separations, then using the equation $F(r) = k_B T v(r)/D(r)$. Both v and D are obtained with particle tracking. As an example, the raw data obtained from the tracking (for which a sample was shown in figure 2.9) produces the histograms in figures 3.6(a) & 3.6(b). Although the lasers are turned off for a total of 25 ms, the tracking data for the first 14 ms only is taken, as any longer and the particles no longer move with a constant velocity due

to the drag force opposing their movement, and because the force between them decreases with increased separation. These histograms show two things. Firstly, the average of each distribution gives the average separation of the particle pair at the time indicated. By plotting these values as a function of time, as in figure 3.6(c), the particle velocity can be calculated from the gradient. The difference in gradient of the two plots given correspond to the faster velocity of the particles held at a separation of 6 μm rather than 15 μm. At $r = 15$ μm, the histogram in figure 3.6(a) shows that the average separation of the pair of particles is not changing over time, whereas when held closer, the force is increased causing the average separation to increase over time, giving the histogram in 3.6(b), and hence a velocity. As the data for $r = 6$ μm shows, taking the gradient over the first 14 ms is reasonable, as the velocity appears constant during this time.

The second obtainable quantity from the histograms is its variance, where a wider distribution indicates a larger deviation in the separation from the mean. All particles undergoing Brownian motion will show an increase in the variance in their location over time, and again by plotting it against time, as in figure 3.6(d), the diffusion coefficient can be calculated from the gradient (eq. (1.44)). It may seem that because the variance is used to calculate the value of D, that different numbers of repeats for a data set would change the value, however, because it is the change in variance over time, the magnitude of each value is not so important. The sample length for each histogram is therefore always set to the same value, so this should not be an issue. Despite this, the actual number of data points collected may be slightly different for each point, as the tracking is sometimes not successful. This occurs for example when one of the particles moves vertically such that its maximum pixel intensity is decreased below a threshold value. This however just highlights the need for a large sample length, which for these experiments took an average of ~ 8000 measurements of r at each time interval t. The sample length does however affect the intercept of the plot, which interestingly gives an indication of the error in the tracking method (379), and as figure 3.6(d) shows, this is non-zero, but small. This slight offset in the data does not however affect the gradient of the plot, and hence the value of D should not need correcting in any way to compensate for such errors. The value of the intercept is ≈ 0.001 μm^2, which gives an error of ≈ 0.02 particle diameters. Comparing this value to the tracking errors determined in section 2.1.2, suggests that the error in the data is larger than the error due to tracking (< 0.01 particle diameters). The fact that these values do not quite agree just shows that the errors arising from this technique are not solely due to the tracking errors. One such origin for errors could be due to the fact that in the experiments, the particles are not confined to the horizontal plane as they were when determining the tracking errors; the particles in the experiment can also diffuse in the vertical direction, which cannot be tracked in our experimental setup.

Diffusion Coefficient D

The effect of the electrolyte concentration and particle separation on the diffusion coefficient alone is interesting. The diffusion coefficient is defined in section 1.2.2, where the self diffusion coefficient (eq. (1.47)) for AC12 in dodecane, using that $\eta = 1.36$ mPa s (*380*) and $a = 0.775$ µm, is $D_0 = 0.207$ µm^2 s^{-1} at 298 K.

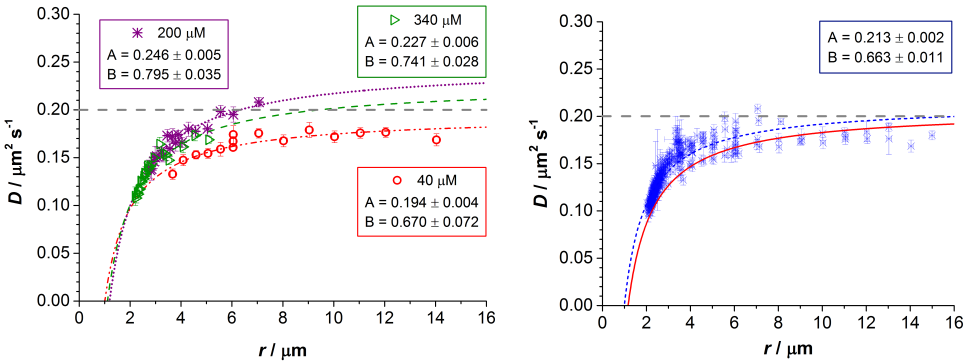

(a) (b)

FIGURE 3.7: The fits to the plots follow the form $D = A\left(1 - \frac{3}{2}\frac{B}{r}\right)$, where following equation (1.48) should produce $A = D_0$ and $B = a$. The fits to the data are shown as dashed lines, and the fitted values for A & B are indicated on each plot. Left: The data for AC12 in dodecane at c_{salt} = 40, 200 & 340 µM. Right: All the data collected over all c_{salt} for AC12 particles in dodecane, where the solid red line is the fit assuming the values $A = D_0 = 0.207$ µm^2 s^{-1} & $B = a = 0.775$ µm. The horizontal line at a value of $D = 0.207$ µm^2 s^{-1} simply indicates the calculated diffusion coefficient at infinite dilution for this system, to which all the data tends to at large r.

The measured values of D are presented in figure 3.7, with figure 3.7(a) presenting the data for just c_{salt} = 40, 200 & 340 µM, and figure 3.7(b) presenting all the data collected for every c_{salt}. In all cases, equation (1.48) is fit to the data, with the fit parameters $A = D_0$ and $B = a$ to give the dashed lines. An additional trend is added to figure 3.7(b) with fixed fit values of $A = D_0 = 0.207$ µm^2 s^{-1} & $B = a = 0.775$ µm. This trend indicates that the data is in fair agreement with the expected values, with $D = D_0$ when the particles are well separated, but decreasing below D_0 when the particles are closer together due to hydrodynamic coupling. The slightly higher values of D measured than expected could be due to a slight difference in temperature (and hence viscosity) or because of the inherent slight polydispersity of the particles. Equation (1.48) is strictly true for a hard sphere interaction, and as the interaction between these particles is more complex, this could also explain the deviations measured. Looking at the individual data for different electrolyte concentrations in figure 3.7(a), the diffusion coefficient appears to show some dependence on the electrolyte concentration, with the data at 40 µM underestimating both a and D_0, and the data at 200 µM overestimating them both.

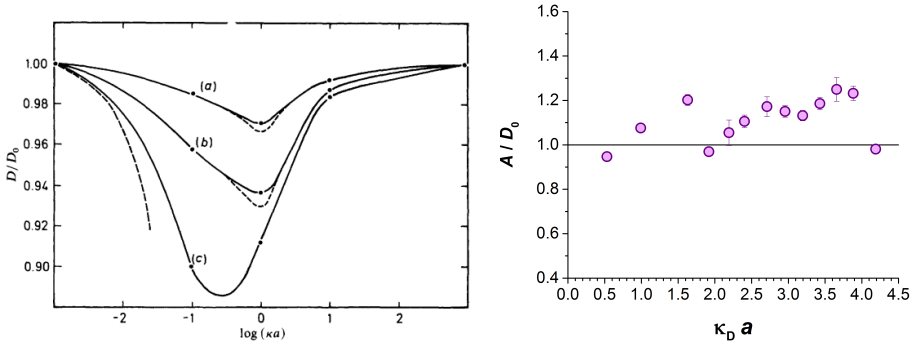

(a) Predictions of equation (3.6) (b) Experimentally measured

FIGURE 3.8: (a) The deviation of the diffusion coefficient as a function of κa with $b_+ = 0.176$ & $b_- = 0.169$ for a: $\Psi_s = 3$, b: $\Psi_s = 5$, & c: $\Psi_s = 8$ from reference (381). (b) The measured ratio of the fitted value A to the self diffusion coefficient D_0 as a function of $\kappa_D a$.

Because the double layer contains a diffuse arrangement of ions, there can be a delay between the sphere moving, and the double layer following it. This causes deviations in the diffusion of a particle from the Stokes's mobility. So for a negligible double layer thickness ($\kappa_D \to \infty$) there is clearly no difference between its diffusion and that of a hard sphere. Equally, for very thick double layers ($\kappa_D \to 0$), the movement of the sphere is small compared with λ_D and therefore equally the diffusion is well described by that of a hard sphere. However, in the regime where $\lambda_D \sim a$, the presence of the double layer can significantly alter the diffusion of the particle as the ions cannot relax into their equilibrium positions as fast as the sphere is diffusing. Outlined neatly in (382) (pages 78-96) is a derivation of the exact effect of the value $\kappa_D a$ on the diffusion coefficient. Also derived in this chapter is the effect of the surface potential, Péclet number (which defines the ratio of fluid flow to the diffusivity of the ion; low Péclet number means that the dynamics are dominated by thermal motion, i.e. Brownian motion) and the ion size. Considering how all these features of a colloid can effect D, it is unsurprising why we see deviations in the measured values from BOT at different electrolyte concentrations. The derived form of the dependence of D on $\kappa_D a$ is (382)

$$D = D_0\left[1 - \bar{b}\Psi_s^2 \tilde{f}(\kappa_D a)\right], \tag{3.6}$$

where $\tilde{f}(\kappa_D a)$ is a function of the double layer thickness, that tends to 0 when $\kappa_D a = 0$ or $\kappa_D a \to \infty$, and has a maximum at $\kappa_D a = 1$. $\bar{b} = (b_1 + b_2)/2$ where b_1 and b_2 are the dimensionless ion radii of the counterions and coions respectively, which are calculated from their limiting conductivities and scaled with the factor $e^2/\varepsilon_r\varepsilon_0 k_B T$. As an example, a hydrogen ion would have a value of $b_+ = 0.056$ and a hydroxide ion a value of $b_- = 0.098$. So effectively, equation (3.6) predicts that a deviation of $D < D_0$ occurs, with a maximum deviation at $\kappa_D a = 1$, and this is given in figure 3.8(a) from reference (381). Additional deviation is also predicted for higher surface potentials,

lower Péclet numbers and large ion sizes. The predictions for this deviation are expected over the entire range of $\kappa_D a$ that we have investigated in our system ($0.5 < \kappa_D a < 4.5$), hence the differences observed in the measured values of D from BOT, and in the fitted values A and B. A plot of the fitted value A at different $\kappa_D a$ is plotted in figure 3.8(b). The trend does not show a deviation solely at $\kappa_D a = 1$ as the theory suggests, nor is the deviation showing that $D < D_0$, but the converse. However, it does indicate that there is a deviation at $\kappa_D a \sim 1.5$ and then another deviation at higher $\kappa_D a$. Though this trend does not show anything particularly useful in terms of predicting when a deviation is likely to occur at different c_{salt}, it does highlight that differences in the values of D at different c_{salt} could be due to complexities of the electrical double layer, or it may simply be due to a completely random effect in the measurement. Either way, the values of D obtained with the BOT method appear to be sensible for the system.

Particle Velocity v

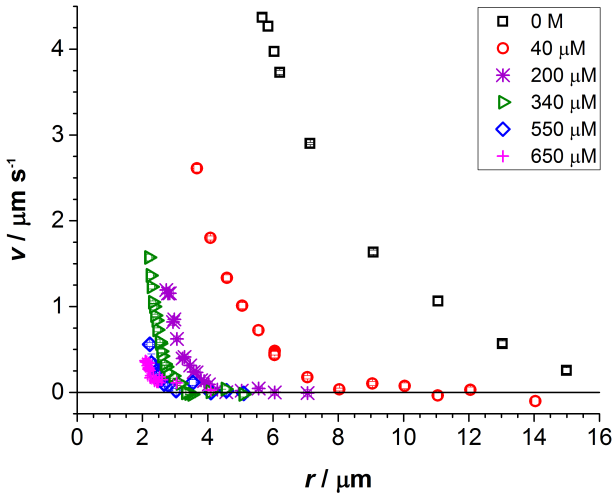

FIGURE 3.9: Velocity profile from BOT measurements as a function of particle separation for a range of c_{salt}.

The velocity of the particles due to their mutual interaction is calculated from their mean displacement over time while the lasers are turned off. For two particles moving away from each other, i.e. repelling, the velocity is a positive value. A few examples of the measured velocity at different electrolyte concentrations are given in figure 3.9. In all samples and at all particle separations, the velocities measured were always positive. At large separations, the velocity was zero, and the slight fluctuation observed about the zero value just highlights the random error in the measurements, and is not a feature of an oscillatory force. The effect of increasing c_{salt} is more obvious in the velocity profiles, with additional ions present decreasing the velocity at a specific particle separation r.

Interaction Force $F(r)$

The force acting between the two particles is calculated via the thermal energy k_BT using $F = k_BTv/D$. These values are plotted as a function of the particle separation in figures 3.10(a) & 3.10(c) for varying electrolyte concentrations. The measured forces with this BOT method are very weak, on the order of fN, indicating the slowly decaying interaction potentials inherent in nonpolar solvents. Despite their weakness, the BOT technique is perfect for measuring them, especially at the very large separations of several microns. These measured repulsions show directly that the particles must be charged, as no other interaction present in the system could act over tens of microns. Although not immediately obvious how these particles are charged, we believe that it is likely due to some dissociation occurring from either the PHSA layer or the dye, both of which contain groups that could ionise. This data is then fit with the Yukawa force derived in DLVO theory (eq. (1.50)). The data is also plotted as r^2F against r in figures 3.10(b) & 3.10(d), which is a clearer way to observe the changes in the decay of the profiles,

$$\ln\left(r^2F\right) = \ln\left[(Z^2\Theta^2\ell_Bk_BT)(1+\kappa r)\right] - \kappa r. \tag{3.7}$$

By taking out the Coulombic contribution (r^{-2}), and plotting the result on a semi-log scale, the gradient of the trends effectively gives the value $-\kappa_{meas}$, where κ_{meas}^{-1} is the measured screening length for the interaction between the two particles. To reiterate the differentiation between the notation used for the measured screening length from fitting the BOT force profiles κ_{meas}^{-1}, and the DH length λ_D determined from measuring the bulk conductivity of the samples. Within the DLVO theory, the screening length κ is defined to be always equal to the DH length λ_D, and it is this equivalence that we are testing here.

With equation (3.7) in mind, the trend in figure 3.10(b) for no electrolyte present, indicates that the interaction is almost unscreened as the gradient is so small. For a completely clean nonpolar solvent, no electrostatic screening is expected as there are no ions present in the system, other than the counterions (eq. (1.35)). In this case, the presence of some impurities, which is difficult to avoid, results in a measurable screening length even in the salt-free system. The strong effect of just small amounts of ions is also obvious in the difference in the gradient after adding just 40 μM of electrolyte.

Another interesting observation that can be made more easily in the r^2F plots in figures 3.10(b) & 3.10(d) is the change in the gradient (-κ_{meas}), and the magnitude of the forces at increased electrolyte concentrations. As expected, figures 3.10(b) & 3.10(d) show that with increasing electrolyte concentration, the separation at which the particles interact with a certain magnitude of force becomes smaller. This is because the double layers become thinner as more ions are added into the solution, thus requiring the particles to be closer together to interact with the same magnitude of force. What is unexpected in figure 3.10(d) however, is that the decay of the

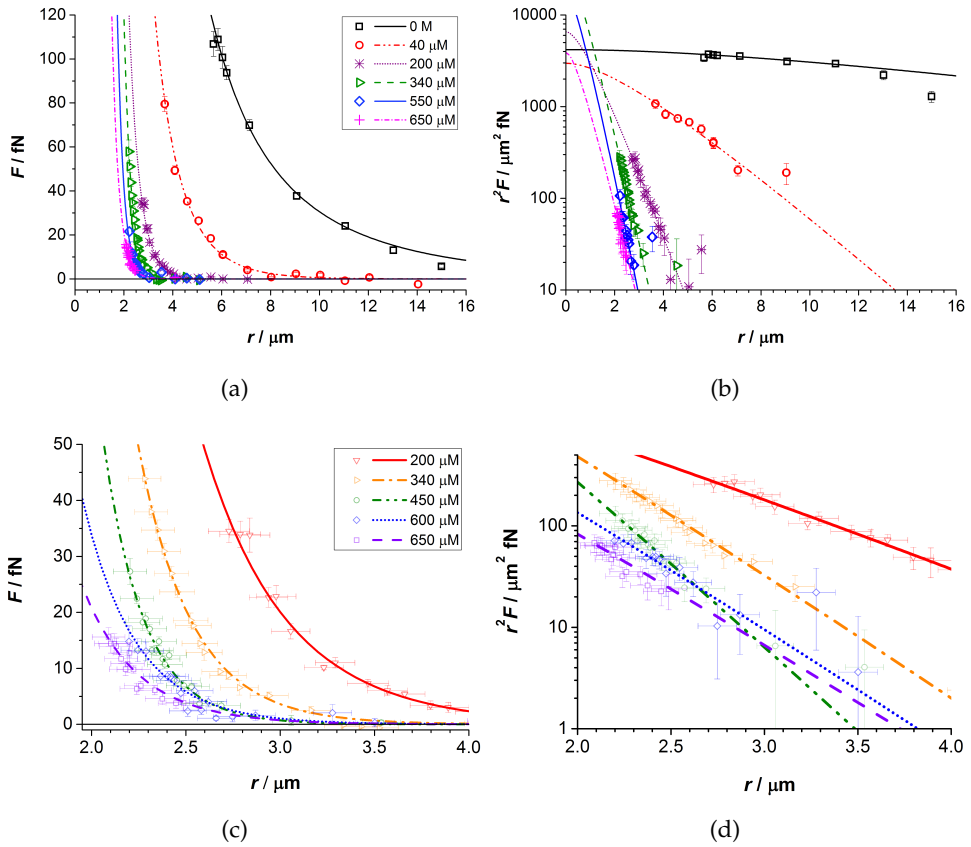

FIGURE 3.10: BOT force profiles $F(r)$ and the equivalent plot of r^2F on a semi-log scale. The fitted curves are the Yukawa force (eq. (1.50)). The bottom two plots give a magnified view of the data at a few of the highest electrolyte concentrations.

interaction starts to become slower when the electrolyte concentration is increased above 450 μM. The decay should be inversely proportional to the thickness of the double layer, i.e. more ions produces a thinner double layer and so the interaction decays more quickly. What is not happening in the data is a hysteresis-type trend; although the decay lengths for the systems at 340 & 650 μM appear almost identical, the force at the higher concentration is always weaker. The decay length of these profiles is represented by the measured screening length $\kappa^{-1}_{\text{meas}}$, whereas the magnitude is represented by the charge of the particles Z. This apparent weakening of the force at closer separations is in contrast to the work of Pashley and coworkers who measured an enhanced repulsion (227, 344).

Before presenting the fitted values for $\kappa^{-1}_{\text{meas}}$, a limitation of this BOT method is first discussed. A combination of effects results in there being a limit of when a force measurement can be made. The first is in the strength of the optical traps. For interactions that are too strong, the particles can overcome the potential barrier of the optical traps and escape them, thus there is an upper limit in the interaction strength measurable. Another limitation of this technique is that the vertical trap stiffness seems to be weaker than the lateral stiffness. This manifested in particle

pairs that, before escaping the traps altogether, would move vertically with respect to each other to maximise their separation. The particle tracking was only possible in the horizontal plane, so vertical motion of the particles was not measurable and led to a reduction in the amount of tracking data collected. Once this noticeable drop occurred, the experiment was ended. This vertical motion is of course more detrimental at closer particle separations; at large separations, the vertical motion is significantly smaller than the horizontal separation, so the vertical motion becomes negligible. This is why stronger forces were able to be measured in the lower c_{salt} samples, as the interactions were longer ranged. With this in mind, every care was taken to use data collected only when the tracking was thought to be giving the correct result.

3.2.3 The Measured Screening Length for the Pair Interaction κ_{meas}^{-1}

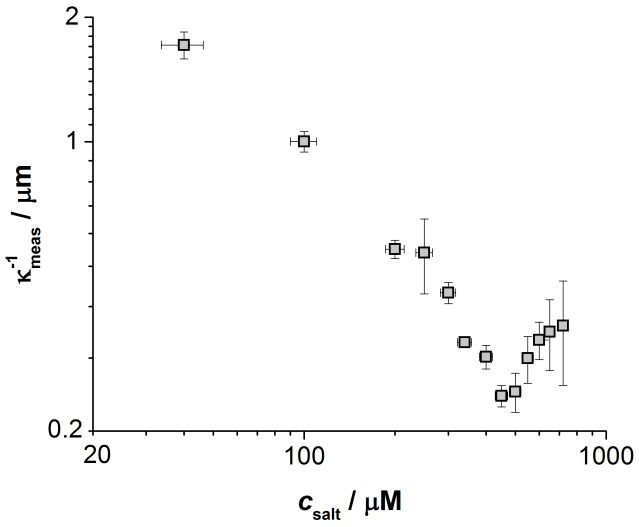

FIGURE 3.11: The measured screening length κ_{meas}^{-1} from the force profiles measured with BOT between pairs of AC12 particles in solutions at different electrolyte concentrations c_{salt}. The plot is presented on a log-log scale to emphasise the expected power law dependence of eq. (1.18).

The fitted screening lengths obtained from the data in figure 3.10 are plotted as a function of the electrolyte concentration in figure 3.11. The data is presented on a log-log scale, because according to equation (1.18), if $\kappa_{meas}^{-1} = \lambda_D$, then it should show a monotonically decreasing trend following a power law (so linear on a log-log scale) with increasing electrolyte concentration. Due to the scale chosen, the value for the salt-free sample is not given, but the measured value was $\kappa_{meas}^{-1} = 9.86$ (± 0.70) µm, showing immediately how long ranged the interactions are in this solvent. As is immediately obvious, the measured screening length does not show a monotonic trend with increasing electrolyte concentration, as suspected from looking at the gradients in figure 3.10(d). What we have already found by measuring

the conductivity of the same samples, is that increasing the electrolyte concentration does increase the number of ions in these solutions, so *the screening length of the pair interaction is increasing with the ion density* at high electrolyte concentrations. To aid in the discussion, the concentration at which the minimum in κ_{meas}^{-1} was measured is defined to be the critical salt concentration c_{salt}^{*}. As will be shown later, several interesting features of the system occur at concentrations above c_{salt}^{*}.

Before discussing the possible physical origins of this unexpected trend in κ_{meas}^{-1}, the details of the fitting are presented to highlight that the results cannot be explained through any anomalies in the data collected at high and low c_{salt}. The potential errors from the tracking methods used have been discussed already in section 2.1.2. In short it showed that over the range of r that measurements have been taken, the tracking errors should not significantly skew the data measured at the smallest r which would affect the data at higher c_{salt} most. Another potential cause for error in the interpretation of the data is the range of r over which κ_{meas}^{-1} is fitted.

Range of Data Fitting

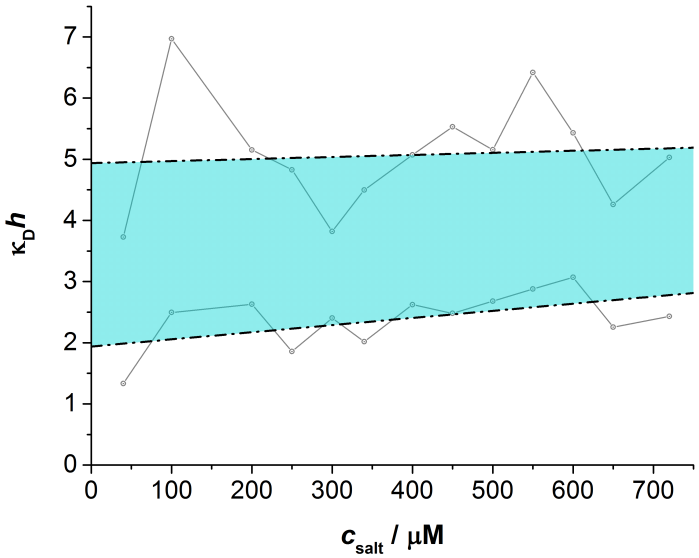

FIGURE 3.12: The range of particle separation over which the data was fit to obtain the values of κ_{meas}^{-1}. The minimum and maximum reduced surface separation $\kappa_D h$ for each electrolyte concentration are plotted, with the rough trend of those values overlaid with the dotted-dashed line, between which is highlighted in blue.

The fit to a data set can only be improved by a larger range of values. For example, most equations will look approximately linear if you fit over a small enough range. Looking at the force data presented in figure 3.10(a), the data clearly covers different particle separations at each electrolyte concentration. What is important with fitting electrostatic force profiles however is the scaled surface separation h/λ_D, which indicates the separation between the two charged surfaces

of the two particles relative to the thickness of the double layer λ_D. As observed by many in the literature, deviations from DLVO force profiles were observed at surface separations of roughly $h < \lambda_D$. The data in our system was collected over a very similar range of $\kappa_D h$ for every electrolyte concentration studied, where $h > 2\lambda_D$ in all cases. This should eliminate the possibility that a similar solvation force that was observed in the literature may be confusing the data (*208*, *212*). The range of the measurements are given in figure 3.12, which shows that each force profile was measured within the approximate range $2 < \kappa_D h < 5$, so the fitting was done over $\sim$ 2-3 DH lengths.

Ideally, the fit for the force profiles would be over several more DH lengths, however, the limitations of the BOT technique used was restricted in both the separations measurable due to the tracking, and the forces measurable due to the fairly weak optical traps. Despite this, given the range of $\kappa_D h$ is the same for each data set, any errors resulting from this issue should be systematic, and not be the cause of the trend in κ_{meas}^{-1} observed.

Fit Statistics

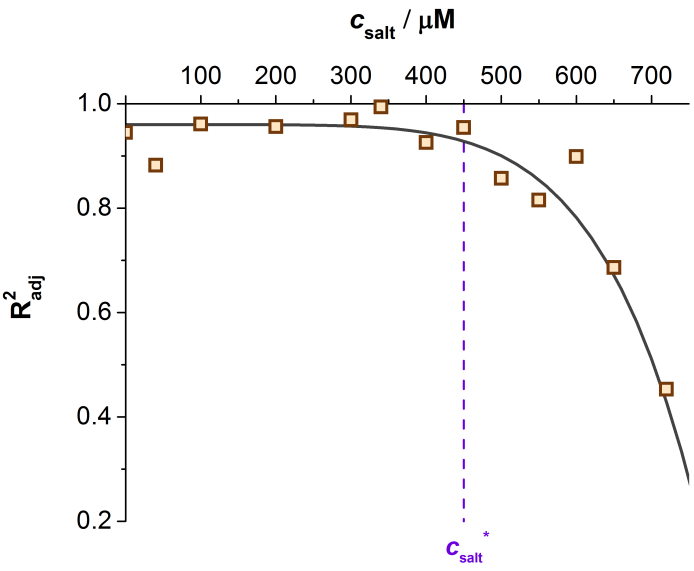

FIGURE 3.13: Fit statistic R^2_{adj} for the Yukawa force fit to the force profiles measured with BOT.

One indication of what may be happening above $c^*_{salt} = 450$ μM is how well the force profiles measured follow a Yukawa force, and this can be done by calculating the adjusted R-Squared value R^2_{adj} for each fit, which is defined in appendix C. The value R^2_{adj} is here used to compare the 'goodness of fit' of the form of the Yukawa force to the data measured with BOT. Deviations from $R^2_{adj} = 1$ indicates that the data does not follow well the form of the fit. The values for the data measured is plotted in figure 3.13, and shows that using a Yukawa fit does not describe well the force profiles above c^*_{salt}. The solid line is not a fit to the data, but a guide for the eye

of the general trend that the Yukawa force becomes an increasingly inappropriate fit with increasing c_{salt} above c^*_{salt}. The fact that the fit quality does decrease at the higher c_{salt} also accounts for the larger error bars associated with the values of κ^{-1}_{meas} at those concentrations. This could be due to a few reasons, either being that the data is less accurate at higher c_{salt} or that there is less data at higher c_{salt}, or that the force profiles follow a different profile due to non-DLVO behaviour. The tracking errors, the error bars accompanying the force measurements, and the range of the data have already been determined not to be the cause of the unexpected trend in the fitted value of κ^{-1}_{meas}, thus the first two suggestions can be dismissed. The final suggestion however cannot be ignored, that the force may no longer follow a Yukawa profile at the higher electrolyte concentrations. This suggests that the fitted values of the screening length κ^{-1}_{meas} may not give the appropriate value for the actual decay of the interaction.

3.2.4 Comparison of κ^{-1}_{meas} and λ_D

To ascertain when and how the deviation from DLVO theory occurs, the two measured length scales are compared directly in figure 3.14, again using a log-log scale. The values for λ_D, which were obtained from conductivity and then smoothed, are presented as a line plot for a clear comparison with κ^{-1}_{meas}.

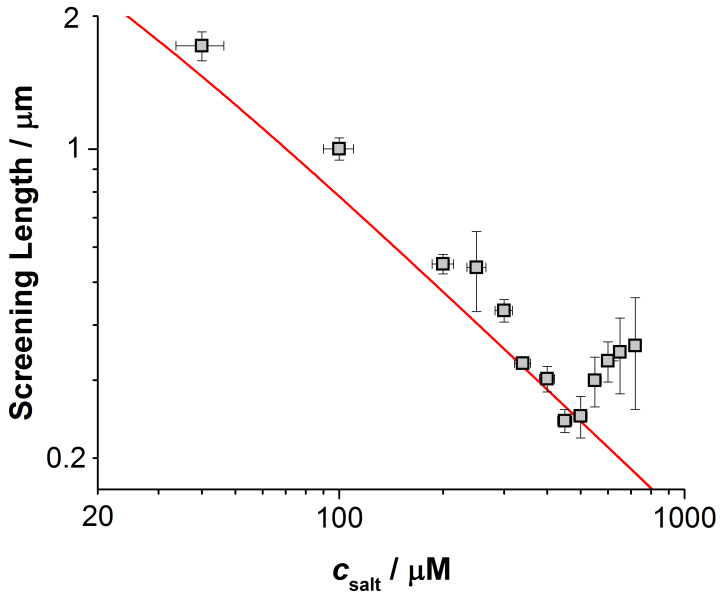

FIGURE 3.14: The measured screening length κ^{-1}_{meas} from BOT (black squares) and the conductivity DH length λ_D (red line).

Another clear way to show the deviation in the force profile from what is expected in DLVO theory is shown in figure 3.15. In these plots, showing four different electrolyte concentrations, the Yukawa fit to the data is again shown as the solid lines, with the decay length of the fit being κ^{-1}_{meas}. What is also overlaid as dashed lines onto each data set is the same force profile but instead using the value of λ_D in place of κ^{-1}_{meas}. The magnitude of the force (Z) was adjusted to give a plot

that passed through the data. Again what is clear is that below c^*_{salt}, the force profiles both fit the data well, with gradients of a very similar magnitude, agreeing with DLVO theory. However, when the same plots are overlaid onto the data above c^*_{salt}, the gradients are very different; the fit using the value λ_D is clearly steeper than the trend of the data.

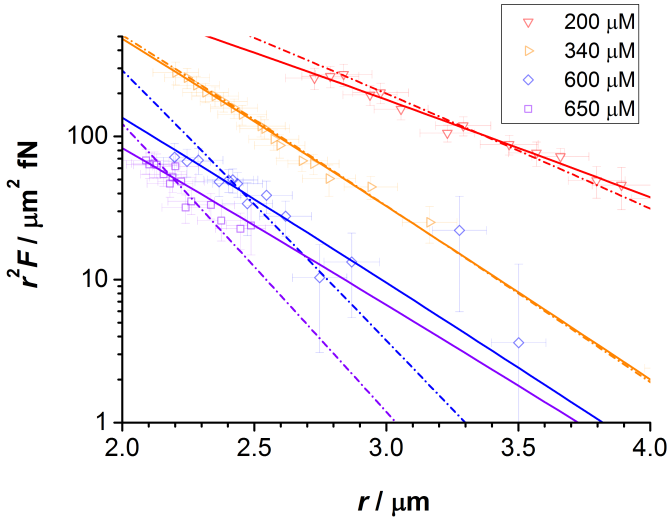

FIGURE 3.15: Comparison of the force profiles if κ^{-1}_{meas} (solid lines) or λ_D (dashed lines) is used to fit the data from BOT.

Figures 3.14 & 3.15 both show that although the DH length is decreasing with addition of electrolyte, as expected within DH theory, the decay length of the interaction between two AC12 particles in dodecane does not agree at high electrolyte concentrations. This deviation from what is expected in DLVO theory, where $\kappa^{-1}_{meas} = \lambda_D$, has occurred in solutions of dilute, univalent electrolyte, where the force was measured always above surface separations of $h > 200$ nm. These systems should therefore still remain within the limits of the classical DH theory, and hence understanding these results is hugely important to fully understand the electrostatics that govern colloid interactions.

3.2.5 The Effective Particle Charge for the Pair Interaction Z_{eff}

Thus far, only one of the fitted parameters from the Yukawa force has been discussed. The other parameter that governs the magnitude of the forces is the charge of the particles Z, which is calculated from the intercept of the force profiles. The intercept in fact gives the value $Z^2 = Z_1 Z_2$ (eq. (3.7)), however it is impossible to decipher Z_1 from Z_2 from the fitted value, and so the assumption is always made that $Z_1 = Z_2$. To account for the added complexity of a colloidal particle over a point charge ion, Alexander et al. utilised an *effective* charge of the particle, which is scaled with the particle radius a and the Bjerrum length ℓ_B as (*383*)

$$Z_{\text{eff}} = \frac{Z\ell_{\text{B}}}{a}. \tag{3.8}$$

This allows for direct comparisons between the charge in different systems, i.e. the equivalent effective charge in an aqueous sample would have a much higher value of Z.

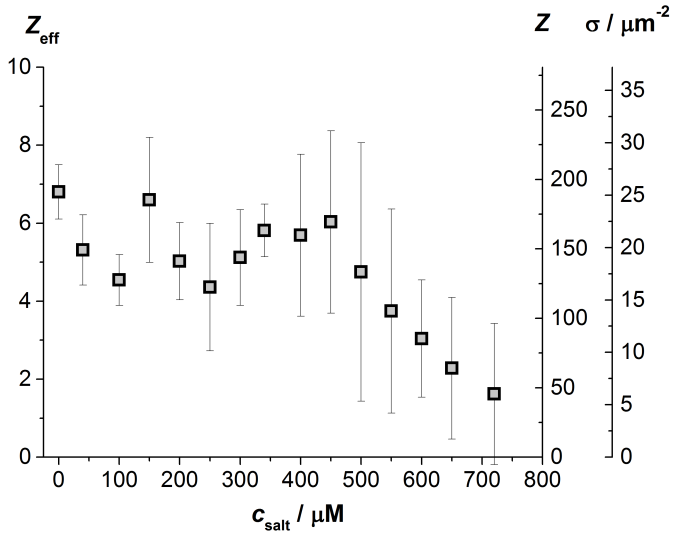

FIGURE 3.16: The fitted value of the particle charge from BOT. The effective charge Z_{eff}, charge Z and surface charge density σ are all plotted as a function of the electrolyte concentration c_{salt}.

The fitted values of Z from the BOT force profiles are plotted as a function of the electrolyte concentration in figure 3.16, alongside the equivalent values of the surface charge density ($\sigma = Z/4\pi a^2$) and the effective particle charge Z_{eff}. The data shows that the charge of the particles remains approximately constant at $Z_{\text{eff}} \approx 5 \pm 1$ until the critical electrolyte concentration $c^*_{\text{salt}} = 450$ μM. The slightly increased value in the salt-free system is probably due to the effect of washing the samples with centrifugation, where previous experiments have shown that increased washing with clean dodecane results in higher particle charges due to increased favourability of counterion release into the cleaner solvent (*145*). Above this concentration, the charge of the particles begins to decrease with increasing electrolyte concentration. This decrease in the particle charge upon addition of electrolyte above c^*_{salt} therefore accounts for the observed weakening of the corresponding force profiles in figure 3.10. It is important to note again that these values of the particle charge are obtained from the fitted intercept of the force profiles, and as such provide the charge expected if one assumed that the profile is in exact agreement with DLVO theory. Above c^*_{salt} we have already observed that the force profiles are not in agreement with DLVO theory, and as such these values of the particle charge may not be the actual charge of the particles. However, given that two unexpected results emerge above the same critical concentration c^*_{salt}, the trend in Z_{eff} does indicate the possibility that

the surface of the particles could be affecting the form of the force profiles and hence the values of κ_{meas}^{-1}.

PALS

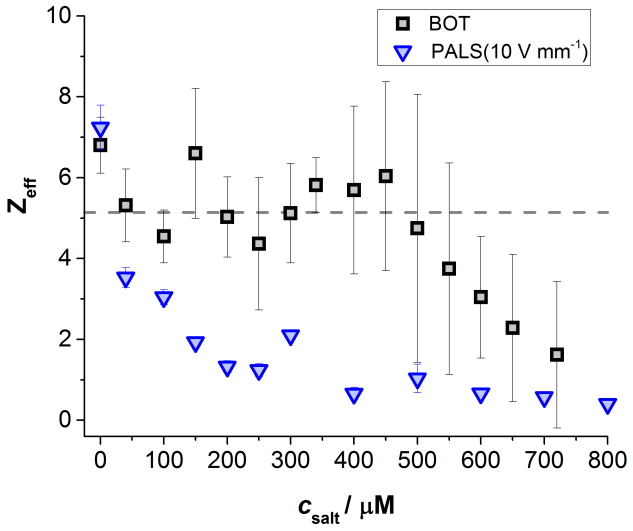

FIGURE 3.17: Comparison of the values for the effective particle charge Z_{eff} measured with PALS (blue triangles) and BOT (black squares). The electric field strength used for the PALS measurement was 10 V mm^{-1}

To ascertain if the values of Z_{eff} from BOT do represent the real charge of the particles, PALS was also used to measure the particle's electrophoretic mobility, from which the charge of the particles can be calculated (eq. (3.1) with the particle, rather than an ion, radius and charge). This data is plotted alongside the fitted values from BOT in figure 3.17. The electrophoretic mobility data was measured at a low electric field strength of 10 V mm^{-1}. The value measured in the low-salt sample showed good agreement with the BOT value. At the other electrolyte concentrations however, the values from PALS were always significantly less than those from BOT. Unfortunately, measuring the electrophoretic mobility in nonpolar systems with this method is notoriously difficult (*384*) due to, for example, long equilibration times and non-trivial dependences on the particle volume fraction (*385*) and on the electric field strength (*145*). What further complicated the systems at high c_{salt} was that the particles began to show aggregation. This aggregation is the focus of the following results chapter. Thus, the apparent disagreement between the two methods on the value of Z_{eff} we attribute to the difficulty in measuring a reproducible value with PALS, rather than the BOT method giving a totally incorrect value. The fact that the values agree in the salt-free system, which is the simplest system to measure with PALS as there were no aggregates present, leads us to conclude that the values obtained from BOT are probably close in magnitude to the correct particle charge, and at least give the qualitative trend with c_{salt} that we are most interested in.

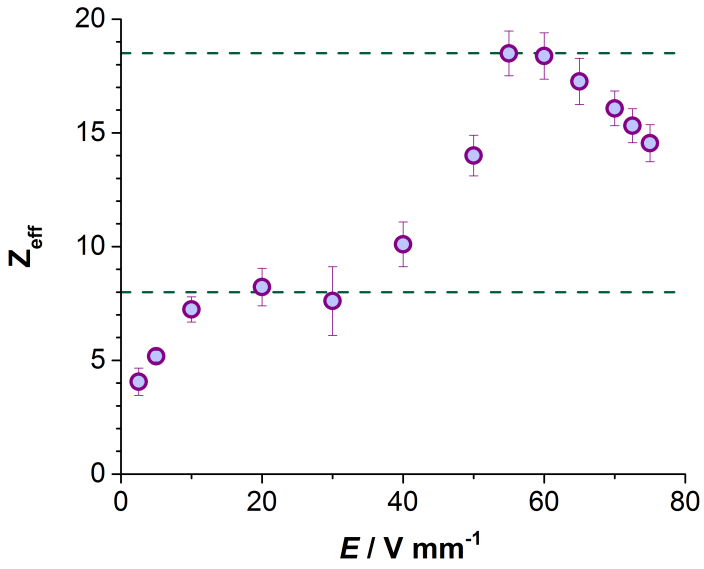

FIGURE 3.18: Effect of the strength of the electric field E on the particle charge Z_{eff}.

As has been previously measured in similar nonpolar systems, the electrophoretic mobility shows a dependence on the strength of the applied electric field E. This dependence was measured in the salt-free system using a range of electric field strengths, and the data is presented in figure 3.18. The choice of using 10 V mm^{-1} for the data in figure 3.17 was due to the fact that the data shows a plateau region here in the low electric field strength limit. This plateau indicates a minimum particle charge where the electric field is weak enough that it is not affecting the number of counterions associated with the surface. The values obtained using weaker fields $<$ 10 V mm^{-1} were assumed to be possibly inaccurate due to the weakness of the electric field. At higher electric field strengths, the charge of the particle was found to increase with electric field strength, in agreement with previous measurements (*145*), due to condensed counterions being stripped from the surface when confined in a strong electric field. Again, a plateau region was reached at $Z_{\text{eff}} \approx 18.5$, indicating the maximum charge of the particles, when all counterions have been removed. The value of the maximum charge of a particle measured here is larger than that found with the same system by Gillespie et al. (*145*), but this again could be due to the fact that increased washing of the particles also results in increased particle charging. As observed at the lowest electric field strengths, the decreasing trend at the highest electric field strengths is likely due to either the applied field not being as strong as stated, or that these high fields result in incorrect interpretation of the particle's mobility. The two plateau regions are indicated on the plot with dashed lines, and these are likely the maximum and minimum possible charge of the particles in solution.

3.2.6 Effect of Particle Charge on c^*_{salt}

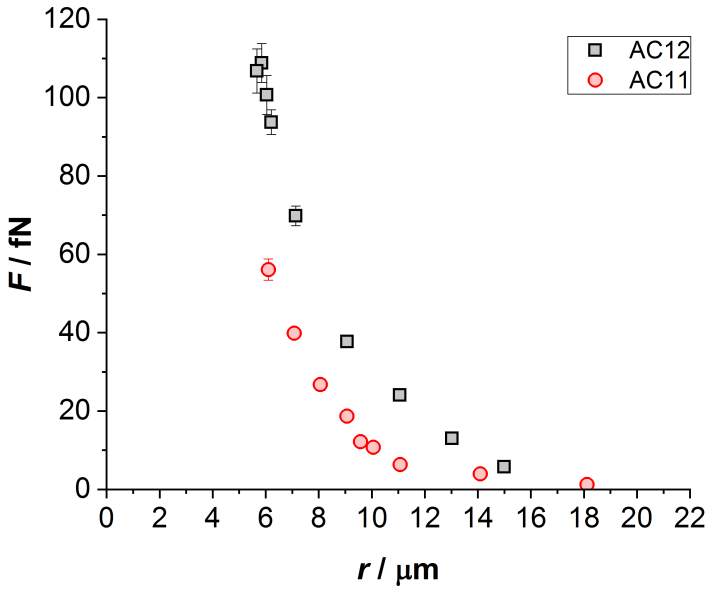

FIGURE 3.19: The force profiles measured between pairs of AC11 and AC12 in dodecane with no electrolyte present highlighting the higher effective charge of the AC12 particles.

The measurement of κ^{-1}_{meas} was repeated with a different batch of particles, AC11, again in dodecane and at different concentrations of the electrolyte TDAT. Firstly this allowed us to check if this unusual trend in κ^{-1}_{meas} was unique to the AC12 system specifically or if it could be repeated, and secondly it would highlight any dependence on the charge density of the particles. The difference between the AC11 particles and the AC12 particles is summarised in table 2.2. The effective charge of the AC11 particles was determined from measuring the pair interactions with BOT in a salt-free sample. This force profile is shown in figure 3.19 alongside the profile for AC12 particles, showing that the weaker force between two AC11 particles is due to their lower effective charge. From fitting the force profile in figure 3.19, the effective charge for AC11 is $Z_{eff} = 5.03 \pm 0.47$. The higher effective charge of AC12 ($Z_{eff} = 6.80 \pm 0.69$) than AC11 is thought to be due to the addition of the fluorescent dye $DiIC_{18}$, which can dissociate adding additional charge to the AC12 particles. This dye was not added to the AC11 particles.

By measuring the force profiles over a range of electrolyte concentrations, the fitted decay length of the interactions could again be plotted as function of c_{salt} for the AC11 particles. This trend is presented in figure 3.20 on a log-log plot again to emphasise the expected power law dependence. What is immediately obvious is that the same nonmonotonic trend of κ^{-1}_{meas} was measured as a function of c_{salt}, with the minimum located at a value $c^*_{salt} = 350$ μM. This critical concentration is reduced from that for the AC12 particles where $c^*_{salt} = 450$ μM. What this comparison in the trends of κ^{-1}_{meas} highlights is that the unexpected decay of the interactions occurs at

lower ionic strengths when the surface of the particles has less propensity to charge.

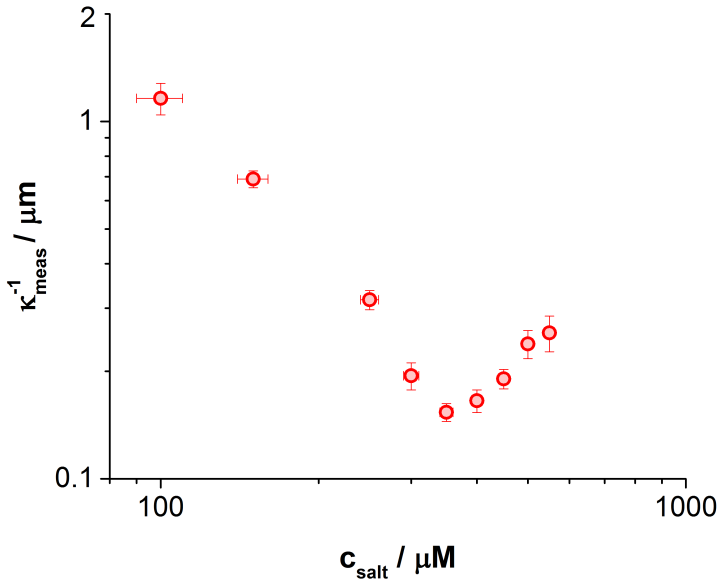

FIGURE 3.20: The measured screening length κ^{-1}_{meas} from the force profiles measured with BOT between pairs of AC11 particles (red circles) in solutions at different electrolyte concentrations c_{salt}. The plot is presented on a log-log scale to emphasise the expected power law dependence. The critical salt concentration at which the minimum in κ^{-1}_{meas} appears for AC11 is 350 μM, as opposed to 450 μM for AC12.

3.3 Comparison with Observations in the Literature

3.3.1 Ionic Liquids

The deviation of κ^{-1}_{meas} from λ_D is re-plotted as the ratio $\kappa^{-1}_{meas}/\lambda_D$ in figure 3.21. The same qualitative trend was measured with the ionic liquids by Perkin and coworkers, with $\kappa^{-1}_{meas}/\lambda_D \approx 1$ at low electrolyte concentrations, and inflation of $\kappa^{-1}_{meas}/\lambda_D > 1$ at the higher electrolyte concentrations (*352*, *353*). Although qualitatively similar, quantitatively the trends are very different.

The inflated screening length in the case of the ionic liquids was found to occur once λ_D became comparable or smaller than the size of the ions. The size of the TDAT ions are larger than that for NaCl, but not significantly larger than the ionic liquids used in their study. The size of the TDAT ions are of order 1.2 nm. At the point of the minimum in κ^{-1}_{meas} at $c^*_{salt} = 450$ μM, conductivity calculates that $\lambda_D \approx 240$ nm. This is orders of magnitude larger than the size of the ions, so the inflation measured occurs well before the DH length becomes equivalent to the size of the ions. The origin of the inflation must therefore be different in the case of the ionic liquids and our dilute, nonpolar electrolyte solutions. This is perhaps an unsurprising conclusion as the ion densities used in our study compared with the values used by Perkin et al. (*352*, *353*) are far lower, even when considering the different solvents.

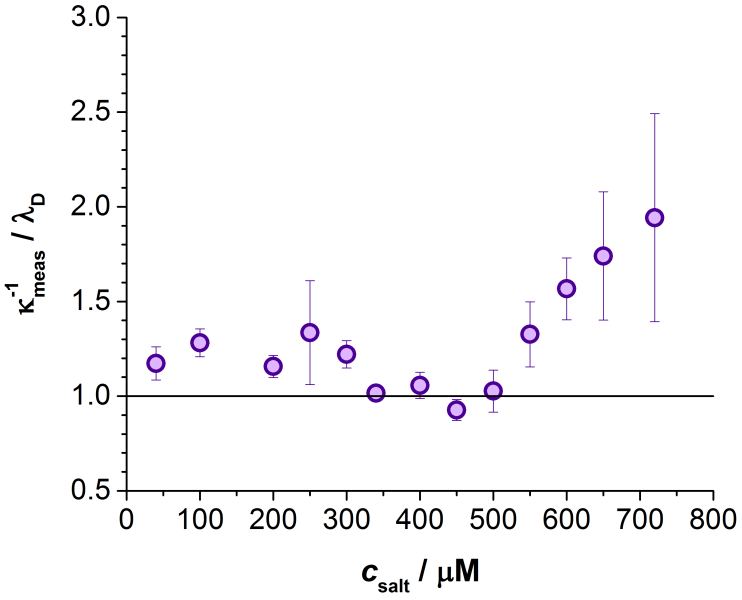

FIGURE 3.21: The ratio $\kappa^{-1}_{meas}/\lambda_D$ showing the disagreement between the two screening lengths at high electrolyte concentrations.

3.3.2 Massive Ion-pairing

Another consequence of having high concentrations of ions in a solution is the possibility that the ions will associate back into an ion pair (*386*). This is particularly poignant in nonpolar systems, where high proportions of undissociated salt is expected due to the large Bjerrum length. This has already been shown to be the case in our system, where the conductivity measurements show that < 1 % of the TDAT molecules dissociate into ions (fig. 3.3(b)). A suggestion made by Zwanikken & van Roij was that the presence of undissociated salt molecules will modify the permittivity of the solution because of their dipolar nature (*356*). The extent to which these ion pairs, or *Bjerrum pairs* as they are sometimes referred to, modify the dielectric constant of a solution $\bar{\varepsilon}_r$ is given by (*356*) to be

$$\bar{\varepsilon}_r = \varepsilon_r + \frac{e^2 \tilde{R}^2 n_d}{3\varepsilon_0 k_B T}, \tag{3.9}$$

where ε_r is the dielectric constant of the pure solvent, $\tilde{R}$ is the mean separation of the two ions in the Bjerrum pair, and n_d is the number density of Bjerrum pairs present. For the electrolyte concentration range investigated here, the maximum number density of pairs would be if all the electrolyte remained undissociated, so $n_d = N_A c_{salt}$, and the physical size of the electrolyte molecule is ≈ 1.2 nm. For 1 mM electrolyte, this would give an inflation in the dielectric constant of the solution of just $\bar{\varepsilon}_r/\varepsilon_r = 1.1$. As already stated by Zwanikken & van Roij, much greater ion concentrations are required to inflate the permittivity enough to see an inflation in the values of κ^{-1}_{meas}. A final note on the effect of Bjerrum pairs forming is that both the conductivity and the interaction between the particles are dependent on

the permittivity of the solution. Therefore, the values of both κ_{meas}^{-1} and λ_D would show a deviation, not just the value of κ_{meas}^{-1}.

To find the cause as to why $\kappa_{meas}^{-1} \neq \lambda_D$, parameters that affect the interaction profile (eq. (1.50)), but not the bulk behaviour of the ions are sought. As already calculated, the permittivity changes negligibly upon addition of electrolyte, and therefore so does the Bjerrum length. These values are also bulk parameters and hence has no dependence on the separation of the two particles, i.e. their effects should modify both λ_D & κ_{meas}^{-1}. The value of $\kappa_D a$ changes with addition of electrolyte, but this is encompassed within the correction factor Θ, and again with λ_D showing expected behaviour, the value $\kappa_D a$ is also as expected and also doesn't alter with the particle separation.

3.3.3 Charge Regulation

The combined evidence that $\kappa_{meas}^{-1} \neq \lambda_D$, R_{adj}^2 of a Yukawa force fit decreases, and Z_{eff} decreases all above the same critical concentration c_{salt}^*, and that c_{salt}^* was found to increase with Z_{eff} for two different particles, could suggest that another parameter that governs the interaction may also depend on the separation as well as the electrolyte concentration. The evidence thus far points to the possibility that the unexpected behaviour in this system is due to a change of the surface properties of the particles during the interaction, and upon addition of electrolyte. The parameter that governs the strength of the interaction is the charge of the particles. Although the PALS data was inconclusive in determining if the BOT fitted charge gave a correct value when electrolyte was present, the dependence of Z_{eff} on the electric field strength does highlight that the charge of the particle can be modified (figure 3.18). Furthermore, sequential washing of the salt-free sample resulted in increased particle charging (*145*). Hence, the number of dissociated charge groups on the particles depends on its local environment.

Most commonly, the interactions between colloids are considered under the assumptions that their surfaces either remain at a fixed surface charge (CC) density or surface potential (CP). As discussed in section 1.1.6, a different possible condition was proposed by Ninham & Parsegian where instead, the chemical equilibrium of the dissociating surface groups is held constant, allowing the charge density of the surface the freedom to adjust to changes in the local electrostatic potential (*61*). This model is termed the *charge regulation* (CR) model and describes a more realistic nature of experimental systems. With the possibility of a modifiable surface charge density in mind, the effects of increased electrolyte concentration and surface separation can be predicted. Surfaces charge due to the gain in entropy of the system by releasing counterions into the bulk. If this entropic gain is insufficient, the energetic cost of separating two opposite charges would result in counterion condensation onto the surface. Decreasing the entropic gain could occur by increasing the number of ions in the vicinity of the surface, so any counterions released would be increasingly confined in the bulk. This can be done either

by increasing the number of ions in the bulk of the system, or by confining the ions between the two surfaces. During each experiment, the optically trapped particles are held at different separations, where the entropic gain of counterion release decreases with decreasing r due to increased ion confinement. In the samples at low electrolyte concentration, this entropic gain remains large enough to maintain a constant particle charge with particle separation. However, at the higher electrolyte concentrations this balance is more fragile, with the combined decrease in r and increase in c_{salt} possibly resulting in a particle charge that decreases with particle separation. The fact that a defined balance exists between the simultaneous energy cost and entropic gain of surface charging explains why a critical electrolyte concentration emerges; the particle charging is always favourable below c^*_{salt} at all the separations measured, but at higher concentrations, the dependence on the particle separation becomes stronger. So, if Z depended on r such that it decreased as the particles were pushed together, the decay of the r^2F profile would no longer be solely defined by the value κ^{-1}_{meas}. Although counterion condensation does reduce the number of ions in the bulk, the relative number lost compared with the total number of ions is not sufficient to noticeably reduce the conductivity, hence why this effect results in κ^{-1}_{meas} being different from λ_D.

This exact effect of the surface separation and ionic strength on the surface charge has been seen in the literature (*62*–*67*). The origin of this is due to the competition between the interactions of ions on the surface with their neighbouring surface ions, and with bulk ions wanting to adsorb. In an extensive study conducted by Trefalt et al. (*67*), the interaction energy between two charge regulating surfaces was calculated for both amine and iron oxide surfaces, where the former is positively charged, and the latter negatively charged. In both cases, when the surface separation was small enough, the charge density decreased to neutral as the surfaces approached to contact. What results is that the interaction energy deviates from the predictions using a CC boundary condition, becoming increasingly weakened with decreasing surface separation. This behaviour has also been simulated for proteins (*65*, *66*) and polyelectrolytes (*64*). The separation at which the surfaces must be to observe these deviations from DLVO theory are reported in the literature to be approximately when $\kappa_D h < 2$ (*387*, *388*) or $h < 5\ell_B$ (*68*), i.e. when the double layers are strongly overlapping (*387*, *388*). We have observed this deviation at larger surface separations at $\kappa_D h \approx 3$ ($\approx 6\ell_B$), however, this is still believed to be a plausible explanation theoretically, despite the long range (*389*). Interestingly, Chan et al. have shown that the range of surface separations over which the regulation occurs depends on the potential of the isolated surface, with less charged surfaces showing charge regulation occurring at larger surface separations (*62*). This suggests why the value of c^*_{salt} was smaller for the less charged AC11 particles. If the charge regulation occurs over a longer range of surface separations, then the deviations in the measured decay length κ^{-1}_{meas} will occur at a lower electrolyte concentration.

3.4 Conclusion

This chapter has presented direct measurements of the electrostatic force between a pair of charged particles dispersed in a nonpolar solvent, measured using BOT. The range of the interactions was modified by adding a hydrophobic electrolyte, TDAT, to the dispersions. By measuring the conductivity of these dispersions, the classical DH length λ_D could be calculated, which was found to decrease with added electrolyte as expected within mean-field theories. What was unexpected was that the decay length of the measured force profiles κ_{meas}^{-1} did not agree with the value λ_D at the highest electrolyte concentrations. Specifically a nonmonotonic dependence of the screening length with the ion concentration was measured, with significantly slower decaying interactions than expected above 450 μM. An indication for how this is possible in this system is in the trend of the particle charge, where it was measured to decrease in magnitude with electrolyte concentration above the same critical concentration $c_{salt}^* = 450$ μM. A change in the surface charge density suggests that these particles may represent a surface that can charge regulate, which has been shown in the literature to result in a reduction in the surface charge density or surface potential as the surface separation is decreased and the ionic strength is increased (*59*, *61*, *67*, *390*, *391*). This nonmonotonic trend of κ_{meas}^{-1} with c_{salt} was also measured in the force profiles between slightly less charged PMMA particles, but the critical concentration at the minimum in κ_{meas}^{-1} was found to be lower at $c_{salt}^* = 350$ μM. The fact that c_{salt}^* depends on the charge of the isolated particles agrees with calculations in the literature for different charge regulating surfaces (*62*).

The charge regulation of the surfaces can therefore offer an explanation for the measured inflation of the screening length above c_{salt}^* presented in figure 3.21. Within DLVO theory, the charge of the particles is assumed to be fixed. If instead the charge is considered as a function of the particle separation, then the apparent discrepancy between the fitted values of κ_{meas}^{-1} and the expected values λ_D can be quantitatively explained. To do this, a Landau model can be used to describe the free energy of the surface during the interaction, and consequently how the charge of the surface depends on both the electrolyte concentration and particle separation. The derivation of this model and the comparison to the experimental data presented in this chapter is the focus of chapter 5.

Chapter 4

Results: Electrolyte-Induced Attraction

In the previous chapter, the interaction between two particles was measured with BOT to ascertain if the electrostatic repulsion was well described by DLVO theory. This chapter focuses on the bulk behaviour of the same system over the same range of electrolyte concentrations. PHSA-stabilised PMMA particles in a low dielectric solvent were observed by Pusey & van Megan to be concordant with hard-sphere particles (392). In their case, the particles had near-to-no charge so had no electrostatic repulsion, and the PHSA stabilising layer was sufficient to prevent vdW attractions. Given the same particles are used here, nearly-hard-sphere behaviour was expected. As the previous results chapter highlighted, the PMMA particles used here are charged and interact at long distances purely repulsively. According to DLVO theory, and in fact within the full PB theory, the interaction between two like-charged (and sterically stabilised) particles should be repulsive at all separations This chapter however presents direct evidence of attractions between the PMMA particles investigated, despite the long-range electrostatic repulsion already measured with BOT.

4.1 Literature Review of Like-Charge Attractions

Particles in the size range $\sim$ 0.01 - 10 μm that comes under the umbrella of 'colloids' have been utilised in a huge range of applications such as cosmetics, pesticides, cleaning products and foods. Their usefulness often comes down to how long they remain stable, i.e. how long they can maintain their beneficial properties until they aggregate and ultimately separate out from the solution rendering them useless. Prediction and control of this stability is hence tremendously important. Specifically in highly ionic systems, stability is difficult when the electrostatics are completely screened. According to the DLVO theory, this results in the vdW attraction dominating the total interaction between the particles and hence aggregation occurs. This instability is often overcome by adding appropriate polymers to the surface of the solute to provide steric stability, which has, for example, been successful for preventing aggregation and deposition of nanoparticles in concentrated brine solutions (393–395). This brush layer prevents the particles from approaching close enough for vdW attractions to cause aggregation. Thus, for two like-charged

particles, with an additional sterically stabilising layer, DLVO theory predicts a purely repulsive interaction.

Polymer particles dispersed in water (sometimes called latex particles) are known to arrange into crystalline structures (*396*, *397*). Such structures form according to the balance of repulsions and attractions acting between the particles. According to DLVO theory, at low ionic strengths, the structures formed should be homogeneous, with the electrostatic repulsions dominating to result in maximum separations between the particles. Then at higher ionic strengths, when the repulsions are screened, simulations show that the system transitions to a fluid phase (*398*, *399*). However, a number of papers emerged by Tata, Ise and co workers that strongly suggested the existence of *long range attractions* between PS particles in deionised water. Their observations have been more thoroughly reviewed in reference (*400*), but briefly they progressed as follows. Firstly, a microscope similar to the one used in earlier work by Kose et al. (*397*) showed that both ordered and disordered regions of particles existed within the same sample (*401*). The average particle separation was $\approx$ 1 μm between 370 nm radii particles, a larger distance than expected if a FCC crystal structure is assumed based on the concentration of particles. Thus, the attraction required to form such structures was assumed not to be due to vdW interactions due to the range, but an electrostatic one. In the subsequent paper, the average particle separation was found to decrease upon addition of electrolyte, with the ordered regions disappearing completely at high electrolyte concentrations, as expected from charge screening effects (*402*). The group also noted that upon addition of a less polar co-solvent or increasing the particle charge density, the average particle separation also decreased, indicating that the attraction was intensified (*403*). Due to the number of puzzling observations already made, Ise collaborated with Sogami to attempt to explain these attractions by deriving the DLVO theory slightly differently (*404*, *405*). By describing the energy landscape with the Gibbs rather than the Helmholtz free energy, Sogami & Ise derived an interaction profile that contained a long-range attraction. Given that this is what their experimental observations indicated, their theory was thus used to explain them. This method of derivation however has sparked controversy and is largely discredited due to the comments of Overbeek himself and others (*406*–*408*). Despite this theoretical debate, experimental observations of like-charge attractions kept being published including coexistence between vapour-like regions, and solid or liquid-like regions (*409*–*414*), the formation of 'voids' in the samples when in density matched solvents (*415*, *416*), and the appearance of amorphous structures (*417*).

The main conclusion of the observations of gas-liquid coexistence were that an electrostatic attraction must exist, as vdW attractions are too short range to be the cause (*418*). Although a seemingly sensible conclusion to make, some groups have shown that such transitions can occur within a system that interacts purely repulsively if you consider an additional 'volume term'. This term combines the

as yet unconsidered interaction between the double layers and their corresponding particle, and the excluded volume due to the particles. When included within the linear PB theory, gas-liquid coexistence is indeed predicted (*418*–*424*). Due to the fact that this is an effect of the volume however, they only account for attractions at high particle volume fractions, and as such do not explain the attractions occurring in dilute, deionised suspensions such as the observations of Tata and others (*425*, *426*). This could however explain observations of attractions made once a sample had been centrifuged, which increases the local particle density at the bottom of the samples due to gravity (*427*).

Other observations of like-charge attractions in the literature have since been explained to be due to specific features of those systems. For example, where the system has been confined by nearby charge interfaces, attractive minima will result owing to hydrodynamic effects of the confined solvent (*428*). This has since explained observations made by Grier et al. (*429*) and others (*430*, *431*).

One system that led to a large number of publications was DNA; despite its charge groups, DNA can adopt very compact structures allowing it to pack into the nucleus (*112*). The compactness, and attractions seen between DNA molecules, was found to correlate with the valency of the counterions present (*144*). Simulations (*122*, *432*) and SFA measurements (*124*) have both confirmed the presence of an attraction arising due to divalent rather than univalent counterions. This dependence is explained with the strong coupling theory already mentioned (see section 1.2.5) (*108*, *136*, *137*, *433*). In systems with large coupling parameters (eq. (1.65)), the condensed layers of counterions near the surface leads to mutual attractions between the two surfaces with a range of the distance between the condensed ions (*434*). Since its establishment, the strong coupling theory has also been used to explain earlier observations (*435*, *436*) such as the phase separation of macroions in the presence of multivalent, but not univalent, electrolytes (*127*, *437*), and observations of charge reversal (*438*, *439*). Physically the attraction is due to the lack of the diffuse double layer of ions above the surface; the strong correlations between the counterions and the surface when $\Xi >> 1$ leads to a condensed, sheet-like layer of counterions instead (*435*). This leads to a depletion of ions from the mid-plane between the two surfaces. This depletion of ions then leads to a depletion-like attraction between the surfaces (*440*). At close surface separations, the two-dimensional, ordered counterion layers will correlate, thus inducing an effective attraction between the surfaces (*441*). Such effects do not occur in systems where $\Xi < 1$, usually in the case of univalent counterions, due to the increased entropic loss of their condensation onto the surface; fewer multivalent counterions are required to screen the surface to the same extent. Hence, the strong coupling theory does not explain the attractions seen in the low coupling limit such as the observations of Tata, Ise and coworkers, and in this system where $\Xi \approx 0.1$ (*442*).

Publications from a group in Nottingham have shown that polarisation of particles can induce attractions (*443*–*445*). If the particles are polarisable (especially

applicable for metallic particles), and one surface charge density is higher than the other, then when in proximity, the more highly charged particle can polarise the other particle such that the closest surfaces become oppositely charged, and hence a short-ranged attraction arises. They do however suggest that in the case of solvents containing electrolytes, the theory may not be so simple as the double layer is not accounted for in their calculations (the simulations are performed in a vacuum). Furthermore, this theory is based on the fact that the two particles must be of either different size & same charge density or the same size & different charge densities, not applicable in our system. Attractions between non-identical particles have also been observed experimentally (*446*).

4.2 Data

4.2.1 Aggregate Formation

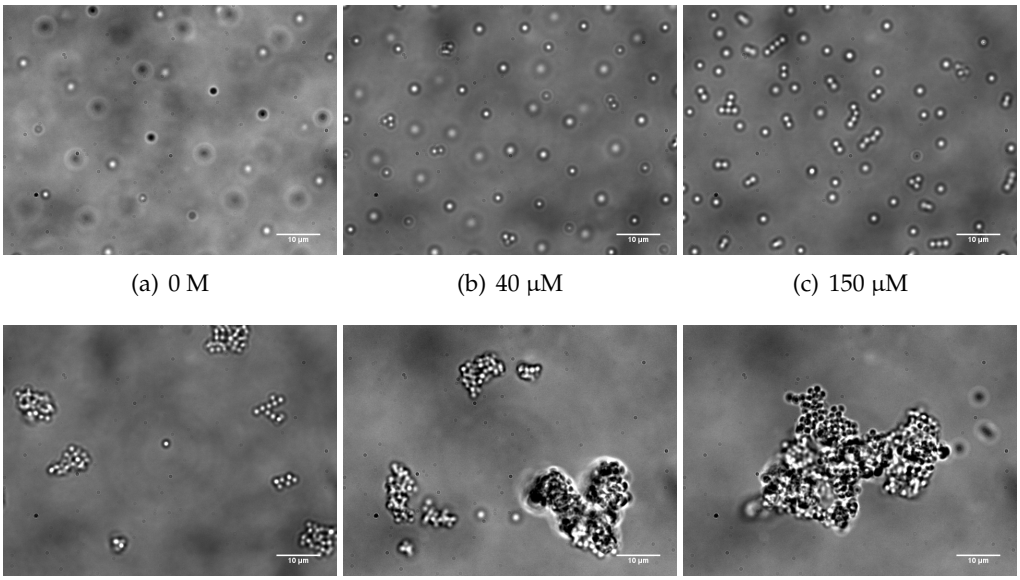

(a) 0 M (b) 40 µM (c) 150 µM

(d) 250 µM (e) 450 µM (f) 650 µM

FIGURE 4.1: Optical microscopy images of AC12 in dodecane over a range of TDAT concentrations $\sim$ 10 minutes after preparation of the sample.

The optical microscope images presented in figure 4.1 show the samples over the range of electrolyte concentrations studied in the previous chapter. The gravitational length of these systems (the height at which the thermal energy equals the gravitational potential energy) is $\ell_g \sim 0.5$ µm, equivalently the Péclet number ($Pe = a/\ell_g$) ~ 1.5. Given that $Pe > 1$, these particles will sediment over time, and as such some of the images shown show all the particles are in one horizontal plane, where they not stuck to the bottom of the capillary, but suspended near the bottom. This sedimentation is prevented however in the systems where electrostatic interactions are strong, and in these images, the particles are observed to be in

different horizontal planes. The salt-free sample shows the stability of the particles in dodecane, with each particle separated by $\approx$ 15 μm. These separations are due to the long-ranging electrostatic repulsions in the nonpolar solvent. The force profile measured with BOT between a pair of particles in this salt-free solution was presented in the previous chapter in figure 3.10(a), showing that even at $r = 15$ μm, a non-zero force was measured between the particles. Such strong repulsions results in the very stable solution in figure 4.1(a) when no electrolyte is present, and is also the reason for the ordered arrangement of the particles. Adding just 40 μM of electrolyte decreases this average separation due to charge screening. What is also apparent in figure 4.1(b) is that a small proportion of the particles have bound together into a dumbbell, suggesting that an attraction is present between the particles. As progressively more electrolyte is added into the solutions, the interactions become increasingly dominated by this attraction, resulting in larger aggregates forming. Not only does the largest aggregate present increase in size, but the proportion of single particles remaining in the samples decreases with increased electrolyte concentration.

4.2.2 Sample Instability

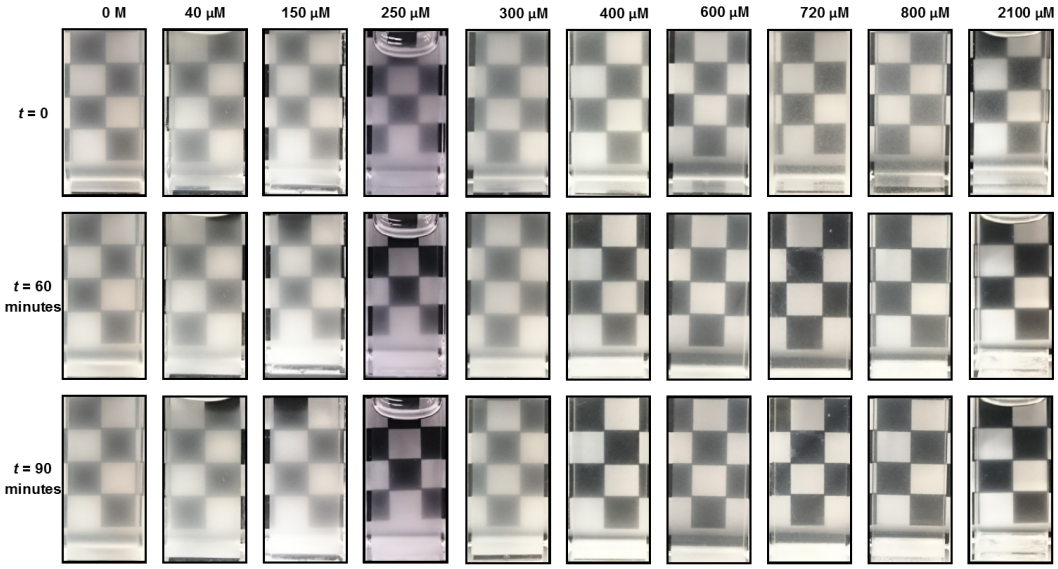

FIGURE 4.2: Photographs of the samples in glass vials in front of a patterned background. The time after dispersion is indicated on the left, and the electrolyte concentration c_{salt} is indicated at the top. Images were taken immediately after dispersion (top), 60 minutes (middle) & 90 minutes (bottom) after dispersion. The vials were 1.2 cm in width and depth.

The reduced stability of the samples with increasing electrolyte concentration is also evident from their sedimentation. Figure 4.2 shows photographs of the samples in vials, taken on a phone camera, at a range of electrolyte concentrations. The photographs were taken of the vials immediately after dispersion, and then 60 &

90 minutes after being left untouched on the laboratory bench. All the images taken immediately after dispersion show turbidity. This directly indicates that the dispersions contain particles due to the scattering of light. This turbidity remains in the sample after 90 minutes in the case of the salt-free sample. This indicates again the stability of the charged particles, where the electrostatic repulsions are strong enough to prevent sedimentation due to gravity. As the electrolyte concentration is increased to 40 & 150 μM, the turbidity at the top of the sample decreases after 90 minutes. This indicates that the particles have sedimented from this region of the vial. The turbidity of the samples disappears faster from the samples at higher electrolyte concentration indicating that the rate of the sedimentation increases with increased electrolyte. At the high electrolyte concentrations of 720 & 800 μM, the turbidity is almost completely gone after 60 minutes. Some aggregates and particles adsorbed to the glass walls of the vials when electrolyte was present, and is hence why the samples don't appear completely transparent once the aggregates in solution had sedimented.

4.2.3 Average Aggregate Size

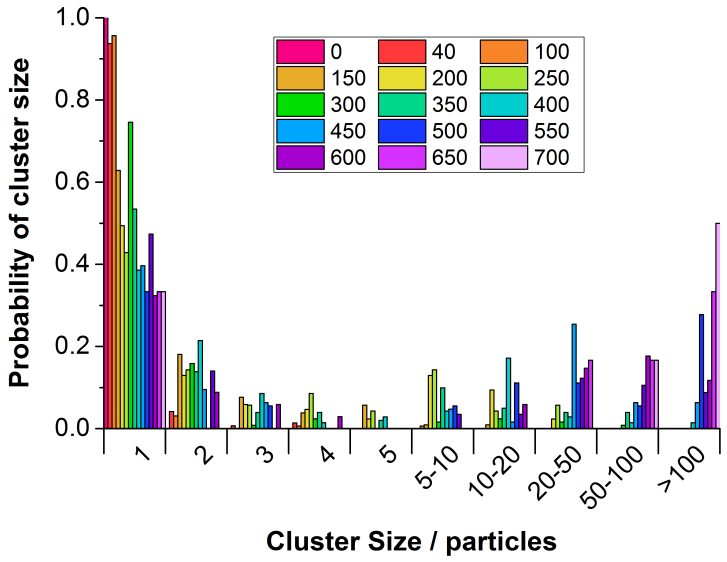

FIGURE 4.3: The bars represent the proportion of the clusters present in those samples that contained a specific number of particles. The larger cluster sizes, being difficult to count exact numbers, are grouped into different ranges of cluster sizes. Each colour represents a sample at a different c_{salt} indicated in the legend. For example, the sample at 150 μM contained ∼60% single particles, ∼20% dumbbells, ∼10% triplets, and the other 10 % were clusters containing 4 or 5 particles.

To quantify the change in the size and structure of the aggregates formed at different electrolyte concentrations, a histogram of the cluster sizes was determined from manually counting the number of particles in the clusters present in the images taken of those samples. These histograms are presented in figure 4.3. Important

to note before discussing these histograms is that the sampling was quite low, with < 10 images taken for each sample. Also, due to the low volume fraction of particles, images were only taken in locations of the sample where clusters existed, which could result in a slight bias towards larger cluster sizes. However, this bias should be systematic across the range of c_{salt}. The histograms presented show the proportion of clusters present in each sample that contains a specific number of particles. Every sample contained at least 30% single particles, and these particles were the ones used to measure their interaction with BOT in the previous chapter. What this histogram shows is that clusters of > 2 particles form even at the low electrolyte concentrations (< 150 μM), then as the electrolyte concentration increases, the number of larger clusters increases. The height of the bars across the cluster sizes 3-10 are small due to the fact that samples at intermediate c_{salt} have a wide spread of cluster sizes present, whereas the low c_{salt} samples are dominated by single and small clusters, and the high c_{salt} samples are dominated by very large aggregates and single particles. At the highest c_{salt}, it appears that if an aggregate forms at all from the single particles, it will contain tens of particles, rather than just a few. This suggests that at the highest c_{salt}, the attractions dominate the interaction. At lower and intermediate c_{salt}, the long-range repulsion remains strong enough to prevent the formation of large aggregates. This trend across the range of c_{salt} is not completely smooth, for example the apparently higher proportion of 20-50 particle clusters in the 450 μM sample than the 700 μM sample, but this is probably due to the small sampling.

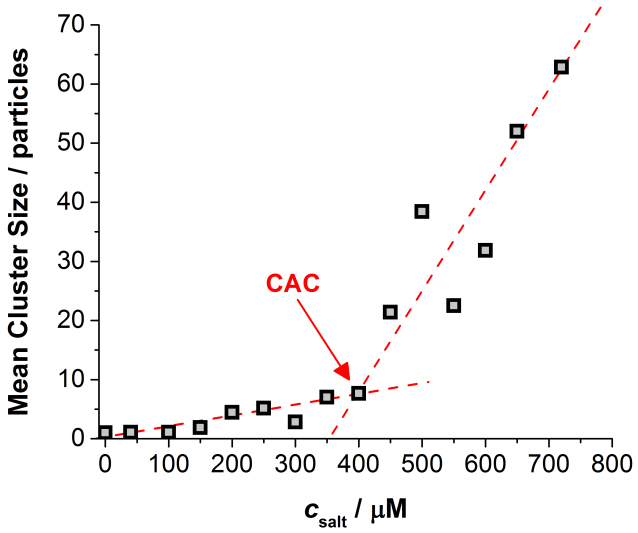

FIGURE 4.4: The mean number of particles in the clusters present in the samples at different c_{salt}, calculated from the histograms in figure 4.3. The point at which the trend in the mean cluster size becomes more dependent on the electrolyte concentration is named the *critical aggregation concentration* (CAC).

Another way of presenting the gradual increase in the size of the aggregates formed with increasing c_{salt} is the mean size of the clusters, and this is presented in

figure 4.4. As expected, the mean cluster size increases with increasing electrolyte concentration. This presentation of the trend with c_{salt} is not as descriptive as the histograms in figure 4.3 as the mean cluster size does not highlight the spread, or lack of, in the size of the aggregates present. Because the distribution of cluster sizes at the highest c_{salt} is dominated by both large aggregates and single particles, the mean value is lower than the size of the large aggregates present. However, the trend in the mean cluster size is useful in determining if the samples show any criticality. What is apparent in figure 4.4 is that two linear regimes exist, a gentle increase in the cluster size until $\sim$ 400 µM, and then a faster increase in size at higher c_{salt}. By overlaying these two trends, one can determine the point at which the trend changes. This point has been noted as a *critical aggregation concentration* (CAC). The benefit of noting such a critical point in the trend of the mean cluster size is that different samples can be more easily compared.

Effect of Particle Charge

To firstly ascertain if this aggregation occurred in systems with different PMMA particles, and to secondly observe the effect of the charge magnitude of the particles, identical dispersions were also made with AC11 & IM6 particles. The differences between these particles are outlined in section 2.2.1. Optical microscope images of these samples were taken and are presented in appendix D, and shows that aggregation occurred with both particles upon addition of electrolyte. The same procedure was then undertaken to find the change in the mean cluster size with c_{salt}, and this is shown in figure 4.5(a).

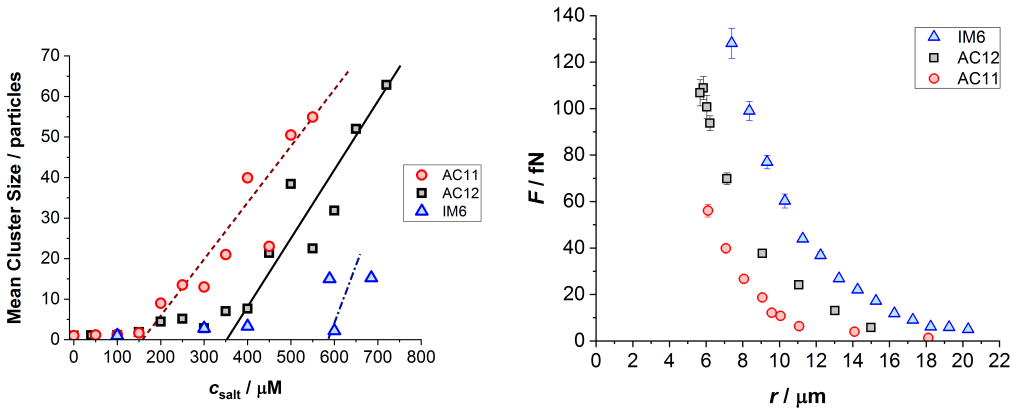

(a) (b)

FIGURE 4.5: (a) The mean cluster size for the different particles AC11, AC12 and IM6 as a function of c_{salt}. (b) The force profiles measured between pairs of AC11, AC12 and IM6 in dodecane with no electrolyte present. The lines added to the plot are a guide for the eye for each different system.

The trend for AC11 is similar to that of AC12, where there is a faster increase in size at higher c_{salt}. It is difficult to conclude if the same trend occurs for IM6 as

fewer concentrations were studied. Despite this, the best estimate for the CAC was determined in the same way as in figure 4.4 for the different particles (see figure D.3 in appendix D) and is presented in figure 4.6 as a function of the effective charge of those particles. The effective particle charge was determined from measuring the pair interactions with BOT in salt-free samples. These force profiles are shown in figure 4.5(b), and show the strength of the repulsion is strongest for the IM6 particles, and weakest for the AC11 particles, corresponding to their higher and lower charge respectively than AC12.

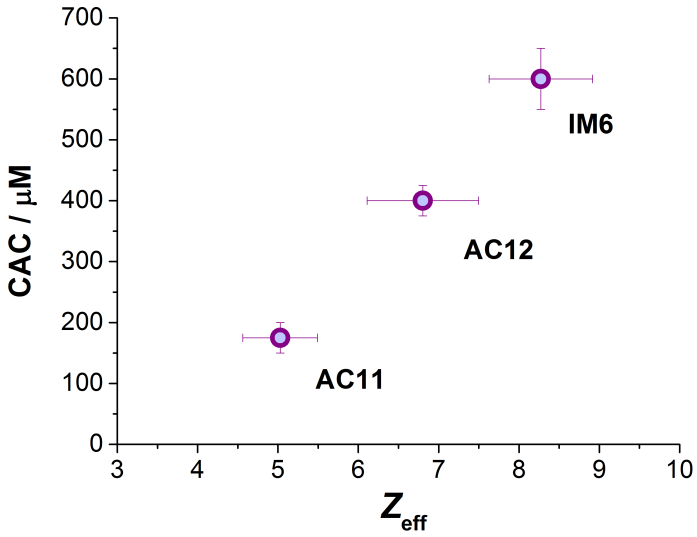

FIGURE 4.6: The CAC determined for the three different particles plotted against their effective particle charge Z_{eff}, which was determined from the fitted BOT force profiles for each of the samples with no electrolyte in dodecane.

The data presented in figure 4.6 shows that by increasing the charge of the particles, the stability of the dispersions is maintained to a higher ionic strength. Equivalently, less salt is required to destabilise the dispersions of lesser charged particles. This is depicted in figure 4.7 where optical microscopy images were taken of AC11, AC12 and IM6, all at TDAT concentrations of 100 μM. As the charge is increased from AC11 to AC12, the largest clusters present decrease in size and are no larger than five particles. Then increasing the charge to IM6 results in only single particles present in the sample. These images are not representative of the mean cluster size in the samples, and the mean is skewed by the high proportion of single particles in the samples.

By comparing the trends in the size of the aggregates formed with c_{salt} for different systems, it has indicated that the attractions only occur in the system once the repulsions are sufficiently screened and/or weakened. In all systems, aggregates were only found in the samples when electrolyte, even just in micro molar amounts, was present.

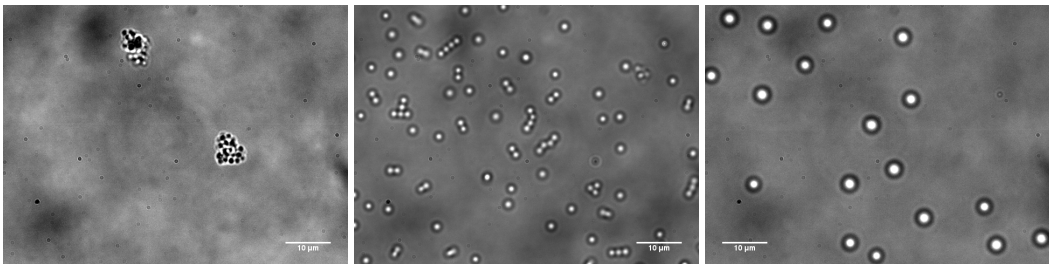

(a) AC11 (b) AC12 (c) IM6

FIGURE 4.7: Images of the AC11, AC12 and IM6 particles in dodecane at 100 μM TDAT. The charge of the particles increases from left to right, accompanied with a decrease in the size of the largest aggregates found in those samples.

4.2.4 Critical Laser Power P^*

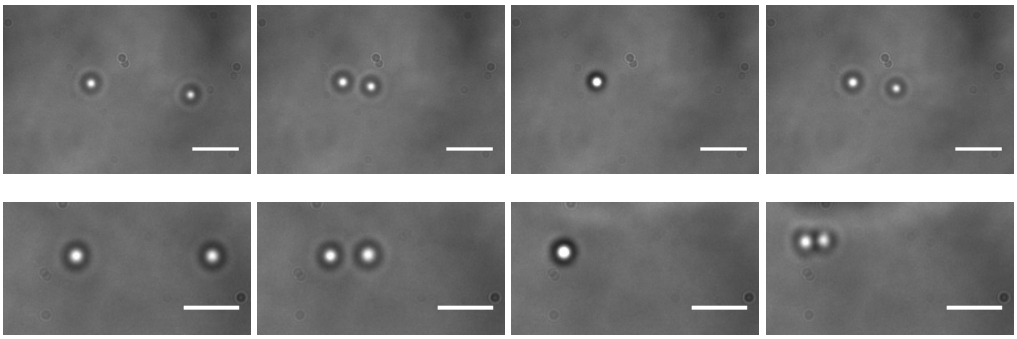

FIGURE 4.8: Images of the process used to determine the critical laser power for binding a pair of particles together. Top: $P < P^*$ resulting in the pair not sticking together. Bottom: $P \geq P^*$ resulting in the pair sticking together. For both rows: Both particles in the left two images are being held in optical traps. In the third image from the left, both particles are held in the same optical trap and hence stack vertically. In the right image there are no optical traps present. Scale bars are 5 μm.

The attractions in these systems are inferred only from the observations of aggregates in the preceding sections. Unfortunately, the BOT technique cannot measure the interactions closer than surface separations of $h \sim 200$ nm. This is why only repulsions were measured in the preceding chapter. However, the optical traps were able to be used to attempt to quantify the strength of the potential barrier to aggregation. To do this, pairs of particles were held in separate, blinking optical traps, then brought together into the same trap where they immediately moved vertically to maximise overlap of both particles with the trap. The other trap was then taken away, and the two particles were held in the same trap for 6 seconds, then the trap was taken away. This process is depicted in figure 4.8. This was repeated a few times to ascertain if this power was sufficient to bind the pair together. If not, the power was increased and the process was repeated until the power was sufficient to bind the pair together irreversibly. The values of the power presented in figure 4.9

are the output power of the laser, not the power of the traps themselves. Because of the holographic method used, the power of the optical traps is much reduced from the output power of the laser. The strength of the optical traps could be determined in the horizontal direction only as tracking in the vertical direction (into the field of view of the images) was not possible. However, the strength of the traps increases with output power, and so the output power is still useful to determine how the height of the potential barrier to aggregation changes with electrolyte concentration.

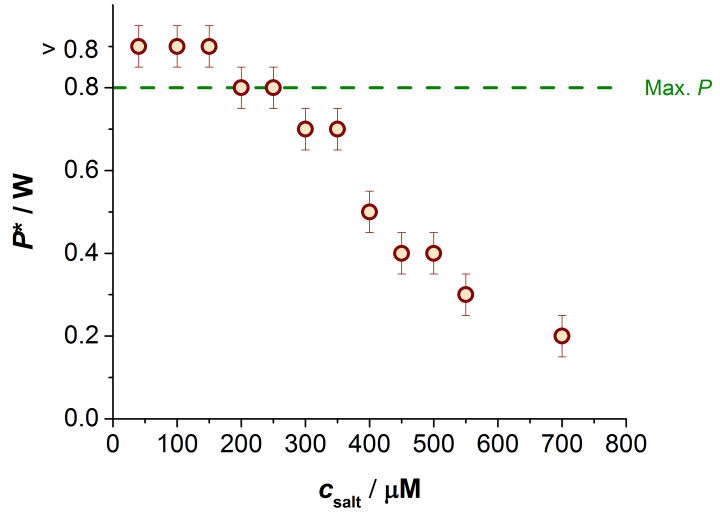

FIGURE 4.9: The critical power P^* required to bind two AC12 particles together as a function of c_{salt}. The maximum output power of the laser is indicated.

The values in figure 4.9 show the minimum power required to overcome the electrostatic repulsion between the particles. In the salt-free system, the laser power was insufficient to bring two particles closer than $r \approx 4$ μm. The values plotted for the samples at 40, 100 & 150 μM also indicate that the repulsion was still too strong for the traps to overcome. The maximum output power of the laser is 0.8 W, and so it must take a power greater than this to bind the particles. The errors in the values are due to the fact that the output power of the laser was increased incrementally by 0.05 W until binding occurred. The trend in the critical output laser power P^* shows a decrease with increased electrolyte concentration. This reaffirms the conclusions made from the observations of cluster sizes, whereby the potential barrier to aggregation is reduced in magnitude upon addition of electrolyte due to charge screening. With the repulsion screened to a shorter range, the particles have a higher probability of coming close enough to irreversibly aggregate. Due to this probability effect, the values of the critical power stated in figure 4.9 in fact represent the power required to bind a high percentage of pairs due to the small sampling of this particular data set.

This probability is eluded to more directly from a similar study, where the probability of pairs that aggregated into a dumbbell was determined at a given

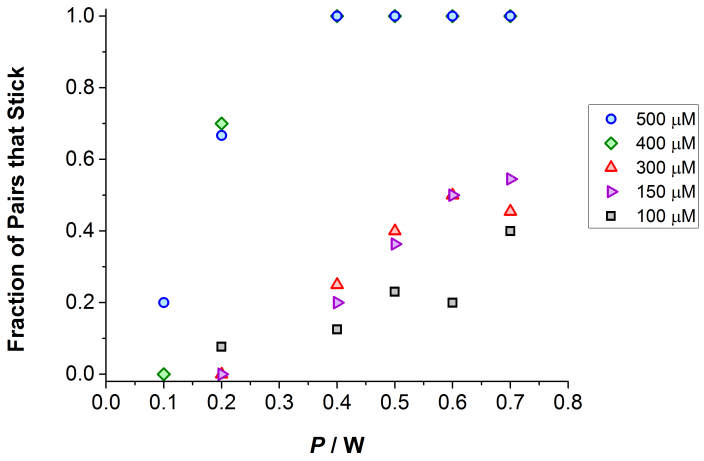

FIGURE 4.10: The proportion of different pairs of particles that bound together once held together for a range of c_{salt}. If the particles did not aggregate after being held in the same, constant optical trap of output power P for 60 seconds, the pair was considered not to stick.

output laser power. Due to the lower number of single particles remaining in the samples at higher c_{salt}, the samples at lower c_{salt} were the focus of this investigation. In these samples, the blinking optical traps were not strong enough to bind any pairs into dumbbells. To increase the effective strength of the traps, the beam chopper was turned off so that the laser remained on all of the time. This effectively doubles the strength of the traps, as when blinked they remain off for half the total time of an experiment. The output power is however the same, and are the values stated in figure 4.10, but as such do not correspond to the values stated in figure 4.9. What is apparent in figure 4.10, is that by increasing the strength of the optical traps, the probability of two particles overcoming the potential barrier to aggregation increases. Once above a certain trap strength, every pair of particles at that electrolyte concentration bound irreversibly. Again, by increasing the electrolyte concentration, this probability was increased for a specific trap strength.

One conclusion from investigating the critical laser power needed to bind particles together is that very strong powers are required for any aggregation to occur in the low c_{salt} samples. This however appears to contradict the naturally formed aggregates found in those same samples (fig. 4.1). This may be due to the following considerations. Firstly, the samples may contain particles with differing charge densities, and as such the single particles that remained (with which these studies were performed) may have higher charge densities than those that have already aggregated. Some inhomogeneity in the samples seems a reasonable assumption. Secondly, the aggregation has a probability, and the sampling for the critical laser power was small compared with the total number of particles in each sample.

Despite not being able to directly measure the attraction with BOT (negative forces), or to ascertain the exact strength of the barrier to aggregation, the observations and measurements presented in this chapter all indicate that there is a higher probability that aggregation will occur with increased electrolyte concentrations due to charge screening. Despite observing the presence of an attraction however, its physical origin has not yet been discussed. Different suggestions for the cause of attractions were made from several scientists during this investigation, and some of those were investigated along the way. Before the final chapter where the most probable cause of the attraction will be debated, other causes found to be unlikely are first discussed.

4.3 Possible Explanations for the Observation of Like-Charge Attraction

Some suggestions for the attractions included:

1. There are strong correlations between the counterions and the surface (strong coupling regime).
2. The attraction was vdW interactions.
3. The PHSA layer was no longer providing steric stability for the particles.
4. The electrolyte forms aggregates, Bjerrum pairs or micelles that caused a depletion attraction.

These suggestions are each discussed in line with the experiments conducted to determine how likely they are to be the origin of attraction.

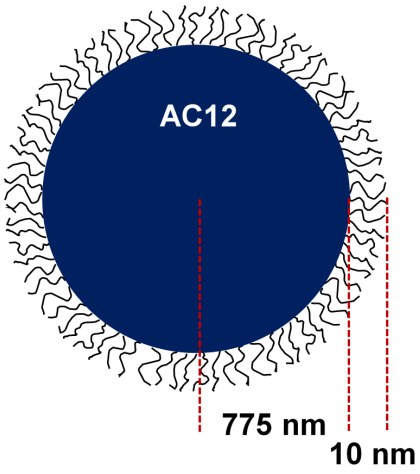

FIGURE 4.11: A diagram of an AC12 PMMA particle showing the thickness of the PHSA stabilising layer on the surface which is ≈ 10 nm (447).

4.3.1 Strong Coupling Regime

The first suggestion, that the system lies in the strong coupling regime, has been used to explain attractions observed in the presence of multivalent ions (*124*, *127*, *437*). However, as discussed in section 1.2.5, this regime occurs when the coupling parameter (eq. (1.65)) $\Xi > 1$. For this system however, $\Xi \approx 0.1$, so the system resides in the weak coupling regime and as such, attractions due to strong correlations between the counterions and the surface is not predicted to occur.

4.3.2 Residual vdW Interaction at Brush Contact

According to DLVO theory, an attraction between particles does exist at close separations due to vdW interactions. A polymer brush layer was synthesised onto the periphery of the particles to prevent their surfaces from coming close enough to aggregate due to vdW attractions. A diagram of the particles with this layer is presented in figure 4.11. Because this stabilising layer is roughly 10 nm thick, the closest separation of the PMMA surfaces is 20 nm. For vdW interactions to be a viable origin of the attraction, they must be strong compared with the double layer repulsion when the surfaces are separated by 20 nm.

Using values from the literature for the Hamaker constants of PMMA (H_A = 65 zJ (*448*)) and dodecane (H_m = 50 zJ (*449*)), the Hamaker constant between two PMMA particles across dodecane ($H \approx (\sqrt{H_A} - \sqrt{H_m})^2$) is then $H \approx 1$ zJ, where 1 zJ $= 10^{-21}$J. In terms of the thermal energy this is just $\approx 0.25\ k_B T$. With the additional retardation effect discussed in the introduction (eq. (1.61)), the Hamaker constant at a surface separation of $h = 20$ nm, which is the separation where the PHSA layers just touch, becomes $H \approx 0.245\ k_B T$, when $\lambda_D \approx 200$ nm. The interaction energy at this surface separation (eq. (1.56)), is then just $0.8\ k_B T$, too weak to overcome the charge and the steric repulsions (*69*).

4.3.3 Collapse of the PHSA Stabilising Layer

The polymer used for the stabilising layer will adopt different structures in different quality solvents, i.e. in a poor quality solvent for PHSA, the polymers would collapse and no longer provide any steric stability to the particles. A decrease in the solvent quality for the PHSA could occur, for example, upon addition of the electrolyte. To ascertain if this was occurring, the size of PHSA alone, in a 5 wt.% solution in dodecane, over a similar range of electrolyte concentrations was measured using DLS. The hydrodynamic diameter measured from DLS is plotted in figure 4.12 up to $c_{salt} = 1500$ μM. The hydrodynamic radius of the polymer in solution directly indicates the solvent quality, as larger sizes suggest a good solvent for the polymer, and a collapsed or aggregated structure suggests a poor solvent. Added onto the plot is the average diameter across the range of c_{salt}. A slight increase in the diameter of the PHSA polymer of ≈ 2 nm was measured upon addition of 500 μM electrolyte. However, generally, the size does not change significantly upon

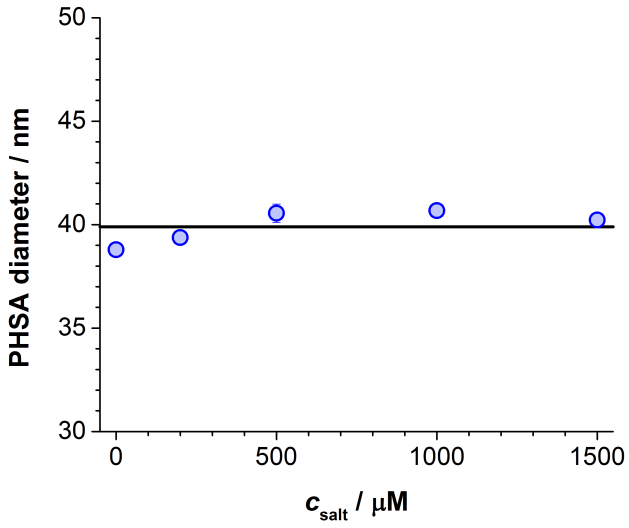

FIGURE 4.12: The hydrodynamic diameter of PHSA polymers in dodecane at various electrolyte concentrations measured with DLS.

addition of electrolyte, indicated by a lack of an overall trend, and with numbers not straying far from the average diameter. Furthermore, the fact that, if anything, the diameter increases suggests that the solvent quality is increasing for the PHSA upon addition of the electrolyte. Previous studies into this exact system by previous group members took this investigation further by looking at the neutron scattering from the particles over a range of electrolyte concentrations (*360*). What they found was that there was no noticeable change in the structure of the PHSA stabilising layer when electrolyte was added, suggesting that the polymer brushes remain extended into the solvent, and hence provides steric stability for the particles at all electrolyte concentrations investigated.

4.3.4 Depletion of Bjerrum Pairs

Another suggestion was that the electrolyte could be causing a depletion attraction between the particles (*450*). Although this seems unlikely in such dilute suspensions, the surface tension of the solutions was measured to ascertain if the electrolyte molecules were forming micellar-like structures, and SAXS was used to ascertain if any aggregates of electrolyte were forming. According to the theory of depletion interactions, the range is defined by the size of the depletant, and the strength is defined by the amount of depletant (see section 1.2.4).

The surface tension of the dodecane-air interface was measured using the pull-off Wilhelmy plate method. The measured values are presented in figure 4.13(a) for a range of electrolyte concentrations. The value for the salt-free system, i.e. pure dodecane, agrees well with values from the literature for the dodecane-air interface of 24.92 mN/m (*451*). Upon addition of electrolyte, the surface tension increases; if micellar-like structures were forming, the surface tension of the solutions would

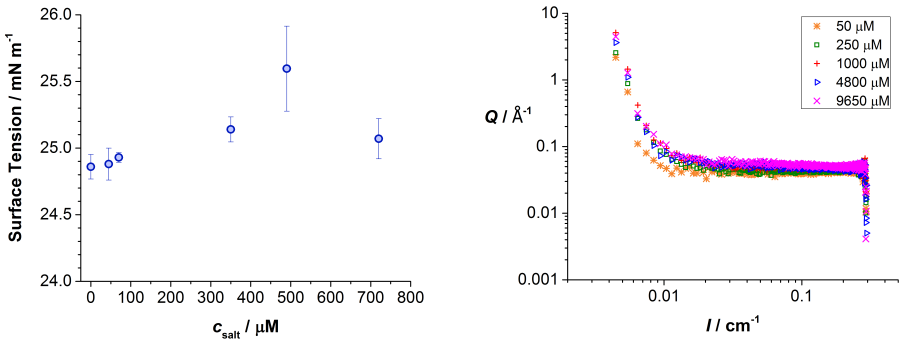

FIGURE 4.13: Left: The surface tension, measured with the Wilhelmy plate method, of the air-dodecane interface at a range of electrolyte concentrations. Right: SAXS of solutions of TDAT in dodecane at a range of concentrations.

be expected to decrease with addition of electrolyte. The slight increase measured suggests that in fact a depletion of ions from the air-dodecane interface occurs, which is expected for a standard electrolyte solution due to the image charge repulsion from the interface, as discussed in section 1.2.5 (*147*, *148*, *151*). Furthermore, the SAXS plots in figure 4.13(b) showed no change in the scattering when the electrolyte concentration was increased, suggesting that the electrolyte also does not form aggregates in the solution. Turbidity of the samples was also not observed in vials of the solutions (see figure 4.14), which would again suggest that large aggregates were forming in the sample, large enough to scatter light. These measurements all suggest that no large aggregates of electrolyte are forming in the solutions, and thus are not the cause of a depletion attraction between the particles.

FIGURE 4.14: Vials of TDAT in dodecane at concentrations of (from left to right) 100, 300, 500, 700, 1000 & 1300 μM.

As was concluded by measuring the conductivity of these dispersions in section 3.2.1, the percentage of electrolyte that remains as undissociated (Bjerrum) pairs is high (fig. 3.3(b)). The effect of neglecting the presence of Bjerrum pairs was noticed by Fisher & Levin (*452*, *453*) where without them, even when including excluded volume terms, the calculation of the critical density of an electrolyte solution was

consistently too low. Agreement with Monte Carlo simulations was then found when the association into Bjerrum pairs, or larger clusters, of the ions was taken into account through an association constant. Since this, several studies have focussed on phase behaviour taking into account electrolyte coupling (*454*–*456*). In terms of colloidal stability, inclusion of Bjerrum pairs has led to the idea that they could induce depletion attractions between particles (*450*) (revised a year later (*457*)). Allahyarov et al. simulated the ion density profiles from a charged particle's surface, showing a depletion zone. The range of this depletion decreases with increased electrolyte concentration, owing to the fact that the mean distance between the ions decreases (and hence the effective size of the Bjerrum pairs decreases) and the depth of the attraction scales with the electrolyte concentration, as expected from depletion theory. A more recent study has suggested that the range of the depletion is in fact of order ℓ_B due to the range of electrostatic repulsion between the electrolyte (ions or Bjerrum pairs) from the particle's surface (*458*). Therefore the range of depletion interactions may be much larger than the physical size of the Bjerrum pairs. Despite predicting an attraction, the concentrations required to induce a strong enough attraction for this system is much higher than μM amounts (*457*). The effects of the presence of Bjerrum pairs in the systems showed promise to explain simultaneously the inflated values of κ_{meas}^{-1} measured in the previous results chapter, and the attraction observed in this chapter. However, to cause either or both of these effects, the concentration of undissociated salt would need to be much higher.

4.4 Directionality of Interactions

There are multiple ways in which > 2 particles can be arranged as a cluster. For example, 3 particles could be arranged as a chain or as a triangle. The cluster shape with the lowest energy will depend on the interactions between those particles, and a sample should contain a higher proportion of clusters of that shape. Therefore, the presence and relative number of a particular cluster shape should suggest the nature of the interaction between the particles. Directionality in the clusters formed by particles in suspension has been known to occur when the particles contain a dipolar nature. The interactions between such particles was discussed in the introduction (section 1.2.5), where the additional monopole-dipole and dipole-dipole interaction forces were given (equations (1.66) & (1.67)) (*189*).

In particular for dipolar particles, chains have been observed to be prevalent due to the aligning of the dipole moments of the particles (*185*, *190*, *459*, *460*). An example of this formation is given in figure 4.15 using magnetic beads. This is of course a different interaction to our system, as it does not account for the electrostatic repulsion between the particles, but it shows nicely how when the magnetic moments align, the particles attract to form a chain of particles. Once the chains reach a certain length, they are also known to exhibit branching (*461*, *462*). What is also expected between dipolar particles is the formation of rings as the two

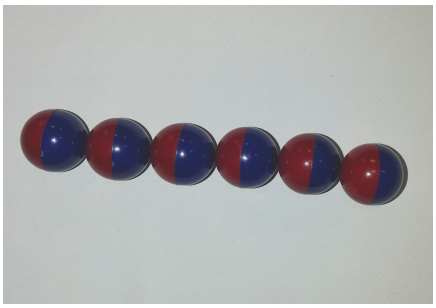

FIGURE 4.15: Chain formed from several magnetic beads, showing that they align their moments.

ends of a dipolar chain are of opposite charge, but this requires a certain degree of flexibility in the chain. Between charged, dipolar particles, chains and rings are only expected if the electrostatic monopole repulsion is sufficiently screened (*463*).

At very high screening levels (large $\kappa_D a$), close packed structures have been simulated (*464*), similar to those expected between homogeneous spheres (*177*). At intermediate screening levels, the different cluster structures can be more easily observed and compared with simulations as the aggregates contain just a few particles. One study by Hieronimus et al. simulated the effect of screening on the structure of clusters of 4 particles (*199*). What they found was that decreasing the screening from $\kappa_D a = 5$ to $\kappa_D a = 2.5$ results in less closely packed clusters, with a diamond formation becoming favourable over the tetrahedral structure. Decreasing the screening again to $\kappa_D a = 1$ changed the lowest energy structure to a square (equivalently a 4 particle ring). We have therefore gathered images of the 4-particle clusters in our samples at 150 μM where $\kappa_D a = 1.3$ to observe if the clusters that formed agree with the predictions of Hieronimus et al. These images are shown in figure 4.16.

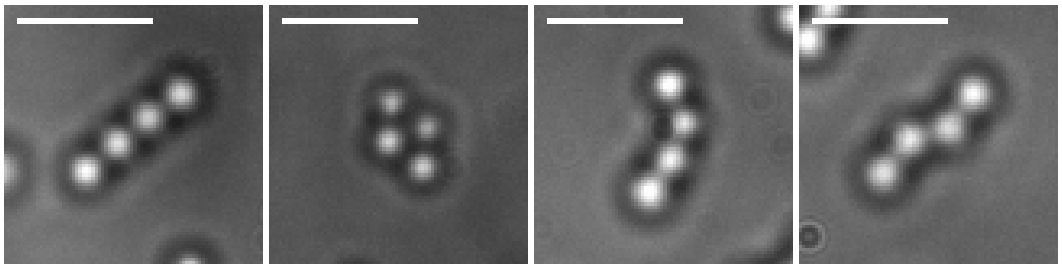

(a) (b) (c) (d)

FIGURE 4.16: Clusters of 4 particles found in the sample at 150 μM ($\kappa_D a = 1.3$). Scale bar is 5 μm.

The first observation to make is that no tetrahedral clusters were found in this sample, or any of the samples in fact, suggesting that the interaction is not just monopolar (*177*). The clusters that formed were always two-dimensional, with the majority forming chains like those in figures 4.16(a), 4.16(c) & 4.16(d). The chains in figures 4.16(c) & 4.16(d) are slightly unexpected as they are skewed from

a straight chain, but this shows that the chains are not completely fixed at the point of contact between the particles and that they have some flexibility, as has been seen by others (*185*). The only structure that formed with 4 particles that was not a chain was the diamond structure in figure 4.16(b). The presence of this particular structure agrees with Hieronimus et al., where a diamond structure is expected when $1.25 < \kappa_D a < 2.5$ (*199*). The sample at 150 μM lies in this range, with $\kappa_D a = 1.3$, and so comparison with these predictions suggests that these particles may have a dipolar nature.

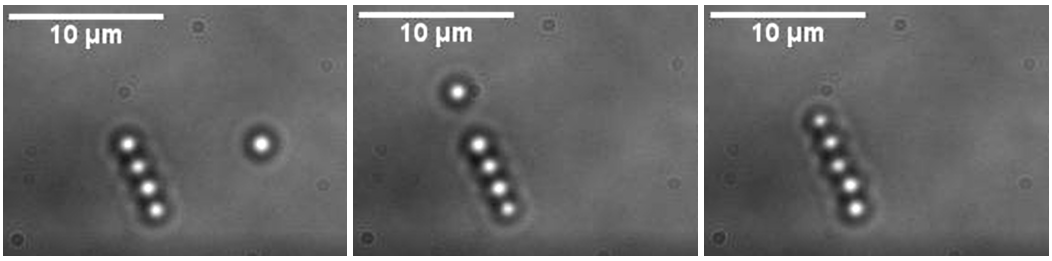

(a) (b) (c)

FIGURE 4.17: A single particle forced with optical traps onto the end of a chain of four particles to make a chain of 5 particles in a 450 μM sample.

Chains were found in the samples at low electrolyte concentrations up to around 6 particles in length. Using the optical traps, longer chains could be made by forcing single particles onto the ends of already formed dumbbells or chains. This process is outlined in figures 4.17(a) - 4.17(c), where an optically trapped particle was pushed into contact with the end particle of a chain which resulted in it attaching and increasing the length of the chain. Examples of different length chains formed in this way are presented in figure 4.18(a). As the chains in this figure suggest, there is some flexibility in the chains when agitated by the solvent, despite the small amount of screening at 40 μM ($\kappa_D a = 0.5$). Also presented in figure 4.18(b) is a branched chain, predicted to occur with sufficient screening (*461*, *462*). Interestingly, this branch contains an angle of $\sim 60°$, which could be recreated with the magnetic beads (see inset). If the particles remained monopolar in the chains, it would be expected that this second chain would either attract to form two rows of particles, or rotate into a linear chain, to maximise the separation of the end particles. The fact that the branch remained stable at the angle of $\sim 60°$ again suggests the particles have a dipole moment.

So, once formed, the clusters behave as if they have some directionally-dependent interactions present. To ascertain if the single particles have a dipole moment, or if it is induced once aggregated, the interaction between a single particle and a chain was observed. Figure 4.19 shows this interaction in the sample at 250 μM. The particles at the ends of the chain were held with optical traps so that the chain was tethered, and the single particle was brought towards the side of the chain with a third optical trap. The chain was found to be repelled from the single particle

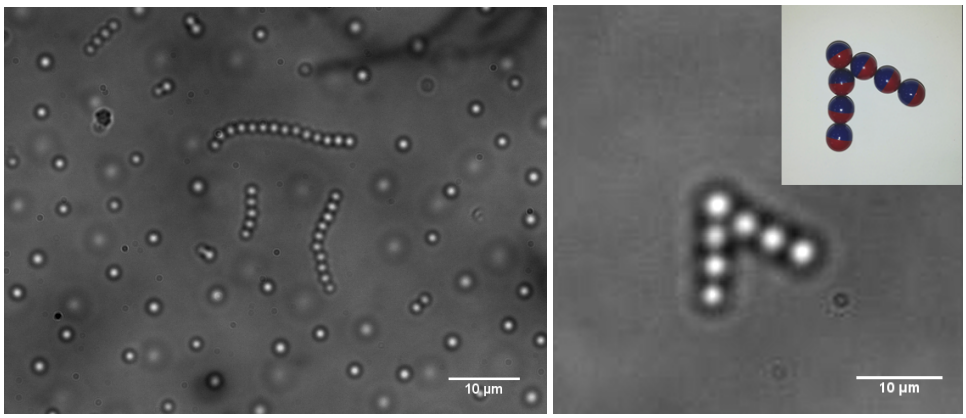

(a) (b)

FIGURE 4.18: (a) The chains that could be formed in a sample at 40 µM using optical traps showing chains of different lengths. (b) Two chains found in a 250 µM sample that were bound into a 'wishbone' shape at an angle $\sim 60^{\circ}$. Inset is the same shape formed using the magnetic beads that remained stable.

when it came to within $r \sim 4a$, indicated by bending away from it. This interaction indicates that the particles in the chain remain charged overall with the same sign as the individual particles, and that the single particle behaves as a monopole. If the single particle was a dipole, then it would be expected to rotate in order to attract to the chain to reduce the interaction energy, but not repel it.

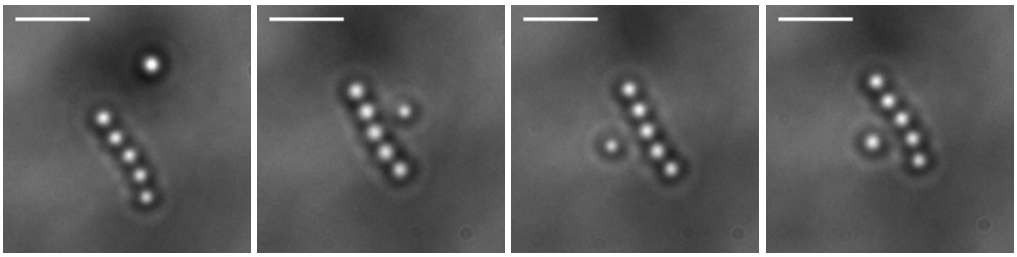

FIGURE 4.19: Repulsive interaction between an optically trapped single particle and a chain of particles in a 250 µM ($\kappa_D a = 1.9$) sample. Scale bar is 5 µm.

The presence of a dipole moment across the particles could be a possible origin for the attraction observed in these dispersions, as if aligned, the interaction between two dipoles is attractive (eq. (1.67)). Indeed, PMMA particles have been observed having a permanent dipole moment (*465*). This could also explain the chains and cluster structures formed at low electrolyte concentrations due to a balance of the monopolar repulsion and a dipolar attraction. It is unlikely that the particles in isolation have a dipole moment and thus act as monopoles, but, as the previous results section suggests, the possibility of a charge regulated surface could mean that proximity to other particles causes the particles to become dipolar; if only the sections of the surface in direct proximity to another surface were discharged,

for example, it would result in an inhomogeneous charge distribution across the particle.

4.4.1 Direct Evidence of Dipolar Chains

One way to determine if a chain of particles has a dipole moment is to observe its orientation in an electric field. The torque applied to a dipole with dipole moment $\vec{\delta}$ at an angle θ to an electric field $\vec{E}$ is $\vec{\tau} = \vec{\delta} \times \vec{E} = |\vec{\delta}||\vec{E}| \sin(\theta)$. So, if dipolar, this torque would cause a chain to rotate to orientate parallel with the field.

To investigate this, a different sample cell was made over which an electric field could be applied, and this is shown in figure 4.20. A coverslip (22×22 mm wide, $0.13 - 0.17$ mm thick) was sputter coated with a $20 - 40$ nm thick layer of silver, then a laser was used to cut a 100 µm wide gap through it. This cover slip was then used to seal the sample between it and a glass microscope slide. Conducting wires were then glued with Araldite to be in contact with the silver layer, and finally the entire sample was sealed with UV adhesive. The wires were attached to a function generator (Aim-TTi, TG320), using an amplifier (Laboratory Power Amplifier, N4L LPA400) in order to apply a sinusoidal wave (0.452 Hz, 2.8 V) across the sample. Using an oscilloscope (ISO-TECH, ISR622, 20 MHz), the amplifier was found to increase the voltage by $\sim 20\times$. A sample at $c_{\text{salt}} = 100$ µM was used, and a chain of 9 particles was formed using the optical traps. This was held in the sample using 3 optical traps, one on the central particle, and two much weaker traps on the end particles. This allowed the chain to pivot freely in the electric field about its central particle whilst also remaining parallel to the view of the objective.

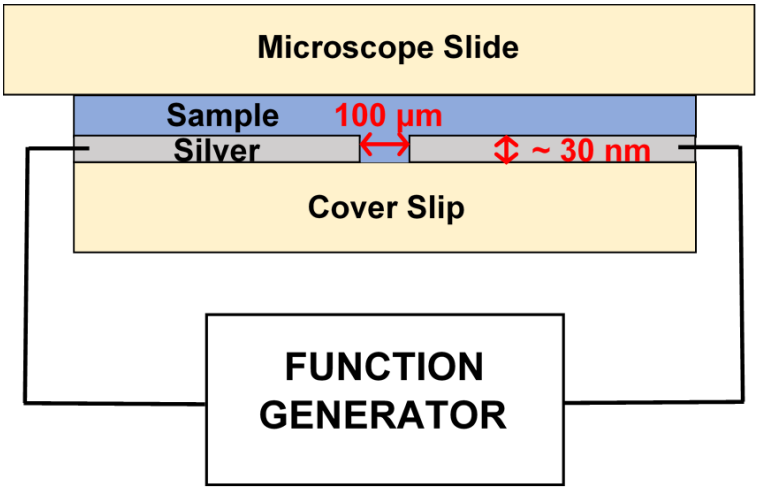

FIGURE 4.20: A diagram showing the setup of the cell in order to observe the behaviour of the chains of particles in an electric field. The field of view (which is vertical in this diagram) is therefore perpendicular to the electric field (horizontal in this diagram).

The observations made during this experiment are shown in figure 4.21. These snapshots are from a video of the orientation of the chain in the oscillating electric field. The video showed that the chain rotated about the trapped, central particle

each time the electric field changed direction. As soon as the field was applied perpendicular to the chain, the chain rotated anti-clockwise (figures 4.21(a)-4.21(b)), indicating that the chain has a dipole moment; this torque would not act on a chain of monopolar particles. As the field oscillated the first couple of times, the chain swung back and forth in response to the applied torque (figures 4.21(b)-4.21(d)). After a couple of these oscillations, the chain rotated anti-clockwise more than it did clockwise, resulting in the chain aligning directly with the electric field (figures 4.21(d)-4.21(e)). Once aligned, the chain did not oscillate any more, even during further oscillations of the field.

This behaviour in an applied electric field shows direct evidence that the chains of particles have a dipole moment, but that the individual particles do not. Unfortunately, it was not possible to observe any rotation of the single particles in the applied field, as optically they appear homogeneous. Such a rotation would again indicate if the individual particles had a dipole moment. To observe this rotation, bleaching or dyeing part of the particle's surface would be required. However, the evidence presented by the interaction of a single particle and a chain (figure 4.19) suggests that the isolated particles remain homogeneously charged. This means that during their interaction, the charge must redistribute across the particle surface. What was already suggested in the previous chapter (section 3.3.3), was that these particles indeed appear to behave as if their charge can regulate during their interaction.

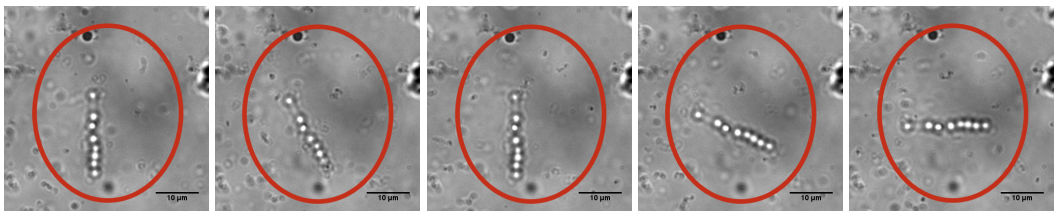

(a) 0 (b) $\longrightarrow$ (c) $\longleftarrow$ (d) $\longrightarrow$ (e) $\longleftrightarrow$

FIGURE 4.21: A chain of 9 AC12 particles in a $c_{salt} = 100$ µM sample, with an optical trap on the central particle in an applied, sinusoidal electric field. The subcaptions note the direction of the field in each snapshot showing the oscillation of the chain before it finally orientates and remains parallel to the field.

4.4.2 Charge Redistribution

The concept of charge regulating surfaces was introduced in section 1.1.6 as a more realistic description of experimental systems that offers an alternative boundary condition under which interacting surfaces can be defined (*59*, *61*). Most studies in the literature have focussed on how charge regulation affects the interaction between two flat surfaces, with the major result being that the surface charge density decreases with the surface separation, thus reducing the magnitude of the repulsion below that for the case of two surfaces held at constant charge (*63*, *64*). In a

study by Maggs & Podgornik, the framework of charge regulation is extended to spherical surfaces (68). With the aim of describing the charge distribution across an entire protein during their interaction, they consider two dielectric particles in an electrolyte solution where the surface charge density is not held constant across the surface, i.e. the distribution of charge is allowed to be heterogeneous. As the separation between the two particles is reduced, they show that only the surfaces facing one another undergo discharging due to the proximity with the second charged surface. On the opposite hemisphere of the particle however, the surface remains at a constant charge as it is not affected by the interaction. As a result of the heterogeneous charge distribution at close particle separations, the particles effectively become dipoles which are anti-aligned, with the lower surface charge density on the surfaces facing one another. This transition from a uniform to a non-uniform charge distribution on the surface we term a *charge redistribution*.

This study by Maggs & Podgornik therefore describes how the interaction between two charged particles can result in the formation of dipolar particles (68), which is what the data presented above suggests is occurring in our system. However, the dipoles remain anti-aligned as only a symmetric interaction is considered. In order to explain the data presented in this chapter, the interaction must result in aligned dipolar particles, which implies that the initially symmetric system must become non-symmetric during the interaction. The concept of symmetry has been discussed in a more recent paper by Majee, Bier & Podgornik, where at a specific surface separation, a *spontaneous symmetry breaking* of the system occurs if the surfaces are allowed to adopt different charge densities (69). The exact location (separation and ionic strength) where this occurs depends on the charging properties of the surface, where in some systems it can result in an *attraction* between two initially identical surfaces as one surface becomes oppositely charged (69, 466). For our system, the surface of the particles is unlikely to become negatively charged due to its surface chemistry, but can become uncharged. Oppositely charged surfaces are not however required for an attraction to exist between the particles. If the charge redistribution results in a dipolar particle (68), then the additional dipolar interaction can become the origin of attraction if aligned with the dipole moment of a neighbouring particle. So, a *spontaneous symmetry breaking* of the system must occur during the interaction at close separations to result in both the long-range repulsion measured in the previous chapter (symmetric interaction), and the short-range attraction presented in this chapter (aligned dipole moments therefore non-symmetric).

4.5 Conclusion

This chapter has presented observations of an attraction between like-charged particles when electrolyte was added into the dispersion. By plotting the mean cluster size as a function of electrolyte concentration, two regimes were apparent.

At first the cluster size increases slowly with electrolyte concentration, but above a certain concentration the dependence was strengthened, with large aggregates ($>$ 20 particles) forming. The boundary between these two regimes was denoted the critical aggregation concentration (CAC), and was found to depend on the effective charge of the particles in the dispersion. This showed that the attraction became dominant when either the surface charge of the particles was reduced, or the ionic strength was increased. This is of course predicted to occur in DLVO theory due to the presence of vdW interactions. However, calculations show that the vdW interaction is too weak to overcome the charge and steric stabilisation of these particles. Thus, attractions not considered within DLVO theory must be the cause. Some interactions known to cause attractions in colloids were then investigated, including depletion due to undissociated electrolyte or a collapse of the stabilising polymer layer. However, these were all shown not to be the origin of attraction in this system. To try to ascertain the possible origin of attraction, the clusters formed at intermediate electrolyte concentrations were analysed. By comparing the clusters found to those predicted in the literature for different systems, it seems likely that the aggregated particles have a dipole moment. This was evidenced from the lack of close-packed structures and the prevalence of chains in the samples. To further investigate this idea, an electric field was applied perpendicular to a chain of particles. What was observed was that the chain rotated to orientate with the electric field, directly indicating that the chain has a dipole moment; no torque would be applied to a chain of homogeneously charged, or uncharged, particles.

The combined evidence of the measured repulsions in chapter 3 and the observed attractions in this chapter shows that the interaction between these particles is repulsive at large separations but attractive at short separations. This suggests that the charge distribution across the surfaces of the particles must redistribute during the interaction for the particles to become dipolar at short separations. This idea has been discussed theoretically in the literature for two charge regulating particles (*68*). What must also occur is a spontaneous symmetry breaking of the system to result in aligned dipoles, and thus the attraction at short separations (*69*, *466*). The next chapter will focus on discussing the consequences of the charge regulation of two interacting surfaces in one theoretical framework, and show how it can simultaneously explain the inflated screening lengths measured in the repulsions, and the unexpected presence of attractions observed in the same system.

Chapter 5

Interactions between Charge Regulated Particles

The two results chapters (3 & 4) presented evidence of the form of the interaction profile between PMMA particles in a dilute, nonpolar electrolyte solution. The first chapter focussed on direct measurements of the repulsion between the charged particles with BOT, and presented evidence that those repulsions were not well described by DLVO theory at high electrolyte concentrations. This was evidenced as the decay length of the pair interactions κ_{meas}^{-1} was not equal to the DH length λ_D (calculated from the bulk conductivity) at all electrolyte concentrations. The second results chapter focussed on observations of short-range attractions between the particles which were deemed too strong to be vdW interactions. The presence of such an attraction is not predicted within DLVO theory, and cannot be accounted for by non-electrostatic origins such as depletion. What the evidence presented in both chapters infers is that the surfaces of the particles do not remain at a fixed surface charge density during their interaction, but in fact exhibit a charge regulation, where the surface charge reduces with decreasing particle separation and increasing ionic strength. This chapter attempts to combine both observations within one theoretical framework for this simple, nonpolar dispersion, in order to present the most probable explanation as to why DLVO theory fails to describe its behaviour. Firstly, a Landau model is used to describe two charge regulating surfaces, and how this directly affects the measured electrostatic repulsion between them. Secondly, the consequences of a charge redistribution across the particle surface is discussed as the probable origin of attraction observed.

5.1 Charge Regulated Systems

Since its emergence, the charge regulation boundary condition has been used by many to describe the behaviour of different systems within the PB theory of electrostatic interactions. Initially this was done by Ninham & Parsegian in their surface dissociation model (*61*), but has also been used in models using the law of mass action (*67*, *467*), or by defining the surface free energy (*468*, *469*). In doing so, the behaviour of many different systems has been investigated, including proteins (*470*, *471*), bacteria (*472*), polyelectrolytes (*64*), and other biological systems (*473*, *474*), as well as inorganic particles and surfaces such as silica (*63*), iron oxide and

amines (67). What these studies have shown is how the surface charge density adapts due to changes in the local potential, either through interacting with other charged surfaces, or by increasing the ionic strength. The origin of this is due to the competition between the interactions of ions on the surface with their neighbouring surface ions, and with bulk ions wanting to adsorb. What has been shown in the literature, is that the surface charge density reduces with separation to another surface if they can both charge regulate, as was discussed in section 3.3.3. What some publications have shown is that in some cases, a spontaneous symmetry breaking can occur between charge regulating surfaces, at which point the charge magnitudes of the two surfaces become different and thus attractions can arise (69, 466). As was also discussed in section 4.4.2, this behaviour has been extended to spherical surfaces, where it has been shown non-uniform charge densities arise at close separations, resulting in particles with a dipole moment (68).

The experimental evidence that the PHSA-stabilised PMMA particles in this study charge regulate during their interactions comes from combining the different observations made that describe different parts of the interaction profile. Firstly, the particles are directly measured with BOT to repel each other at long distances due to their charged surfaces. The decay length of these repulsions κ_{meas}^{-1} was found to agree with the DH length λ_D, as predicted in DLVO theory, at low electrolyte concentrations. However, above a critical electrolyte concentration c_{salt}^*, this agreement fails, with $\kappa_{meas}^{-1} > \lambda_D$ and a nonmonotonic dependence of κ_{meas}^{-1} on c_{salt} (figure 3.14). Also noted was a decrease in the quality of fit of a Yukawa force to the data (figure 3.13). Above the same critical concentration, the fitted particle charge Z_{eff} from the same BOT profiles decreases with c_{salt} (figure 3.16). The fact that the particle charge decreases at high ionic strength suggests that the surface can charge regulate according to the local conditions at the surface. As predicted in the literature, the reduction in the surface charge can also occur when the separation of the surfaces is reduced due to the increased electrostatic interaction. In such cases, the decay of the interaction becomes dependent on both the ionic strength and the particle charge. By fitting the force profiles whilst assuming a constant particle charge during the interaction therefore results in the fitted value of κ_{meas}^{-1} becoming larger than expected.

What was also observed in the same experimental systems was that the particles form aggregates, indicating a short-range attraction. The prevalence of chains and the absence of tetrahedral structures suggests that the particles contain some dipolar nature. This was investigated by observing the behaviour of a chain of particles, tethered in the centre with an optical trap, in an applied electric field. The fact that the chain rotated to orientate with the field is direct evidence that these particles, once aggregated, have a dipole moment. Given that dipoles have an attractive interaction when aligned, this immediately indicates the origin of the short-range attraction. Most of the literature on charge regulation discusses the interaction between flat surfaces, however one publication has shown how charge regulation of a spherical surface can result in the particles having a dipole moment

at short separations due to a redistribution of the charge density to be heterogeneous (*68*). However, the symmetry of such an interaction results in anti-aligned dipolar particles rather than aligned which was observed in our system. Therefore to account for the initially symmetric repulsion between these particles, and then an attraction due to aligned dipolar particles, the symmetry of the system must be broken (*69*, *466*).

By following the formalism of Podgornik and co workers, where the free energy of the surface is used to describe its charge regulation, this chapter shows how all the above experimental observations can be explained within one framework used to describe the interaction between two charge regulating particles.

5.2 Surface Charge-Collapse Transition

The equilibrium surface potential (and equivalently the charge density) of a particle can be determined from the minimum in the free energy landscape (*469*). Many factors contribute to this total free energy profile $\mathcal{F}_{\text{Tot}}$, including interactions on the surface $\mathcal{F}_{\text{s}}$ and in the double layer $\mathcal{F}_{\text{DL}}$. Despite the energy required for charging, the driving force for surface charging in solution is the favourable gain in entropy due to counterion release. Due to the interplay of these energetic and entropic contributions, there will be conditions under which surface charging is either favourable or unfavourable. As already mentioned, many real systems show an additional dependence of its surface potential on the separation to another charged surface, and are said to be charge regulated. Generally, the surface potential (and charge) decreases when pushed closer to another surface due to the competition between ion adsorption and the interactions between already adsorbed ions. When two surfaces are pushed together very quickly compared with the time for charge association/dissociation at the surface, then this equilibration does not occur, and the assumption of a constant charge boundary condition can be appropriate. However, in our experiments, the separation between the two particles is reduced slowly, allowing enough time for charge equilibration to occur. In terms of the free energy, this is attributed to an additional term that describes the free energy of the electrostatic interaction between the two surfaces $\mathcal{F}_{\text{Int}}$. Now, the total free energy profile, and hence the equilibrium surface potential, depends on both the surface separation and on the intervening ionic strength.

If we consider that there are two phases for the surface, charged or uncharged, we can describe how the surface transitions from one to the other as a function of the surface separation and the ionic strength. We call this transition a '*charge-collapse*' transition. Given that this transition is expected to be continuous, it can be described using Landau's model for second order phase transitions by equating the order parameter with the surface potential ψ_{s} (*475*). This particular model is just one way to describe how the charge of a surface changes under different conditions, i.e. with separation to another surface, and is derived differently to the model used

by Ninham & Parsegian, discussed in section 1.1.6, where the charge dissociation equilibrium of the surface was considered.

This section will discuss the effect of such a charge-collapse transition of the surface on the measured force of interaction between two charged surfaces, with emphasis on how it can explain the trend in the screening length and particle charge as a function of electrolyte concentration that was measured using BOT.

5.2.1 Landau Model of Phase Transitions

Phase transitions are usually considered to be when a phase of one symmetry changes into a phase of a different symmetry. For example, a liquid has a more symmetric structure than a solid, and again a gas is even more symmetric than a liquid. With different amounts of symmetry, two phases also have different entropies and therefore different free energies. How this energy changes between phases determines how we treat that phase transition.

Phase transitions can usually be categorised into two types, either by having a discontinuous or a continuous change in free energy. Equivalently there is a discontinuity (a jump) in either the first derivative of the free energy (which is the entropy and also the volume or pressure according to Maxwell's equations) or second derivative of the free energy (which could be the heat capacity or isothermal compressibility) at the transition respectively. Discontinuous phase transitions are hence often called 'first order' and continuous transitions called 'second order'. At a first order phase transition there is often a coexistence of the phases either side of the transition, e.g. boiling water is a mixture of gas and liquid water, hence why a kettle bubbles as you boil it. This is because there is additional energy required to change phases, quantified by a latent heat. For the example of water freezing to ice, 'classical nucleation theory' is often used to describe that this energy requirement is due to the need to first form nuclei of ice in the water phase that must reach a certain critical size before a spontaneous transition can occur to the solid state. Because this nucleation step is stochastic, it means that a delay is often observed during a first order transition from one phase to another. The existence of second order phase transitions was disputed for a while (*476*), until Landau published his theory in 1937 (*475*). These transitions are accompanied by a discontinuous second derivative of the free energy, or equivalently where the derivative of the entropy is discontinuous. This means that there is no phase coexistence or delay in changing phase as it happens spontaneously. Physically this jump can be in the value of the heat capacity, isothermal compressibility, or capacitance, and examples of such transitions are towards superconductivity, ferromagnetic to paramagnetic and order-disorder transitions of a liquid crystal.

Landau's theory is an effective, general theory for the behaviour near a second order phase transition (e.g. at a critical point). It uses a single order parameter φ that is non-zero in one phase, and zero in the other, and it smoothly converges to zero at a critical point. At a fixed value of φ, the free energy $\mathcal{F}(\varphi)$ is assumed analytic.

This means that for small φ, $\mathcal{F}(\varphi)$ is well approximated by a Taylor series about the critical point, and this expansion must reflect the symmetry of the system, i.e. does $\mathcal{F}(\varphi) = \mathcal{F}(-\varphi)$? By making this approximation, the Landau model becomes a mean field theory, and as such fluctuations in the value of the order parameter are ignored. However, this also means that Landau theory becomes a general theory that describes the behaviour of all second order transitions, irrespective of the specific details of the system.

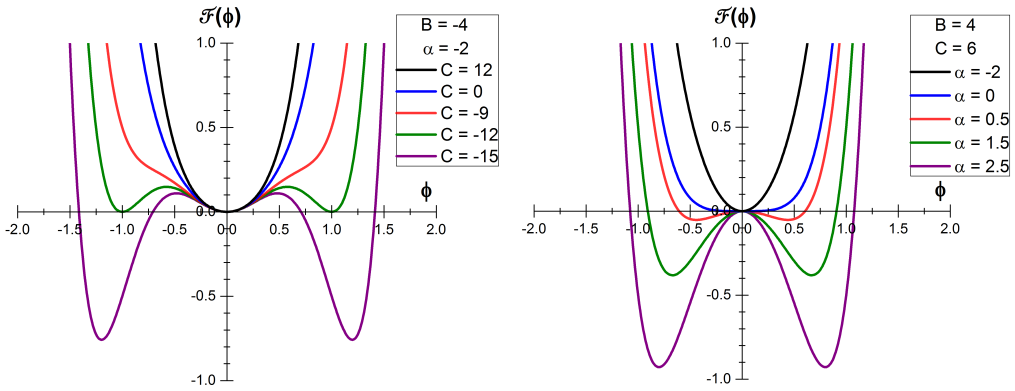

(a) First Order Transition (b) Second Order Transition

FIGURE 5.1: An example of the free energy profile following the form of $\mathcal{F} = -\frac{\alpha}{2}\varphi^2 + \frac{B}{4}\varphi^4 + \frac{C}{6}\varphi^6$ (eq. (5.5) with $C = 0$). Left: A first order transition where $B = -4$, $\alpha = -2$ and varying the magnitude of C in order to show the discontinuous transition of the minima to $\varphi = 0$. Right: A second order transition where $B = 4$, $C = 6$ and varying the magnitude of α in order to show the continuous transition of the minima to $\varphi = 0$.

The difference in the form of the free energy during first and second order transitions is given in figure 5.1. For these plots, a power law was used ($\mathcal{F} = -\frac{\alpha}{2}\varphi^2 + \frac{B}{4}\varphi^4 + \frac{C}{6}\varphi^6$) (*477*), where the sign of the parameter B determines if the transition is of first ($B < 0$) or second ($B > 0$) order. Then, the values of C or α can be varied to show how the location of the free energy minima vary towards the state where $\varphi = 0$. This example shows a symmetric free energy in the order parameter, where $\mathcal{F}(\varphi) = \mathcal{F}(-\varphi)$. What defines a second order transition is that the free energy minimum transitions to $\varphi = 0$ continuously, and for the example in figure 5.1(b), $\varphi \to 0$ is reached by altering the value of α. During a first order transition however, the transition of the free energy minimum to $\varphi = 0$ is not continuous, but jumps to $\varphi = 0$ at a specific value of C. In the case given in figure 5.1(a), this occurs between $-12 < C < -9$.

Generally the following steps can be followed to find the function of the order parameter near the critical point, and consequently the location of the critical point:

1. Identify the order parameter φ (decreases continuously to zero at the critical point).

2. Expand the free energy $\mathcal{F}(\varphi)$ as a power series in φ.

3. Minimise the free energy to locate the stable states of $\varphi(x)$ where x is a variable you are altering in the system to get to the critical point, e.g. separation, temperature, pressure, etc.

4. Locate the critical point by finding when $\varphi(x) = 0$.

5.2.2 Applying Landau's Theory to our System

As suggested by Podgornik and coworkers, the free energy of a charged surface can be defined with Landau's theory, as can the free energy of the entire system (*478*). To do so, the order parameter is equated with the surface potential ψ_s, and instead of a critical point, the surface simply discharges ($\psi_s \to 0$). The factors that change the form of the free energy, and hence reduce ψ_s, are by reducing the surface separation and increasing the ionic strength.

As stated earlier, the free energy of the system contains several different contributions. These include the 'chemical' non-electrostatic contributions of the surface free energy $\mathcal{F}_s$ and the electrostatic contribution from the double layer $\mathcal{F}_{DL}$ encompassing the energy gain of counterion release and the cost of dissociation (*479*). $\mathcal{F}_{DL}$ can be defined as a function of the surface charge density σ and the surface potential ψ_s via

$$\begin{aligned}\mathcal{F}_{DL} &= -\sigma\psi_s + \int_0^{\sigma} \psi_s' \, d\sigma' \\ &= -\int_0^{\psi_s} \sigma \, d\psi \\ &= -\int_0^{\psi_s} \sigma_\infty \, d\psi + \mathcal{F}_{Int}(L).\end{aligned} \tag{5.1}$$

The second line is achieved using integration by parts $\int u \, dv = uv - \int v \, du$, and the third line is rewritten into two parts, one being the free energy of a single plate at a charge density σ_∞, and the other the interaction of two plates $\mathcal{F}_{Int}(L)$ at a separation L. The interaction free energy of two surfaces at a constant potential is derived to be, in units of $k_B T$ and per unit surface area (*480*),

$$\mathcal{F}_{Int}(L) = \frac{\Psi_s^2}{4\pi}\left(\frac{\kappa}{\ell_B}\right)\frac{1-\exp(-\kappa L)}{\sinh \kappa L}, \tag{5.2}$$

where $\Psi_s = e\psi_s/k_B T$. At large dimensionless separations $\kappa L \to \infty$, this reduces to

$$\mathcal{F}_{Int}(L) = 2\beta C \psi_s^2 \exp(\kappa L), \tag{5.3}$$

where $\beta = (k_B T)^{-1}$, $C = \varepsilon_r \varepsilon_0 \kappa$ is the capacitance of the double layer, and $\ell_B = \beta e^2/4\pi\varepsilon_r\varepsilon_0$ is the Bjerrum length, showing that $\mathcal{F}_{Int}(L) \propto \kappa$ at a fixed κL. The system free energy is then

$$\mathcal{F}_{Tot}(\psi_s) = \mathcal{F}_s(\psi_s) - \int_0^{\psi_s} \sigma_\infty \, d\psi + \mathcal{F}_{Int}(L). \tag{5.4}$$

Now the free energy of the system has been identified, the steps outlined above can be followed to apply Landau's theory.

Step 1 - Identify the order parameter φ

For this system, the order parameter is the surface potential as this reduces to zero at the 'critical point' when the surface discharges, i.e. $\varphi = \psi_s$.

Step 2 - Expand the free energy $\mathcal{F}(\varphi)$ as a power series

We can do this separately with both the surface and the electrostatic free energies. The surface term is a symmetric function in ψ_s as $\mathcal{F}_s(\psi_s) = \mathcal{F}_s(-\psi_s)$, and can be approximated to fourth order,

$$\mathcal{F}_s \simeq -\frac{\alpha}{2}\psi_s^2 + \frac{B}{4}\psi_s^4. \tag{5.5}$$

This form shows that the surface can either be charged or uncharged, determined by the location of its free energy minimum. For minima to be present, $B > 0$, and this parameter contains all the surface interactions that result in higher association of counterions when the surface potential is increased. The first parameter α describes the interactions between the surface groups. The sign of α determines if the free energy minima will occur at $\psi_s = 0$ ($\alpha < 0$) or a non-zero value ($\alpha > 0$). So when $\alpha > 0$, it describes the case where the interactions between the surface groups results in increasing dissociation at higher surface potentials. Figure 5.1 shows an example of the surface free energy of the form in equation (5.5) for the cases where $\alpha < 0$ and $\alpha > 0$. The minima in each case represent the thermodynamically stable state for the surface. For the example given earlier of the critical point, $\alpha > 0$ corresponds to being below the critical temperature, and $\alpha < 0$ being above the critical temperature, where the free energy minimum, and hence the equilibrium value of the order parameter, is always 0.

The electrostatic term is again approximated by using the definition of a Taylor series for a function $f(x)$ about a point ($x = c$) for the two components in equation (5.1),

$$f(x) \simeq \sum_{k=0}^{\infty} \frac{f^{(k)}(c)}{k!}(x-c)^k. \tag{5.6}$$

So, for the first term $\int_0^{\psi_s} \sigma_\infty d\psi_s$ about the point where $\psi_s = 0$, the approximation is

$$\begin{aligned} \int_0^{\psi_s} \sigma_\infty d\psi_s &\simeq \frac{\partial^2}{\partial \psi_s^2} \int_0^{\psi_s} \sigma_\infty d\psi_s \\ &= \frac{1}{2}\frac{\partial \sigma_\infty}{\partial \psi_s}\bigg|_{\psi_s=0} \psi_s^2, \end{aligned} \tag{5.7}$$

and for the function $\mathcal{F}_{\text{Int}}(L)$ about the same point, the approximation is

$$\mathcal{F}_{\text{Int}}(L) \simeq \frac{1}{2}\frac{\partial^2 \mathcal{F}_{\text{Int}}(L)}{\partial \psi_s^2}\bigg|_{\psi_s=0} \psi_s^2. \tag{5.8}$$

To keep the symmetry of the system only the ψ_s^2 components are taken. So the total free energy for the system (eq. (5.4)) can be rewritten as a Landau expansion for the free energy of the electrostatics (eq. (5.8) & (5.7)) and the surface (eq. (5.5)) that gives

$$\mathcal{F}_{\text{Tot}}(\psi_s) \simeq -\frac{1}{2}\big[A - \Gamma(L)\big]\psi_s^2 + \frac{B}{4}\psi_s^4, \tag{5.9}$$

where

$$A = \alpha + \frac{\partial \sigma_\infty}{\partial \psi_s}\bigg|_{\psi_s=0}, \tag{5.10a}$$

$$\Gamma(L) = \frac{\partial^2 \mathcal{F}_{\text{Int}}(L)}{\partial \psi_s^2}\bigg|_{\psi_s=0}. \tag{5.10b}$$

Now, the sign of the parameter A determines the relative strength of the electrostatic to non-electrostatic constituents. In order for the surface in isolation to be charged, which is what we expect, minima of $\mathcal{F}_{\text{Tot}}(\psi_s)$ must be at non-zero ψ_s and thus $A > 0$. Given that we also expect for most cases that $\frac{\partial \sigma_\infty}{\partial \psi_s}\Big|_{\psi_s=0}$ is positive, $A > 0$ occurs when α is either also positive, or negative with a magnitude less than $\frac{\partial \sigma_\infty}{\partial \psi_s}\Big|_{\psi_s=0}$.

The interaction term contained within the parameter $\Gamma(L)$ also determines the charge of the system. Because it is a second derivative of a free energy, $\Gamma(L) > 0$ within a thermodynamically stable state. For large separations κL, this parameter is then approximately

$$\Gamma(L) = \Gamma_0 \exp(-\kappa L), \tag{5.11}$$

where $\Gamma_0 = 4\beta C$. When the surfaces are well separated, $\Gamma(L) \to \Gamma_0$. To simplify things, a parameter $\gamma = \Gamma_0/A$ can be introduced that describes the relative strength of A & Γ_0. Effectively γ indicates how strong the electrostatics of the system is compared with the surface 'chemistry' terms, as $\gamma \propto \kappa/A$. Figure 5.2 gives an example of the system free energy according to equation (5.9), for well separated plates at various values of γ. When $\gamma < 1$, the surface terms dominate resulting in charged surfaces (free energy minima at $\psi_s \neq 0$), but when $\gamma > 1$, the electrostatic contribution becomes too strong that the surface discharges. Given that $\gamma \propto \kappa/A$, this discharging occurs as the ionic strength of the system is increased, which in our case is achieved by increasing the electrolyte concentration. As is also clear in figure 5.2 is that the lowest energy state for the surface is a charged state, and upon increasing γ the free energy of the system is increased. This shows that an additional

electrostatic energy is required to discharge the surface, and the parameter γ makes this a general theory for many different systems.

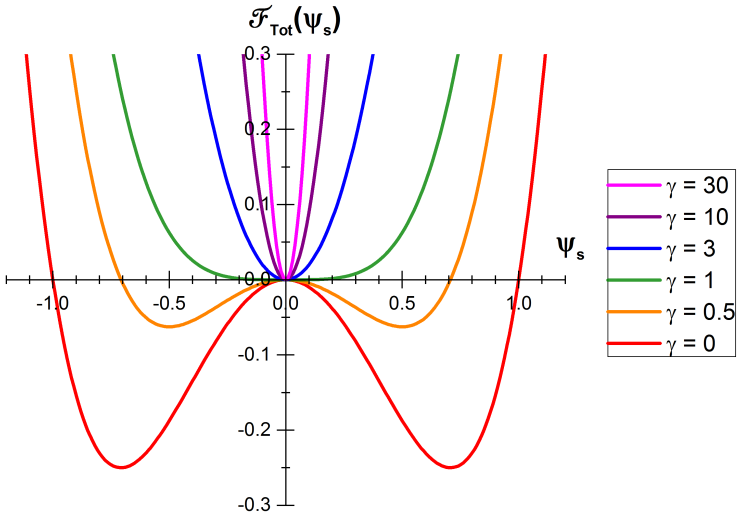

FIGURE 5.2: The free energy profile of the system following the form of equation (5.9), showing the case for when $\gamma = \Gamma_0/A < 1$, $\gamma = 1$ & $\gamma > 1$, with $B = 4$, $A = 2$ and at a large and constant L.

When closer in separation however, the electrostatic interaction term in equation (5.11) increases, and the system free energy starts to depend on the surface separation L as well as the ionic strength. To observe how the surface potential varies with both L and κ, the minima in the free energy must be located.

Step 3 - Minimise the free energy to locate the stable states of $\varphi(x)$

The minimum is located where the first derivative of the free energy $\mathcal{F}'(\varphi)$ is zero,

$$\frac{\partial \mathcal{F}_{Tot}(\psi_s)}{\partial \psi_s} = \left(\left[A - \Gamma(L) \right] + B{\psi_s}^2 \right) \psi_s = 0. \tag{5.12}$$

This occurs at the equilibrium values of the surface potential (locations of the free energy minima), denoted by $\overline{\psi}_s$, at

$$\overline{\psi}_s = 0, \tag{5.13a}$$

$$\overline{\psi}_s = \pm \sqrt{\frac{A - \Gamma(L)}{B}}. \tag{5.13b}$$

For a real, non-zero root, $A > 4\beta C \exp(-\kappa L)$. $\overline{\psi}_s$ is now a function of κL, the two parameters which are varied in this study,

$$\overline{\psi}_s = \pm \psi_\infty \sqrt{1 - \gamma \exp(-\kappa L)}, \tag{5.14}$$

where $\overline{\psi}_s \to \psi_\infty = \sqrt{A/B}$ at large plate separations as $\Gamma(L \to \infty) \to 0$. The change in the surface potential as a function of the dimensionless surface separation κL can

now be described by varying the single parameter γ. These effects are shown in figure 5.3 where $\overline{\psi}_s/\psi_\infty$ is plotted as a function of κL at various values of γ. This shows how discharging of the surface occurs when the surfaces are brought closer together, with a stronger effect occurring at increasing values of γ (equivalently higher ionic strengths).

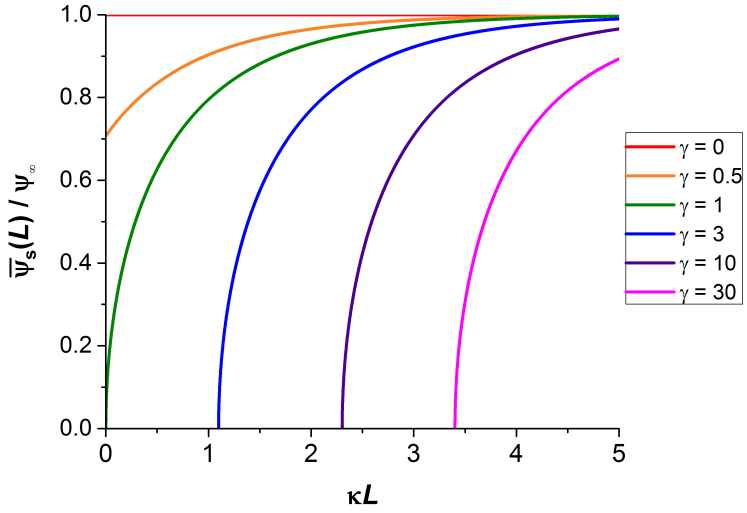

FIGURE 5.3: Plots of the dependence of the surface potential as a function of the surface separation and ionic strength (eq. (5.14)). When $\gamma < 1$ (low ionic strength) the surface remains charged when the surfaces are in contact.

Step 4 - Locate the critical point:

The 'critical point' in this case is where $\overline{\psi}_s = 0$, and this occurs at a critical plate separation $L = L_c$. In figure 5.3, this is the values of γ and κL when $\overline{\psi}_s/\psi_\infty$ intercepts the x-axis. From equation (5.14), $\overline{\psi}_s = 0$ when $\gamma \exp(-\kappa L) = 1$, so

$$\kappa L_c = \ln \gamma. \tag{5.15}$$

This means that a stable result of equation (5.14) is only possible for $L > L_c$, smaller separations give an unstable solution within this single parameter Landau model. So for large γ, the collapse transition occurs at a larger κL. The collapse transition is therefore only possible for $\gamma \geq 1$, otherwise $L_c < 0$. When $\gamma < 1$, the surface always dominates the system free energy, as is the case in a highly charged aqueous system where A is large (usually larger value of $\left.\frac{\partial \sigma_\infty}{\partial \psi_s}\right|_{\psi_s=0}$ in more polar solvents), and this charge collapse never happens, but when the electrostatics are comparable or dominant ($\gamma \geq 1$) then it can, as is expected in our nonpolar system.

An additional stability criteria is imposed on the system within this model, and that is that it must be located in a free energy minimum rather than a maximum, i.e. $\mathcal{F}''_{\text{Tot}}(\psi_s) > 0$. So differentiating equation (5.9) again we get that

$$\psi_s > \sqrt{\frac{A - \Gamma(L)}{3B}} > \frac{\overline{\psi}_s}{\sqrt{3}}. \tag{5.16}$$

This means that within the confines of this particular model, no stable states for the system exist in the region where $L < L_c$, i.e. in the region below κL_c in figure 5.3. However, physically we could have the surfaces in this regime, but this model does not explain what would happen in that case after the transition of the surface to an unchanged state. In order to describe the behaviour in this regime, an added freedom must be included into the model, and this is done so in a following section 5.3.1. Firstly, the consequences of the dependence of the surface charge density on the surface separation and ionic strength described above on the measured force is discussed.

5.2.3 Consequences of a Surface Charge-Collapse Transition for the Measured Force

The Derjaguin transform, discussed in section 1.2.3, allows the force $F(h)$ between two spheres of radius a at a surface-surface separation h to be approximated from the free energy of the interaction of two flat plates at the same surface separation $L = h$, valid in the limit of thin double layers ($\kappa_D a >> 1$),

$$F(h) = \pi a \Delta\mathcal{F}_{\text{Tot}}(h), \tag{5.17}$$

where $\Delta\mathcal{F}_{\text{Tot}}(h) = \mathcal{F}_{\text{Tot}}(h) - \mathcal{F}_{\text{Tot}}(h \to \infty)$.

To obtain a function of $F(h)$ that is dependent only on the distance h and the surface potential ψ_s, we first rewrite the Landau coefficients A and B in equation (5.9) as a function of ψ_s and $\Gamma(h)$. Using that $\psi_\infty = \sqrt{A/B}$ determined earlier, equation (5.14) gives the Landau coefficients to be

$$A = -\frac{\Gamma(h)\psi_\infty^2}{\psi_s^2(h) - \psi_\infty^2}, \tag{5.18a}$$

$$B = -\frac{\Gamma(h)}{\psi_s^2(h) - \psi_\infty^2}. \tag{5.18b}$$

Then, with equation (5.9) giving $\mathcal{F}_{\text{Tot}}(h \to \infty) = -A^2/4B = -A\psi_\infty^2/4$, we obtain

$$\begin{aligned}\Delta\mathcal{F}_{\text{Tot}}(h) &= -\frac{1}{2}\big[A-\Gamma(h)\big]\psi_s^2(h)+\frac{1}{4}B\psi_s^4(h)+\frac{1}{4}A\psi_\infty^2 \\ &= \frac{1}{4}\left[\frac{2\Gamma(h)\psi_s^2(h)\psi_\infty^2}{\psi_s^2(h)-\psi_\infty^2}-2\Gamma(h)\psi_s^2(h)+\frac{\Gamma(h)\psi_s^4(h)}{\psi_s^2(h)-\psi_\infty^2}+\frac{\Gamma(h)\psi_\infty^4}{\psi_s^2(h)-\psi_\infty^2}\right] \\ &= \frac{1}{4}\left[\frac{\Gamma(h)\psi_s^4(h)-\Gamma(h)\psi_\infty^4}{\psi_s^2(h)-\psi_\infty^2}\right] \\ &= \frac{1}{4}\Gamma(h)\left[\psi_s^2(h)+\psi_\infty^2\right].\end{aligned} \tag{5.19}$$

Then substituting in the definition for $\Gamma(h)$ (eq. (5.10b)) and $\psi_s(h)$ (eq. (5.14)) we get

$$\begin{aligned}\Delta\mathcal{F}_{\text{Tot}}(h) &= \frac{1}{4}4\beta C\exp(-\kappa h)\left[\psi_\infty^2\big(1-\gamma\exp(-\kappa h)\big)+\psi_\infty^2\right] \\ &= 2\beta C\psi_\infty^2\exp(-\kappa h)\left[1-\frac{\gamma}{2}\exp(-\kappa h)\right],\end{aligned} \tag{5.20}$$

so the total force of interaction is

$$F(h) = 2\pi a\beta C\psi_\infty^2\exp(-\kappa h)-\pi a\beta C\psi_\infty^2\gamma\exp(-2\kappa h). \tag{5.21}$$

The second, *negative* term acts as an *effective attraction* but really it is just a *weakening of the repulsive force* ($F(h) = (2\pi a\beta C\psi_\infty^2)\exp(-\kappa h)\big[1-\frac{\gamma}{2}\exp(-\kappa h)\big]$) with a distance dependence that is *doubly-screened*, and the magnitude of this is determined by γ, and therefore κ. Being doubly-screened, this negative term become more effective on the total interaction force at closer separation.

At the collapse transition $h = L_c$ and $\gamma = \exp(\kappa L_c)$ (eq. (5.15)) and the force becomes $F(h) = \pi a\beta C\psi_\infty^2\exp(-\kappa L_c) = \dfrac{\pi a\beta C\psi_\infty^2}{\gamma}$. Therefore the total interaction remains repulsive even at the collapse transition. The scaled force profile $\dfrac{F(\kappa h)}{2\pi a\beta C\psi_\infty^2}$ as a function of the scaled separation κh for different values of γ (eq. (5.21)) is given in figure 5.4. What this figure shows is the increased weakening of the repulsive force from that expected in DLVO theory (fixed surface charge density, $\gamma = 0$) as the separation of the particles is reduced. Again, this model can only describe the behaviour of the system when $\kappa h > \kappa L_c$ and hence why the force profiles stop before reaching contact in the cases where $\gamma > 1$. This form of the interaction force was derived by Podgornik & Parsegian, and they showed how this model of charge regulation fits well to data measured with the SFA between two mica surfaces covered in the surfactant CTAB (*479*).

Again, in order to describe the behaviour of the surfaces when $\kappa h < \kappa L_c$, an added freedom must be included into the model, and this is done so in a following

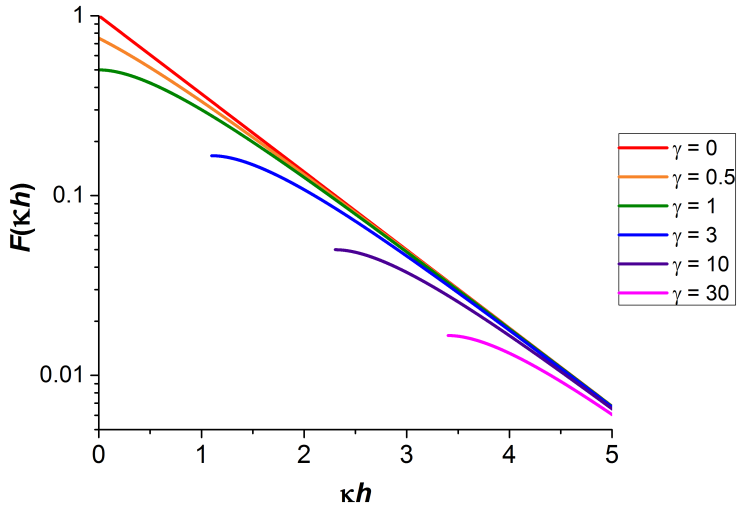

FIGURE 5.4: The scaled interaction force between two spheres as a function of the dimensionless surface separation κh: $\frac{F(h)}{2\pi a\beta C\psi_\infty^2} = \exp(-\kappa h)\left[1 - \frac{\gamma}{2}\exp(-\kappa h)\right]$.

section 5.3.1. Before showing this model, the gradients obtained from the force profiles in figure 5.4 at a specific value of κh are shown to be a function of γ, and therefore so is the measured screening length $\kappa_{\text{meas}}^{-1}$.

5.2.4 The Effect of a Surface Charge-Collapse Transition on the Measured Screening Length

Upon observation of the force profiles shown in figure 5.4, it is clear that at a specific value of κh, the gradients of those profiles decrease with increasing γ. The exact dependence of this gradient, which is inversely proportional to $-\kappa_{\text{meas}}^{-1}$, can be determined as follows. When $\gamma = 0$, the DLVO result for the force profiles is obtained, thus when fitting the force profiles measured with BOT the measured screening length $\kappa_{\text{meas}}^{-1}$ was taken to be

$$\kappa_{\text{meas}}^{-1} \approx -\left[\frac{\partial}{\partial h}\ln F(h)\right]^{-1}, \tag{5.22}$$

so using equation (5.21) we get that

$$\begin{aligned}\kappa_{\text{meas}}^{-1} &= -\left[\frac{\partial}{\partial h}\ln\left[2\pi a\beta C\psi_\infty^2\exp(-\kappa h)\left(1-\frac{\gamma}{2}\exp(-\kappa h)\right)\right]\right]^{-1} \\ &= -\left[-\kappa + \frac{\kappa\gamma}{2\exp(\kappa h)-\gamma}\right]^{-1}.\end{aligned} \tag{5.23}$$

If we then assume that the assumption of DLVO theory is true where $\kappa = \lambda_D^{-1}$ we get the ratio

$$\frac{\kappa_{meas}^{-1}}{\lambda_D} = \left[1 - \frac{\gamma}{2\exp(\kappa_D h) - \gamma}\right]^{-1}. \tag{5.24}$$

This ratio then determines how much the measured screening length from the BOT force profiles κ_{meas}^{-1} deviates from the DLVO prediction that the screening length should equal the DH length λ_D. This deviation predicted in this model is plotted in figure 5.5, where the different lines correspond to where κ_{meas}^{-1} was measured from the force profiles in figure 5.4. For example, for the case where $\gamma = 3$ in figure 5.4, measuring κ_{meas}^{-1} at a separation of $\kappa_D h = 2.5$ will give a larger deviation of κ_{meas}^{-1} from λ_D than measuring it at $\kappa_D h = 5$. This is because the solutions for equation (5.21) all converge on the DLVO prediction for the force ($\gamma = 0$) at large $\kappa_D h$.

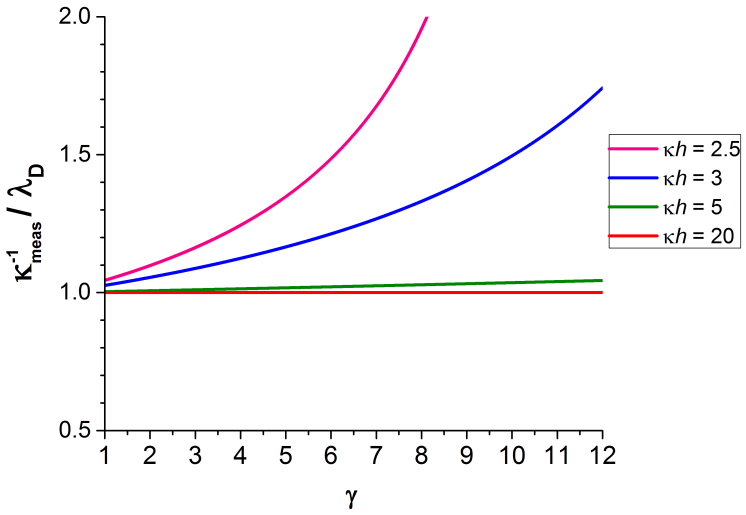

FIGURE 5.5: The resultant ratio of the measured screening length κ_{meas}^{-1} with the DH length λ_D as a function of γ (eq. (5.24)). The different lines represent the ratio measured when κ_{meas}^{-1} is measured at different surface separations $\kappa_D h$.

5.2.5 The Effect of a Surface Charge-Collapse Transition on the Measured Particle Charge

The ratio predicted as a function of γ in figure 5.5 gives the difference in the gradients of the lines plotted in figure 3.15. This then has a direct effect on the fitted value of the intercept, and hence the charge of the particle, as the intercept of the log of the force (eq. (3.7)) is proportional to the value $\ln(Z^2)$. So, at the point where κ_{meas}^{-1} is fit to the data, the two approximately linear lines in figure 3.15 intercept and thus at this point (x, y),

$$y = -\kappa_D x + c_1 = -\kappa_{meas} x + c_2, \tag{5.25}$$

where $y = \ln\left[h^2 F(h)\right]$ & $x = h$. Given that at each value of γ we now have a value of $\kappa_D/\kappa_{meas} = \kappa_{meas}^{-1}/\lambda_D$, the difference in the two intercepts is given by

$$c_2 = c_1 - \kappa_D h\left(1 - \frac{\lambda_D}{\kappa_{meas}^{-1}}\right), \tag{5.26}$$

and thus the difference in the fitted particle charge is

$$Z_{eff} = \sqrt{\exp\left[c_2\right]} = \sqrt{\exp\left[c_1 - \kappa_D h\left(1 - \frac{\lambda_D}{\kappa_{meas}^{-1}}\right)\right]}. \tag{5.27}$$

When reducing Z to the effective charge Z_{eff} in accordance with the data in figure 3.16, $\sqrt{\exp\left[c_2\right]} \approx 5.1$, so $c_1 \approx 3.26$. The fitted effective charge as a function of γ is given in figure 5.6, showing how at increasing values of γ, the fitted particle charge decreases, with a strong dependence found when the value is obtained at a closer particle separation $\kappa_D h$.

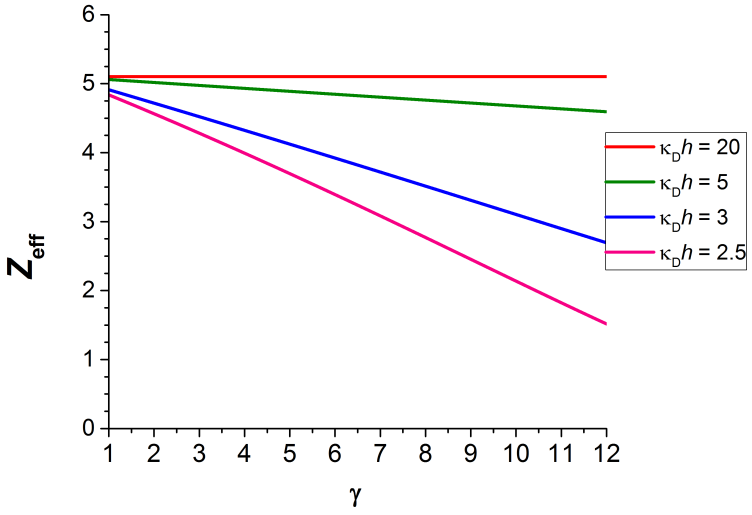

FIGURE 5.6: The resultant measured effective particle charge Z_{eff} as a function of γ. The different lines represent the ratio measured when κ_{meas}^{-1} is measured at different surface separations $\kappa_D h$.

5.2.6 Comparison of the Model with Experimental Data

The general trends in figures 5.5 & 5.6 show the same qualitative dependence on the ionic strength as the experimental data presented in figures 3.21 & 3.16. Because of the linear dependence of γ on κ_D, and without knowing the exact value of A and B for our system, the experimental data can be plotted alongside the predictions from the Landau model using the mapping $\gamma = M\kappa_D - N$. The values of M and N can be adjusted to show where the inflation in κ_{meas}^{-1} and the decrease in Z_{eff} were

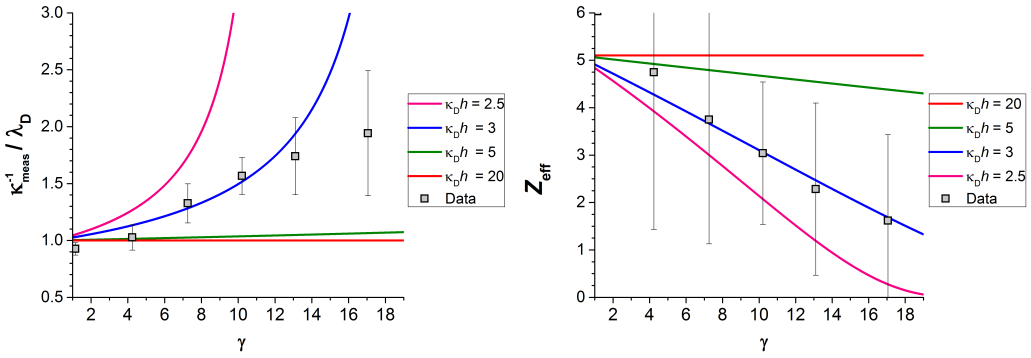

FIGURE 5.7: The experimental data for measured $\kappa^{-1}_{meas}/\lambda_D$ and Z_{eff} are plotted alongside the predictions from the Landau model.

measured above c^*_{salt} when fitted at the dimensionless separation $\kappa_D h \approx 3$, which was done with our data. The factor N is required in the mapping to ensure that $\gamma = 1$ corresponds with the critical concentration c^*_{salt}. The comparison of the predictions from this model and the experimental data are given in figure 5.7, showing both the inflated screening length $\kappa^{-1}_{meas}/\lambda_D$ and the fitted particle charge Z_{eff} as functions of γ. To achieve this overlap, the values for the mapping of $M = 4\beta\varepsilon_r\varepsilon_0/A = 10$ & $N = 37$ was used. This would then correspond to a value of $A \approx 0.4\beta\varepsilon_r\varepsilon$ for our system.

5.3 A Possible Origin for Like-Charge Attraction

The model used thus far to describe the charge regulation of two interacting surfaces has been constrained by a few assumptions for simplicity. Despite these assumptions, the model has described very well the results in chapter 3, where the value of the measured decay length $\kappa^{-1}_{meas} > \lambda_D$ upon increasing the electrolyte concentration. However, as noted in figures 5.3 & 5.4, the model cannot describe the behaviour of the surfaces when they are closer than a critical separation κL_c, at which point, the surfaces are discharged. By removing these constraints, the model can predict the behaviour of the two surfaces at all separations. As the following sections will show, this model of charge regulation predicts conditions under which the two surfaces will *attract* each other. The cause for this attraction is a spontaneous symmetry breaking of the system, where the charge densities of the interacting surfaces become different to each other.

5.3.1 Bilinearly-Coupled Order Parameter Model

One of the constrictions applied to the one-parameter model already discussed is that the two surfaces must have an identical surface potential under all conditions. Given that both surfaces can adapt their surface potential due to the local environment, it is not unreasonable to assume that they can adapt differently, resulting in different surface potentials. This idea was discussed by Podgornik and coworkers

recently where they showed how an initially symmetric system can spontaneously become non-symmetric if the surfaces are allowed the freedom to obtain a different surface potential (69). This publication focusses mainly on a system in which the surfaces can be negatively or positively charged, and thus when the symmetry breaks, the two surfaces could become oppositely charged. This is not likely in our system, where the particles remain positively charged, but they state that even in such systems, spontaneous symmetry breaking still occurs and results in two surfaces of different charge magnitude but the same sign. This highlights a second modification of the model required to better describe our system. By being a symmetric function in the surface potential, the free energy shown in figure 5.2 describes a surface that can be either positively charged or negatively charged; the free energy minima are of equal magnitude for a negative or positive surface potential. To better describe the free energy of our system, an additional term can be added that results in a positive surface potential being of lower energy than the negative potential. This can be thought of as an 'external field' H. The sign of H is determined by the surface chemistry, i.e. if the surface only contains groups that dissociate into positive groups with a negative counterion, then the surface can only charge positively. For example, the free energy can be defined by

$$\mathcal{F}_{\text{Tot}}(\psi_s) \simeq -\frac{1}{2}\big[A - \Gamma(L)\big]\psi_s^2 + \frac{B}{4}\psi_s^4 - H\psi_s, \tag{5.28}$$

where a value $H > 0$ corresponds to a system that will charge positively. The form of this free energy, and how it differs to the 'zero-field' case ($H = 0$), is given in figure 5.8 for various values of γ. As the profiles show, by introducing the parameter $H > 0$, the free energy is reduced for the $\overline{\psi}_s > 0$ state, but increased for the $\overline{\psi}_s < 0$ state, hence stabilising the positive surface potential with respect to the negative one, making the negative state metastable. When $\gamma > 1$, the negative potential is no longer a stable state. As with the situation when $H = 0$, the surface charge still reduces as γ is increased.

Finally, the extra freedom that the two surface potentials need not be the same can be included into the system free energy as follows,

$$\mathcal{F}_{\text{Tot}}(\psi_1, \psi_2) = -\frac{A}{4}\big(\psi_1^2 + \psi_2^2\big) + \frac{B}{8}\big(\psi_1^4 + \psi_2^4\big) + \frac{1}{2}\Gamma(L)\psi_1\psi_2 - H\big(\psi_1 + \psi_2\big), \tag{5.29}$$

where the surface potential of surface 1 & 2 is $\psi_s(1) = \psi_1$ & $\psi_s(2) = \psi_2$ respectively. The parameters A & B are assumed to be identical for both surfaces, as these are descriptive of the surfaces in isolation and do not alter as they interact.

So following again from step 3, minimisation of the free energy gives the equilibrium values of the surface potentials $\overline{\psi}_1$ & $\overline{\psi}_2$,

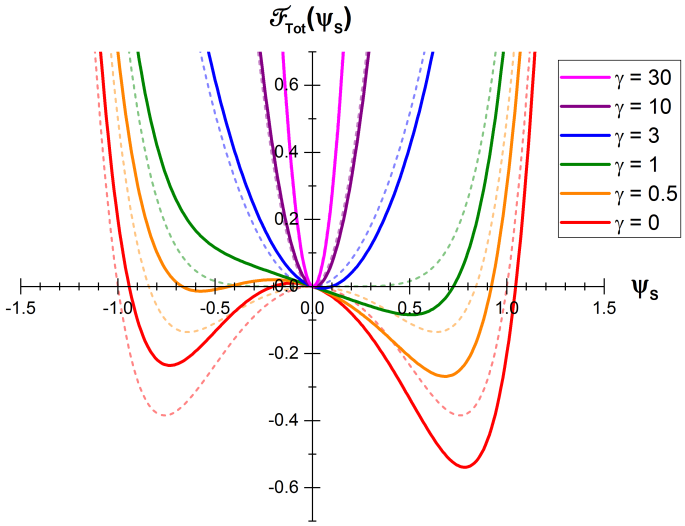

FIGURE 5.8: The free energy of the system following equation (5.29), with the magnitude of the additional 'external field' $H = 0.2$, and as in figure 5.2, $B = 4$ & $A = 2$ at a large and constant L. The dashed lines show the identical system but in the 'zero-field' case ($H = 0$) for comparison.

$$\begin{aligned} -\frac{A}{2}\overline{\psi}_1 + \frac{B}{2}\overline{\psi}_1^3 + \frac{1}{2}\Gamma(L)\overline{\psi}_2 &= H, \\ -\frac{A}{2}\overline{\psi}_2 + \frac{B}{2}\overline{\psi}_2^3 + \frac{1}{2}\Gamma(L)\overline{\psi}_1 &= H. \end{aligned} \tag{5.30}$$

Equating these then gives

$$\begin{aligned} (\overline{\psi}_1 + \overline{\psi}_2)\left[\Gamma(L) - A + B(\overline{\psi}_1^2 + \overline{\psi}_2^2 - \overline{\psi}_1\overline{\psi}_2)\right] &= 4H, \\ (\overline{\psi}_1 - \overline{\psi}_2)\left[-\Gamma(L) - A + B(\overline{\psi}_1^2 + \overline{\psi}_2^2 + \overline{\psi}_1\overline{\psi}_2)\right] &= 0. \end{aligned} \tag{5.31}$$

Of the nine possible values for $\overline{\psi}_1$ & $\overline{\psi}_2$, only two possibilities satisfy the stability criteria $\mathcal{F}''_{Tot}(\psi_1) > 0$ & $\mathcal{F}''_{Tot}(\psi_2) > 0$ and the additional criteria that the determinant,

$$\det\left(\frac{\partial^2 \mathcal{F}_{Tot}}{\partial\psi_1 \partial\psi_2}\right) > 0. \tag{5.32}$$

Solution when $H = 0$

Firstly, for the case when the free energy is symmetric in the surface potential ($H = 0$), the two possible solutions are that of a symmetric ($\overline{\psi}_1 = \overline{\psi}_2$) or anti-symmetric case ($\overline{\psi}_1 = -\overline{\psi}_2$). The symmetric result is the solution to the first part of equation (5.30) and is identical to the result from the initial one-parameter model. The anti-symmetric case is the solution to the second part of equation (5.30), and describes the spontaneous symmetry breaking discussed by Podgornik and coworkers to a

system with oppositely charged surfaces (69). Solving this second, anti-symmetric result, $\overline{\psi}_1 = -\overline{\psi}_2 = \overline{\psi}_{AS}$, then gives for the surface potential

$$\overline{\psi}_{AS} = 0, \tag{5.33a}$$

$$\overline{\psi}_{AS} = \pm\sqrt{\frac{A + \Gamma(L)}{B}}, \tag{5.33b}$$

so the separation dependence then becomes

$$\overline{\psi}_{AS} = \pm\psi_\infty\sqrt{1 + \gamma\exp(-\kappa L)}. \tag{5.34}$$

The difference in the free energy between the symmetric $\mathcal{F}_S$ and anti-symmetric $\mathcal{F}_{AS}$ states is then (by inputting equations (5.13b), (5.33b) into equations (5.9), (5.29) respectively)

$$\mathcal{F}_S = -\frac{(A - \Gamma(L))^2}{4B}, \tag{5.35a}$$

$$\mathcal{F}_{AS} = -\frac{(A + \Gamma(L))^2}{4B}, \tag{5.35b}$$

so clearly the anti-symmetric state is always at a lower free energy than the symmetric state (apart from at $L \to \infty$ where they are degenerate), and the difference becomes larger at smaller L. The system therefore undergoes a second order transition from the symmetric to anti-symmetric case (466). As already explained, for our system the surfaces both remain positively charged when interacting, hence the repulsion measured with BOT for $\kappa_D h > 2$. As such, the solution when $H > 0$ is more applicable, where the symmetric state is stabilised over the anti-symmetric state at finite surface separations (see figure 5.8).

Solution when $H \neq 0$

Solving the equations in (5.31) when $H \neq 0$ is fairly involved, and as such, the reader is referred to the literature that outlines the derivations for such a case (466, 481). What is derived by Kornyshev et al. is a system that remains symmetric ($\overline{\psi}_1 = \overline{\psi}_2$) at large surface separations, then as the separation is reduced, there is a spontaneous symmetry breaking in the system resulting in surfaces of different surface potentials ($\overline{\psi}_1 \neq \overline{\psi}_2$). The transition between these states is shown by Kornyshev et al. to be either first or second order, depending on the system parameters A, B, $\Gamma(L)$ and H (466).

To determine the exact regimes where the symmetric or non-symmetric states are stable, the free energy in equation (5.29) can be rearranged in order to directly compare it to the solutions derived by Kornyshev et al. (466). This can be done by reducing the surface potential such that $\widetilde{\psi}_1 = 1$ as $L \to \infty$, i.e. $\widetilde{\psi}_1 = \sqrt{B/A}\,\psi_1$ (from eq. (5.13b)). Then, the scaled free energy becomes

$$\widetilde{\mathcal{F}}_{\text{Tot}}(\widetilde{\psi}_1,\widetilde{\psi}_2) = -\left(\widetilde{\psi}_1^2+\widetilde{\psi}_2^2\right)+\frac{1}{2}\left(\widetilde{\psi}_1^4+\widetilde{\psi}_2^4\right)+\widetilde{\Gamma}(L)\widetilde{\psi}_1\widetilde{\psi}_2-\widetilde{H}\left(\widetilde{\psi}_1+\widetilde{\psi}_2\right), \tag{5.36}$$

where the scaled parameters that now define the free energy are

$$\widetilde{\mathcal{F}}_{\text{Tot}}(\widetilde{\psi}_1,\widetilde{\psi}_2) = \frac{4B}{A^2}\mathcal{F}_{\text{Tot}}(\psi_1,\psi_2), \tag{5.37a}$$

$$\widetilde{\Gamma} = \frac{2\Gamma(L)}{A}, \tag{5.37b}$$

$$\widetilde{H} = \frac{4HB^{1/2}}{A^{3/2}}. \tag{5.37c}$$

These parameters are then directly comparable to parameters used by Kornyshev et al. (*466*), and therefore the regions of stability of the symmetric and non-symmetric phases can be determined in our notation. Before discussing the phase boundaries of the different possibilities for ψ_1 & ψ_2, it is important to note that in our system, we have assumed that $\Gamma(L) > 0$, $A > 0$ & $H > 0$, and as such, the second order transition predicted by Kornyshev et al. when $\widetilde{\Gamma} < -1.5$ is not accessible (*466*). As such, only the first order transition is accessible, and this is given by Kornyshev et al. to be when

$$\widetilde{H}_\star = \frac{2^{3/2}\sqrt{\left(\widetilde{\Gamma}+1\right)\left(\cosh(\kappa L)-1\right)}\left(2\widetilde{\Gamma}\cosh(\kappa L)+1\right)}{\left(2\cosh(\kappa L)-1\right)^{3/2}}, \tag{5.38}$$

where the $\star$ denotes the location of the first order transition between the system having a stable symmetric (S) state to having a stable non-symmetric (NS) state. Because the boundary is of first order, it is accompanied by a region either side of it where metastable S or NS states also exist. Again, the boundaries containing these phases are given by Kornyshev et al. to be (*466*)

$$\widetilde{H}_{\text{S}} = \frac{4}{3\sqrt{3}}\left(2\widetilde{\Gamma}-1\right)\sqrt{\widetilde{\Gamma}+1}, \tag{5.39a}$$

$$\widetilde{H}_{\text{NS}} = \frac{4}{3\sqrt{3}}\left(2\widetilde{\Gamma}+1\right)^{3/2}. \tag{5.39b}$$

These three boundaries lead to the phase diagram in figure 5.9. In Kornyshev et al.'s case, they set the value of H in their phase diagrams, in our case, we have set the value of $\kappa L = 3$ instead, in order to define the first order transition in equation (5.38). The phase diagram, defined by the values $(\widetilde{H},\widetilde{\Gamma})$, shows the regions where the symmetric state (shaded blue) or non-symmetric state (shaded red) is stable. Due to the additional freedoms within this two-parameter model, the behaviour of the system can now be described at all surface separations, even below the critical separation L_c defined in the one-parameter model.

What the phase diagram in figure 5.9 depicts, is that for a given value of $\widetilde{H}$ & $\widetilde{\Gamma}$, the potentials of two interacting surfaces decrease *symmetrically* as the surfaces are

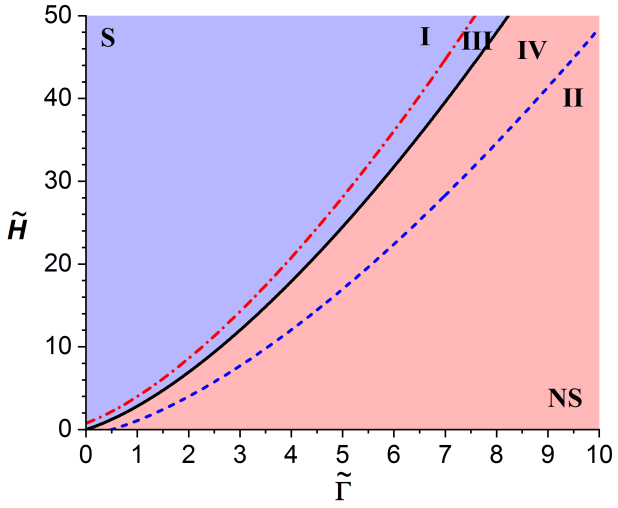

FIGURE 5.9: The phase diagram showing the regions of stability for the symmetric (S, shaded blue) and non-symmetric (NS, shaded red) states, separated by the first order phase boundary (black solid line (eq. (5.38))). The four different regions (I-IV) bounded by the red dash-dotted line $\widetilde{H}_{\text{NS}}$ (eq. (5.39b)) and the blue dashed line $\widetilde{H}_{\text{S}}$ (eq. (5.39a)), show I: stable S & unstable NS; II: unstable S & stable NS; III: stable S & metastable NS; IV: metastable S & stable NS.

pushed closer together (increasing $\widetilde{\Gamma}$). Once the system reaches the red dash-dotted line, the system remains symmetric at equilibrium, but a metastable state arises where the surfaces may obtain different potentials. As the surfaces are pushed even closer, the system reaches the first order transition boundary where the symmetry of the system is spontaneously broken. At this transition, the equilibrium state for the system spontaneously becomes the non-symmetric state. The symmetric state remains metastable at this point, however, only becoming fully unstable when the surfaces are pushed closer together and the blue dashed line is reached.

This spontaneous symmetry breaking at this transition point can therefore be triggered if either the separation is decreased or if γ is increased (larger $\widetilde{\Gamma}$), or if the 'external field' strength is decreased (reduced $\widetilde{H}$). By following the line where $\widetilde{H} = 0$, the phase diagram shows the 'zero-field' case, where the S phase is only stable at infinite separation ($\widetilde{\Gamma} = 0$), and only metastable below $\widetilde{\Gamma} \approx 0.5$, at all other times, only the anti-symmetric state is stable. By increasing the magnitude of the 'external field' term, the S phase is clearly stabilised to smaller surface separations. This two-parameter model also indicates the limits of the one-parameter model used earlier. Due to the assumption that the symmetric phase is the only possible state for the system, metastable or stable non-symmetric states are clearly never predicted, and as such, the model could only describe the system above the first order transition line. This two-parameter model allows for the system to be defined under a wider variety of conditions, which is necessary in order to explain the origin of attraction between these same particles that dominates the interaction at closer separations.

5.3.2 Like-Charge Attraction

What Kornyshev et al. also go on to discuss is the force between the two surfaces in the different phases I-IV (*466*). Due to the breaking of the symmetry of the system, the first order transition curve in equation (5.38) also defines the boundary between when the two surfaces interact repulsively or attractively. The origin of this attraction is due to the dissimilarity of the two surfaces. The attraction caused by non-symmetric surfaces was discussed in section 1.1.5, where the electrostatic interaction was plotted using different boundary conditions. When any asymmetry was introduced into the surface potentials of the system, the predictions from reference (*60*) always showed attractions at small surface separations. These plots were of course not made under CR boundary conditions, which is what this model utilises, but it does highlight that attractions arise when the symmetry of the electrostatic interaction is disrupted. By considering the charge regulation of a spherical surface instead, Maggs & Podgornik show that the charge regulation results in heterogeneous charge distributions across the surface, resulting in two dipolar particles at close separation which are anti-aligned (*68*). By combining this prediction with the predictions of a spontaneous symmetry breaking of the system (*69*), results in the two anti-aligned dipolar particles spontaneously aligning during their interaction, and therefore attracting. The boundary between repulsion and attraction for our system occurs at surface separations smaller than what is accessible with the BOT technique ($\kappa_D h > 2$). This is why an attraction was never measured in the BOT force profiles, despite clearly being present to form the aggregates in those systems. Again, this strengthens the necessity for a value $H > 0$ to describe our system, as this stabilises the symmetric state and hence the interaction remains repulsive for $\kappa_D h > 2$.

A diagram of the possible charge distributions of two interacting particles is given in figure 5.10. Initially, the interaction causes a decrease in the charge of the two surfaces facing each other symmetrically, such that their dipole moments oppose. When the surfaces are pushed closer together, the symmetry of the interaction is spontaneously broken as the charge densities on the opposing hemispheres become different. Because the symmetry is broken, the charge can redistribute across the two surfaces in order to align their dipole moments as this is a lower energy configuration for the interaction. If further particles interact with the chain, they will also show the same charge redistribution resulting in an aligned dipole moment with the rest of the chain.

This model has therefore firstly explained the unexpected deviation from DLVO theory in the measured repulsions by describing the surfaces as being charge regulated, and as a consequence, provided a possible origin of attraction between the same particles at small separations.

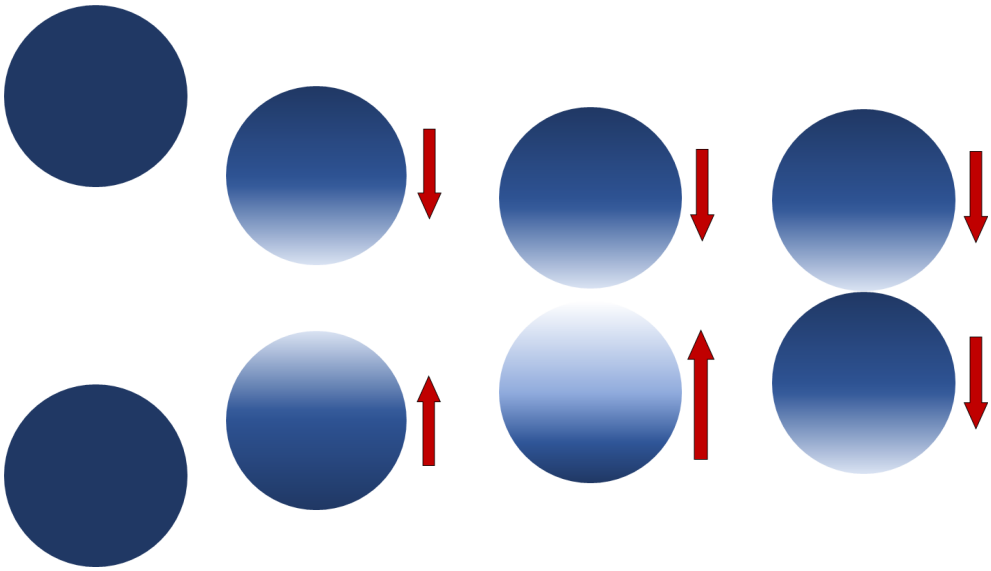

(a) Charge symmetry (b) Anti-aligned dipoles induced (c) Spontaneous symmetry breaking (d) Aligned dipoles

FIGURE 5.10: A diagram showing the modification of the distribution of surface charges on the opposing surfaces of two interacting particles. The dark blue regions indicate postive charge density, and the white indicates regions where the surface is discharged. The direction of the resulting dipole moment of each particle is indicated to their right. The surface separation is decreased from figure (a)-(d).

5.4 Conclusion

This final chapter has derived a model that can describe the charge regulation of two interacting surfaces. To do so, a Landau model was used to define the free energy of the surface, in which different parameters can be modified to cause a change in the surface charge density of the two surfaces. By initially simplifying the model to account for a symmetric interaction only between two identical surfaces, both the ionic strength and the surface separation are shown to reduce the charge of the two surfaces. As a result, the measured force between the two surfaces is shown to have an increasingly weaker interaction from that expected from DLVO theory (constant charge surfaces) with decreasing surface separation. As a result, the fitted decay lengths of these force profiles were found to increase with the ionic strength of the systems, due to the increased electrostatic interaction. As a result, the model predicts qualitatively the experimentally measured inflated screening length above the DH length, and the reduced particle charge as a function of the electrolyte concentration above c^*_{salt} presented in chapter 3 (figure 5.7).

This model however was found to have limits on its validity due to the assumption made that the surfaces remain identical at all separations. To allow the surfaces more freedom, this constraint was then removed to show how the charge of the surfaces adapt beyond the limits of the one-parameter model. With this additional freedom, the two-parameter model shows how, at a specific surface

separation, the system undergoes a spontaneous symmetry breaking, resulting in the two surfaces acquiring different charge densities when they are close together. The model was then extended to charge regulating particles, where just the sections of the surface facing each other charge regulate. As a result, two interacting particles become dipolar, and if the symmetry is maintained, then these dipoles remain anti-aligned and repulsive. If however there is a spontaneous symmetry breaking, then the dipolar particles can align and therefore attract. The presence of aligned dipole moments along the chains of particles in the samples was evidenced by observing their orientation with an applied electric field.

The model describing the charge regulation of two interacting particles outlined here has simultaneously explained two observations made in this simple, nonpolar colloidal system that deviated from that expected in DLVO theory. The first was the unexpected slow decay of the repulsive force at higher electrolyte concentrations, qualitatively explained by the decrease in the charge of the interacting surfaces. The second was the presence of a short range attraction between these particles which resulted in aggregates with a dipole moment. The charge regulation of two particle surfaces has been shown to result in dipolar particles forming, however in order for the dipoles to align, and thus attract, the symmetry must spontaneously break during the interaction, predicted to occur when the model is allowed the freedoms expected for a real, experimental system.

Chapter 6

Conclusions

This thesis has presented an investigation of the interactions between particles in suspension. To do so, optical traps were used to directly measure the force between pairs of electrically charged PMMA particles in dodecane. To fully probe the electrostatic interactions in this system, the force was measured over a range of ionic strengths by adding a hydrophobic electrolyte at concentrations up to 1 mM. The force profiles measured were compared with the expected interaction according to the classical DLVO theory of colloid stability. The repulsive interactions measured were found to agree with DLVO theory at the lowest electrolyte concentrations studied. However, above 450 μM, the repulsive force did not follow the expected Yukawa force profile, but began to decay more slowly than expected, resulting in a nonmonotonic trend of the decay length with the electrolyte concentration. The ionic strength of the solutions was determined by measuring the conductivity of the suspensions, from which the classical DH length could be calculated, which was found to have the expected monotonic decrease with electrolyte concentration. Within DLVO theory, the decay length of the particle interactions should equate with the DH length, but above 450 μM, these values clearly disagreed.

A second unexpected observation was made with the same system, over the same range of electrolyte concentrations. Despite the steric stability inferred to the particles from a PHSA brush layer on their surfaces, which should prevent any attractions due to vdW interactions, attractions were present between the like-charged particles. Such an attraction was observed by the presence of aggregates in the solutions, with dumbbells forming upon addition of just 40 μM electrolyte, and massive aggregates containing 100s particles forming at 650 μM. The increased size of the aggregates with electrolyte concentration shows the increasing dominance of the attraction present over the electrostatic repulsion due to charge screening. Upon inspection, the cluster shapes that formed in these samples suggested that the particles were no longer homogeneously charged across their surfaces. The prevalence of linear chains and the absence of three-dimensional structures such as tetrahedrons directly suggests that the particles have some dipolar nature once bound to another particle, suggesting that the charge density across the particles redistributes. To investigate this idea, an electric field was applied across a sample containing a chain of particles. This chain was tethered using an optical trap such

that it could freely rotate, but not translate. Once the field was applied, the chain was observed to rotate such that it orientated with the electric field direction. This presented direct evidence that chains of aggregated particles had a dipole moment, as no torque would be applied to a chain of homogeneously charged, or uncharged, particles.

Considering both these major observations, it was clear that the interaction between these particles is repulsive at large separations but attractive at short separations, and that the origin of the attraction is the alignment of the dipole moments of each particle. This directly suggests that during their interaction, the surface charge must firstly redistribute to account for the formation of dipolar particles, and secondly the symmetry must be broken to result in aligned dipoles. For the surface charge to adapt in this way, their interaction must be considered with charge regulation boundary conditions, rather than maintaining a constant charge as assumed in DLVO theory.

The final chapter of this investigation derived a theoretical framework to explain how such a charge redistribution can occur as the surface separation is reduced between the particles. The model utilises a Landau model to describe the charge regulation of two interacting surfaces, specifically how the charge density reduces with the surface separation. The result of this on the measured force profiles shows how the fitted decay length becomes larger than the DH length above a critical ionic strength and at small surface separations, thus qualitatively explaining the experimental data. If this model is applied to particles rather than flat plates, then the charge regulation occurs only on the two surfaces facing each other, thus forming a dipolar charge distribution across the two particles. During a symmetric interaction, where both surfaces are assumed to always have the same charge density, the dipolar particles remain anti-aligned and therefore do not attract. To explain the dipolar particle chains observed in the system, the dipolar particles must end up aligned, and thus the symmetry of the system must be broken. By adding a freedom to the surfaces to adopt different charge densities, the model was shown to predict a spontaneous symmetry breaking during the interaction, which results in different charge densities on the two interacting surfaces. This directly infers that the charge redistribution across both particles can result in aligned dipolar particles, thus accounting for the attraction, and the dipole moment across the chain of particles. This model therefore qualitatively explains the interaction between two charged particles at all separations, accounting for the long range repulsion, the inflated measured decay length of the repulsion at high electrolyte concentrations, and the formation of aggregates with a dipole moment.

The results presented in this thesis thus highlights the importance of the surface of particles when investigating electrostatic interactions. Previously this was not taken into account in systems that remain within the weak coupling limit where the classical theories are expected to hold true, especially when the interactions are measured at large surface separations due to a nonpolar environment. This

investigation of the electrostatics in colloidal suspensions is therefore mutually beneficial towards both the understanding of electrostatics, and in the possibility of improving colloidal formulations.

Appendix A

Grahame Equation: A Derivation

By multiplying both sides of the PB equation (eq. 1.6 in one-dimension) by a factor $2\,\mathrm{d}\psi/\mathrm{d}x$:

$$2\frac{\mathrm{d}\psi}{\mathrm{d}x}\,\frac{\mathrm{d}^2\psi}{\mathrm{d}x^2} = 2\frac{\mathrm{d}\psi}{\mathrm{d}x}\,\frac{zen_{\mathrm{ion}}}{\varepsilon_r\varepsilon_0}\sinh\left(\beta ze\psi\right) \tag{A.1}$$

Then using the identity $y'^2 = 2\int y'y''$ and integrating both sides:

$$\left(\frac{\mathrm{d}\psi}{\mathrm{d}x}\right)^2 = \int 2\frac{\rho_{\mathrm{ion}}}{2\varepsilon_r\varepsilon_0}\left[\sinh\left(\beta ze\psi\right)\right]\,\frac{\mathrm{d}\psi}{\mathrm{d}x}\,\mathrm{d}x \tag{A.2}$$

Then applying the boundary conditions for integration that as $x \to \infty$, $\psi \to 0$ & $\mathrm{d}\psi/\mathrm{d}x \to 0$, this gives the result:

$$\left(\frac{\mathrm{d}\psi}{\mathrm{d}x}\right)^2 = \frac{\rho_{\mathrm{ion}}}{\varepsilon_r\varepsilon_0\beta ze}\left[2\cosh\left(\beta ze\psi\right) - 2\right] \tag{A.3}$$

With the term in the brackets being $4\left[\sinh\left(\beta ze\psi/2\right)\right]^2$ we arrive at:

$$\frac{\mathrm{d}\psi}{\mathrm{d}x} = -\sqrt{\frac{4\rho_{\mathrm{ion}}}{\varepsilon_r\varepsilon_0\beta ze}}\sinh\left(\beta ze\psi/2\right) \tag{A.4}$$

Appendix B

Gouy-Chapman Theory: A Derivation

Following on from the derivation of the Grahame equation in appendix A by taking all functions of ψ to the left and those in x to the right of equation A.4

$$\int \operatorname{csch}\left(\frac{\beta z e \psi}{2}\right) \mathrm{d}\psi = -\int \sqrt{\frac{4\rho_{\text{ion}}}{\varepsilon_r \varepsilon_0 \beta z e}}\, \mathrm{d}x \tag{B.1}$$

Using the identity that $\int \operatorname{csch}(x) = \ln|\tanh(x/2)| + constant$ gives for the form of the potential from a charged surface, where the integration constant is taken from assuming the value $\psi(x=0) = \psi_s$:

$$\frac{2}{\beta z e} \ln\left|\tanh\left(\frac{\beta z e \psi}{4}\right)\right| - \frac{2}{\beta z e} \ln\left|\tanh\left(\frac{\beta z e \psi_s}{4}\right)\right| = -\sqrt{\frac{4\rho_{\text{ion}}}{\varepsilon_r \varepsilon_0 \beta z e}}\, x \tag{B.2}$$

Which can be simplified to:

$$Y = Y_s \exp(-\kappa x) \tag{B.3}$$

Where $Y = \tanh(\beta z e \psi/4)$ & $Y_s = \tanh(\beta z e \psi_s/4)$. So as is now apparent, for small surface potentials, this reduces to the form of the DH result (eq. (1.17)) with $\kappa = \kappa_D = \sqrt{\beta z e^2 n_{\text{ion}}/\varepsilon_r \varepsilon_0} = \sqrt{4\pi \ell_B n_{\text{ion}}}$, as $Y \to \psi$. This result also gives an indication for the form at large x ($\psi \to (4/\beta z e) Y_s \exp(-\kappa_D x)$), and high ψ_s ($\psi \to (4/\beta z e)\exp(-\kappa_D x)$) as $\tanh(x \to \infty) \to 1$.

Appendix C

R-Squared Fit Statistic: A Definition

If a data set has n values denoted as y_i with $i = 1, ..., n$, then its mean is $\bar{y} = \sum_{i=1}^{n} y_i \ / n$. The *residual* is defined as $e_i = y_i - f_i$ where f_i is the value predicted by the fitted function or model. So the following sums of squares (SOS) describe the statistics:

$$\text{variance (total SOS)} = SS_{\text{tot}} = \sum_{i=1}^{n} \left(y_i - \bar{y}\right)^2$$

$$\text{regression SOS} = SS_{\text{reg}} = \sum_{i=1}^{n} \left(f_i - \bar{y}\right)^2 \tag{C.1}$$

$$\text{residual SOS} = SS_{\text{res}} = \sum_{i=1}^{n} \left(y_i - f_i\right)^2 = \sum_{i=1}^{n} e_i^2$$

If $SS_{\text{res}} + SS_{\text{reg}} = SS_{\text{tot}}$, then the coefficient of determination, also known as "*R squared*", is defined as the fraction of variance unexplained, i.e. the comparison of the variance in the model's error (SS_{res}) with the total variance of the data (SS_{tot}):

$$R^2 = 1 - \frac{SS_{\text{res}}}{SS_{\text{tot}}} \tag{C.2}$$

The "*adjusted r squared*" R^2_{adj} value is often used instead of just R^2 because it allows for comparison between two models with different degrees of freedom (or variables or predictors). This is because R^2 will always increase when you add more variables in the model, even if those variables are unused or useless, whereas R^2_{adj} will not, and will only improve if useful variables are added to the model. R^2_{adj} is defined as follows and includes the number of data points n and the number of explanatory (useful) variables p:

$$R^2_{\text{adj}} = 1 - \frac{SS_{\text{res}}}{SS_{\text{tot}}} \frac{n-1}{n-p-1} \tag{C.3}$$

Appendix D

Results for AC11 and IM6

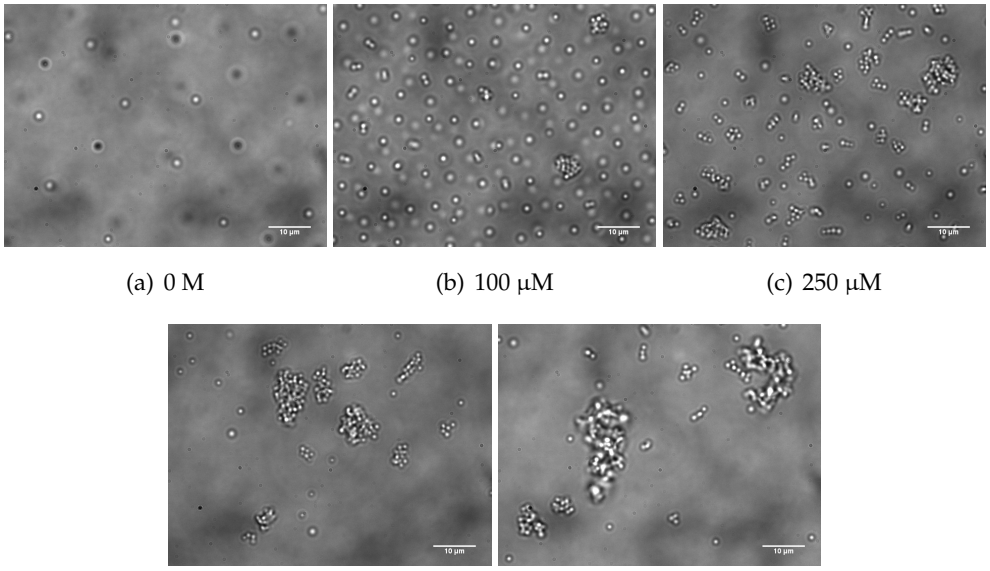

(a) 0 M (b) 100 μM (c) 250 μM

(d) 400 μM (e) 550 μM

FIGURE D.1: Optical microscopy images of AC11 particles in dodecane at a range of electrolyte concentrations. Aggregates were found to form upon addition of electrolyte as with AC12, with the size of the aggregates increasing with increasing ionic strength.

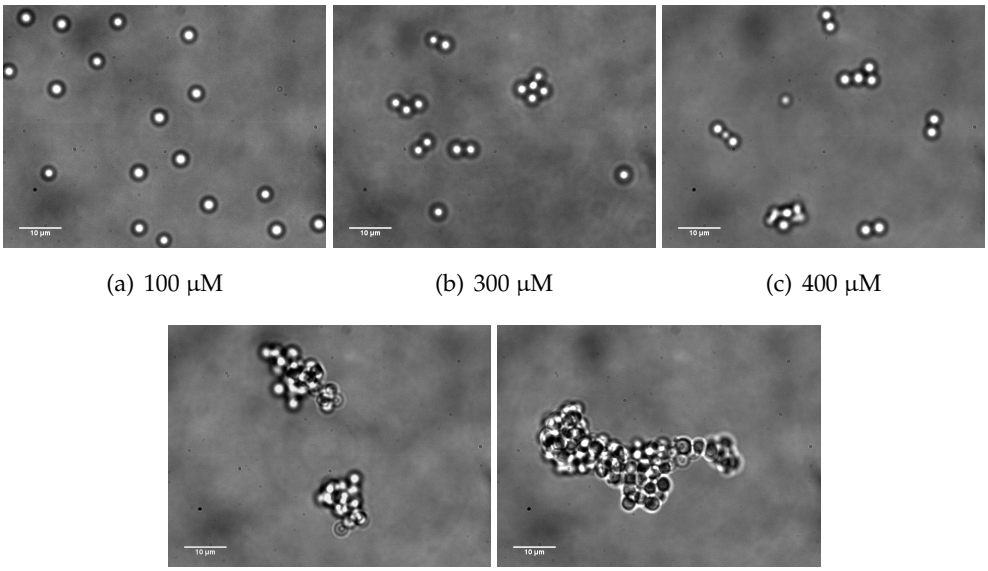

(a) 100 µM (b) 300 µM (c) 400 µM

(d) 600 µM (e) 700 µM

FIGURE D.2: Optical microscopy images of IM6 particles in dodecane at a range of electrolyte concentrations. Aggregates were found to form upon addition of electrolyte as with AC12 & AC11, with the size of the aggregates increasing with increasing ionic strength.

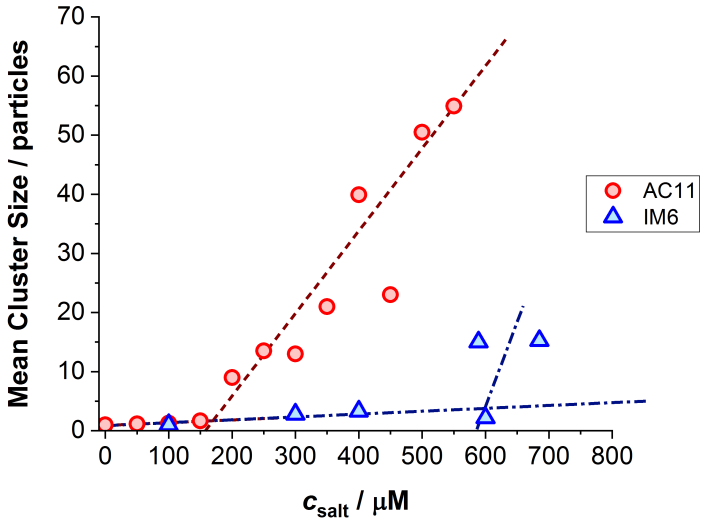

FIGURE D.3: The mean cluster size for the different particles AC11, AC12 and IM6 as a function of c_{salt}. The lines added to the plots helped to determine the critical aggregation concentration (CAC) for the two different dispersions from their intersection. So for AC11, CAC=175 $\pm$ 25, and for IM6, CAC=600 $\pm$ 50. The errors in these are estimated from the range in where the overlaid lines could be positioned through the two data sets.

Bibliography

1. J. A. Bittencourt, *Fundamentals of Plasma Physics* (Springer, New York, 3rd ed. 2004 edition, 2004).
2. R. D. Wells, J. E. Larson, R. C. Grant, B. E. Shortle, C. R. Cantor, *Journal of Molecular Biology* **54**, 465–497 (1970).
3. D. S. Dean, J. Dobnikar, A. Naji, R. Podgornik, *Electrostatics of Soft and Disordered Matter* (CRC Press, 2014).
4. J. Li, S. S. Wijeratne, X. Qiu, C.-H. Kiang, *Nanomaterials* **5**, 246–267 (2015).
5. E. H. Erickson, *Journal of Apicultural Research* **14**, 141–147 (1975).
6. M. E. Colin, D. Richard, S. Chauzy, *Journal of Bioelectricity* **10**, 17–32 (1991).
7. Y. Vaknin, S. Gan-Mor, A. Bechar, B. Ronen, D. Eisikowitch, in *Pollen and Pollination*, ed. by A. Dafni, M. Hesse, E. Pacini (Springer Vienna, Vienna, 2000), pp. 133–142.
8. H. Dettling *et al.*, pat., US4649703A (1987).
9. Y.-S. Song, pat., US6010550A (2000).
10. C. I. Calle *et al.*, *Proc. ESA Annual Meeting on Electrostatics.* 14 (2008).
11. J. L. Anderson, D. W. Armstrong, G.-T. Wei, *Ionic Liquids in Analytical Chemistry*, 2892–2902 (2006).
12. P. Wasserscheid, T. Welton, *Ionic Liquids in Synthesis* (John Wiley & Sons, 2008).
13. P. Walden, *Bull. Acad. Imper. Sci. (St. Petersburg)* **1800** (1914).
14. M. Freemantle, *Chemical Engineering News* **76**, 32–37 (1998).
15. M. Freemantle, *An Introduction to Ionic Liquids* (Royal Society of Chemistry, 2010).
16. K. R. Seddon, *Journal of Chemical Technology & Biotechnology* **68**, 351–356 (1997).
17. T. Welton, *Chemical Reviews* **99**, 2071–2084 (1999).
18. J. G. Huddleston, H. D. Willauer, R. P. Swatloski, A. E. Visser, R. D. Rogers, *Chemical Communications* **0**, 1765–1766 (1998).
19. M. L. Dietz, *Separation Science and Technology* **41**, 2047–2063 (2006).
20. E. D. Bates, R. D. Mayton, I. Ntai, J. H. Davis, *Journal of the American Chemical Society* **124**, 926–927 (2002).
21. M. Hasib-ur Rahman, M. Siaj, F. Larachi, *Chemical Engineering and Processing: Process Intensification* **49**, 313–322 (2010).
22. D. Camper, J. E. Bara, D. L. Gin, R. D. Noble, *Industrial & Engineering Chemistry Research* **47**, 8496–8498 (2008).
23. J. Dupont, R. F. de Souza, P. A. Z. Suarez, *Chemical Reviews* **102**, 3667–3692 (2002).
24. J. R. Miller, P. Simon, *Science* **321**, 651–652 (2008).

25. P. Simon, Y. Gogotsi, B. Dunn, *Science* **343**, 1210–1211 (2014).

26. G. Hussain, A. Robinson, P. Bartlett, *Langmuir* **29**, 4204–4213 (2013).

27. M. Eigen, E. Wicke, *The Journal of Physical Chemistry* **58**, 702–714 (1954).

28. E. E. Havinga, *Journal of Physics and Chemistry of Solids* **18**, 253–255 (1961).

29. A. J. Bosman, E. E. Havinga, *Physical Review* **129**, 1593–1600 (1963).

30. A. Andryieuski, S. M. Kuznetsova, S. V. Zhukovsky, Y. S. Kivshar, A. V. Lavrinenko, *Scientific Reports* **5**, 13535 (2015).

31. V. G. Artemov, A. A. Volkov, *Ferroelectrics* **466**, 158–165 (2014).

32. R. N. Kumar, C. P. G. Vallabhan, *Journal of Physics: Condensed Matter* **1**, 6095 (1989).

33. Peter Debye, Erich Hückel, *Physikalische Zeitschrift* **24**, 185–206 (1923).

34. N. Jonassen, *Electrostatics* (Springer Science & Business Media, 2002).

35. N. Davidson, *Statistical Mechanics* (McGraw-Hill, 1962).

36. D. A. McQuarrie, *Statistical Mechanics* (University Science Books, 2000).

37. Y. Levin, *Brazilian Journal of Physics* **34**, 1158–1176 (2004).

38. C. P. Royall, M. E. Leunissen, A. v. Blaaderen, *Journal of Physics: Condensed Matter* **15**, S3581 (2003).

39. H. Wennerström, presented at the Surface Forces and Surfactant Systems, pp. 31–37.

40. A. C. Cowley, N. L. Fuller, R. P. Rand, V. A. Parsegian, *Biochemistry* **17**, 3163–3168 (1978).

41. S. Engström, H. Wennerström, *The Journal of Physical Chemistry* **82**, 2711–2714 (1978).

42. B. Jönsson, H. Wennerstroem, B. Halle, *The Journal of Physical Chemistry* **84**, 2179–2185 (1980).

43. D. Andelman, in *Handbook of Biological Physics*, ed. by R. Lipowsky, E. Sackmann (North-Holland, 1995), vol. 1, pp. 603–642.

44. A. Delville, P. Laszlo, *Langmuir* **6**, 1289–1294 (1990).

45. A. Delville, *Langmuir* **7**, 547–555 (1991).

46. E. S. Boek, P. V. Coveney, N. T. Skipper, *Journal of the American Chemical Society* **117**, 12608–12617 (1995).

47. W. H. Briscoe, R. G. Horn, *Langmuir* **18**, 3945–3956 (2002).

48. G. Kokot, M. I. Bespalova, M. Krishnan, *The Journal of Chemical Physics* **145**, 194701 (2016).

49. D. J. Evans, A. D. Hollingsworth, D. G. Grier, *Physical Review E* **93**, 042612 (2016).

50. M. F. Hsu, E. R. Dufresne, D. A. Weitz, *Langmuir* **21**, 4881–4887 (2005).

51. G. S. Roberts, R. Sanchez, R. Kemp, T. Wood, P. Bartlett, *Langmuir* **24**, 6530–6541 (2008).

52. Q. Guo, J. Lee, V. Singh, S. H. Behrens, *Journal of Colloid and Interface Science* **392**, 83–89 (2013).

53. J. Lee, Z.-L. Zhou, G. Alas, S. H. Behrens, *Langmuir* **31**, 11989–11999 (2015).

54. T. Markovich, D. Andelman, R. Podgornik, *arXiv:1603.09451* (2016).

55. H. Von Helmholtz, *Annalen der Physik* **7**, 337–382 (1879).

56. M Gouy, *Journal of Theoretical and Applied Physics* **9**, 457–468 (1910).

57. Chapman, D. L., *The London, Edinburgh, and Dublin philosophical magazine and journal of science* **25**, 475–481 (1913).

58. O. Stern, *Zeitschrift für Elektrochemie* **30**, 1014–1020 (1924).

59. T. Markovich, D. Andelman, R. Podgornik, *Europhysics Letters* **113**, 26004 (2016).

60. D. Ben-Yaakov, D. Andelman, *Physica A: Statistical Mechanics and its Applications*, Statistical, Fluid and Biological Physics ProblemsAn MIT Symposium and Articles dedicated to A. Nihat Berker on his 60th Birthday **389**, 2956–2961 (2010).

61. B. W. Ninham, V. A. Parsegian, *Journal of Theoretical Biology* **31**, 405–428 (1971).

62. D. Chan, J. W. Perram, L. R. White, T. W. Healy, *Journal of the Chemical Society, Faraday Transactions 1: Physical Chemistry in Condensed Phases* **71**, 1046–1057 (1975).

63. S. H. Behrens, D. G. Grier, *The Journal of Chemical Physics* **115**, 6716–6721 (2001).

64. R. R. Netz, *Journal of Physics: Condensed Matter* **15**, S239–S244 (2002).

65. M. Lund, B. Jönsson, *Biochemistry* **44**, 5722–5727 (2005).

66. M. Lund, T. Akesson, B. Jönsson, *Langmuir* **21**, 8385–8388 (2005).

67. G. Trefalt, S. H. Behrens, M. Borkovec, *Langmuir* **32**, 380–400 (2016).

68. A. C. Maggs, R. Podgornik, *Europhysics Letters* **108**, 68003 (2014).

69. A. Majee, M. Bier, R. Podgornik, *Soft Matter* **14**, 985–991 (2018).

70. T. Graham, *Philosophical Transactions of the Royal Society of London* **151**, 183–224 (1861).

71. B. W. Ninham, *Advances in Colloid and Interface Science* **83**, 1–17 (1999).

72. *Michael Faraday's Gold Colloids at The Royal Institute, London*.

73. B Derjaguin, L Landau, *Acta Physicochim. (USSR)* **14**, 633 (1941).

74. E. J. W. Verwey, J. T. G. Overbeek, *Theory of the Stability of Lyophobic Colloids* (Elsevier, Amsterdam, 1948).

75. D. Fennell Evans, Hakan Wennerström, *The Colloidal Domain: Where Physics, Chemistry, Biology, and Technology Meet* (Wiley-VCH, New York, 2nd, 1999).

76. M. Faraday, *Philosophical Transactions of the Royal Society of London* **147**, 145–181 (1857).

77. J. Tyndall, *Proceedings of the Royal Society of London* **17**, 223–233 (1869).

78. J. Rayleigh (1871).

79. G. Mie, *Annalen der Physik* **330**, 377–445 (1908).

80. R. Brown, *The Philosophical Magazine* **4**, 161–173 (1828).

81. A. Einstein, *Annalen der Physik* **324**, 371–381 (1906).

82. A. Fick, *Annalen der Physik* **170**, 59–86 (1855).

83. P. C. Hiemenz, R. Rajagopalan, R. Rajagopalan, *Principles of Colloid and Surface Chemistry, Revised and Expanded* (CRC Press, 1997).

84. G. K. Batchelor, J. T. Green, *Journal of Fluid Mechanics* **56**, 375–400 (1972).

85. G. K. Batchelor, *Journal of Fluid Mechanics* **74**, 1–29 (1976).

86. S. Levine, G. P. Dube., *Transactions of the Faraday Society* **35**, 1125–1140 (1939).

87. B. Derjaguin, *Kolloid-Zeitschrift* **69**, 155–164 (1934).

88. J. D. van der Waals, PhD thesis, Leiden, Netherlands, 1873.

89. H. B. G. Casimir, *Proceedings of the Koninklijke Nederlandse Akademie van Wetenschappen* **51**, 793 (1948).

90. B. C. Denardo, J. J. Puda, A. Larraza, *American Journal of Physics* **77**, 1095–1101 (2009).

91. S. L. Boersma, *American Journal of Physics* **64**, 539–541 (1996).

92. E. M. Lifshitz, *Journal of Experimental and Theoretical Physics (USSR)* **29**, 94 (1955).

93. I. E. Dzyaloshinskii, E. M. Lifshitz, L. P. Pitaevskii, *Soviet Physics Uspekhi* **4**, 153 (1961).

94. H. C. Hamaker, *Physica* **4**, 1058–1072 (1937).

95. F. L. Leite, C. C. Bueno, A. L. Da Róz, E. C. Ziemath, O. N. Oliveira, *International Journal of Molecular Sciences* **13**, 12773–12856 (2012).

96. S. Biggs, P. Mulvaney, *The Journal of Chemical Physics* **100**, 8501–8505 (1994).

97. A. Brossa, H. Freundlich, *Zeitschrift für Physikalische Chemie* **89**, 306–337 (1915).

98. R. A. Ruehrwein, D. W. Ward, *Soil Science* **73**, 485 (1952).

99. B. Vincent, *Advances in Colloid and Interface Science* **4**, 193–277 (1974).

100. D. H Napper, A Netschey, *Journal of Colloid and Interface Science* **37**, 528–535 (1971).

101. D. H Napper, *Journal of Colloid and Interface Science* **58**, 390–407 (1977).

102. P. de Gennes, *Macromolecules* **13**, 1075–1080 (1980).

103. P. G. de Gennes, *Advances in Colloid and Interface Science* **27**, 189–209 (1987).

104. S. Asakura, F. Oosawa, *The Journal of Chemical Physics* **22**, 1255–1256 (1954).

105. S. Asakura, F. Oosawa, *Journal of Polymer Science* **33**, 183–192 (1958).

106. H.-J. Butt, M. Kappl, *Surface and Interfacial Forces* (John Wiley & Sons, 2018).

107. J. C. Crocker, D. G. Grier, *Physical Review Letters* **73**, 352–355 (1994).

108. I. Rouzina, V. A. Bloomfield, *The Journal of Physical Chemistry* **100**, 9977–9989 (1996).

109. L. C. Gosule, J. A. Schellman, *Nature* **259**, 333–335 (1976).

110. R. W. Wilson, V. A. Bloomfield, *Biochemistry* **18**, 2192–2196 (1979).

111. J. Widom, R. L. Baldwin, *Journal of Molecular Biology* **144**, 431–453 (1980).

112. W. M. Gelbart, R. F. Bruinsma, P. A. Pincus, V. A. Parsegian, *Physics Today* **53**, 38 (2007).

113. A. Y. Grosberg, T. T. Nguyen, B. I. Shklovskii, *Reviews of Modern Physics* **74**, 329–345 (2002).

114. Y. Levin, *Reports on Progress in Physics* **65**, 1577 (2002).

115. A. G. Moreira, R. R. Netz, *Europhysics Letters* **52**, 705 (2000).

116. R. R. Netz, *The European Physical Journal E* **5**, 557–574 (2001).

117. A. Moreira, R. Netz, *The European Physical Journal E* **8**, 33–58 (2002).

118. A. Naji, S. Jungblut, A. G. Moreira, R. R. Netz, *Physica A: Statistical Mechanics and its Applications*, Physics Applied to Biological Systems **352**, 131–170 (2005).

119. H. Boroudjerdi *et al.*, *Physics Reports* **416**, 129–199 (2005).

120. R. Kjellander, S. Marcelja, R. M. Pashley, J. P. Quirk, *The Journal of Physical Chemistry* **92**, 6489–6492 (1988).

121. R. Kjellander, S. Marčelja, R. M. Pashley, J. P. Quirk, *The Journal of Chemical Physics* **92**, 4399 (1990).

122. J. P. Valleau, R. Ivkov, G. M. Torrie, *The Journal of Chemical Physics* **95**, 520–532 (1991).

123. H. Wennerstrom, A. Khan, B. Lindman, *Advances in Colloid and Interface Science* **34**, 433–449 (1991).

124. P. Kékicheff, S. Marčelja, T. J. Senden, V. E. Shubin, *The Journal of Chemical Physics* **99**, 6098–6113 (1993).

125. J. X. Tang, P. A. Janmey, *Journal of Biological Chemistry* **271**, 8556–8563 (1996).

126. A. P. Lyubartsev, J. X. Tang, P. A. Janmey, L. Nordenskiöld, *Physical Review Letters* **81**, 5465–5468 (1998).

127. P. Linse, V. Lobaskin, *Physical Review Letters* **83**, 4208–4211 (1999).

128. A. A. Kornyshev, S. Leikin, *Physical Review Letters* **82**, 4138–4141 (1999).

129. M. J. Stevens, *Physical Review Letters* **82**, 101–104 (1999).

130. J. Arenzon, J. Stilck, Y. Levin, *The European Physical Journal B - Condensed Matter and Complex Systems* **12**, 79–82 (1999).

131. V. Lobaskin, A. Lyubartsev, P. Linse, *Physical Review E* **63**, 020401 (2001).

132. K.-C. Lee, I. Borukhov, W. M. Gelbart, A. J. Liu, M. J. Stevens, *Physical Review Letters* **93**, 128101 (2004).

133. L. Dai, Y. Mu, L. Nordenskiöld, J. R. C. van der Maarel, *Physical Review Letters* **100**, 118301 (2008).

134. Y. S. Jho *et al.*, *Physical Review Letters* **101**, 188101 (2008).

135. L. Sjöström, T. Akesson, B. Jönsson, *Berichte der Bunsengesellschaft für physikalische Chemie* **100**, 889–893 (1996).

136. B. I. Shklovskii, *Physical Review E* **60**, 5802–5811 (1999).

137. T. T. Nguyen, A. Y. Grosberg, B. I. Shklovskii, *The Journal of Chemical Physics* **113**, 1110–1125 (2000).

138. T. T. Nguyen, A. Y. Grosberg, B. I. Shklovskii, *Physical Review Letters* **85**, 1568–1571 (2000).

139. K. Besteman, M. A. G. Zevenbergen, H. A. Heering, S. G. Lemay, *Physical Review Letters* **93**, 170802 (2004).

140. S. Pianegonda, M. C. Barbosa, Y. Levin, *Europhysics Letters* **71**, 831 (2005).

141. R. Kjellander, *Journal of Physics: Condensed Matter* **21**, 424101 (2009).

142. M. Miller, M. Chu, B. Lin, M. Meron, P. Dutta, *Langmuir* **32**, 73–77 (2016).

143. R. Messina, C. Holm, K. Kremer, *Physical Review Letters* **85**, 872–875 (2000).

144. E. Allahyarov, G. Gompper, H. Löwen, *Physical Review E* **69**, 041904 (2004).

145. D. A. J. Gillespie *et al.*, *Soft Matter* **10**, 566–577 (2014).

146. A. Naji, R. R. Netz, *The European Physical Journal E* **13**, 43–59 (2004).

147. C Wagner, *Zeitschrift für Physik* **25**, 474–477 (1924).

148. L. Onsager, N. N. T. Samaras, *The Journal of Chemical Physics* **2**, 528 (1934).

149. B. C. Garrett, *Science* **303**, 1146–1147 (2004).

150. A. Onuki, *The Journal of Chemical Physics* **128**, 224704 (2008).

151. Y. Levin, A. P. dos Santos, A. Diehl, *Physical Review Letters* **103**, 257802 (2009).

152. Y. Levin, *Physical Review Letters* **102**, 147803 (2009).

153. R. Wang, Z.-G. Wang, *The Journal of Chemical Physics* **139**, 124702 (2013).

154. T. Croxton, D. A. McQuarrie, G. N. Patey, G. M. Torrie, J. P. Valleau, *Canadian Journal of Chemistry* **59**, 1998–2003 (1981).

155. G. M. Torrie, J. P. Valleau, *The Journal of Chemical Physics* **73**, 5807 (1980).

156. G. M. Torrie, J. P. Valleau, G. N. Patey, *The Journal of Chemical Physics* **76**, 4615 (1982).

157. Z. Zhang, S. C. Glotzer, *Nano Letters* **4**, 1407–1413 (2004).

158. C. De Michele, S. Gabrielli, P. Tartaglia, F. Sciortino, *The Journal of Physical Chemistry B* **110**, 8064–8079 (2006).

159. A. van Blaaderen, *Nature* **439**, 545–546 (2006).

160. P. Attard, *The Journal of Physical Chemistry* **93**, 6441–6444 (1989).

161. S. Perkin, N. Kampf, J. Klein, *The Journal of Physical Chemistry B* **109**, 3832–3837 (2005).

162. Y. H. Tsao, D. F. Evans, H. Wennerstrom, *Science* **262**, 547–550 (1993).

163. E. E. Meyer, K. J. Rosenberg, J. Israelachvili, *Proceedings of the National Academy of Sciences* **103**, 15739–15746 (2006).

164. P. M. Claesson, H. K. Christenson, *The Journal of Physical Chemistry* **92**, 1650–1655 (1988).

165. H. K. Christenson, P. M. Claesson, *Science* **239**, 390–392 (1988).

166. H. K. Christenson, J. Fang, B. W. Ninham, J. L. Parker, *The Journal of Physical Chemistry* **94**, 8004–8006 (1990).

167. J. Wood, R. Sharma, *Langmuir* **11**, 4797–4802 (1995).

168. M. Hato, *The Journal of Physical Chemistry* **100**, 18530–18538 (1996).

169. E. E. Meyer, Q. Lin, T. Hassenkam, E. Oroudjev, J. N. Israelachvili, *Proceedings of the National Academy of Sciences* **102**, 6839–6842 (2005).

170. S. Perkin, N. Kampf, J. Klein, *Physical Review Letters* **96**, 038301 (2006).

171. G. Silbert *et al.*, *Physical Review Letters* **109**, 168305 (2012).

172. R. M. Adar, D. Andelman, H. Diamant, *Physical Review E* **94**, 022803 (2016).

173. R. M. Adar, D. Andelman, H. Diamant, *Advances in Colloid and Interface Science*, Dominique Langevin Festschrift: Four Decades Opening Gates in Colloid and Interface Science **247**, 198–207 (2017).

174. C. Casagrande, P. Fabre, E. Raphaël, M. Veyssié, *Europhysics Letters* **9**, 251 (1989).

175. P. G. de Gennes, *Reviews of Modern Physics* **64**, 645–648 (1992).

176. A. Walther, A. H. E. Müller, *Soft Matter* **4**, 663–668 (2008).

177. L. Hong, A. Cacciuto, E. Luijten, S. Granick, *Nano Letters* **6**, 2510–2514 (2006).

178. E. W. Edwards, D. Wang, H. Möhwald, *Macromolecular Chemistry and Physics* **208**, 439–445 (2007).

179. A. Goyal, C. K. Hall, O. D. Velev, *Physical Review E* **77**, 031401 (2008).

180. Q. Chen, S. C. Bae, S. Granick, *Nature* **469**, 381–384 (2011).

181. A. Walther, A. H. E. Müller, *Chemical Reviews* **113**, 5194–5261 (2013).

182. K.-H. Roh, D. C. Martin, J. Lahann, *Nature Materials* **4**, 759–763 (2005).

183. L. Hong, S. Jiang, S. Granick, *Langmuir* **22**, 9495–9499 (2006).

184. S. Jiang, S. Granick, *Langmuir* **24**, 2438–2445 (2008).

185. S. Jiang, M. J. Schultz, Q. Chen, J. S. Moore, S. Granick, *Langmuir* **24**, 10073–10077 (2008).

186. B. Liu, W. Wei, X. Qu, Z. Yang, *Angewandte Chemie* **120**, 4037–4039 (2008).

187. S. Jiang *et al.*, *Advanced Materials* **22**, 1060–1071 (2010).

188. C. Zhang *et al.*, *Chemical Communications* **46**, 4610–4612 (2010).

189. J. de Graaf, N. Boon, M. Dijkstra, R. van Roij, *The Journal of Chemical Physics* **137**, 104910 (2012).

190. K. Van Workum, J. F. Douglas, *Physical Review E* **73**, 031502 (2006).

191. L. Hong, A. Cacciuto, E. Luijten, S. Granick, *Langmuir* **24**, 621–625 (2008).

192. A. Goyal, C. K. Hall, O. D. Velev, *Soft Matter* **6**, 480–484 (2010).

193. Q. Chen, J. Yan, J. Zhang, S. C. Bae, S. Granick, *Langmuir* **28**, 13555–13561 (2012).

194. P. G. de Gennes, P. A. Pincus, *Physik der kondensierten Materie* **11**, 189–198 (1970).

195. J. J. Weis, D. Levesque, *Physical Review Letters* **71**, 2729–2732 (1993).

196. J. M. Tavares, J. J. Weis, M. M. Telo da Gama, *Physical Review E* **59**, 4388–4395 (1999).

197. Z. Wang, C. Holm, H. W. Müller, *Physical Review E* **66**, 021405 (2002).

198. I. Muševič, M. Škarabot, U. Tkalec, M. Ravnik, S. Žumer, *Science* **313**, 954–958 (2006).

199. R. Hieronimus, S. Raschke, A. Heuer, *The Journal of Chemical Physics* **145**, 064303 (2016).

200. J. G. Kirkwood, J. B. Shumaker, *Proceedings of the National Academy of Sciences* **38**, 855–862 (1952).

201. J. G. Kirkwood, J. B. Shumaker, *Proceedings of the National Academy of Sciences* **38**, 863–871 (1952).

202. N. Adžić, R. Podgornik, *arXiv:1401.5252* (2014).

203. N. Adžić, R. Podgornik, *Physical Review E* **91**, 022715 (2015).

204. V. A. Parsegian, *Van der Waals Forces: A Handbook for Biologists, Chemists, Engineers, and Physicists* (Cambridge University Press, New York, USA, 2005).

205. M. Kappl, H.-J. Butt, *Particle & Particle Systems Characterization* **19**, 129–143 (2002).

206. J. N. Israelachvili, *Intermolecular and Surface Forces: Revised Third Edition* (Academic Press, 2011).

207. J. N. Israelachvili, G. E. Adams, *Nature* **262**, 774–776 (1976).

208. R. M Pashley, *Journal of Colloid and Interface Science* **83**, 531–546 (1981).

209. V. E. Shubin, P. Kékicheff, *Journal of Colloid and Interface Science* **155**, 108–123 (1993).

210. A. Grabbe, R. G. Horn, *Journal of Colloid and Interface Science* **157**, 375–383 (1993).

211. J. N. Israelachvili, D. Tabor, *Proceedings of the Royal Society of London: A* **331**, 19–38 (1972).

212. R. M Pashley, *Journal of Colloid and Interface Science* **80**, 153–162 (1981).

213. J. Klein, E. Kumacheva, D. Mahalu, D. Perahia, L. J. Fetters, *Nature* **370**, 634–636 (1994).

214. M. Urbakh, J. Klafter, D. Gourdon, J. Israelachvili, *Nature* **430**, 525–528 (2004).

215. M. Chen, W. H. Briscoe, S. P. Armes, J. Klein, *Science* **323**, 1698–1701 (2009).

216. P. M. Claesson, C. E. Blom, P. C. Herder, B. W. Ninham, *Journal of Colloid and Interface Science* **114**, 234–242 (1986).

217. E. A. Vogler, *Advances in Colloid and Interface Science* **74**, 69–117 (1998).

218. J. Klein, P. Luckham, *Nature* **300**, 429–431 (1982).

219. J. Klein, P. F. Luckham, *Nature* **308**, 836–837 (1984).

220. J. Marra, J. Israelachvili, *Biochemistry* **24**, 4608–4618 (1985).

221. R. P. Rand, V. A. Parsegian, *Biochimica et Biophysica Acta (BBA) - Reviews on Biomembranes* **988**, 351–376 (1989).

222. R. G. Horn, J. N. Israelachvili, *The Journal of Chemical Physics* **75**, 1400–1411 (1981).

223. D. Y. C. Chan, R. G. Horn, *The Journal of Chemical Physics* **83**, 5311–5324 (1985).

224. J. N. Israelachvili, P. M. Mcguiggan, A. M. Homola, *Science* **240**, 189–191 (1988).

225. S. Granick, *Science* **253**, 1374–1379 (1991).

226. J. Klein, E. Kumacheva, *Science* **269**, 816–819 (1995).

227. W. A. Ducker, T. J. Senden, R. M. Pashley, *Nature* **353**, 239–241 (1991).

228. H.-J. Butt, *Biophysical Journal* **60**, 1438–1444 (1991).

229. H.-J. Butt, B. Cappella, M. Kappl, *Surface Science Reports* **59**, 1–152 (2005).

230. R. F. Considine, R. A. Hayes, R. G. Horn, *Langmuir* **15**, 1657–1659 (1999).

231. M. Borkovec *et al.*, *Advances in Colloid and Interface Science*, Interfaces, Wettability, Surface Forces and Applications: Special Issue in honour of the 65th Birthday of John Ralston **179-182**, 85–98 (2012).

232. P. Sinha, I. Szilagyi, F. J. Montes Ruiz-Cabello, P. Maroni, M. Borkovec, *The Journal of Physical Chemistry Letters* **4**, 648–652 (2013).

233. F. J. Montes Ruiz-Cabello *et al.*, *The Journal of Physical Chemistry B* **119**, 8184–8193 (2015).

234. S.-w. Lee, W. M. Sigmund, *Colloids and Surfaces A: Physicochemical and Engineering Aspects* **204**, 43–50 (2002).

235. X. Zhang, Y. Lu, E. Liu, G. Yi, J. Jia, *Colloids and Surfaces A: Physicochemical and Engineering Aspects* **401**, 90–96 (2012).

236. C. T. McKee, J. Y. Walz, *Journal of Colloid and Interface Science* **365**, 72–80 (2012).

237. G. Francius *et al.*, *Microscopy Research and Technique* **69**, 84–92 (2006).

238. J. P. Cleveland, S. Manne, D. Bocek, P. K. Hansma, *Review of Scientific Instruments* **64**, 403–405 (1993).

239. K.-H. Chung, G. A. Shaw, J. R. Pratt, *Review of Scientific Instruments* **80**, 065107 (2009).

240. N. Maeda, T. J. Senden, *Langmuir* **16**, 9282–9286 (2000).

241. V. S. J. Craig, C. Neto, *Langmuir* **17**, 6018–6022 (2001).

242. P. A. Temple, *Applied Optics* **20**, 2656 (1981).

243. D. C. Prieve, F. Luo, F. Lanni, *Faraday Discussions of the Chemical Society* **83**, 297 (1987).

244. D. C. Prieve, S. G. Bike, N. A. Frej, *Faraday Discussions of the Chemical Society* **90**, 209 (1990).

245. S. G. Bike, D. C. Prieve, *International Journal of Multiphase Flow* **16**, 727–740 (1990).

246. M. A. Bevan, D. C. Prieve, *Langmuir* **15**, 7925–7936 (1999).

247. R. F. Tabor, R. Manica, D. Y. C. Chan, F. Grieser, R. R. Dagastine, *Physical Review Letters* **106**, 064501 (2011).

248. M. Nayeri, Z. Abbas, J. Bergenholtz, *Colloids and Surfaces A: Physicochemical and Engineering Aspects* **429**, 74–81 (2013).

249. P. C. Odiachi Jr., D. C. Prieve, *Colloids and Surfaces A: Physicochemical and Engineering Aspects* **146**, 315–328 (1999).

250. D. Rudhardt, C. Bechinger, P. Leiderer, *Physical Review Letters* **81**, 1330–1333 (1998).

251. D. Kleshchanok, R. Tuinier, P. R. Lang, *Langmuir* **22**, 9121–9128 (2006).

252. A. Ashkin, J. M. Dziedzic, J. E. Bjorkholm, S. Chu, *Optics Letters* **11**, 288 (1986).

253. R. J. Hopkins, L. Mitchem, A. D. Ward, J. P. Reid, *Physical Chemistry Chemical Physics* **6**, 4924–4927 (2004).

254. D. R. Burnham, D. McGloin, *Optics Express* **14**, 4175–4181 (2006).

255. M. D. Wang, H. Yin, R. Landick, J. Gelles, S. M. Block, *Biophysical Journal* **72**, 1335–1346 (1997).

256. M. D. Wang *et al.*, *Science* **282**, 902–907 (1998).

257. U. Bockelmann, P. Thomen, B. Essevaz-Roulet, V. Viasnoff, F. Heslot, *Biophysical Journal* **82**, 1537–1553 (2002).

258. K. C. Neuman, E. A. Abbondanzieri, R. Landick, J. Gelles, S. M. Block, *Cell* **115**, 437–447 (2003).

259. V Novotny, *Colloids and Surfaces*, International Conference on Surface and Colloid and the 59th Colloid and Surface Science Symposium **24**, 361–375 (1987).

260. J. Heikenfeld, P. Drzaic, J.-S. Yeo, T. Koch, *Journal of the Society for Information Display* **19**, 129–156 (2012).

261. A. Klinkenberg, J. L. v. d. Minne, *Electrostatics in the Petroleum Industry. The prevention of explosion hazards. A Royal Dutch/Shell research and development report.* (Elsevier, 1958).

262. R. M. Fuoss, C. A. Kraus, *Journal of the American Chemical Society* **55**, 3614–3620 (1933).

263. G. S. Hooper, C. A. Kraus, *Journal of the American Chemical Society* **56**, 2265–2268 (1934).

264. W. F. Luder, P. B. Kraus, C. A. Kraus, R. M. Fuoss, *Journal of the American Chemical Society* **58**, 255–258 (1936).

265. L. E. Strong, C. A. Kraus, *Journal of the American Chemical Society* **72**, 166–171 (1950).

266. V. K. l. Mer, H. C. Downes, *Journal of the American Chemical Society* **53**, 888–896 (1931).

267. V. K. L. Mer, H. C. Downes, *Chemical Reviews* **13**, 47–60 (1933).

268. R. Deul, S. Rosenzweig, E. U. Franck, *Berichte der Bunsengesellschaft für physikalische Chemie* **95**, 515–519 (1991).

269. J. L van der Minne, P. H. J Hermanie, *Journal of Colloid Science* **7**, 600–615 (1952).

270. J. L van der Minne, P. H. J Hermanie, *Journal of Colloid Science* **8**, 38–52 (1953).

271. H. Koelmans, J. T. G. Overbeek, *Discussions of the Faraday Society* **18**, 52 (1954).

272. W. Albers, J. T. G. Overbeek, *Journal of Colloid Science* **14**, 501–509 (1959).

273. W. Albers, J. T. G. Overbeek, *Journal of Colloid Science* **14**, 510–518 (1959).

274. L. A. Romo, *The Journal of Physical Chemistry* **67**, 4 (1963).

275. T. Sato, *Journal of Applied Polymer Science* **15**, 1053–1067 (1971).

276. M. E. Labib, R. Williams, *Journal of Colloid and Interface Science* **97**, 356–366 (1984).

277. D. N. L McGown, G. D Parfitt, E Willis, *Journal of Colloid Science* **20**, 650–664 (1965).

278. J. Lyklema, *Advances in Colloid and Interface Science* **2**, 67–114 (1968).

279. L. A. Romo, *Discussions of the Faraday Society* **42**, 232–237 (1966).

280. A. Kitahara, S. Karasawa, H. Yamada, *Journal of Colloid and Interface Science* **25**, 490–495 (1967).

281. G. D Parfitt, E Willis, *Journal of Colloid and Interface Science* **22**, 100–106 (1966).

282. G. Bakale, K. Lacmann, W. F. Schmidt, *The Journal of Physical Chemistry* **100**, 12477–12482 (1996).

283. M. N. Martin, J. I. Basham, P. Chando, S.-K. Eah, *Langmuir* **26**, 7410–7417 (2010).

284. L. S. Park *et al.*, *Current Applied Physics*, 15th Molecular Electronics and Devices Symposium **6**, 644–648 (2006).

285. F. Pontiga, A. Castellanos, *IEEE Transactions on Industry Applications* **32**, 816–824 (1996).

286. B. Kim, S. Kim, K. Park, *Molecular Crystals and Liquid Crystals* **425**, 93–97 (2004).

287. R. Sánchez, P. Bartlett, *Soft Matter* **7**, 887–890 (2011).

288. G. N. Smith, Ph.D. University of Bristol, 2015.

289. S. M. Nelson, R. C. Pink, *Journal of the Chemical Society (Resumed)* **0**, 4412–4417 (1954).

290. Q. Guo, V. Singh, S. H. Behrens, *Langmuir* **26**, 3203–3207 (2010).

291. I. D. Morrison, *Colloids and Surfaces A: Physicochemical and Engineering Aspects* **71**, 1–37 (1993).

292. K Svoboda, S. M. Block, *Annual Review of Biophysics and Biomolecular Structure* **23**, 247–285 (1994).

293. C. Bustamante, S. B. Smith, J. Liphardt, D. Smith, *Current Opinion in Structural Biology* **10**, 279–285 (2000).

294. A. Ashkin, *Physical Review Letters* **24**, 156–159 (1970).

295. A. Ashkin, J. M. Dziedzic, *Applied Physics Letters* **19**, 283–285 (1971).

296. A. Ashkin, *Biophysical Journal* **61**, 569–582 (1992).

297. Y. Harada, T. Asakura, *Optics Communications* **124**, 529–541 (1996).

298. P. Jones, O. Marago, G. Volpe, *Optical Tweezers: Principles and Applications* (Cambridge University Press, Cambridge, 2015).

299. T. Cosgrove, Ed., *Colloid Science: Principles, Methods and Applications* (Wiley-Blackwell, Chichester, West Sussex, 2nd Edition edition, 2010).

300. D. G. Grier, Y. Roichman, *Applied Optics* **45**, 880 (2006).

301. J. P. Hoogenboom, D. L. J. Vossen, C. Faivre-Moskalenko, M. Dogterom, A. v. Blaaderen, *Applied Physics Letters* **80**, 4828–4830 (2002).

302. K. Visscher, S. P. Gross, S. M. Block, *IEEE Journal of Selected Topics in Quantum Electronics* **2**, 1066–1076 (1996).

303. J. P. Pantina, E. M. Furst, *Langmuir* **20**, 3940–3946 (2004).

304. E. R. Dufresne, D. G. Grier, *Review of Scientific Instruments* **69**, 1974–1977 (1998).

305. I. Williams, Ph.D. University of Bristol, 2013.

306. M. Polin, K. Ladavac, S.-H. Lee, Y. Roichman, D. G. Grier, *Optics Express* **13**, 5831 (2005).

307. Finlayson, Samuel D., PhD thesis, University of Bristol, 2016.

308. Padgett, M., and co-workers, *Holographic Optical Tweezers LabView code for SLM control and particle tracking*, (`http://www:gla:ac:uk/schools/physics/research/groups/optics/research/opticaltweezers/software/`).

309. J. C. Crocker, D. G. Grier, *Journal of Colloid and Interface Science* **179**, 298–310 (1996).

310. J Baumgartl, C Bechinger, *Europhysics Letters* **71**, 487–493 (2005).

311. M. Gyger, F. Rückerl, J. A. Käs, J. Ruiz-García, *Journal of Colloid and Interface Science* **326**, 382–386 (2008).

312. C. Gutsche, U. F. Keyser, K. Kegler, F. Kremer, P. Linse, *Physical Review E* **76**, 031403 (2007).

313. A. Van Blaaderen, A. Vrij, *Langmuir* **8**, 2921–2931 (1992).

314. R. P. A. Dullens, Claesson, D. Derks, A. van Blaaderen, W. K. Kegel, *Langmuir* **19**, 5963–5966 (2003).

315. M. M. Elmahdy, C. Gutsche, F. Kremer, *The Journal of Physical Chemistry C* **114**, 19452–19458 (2010).

316. C. Zhang, G. Brügger, F. Scheffold, *Optics Express* **23**, 22579 (2015).

317. C. Zhang, G. Brüugger, and F. Scheffold, *MATLAB code for template based tracking of colloids*, 2015, (http://physics.unifr.ch/en/page/474/).

318. R. Verma, J. C. Crocker, T. C. Lubensky, A. G. Yodh, *Macromolecules* **33**, 177–186 (2000).

319. A. Chandra, B. Bagchi, *The Journal of Chemical Physics* **112**, 1876–1886 (2000).

320. Y. Marcus, *Journal of Solution Chemistry* **37**, 1071 (2008).

321. A. P. Abbott, T. A. Claxton, J. Fawcett, J. C. Harper, *Journal of the Chemical Society, Faraday Transactions* **92**, 1747 (1996).

322. A. Campbell, PhD thesis, Bristol, 2003.

323. L. Antl *et al.*, *Colloids and Surfaces* **17**, 67–78 (1986).

324. R. J. R Cainrs, R. H Ottewill, D. W. J Osmond, I Wagstraff, *Journal of Colloid and Interface Science* **54**, 45–51 (1976).

325. G. Hussain, PhD thesis, Bristol.

326. R. Kjellander, D. J. Mitchell, *Chemical Physics Letters* **200**, 76–82 (1992).

327. J. N. Israelachvili, G. E. Adams, *Journal of the Chemical Society, Faraday Transactions 1: Physical Chemistry in Condensed Phases* **74**, 975–1001 (1978).

328. S. J. Miklavcic, E. Thulin, B. Jönsson, *The Journal of Physical Chemistry* **100**, 5554–5561 (1996).

329. M. M. Kohonen, M. E. Karaman, R. M. Pashley, *Langmuir* **16**, 5749–5753 (2000).

330. R. F. Considine, C. J. Drummond, D. R. Dixon, *Australian Journal of Chemistry* **58**, 837–844 (2006).

331. M. Leivers, J. M. Seddon, M. Declercq, E. Robles, P. Luckham, *Langmuir* (2018).

332. S. G. Flicker, J. L. Tipa, S. G. Bike, *Journal of Colloid and Interface Science* **158**, 317–325 (1993).

333. M. R. Griffiths, A. Raudsepp, K. M. McGrath, M. A. K. Williams, *RSC Advances* **6**, 14538–14546 (2016).

334. L. Helden, G. H. Koenderink, P. Leiderer, C. Bechinger, *Langmuir* **20**, 5662–5665 (2004).

335. Z. Ao, G. Liu, G. Zhang, *The Journal of Physical Chemistry C* **115**, 2284–2289 (2011).

336. J. D. Mitchell, B. W. Ninham, *Chemical Physics Letters* **53**, 397–399 (1978).

337. M. A. Knackstedt, B. W. Ninham, *The Journal of Physical Chemistry* **100**, 1330–1335 (1996).

338. A. McBride, M. Kohonen, P. Attard, *The Journal of Chemical Physics* **109**, 2423–2428 (1998).

339. P. Kékicheff, B. W. Ninham, *Europhysics Letters* **12**, 471 (1990).

340. D. C. Rau, V. A. Parsegian, *Biophysical Journal* **61**, 246–259 (1992).

341. T. Nylander, P. Kékicheff, B. W. Ninham, *Journal of Colloid and Interface Science* **164**, 136–150 (1994).

342. D. F. Evans, B. W. Ninham, *The Journal of Physical Chemistry* **87**, 5025–5032 (1983).

343. R. M Pashley, P. M McGuiggan, R. G Horn, B. W Ninham, *Journal of Colloid and Interface Science* **126**, 569–578 (1988).

344. W. A. Ducker, T. J. Senden, R. M. Pashley, *Langmuir* **8**, 1831–1836 (1992).

345. J. J. Valle-Delgado *et al.*, *The Journal of Chemical Physics* **123**, 034708 (2005).

346. H. K Christenson, R. G Horn, J. N Israelachvili, *Journal of Colloid and Interface Science* **88**, 79–88 (1982).

347. H. K. Christenson, *The Journal of Chemical Physics* **78**, 6906–6913 (1983).

348. M. L. Gee, J. N. Israelachvili, *Journal of the Chemical Society, Faraday Transactions* **86**, 4049–4058 (1990).

349. E. B. Sirota *et al.*, *Physical Review Letters* **62**, 1524–1527 (1989).

350. A. M. Smith, A. A. Lee, S. Perkin, *The Journal of Physical Chemistry Letters* **7**, 2157–2163 (2016).

351. M. A. Gebbie *et al.*, *Proceedings of the National Academy of Sciences* **110**, 9674–9679 (2013).

352. A. A. Lee, C. S. Perez-Martinez, A. M. Smith, S. Perkin, *Faraday Discussions* **199**, 239–259 (2017).

353. A. A. Lee, C. S. Perez-Martinez, A. M. Smith, S. Perkin, *Physical Review Letters* **119**, 026002 (2017).

354. M. A. Gebbie *et al.*, *Chemical Communications* **53**, 1214–1224 (2017).

355. J. Huang, *The Journal of Physical Chemistry C* **122**, 3428–3433 (2018).

356. J. Zwanikken, R. v. Roij, *Journal of Physics: Condensed Matter* **21**, 424102 (2009).

357. R. Lhermerout, S. Perkin, *Physical Review Fluids* **3**, 014201 (2018).

358. N. Hjalmarsson, R. Atkin, M. W. Rutland, *Chemical Communications* **53**, 647–650 (2017).

359. M. A. Gebbie, H. A. Dobbs, M. Valtiner, J. N. Israelachvili, *Proceedings of the National Academy of Sciences* **112**, 7432–7437 (2015).

360. A. M. Smith, A. A. Lee, S. Perkin, *Physical Review Letters* **118**, 096002 (2017).

361. S. W. Coles, A. M. Smith, M. V. Fedorov, F. Hausen, S. Perkin, *Faraday Discussions* **206**, 427–442 (2017).

362. R. M. Adar, S. A. Safran, H. Diamant, D. Andelman, *arXiv:1812.07217* (2018).

363. P. Attard, *Physical Review E* **48**, 3604–3621 (1993).

364. B. Rotenberg, O. Bernard, J.-P. Hansen, *Journal of Physics: Condensed Matter* **30**, 054005 (2018).

365. F. Coupette, A. A. Lee, A. Härtel, *Physical Review Letters* **121** (2018).

366. A. J. Archer, P. Hopkins, R. Evans, *Physical Review E* **74**, 010402 (2006).

367. L. Blum, J. S. Hoeye, *The Journal of Physical Chemistry* **81**, 1311–1316 (1977).

368. S. K. Sainis, V. Germain, C. O. Mejean, E. R. Dufresne, *Langmuir* **24**, 1160–1164 (2008).

369. S. K. Sainis, J. W. Merrill, E. R. Dufresne, *Langmuir* **24**, 13334–13337 (2008).

370. R. M. Fuoss, C. A. Kraus, *Journal of the American Chemical Society* **55**, 2387–2399 (1933).

371. E. H. Oelkers, H. C. Helgeson, *Science* **261**, 888–891 (1993).

372. Y. Miyauchi, M. Hojo, N. Ide, Y. Imai, *Journal of the Chemical Society, Faraday Transactions* **88**, 1425–1431 (1992).

373. C. A. Kraus, R. M. Fuoss, *Journal of the American Chemical Society* **55**, 21–36 (1933).

374. R. M. Fuoss, C. A. Kraus, *Journal of the American Chemical Society* **55**, 476–488 (1933).

375. R. M. Fuoss, C. A. Kraus, *Journal of the American Chemical Society* **55**, 1019–1028 (1933).

376. S. Boileau, P. Hemery, *Electrochimica Acta* **21**, 647–655 (1976).

377. M. Salomon, M. C. Uchiyama, *Journal of Solution Chemistry* **16**, 21–30 (1987).

378. Y. Liang, N. Hilal, P. Langston, V. Starov, *Advances in Colloid and Interface Science*, Surface forces: wetting phenomena, membrane separation, rheology. Topical issue in honour of Victor Starov **134–135**, 151–166 (2007).

379. T. Savin, P. S. Doyle, *Biophysical Journal* **88**, 623–638 (2005).

380. Y. Liu, R. DiFoggio, K. Sanderlin, L. Perez, J. Zhao, *Sensors and Actuators A: Physical*, Solid-State Sensors, Actuators and Microsystems Workshop **167**, 347–353 (2011).

381. G. A. Schumacher, T. G. M. v. d. Ven, *Faraday Discussions of the Chemical Society* **83**, 75–85 (1987).

382. V. d. Ven, T. G. M, *Colloidal hydrodynamics*, ed. by R. H. Ottewill, R. L. Rowell (Academic Press, 1989).

383. S. Alexander *et al.*, *The Journal of Chemical Physics* **80**, 5776–5781 (1984).

384. J. Lyklema, *Current Opinion in Colloid & Interface Science* **18**, 116–128 (2013).

385. J. E. Hallett, D. A. J. Gillespie, R. M. Richardson, P. Bartlett, *Soft Matter* **14**, 331–343 (2018).

386. Z. A. H. Goodwin, A. A. Kornyshev, *Electrochemistry Communications* **82**, 129–133 (2017).

387. S. H. Behrens, M. Borkovec, *The Journal of Chemical Physics* **111**, 382–385 (1999).

388. M. Borkovec, S. H. Behrens, *The Journal of Physical Chemistry B* **112**, 10795–10799 (2008).

389. Y. Avni, D. Andelman, R. Podgornik, *Current Opinion in Electrochemistry* **13**, 70–77 (2019).

390. S. H. Behrens, M. Borkovec, *Physical Review E* **60**, 7040–7048 (1999).

391. I. Popa *et al.*, *Physical Review Letters* **104**, 228301 (2010).

392. P. N. Pusey, W. van Megen, *Nature* **320**, 340–342 (1986).

393. H. G. Bagaria *et al.*, *ACS Applied Materials and Interfaces* **5**, 3329–3339 (2013).

394. A. J. Worthen, V. Tran, K. A. Cornell, T. M. Truskett, K. P. Johnston, *Soft Matter* **12**, 2025–2039 (2016).

395. K. Y. Yoon *et al.*, *Langmuir* **27**, 10962–10969 (2011).

396. T. Alfrey, E. B. Bradford, J. W. Vanderhoff, G. Oster, *Journal of the Optical Society of America* **44**, 603–609 (1954).

397. A. Kose, M. Ozaki, K. Takano, Y. Kobayashi, S. Hachisu, *Journal of Colloid and Interface Science* **44**, 330–338 (1973).

398. M. O. Robbins, K. Kremer, G. S. Grest, *The Journal of Chemical Physics* **88**, 3286–3312 (1988).

399. S. Hamaguchi, R. T. Farouki, D. H. E. Dubin, *The Journal of Chemical Physics* **105**, 7641–7647 (1996).

400. A. K. Arora, B. V. R. Tata, *Advances in Colloid and Interface Science* **78**, 49–97 (1998).

401. N. Ise, T. Okubo, M. Sugimura, K. Ito, H. J. Nolte, *The Journal of Chemical Physics* **78**, 536–540 (1983).

402. N. Ise, K. Ito, T. Okubo, S. Dosho, I. Sogami, *Journal of the American Chemical Society* **107**, 8074–8077 (1985).

403. K. Ito, H. Nakamura, N. Ise, *The Journal of Chemical Physics* **85**, 6143–6146 (1986).

404. I. Sogami, *Physics Letters A* **96**, 199–203 (1983).

405. I. Sogami, N. Ise, *The Journal of Chemical Physics* **81**, 6320–6332 (1984).

406. J. T. G. Overbeek, *The Journal of Chemical Physics* **87**, 4406–4408 (1987).

407. C. E. Woodward, *The Journal of Chemical Physics* **89**, 5140–5144 (1988).

408. J. Wu, D. Bratko, J. M. Prausnitz, *Proceedings of the National Academy of Sciences* **95**, 15169–15172 (1998).

409. J. G. Daly, R. Hastings, *The Journal of Physical Chemistry* **85**, 294–300 (1981).

410. A. K. Arora, R. Kesavamoorthy, *Solid State Communications* **54**, 1047–1050 (1985).

411. A. K. Arora, B. V. R. Tata, A. K. Sood, R. Kesavamoorthy, *Physical Review Letters* **60**, 2438–2441 (1988).

412. R. Kesavamoorthy, M. Rajalakshmi, C. B. Rao, *Journal of Physics: Condensed Matter* **1**, 7149–7161 (1989).

413. N. Ise, H. Matsuoka, K. Ito, H. Yoshida, *Faraday Discussions of the Chemical Society* **90**, 153–162 (1990).

414. B. V. R. Tata, M. Rajalakshmi, A. K. Arora, *Physical Review Letters* **69**, 3778–3781 (1992).

415. S. Dosho *et al.*, *Langmuir* **9**, 394–411 (1993).

416. H. Yoshida, N. Ise, T. Hashimoto, *The Journal of Chemical Physics* **103**, 10146–10151 (1995).

417. B. V. R. Tata, E. Yamahara, P. V. Rajamani, N. Ise, *Physical Review Letters* **78**, 2660–2663 (1997).

418. R. van Roij, J.-P. Hansen, *Physical Review Letters* **79**, 3082–3085 (1997).

419. E. Ruckenstein, *Advances in Colloid and Interface Science* **75**, 169–180 (1998).

420. R. van Roij, M. Dijkstra, J.-P. Hansen, *Physical Review E* **59**, 2010–2025 (1999).

421. A. R. Denton, *Journal of Physics: Condensed Matter* **11**, 10061 (1999).

422. P. B. Warren, *The Journal of Chemical Physics* **112**, 4683–4698 (2000).

423. R. v. Roij, *Journal of Physics: Condensed Matter* **12**, A263 (2000).

424. A. Diehl, M. C. Barbosa, Y. Levin, *Europhysics Letters* **53**, 86 (2001).

425. H. H. v. Grünberg, R. v. Roij, G. Klein, *Europhysics Letters* **55**, 580 (2001).

426. M. N. Tamashiro, H. Schiessel, *Physical Review E* **68**, 066106 (2003).

427. M. N. v. d. Linden, D. E. Masri, M. Dijkstra, A. v. Blaaderen, *Soft Matter* **9**, 11618–11633 (2013).

428. T. M. Squires, M. P. Brenner, *Physical Review Letters* **85**, 4976–4979 (2000).

429. A. E. Larsen, D. G. Grier, *Nature* **385**, 230–233 (1997).

430. G. M. Kepler, S. Fraden, *Physical Review Letters* **73**, 356–359 (1994).

431. M. D. Carbajal-Tinoco, F. Castro-Román, J. L. Arauz-Lara, *Physical Review E* **53**, 3745–3749 (1996).

432. R. Kjellander, T. Akesson, B. Jönsson, S. Marčelja, *The Journal of Chemical Physics* **97**, 1424–1431 (1992).

433. M. S. Loth, B. I. Shklovskii, *Journal of Physics: Condensed Matter* **21**, 424104 (2009).

434. Y. Levin, *Physica A: Statistical Mechanics and its Applications* **265**, 432–439 (1999).

435. L. Guldbrand, B. Jönsson, H. Wennerström, P. Linse, *The Journal of Chemical Physics* **80**, 2221–2228 (1984).

436. R. Kjellander, S. Marcělja, *Chemical Physics Letters* **112**, 49–53 (1984).

437. P. Linse, V. Lobaskin, *The Journal of Chemical Physics* **112**, 3917–3927 (2000).

438. A. Diehl, H. A. Carmona, Y. Levin, *Physical Review E* **64**, 011804 (2001).

439. A. Diehl, Y. Levin, *The Journal of Chemical Physics* **129**, 124506 (2008).

440. E. Allahyarov, I. D'Amico, H. Löwen, *Physical Review Letters* **81**, 1334–1337 (1998).

441. J.-P. Hansen, H. Löwen, *Annual Review of Physical Chemistry* **51**, 209–242 (2000).

442. A. Ohshima, T. Konishi, J. Yamanaka, N. Ise, *Physical Review E* **64**, 051808 (2001).

443. A. J. Stace, E. Bichoutskaia, *Soft Matter* **8**, 6210 (2012).

444. E. Bichoutskaia, A. L. Boatwright, A. Khachatourian, A. J. Stace, *The Journal of Chemical Physics* **133**, 024105 (2010).

445. E. B. Lindgren, H.-K. Chan, A. J. Stace, E. Besley, *Physical Chemistry Chemical Physics* **18**, 5883–5895 (2016).

446. J. C. Everts, M. N. van der Linden, A. van Blaaderen, R. van Roij, *Soft Matter* **12**, 6610–6620 (2016).

447. A. I. Campbell, P. Bartlett, *Journal of Colloid and Interface Science* **256**, 325–330 (2002).

448. P. Schissel, C. Kennedy, R. Goggin, *Journal of Adhesion Science and Technology* **9**, 413–424 (1995).

449. B. F. Macdonald, R. J. Cole, V. Koutsos, *Surface Science* **548**, 41–50 (2004).

450. E. Allahyarov, E. Zaccarelli, F. Sciortino, P. Tartaglia, H. Löwen, *Europhysics Letters* **78**, 38002 (2007).

451. C. Wohlfarth, in *Surface Tension of Pure Liquids and Binary Liquid Mixtures: Supplement to Volume IV/24*, ed. by C. Wohlfarth, M. D. Lechner (Springer Berlin Heidelberg, Berlin, Heidelberg, 2016), pp. 182–182.

452. M. E. Fisher, Y. Levin, *Physical Review Letters* **71**, 3826–3829 (1993).

453. Y. Levin, M. E. Fisher, *Physica A: Statistical Mechanics and its Applications* **225**, 164–220 (1996).

454. A. Nikoubashman, J.-P. Hansen, G. Kahl, *The Journal of Chemical Physics* **137**, 094905 (2012).

455. P. B. Warren, A. J. Masters, *The Journal of Chemical Physics* **138**, 074901 (2013).

456. P. Linse, *The Journal of Chemical Physics* **113**, 4359–4373 (2000).

457. E. Allahyarov, E. Zaccarelli, F. Sciortino, P. Tartaglia, H. Löwen, *Europhysics Letters* **81**, 59901 (2008).

458. R. A. Curtis, L. Lue, *Current Opinion in Colloid & Interface Science* **20**, 19–23 (2015).

459. J. Dudowicz, K. F. Freed, J. F. Douglas, *Physical Review Letters* **92**, 045502 (2004).

460. K. Van Workum, J. F. Douglas, *Physical Review E* **71**, 031502 (2005).

461. T. Tlusty, S. A. Safran, *Science* **290**, 1328–1331 (2000).

462. J. T. Kindt, *The Journal of Physical Chemistry B* **106**, 8223–8232 (2002).

463. M. M. Moghani, B. Khomami, *Soft Matter* **9**, 4815–4821 (2013).

464. J. M. Dempster, M. Olvera de la Cruz, *ACS Nano* **10**, 5909–5915 (2016).

465. E. Janai *et al.*, *Scientific Reports* **6** (2016).

466. A. A. Kornyshev, D. A. Kossakowski, S. Leikin, *The Journal of Chemical Physics* **97**, 6809–6820 (1992).

467. R. Pericet-Camara, G. Papastavrou, S. H. Behrens, M. Borkovec, *The Journal of Physical Chemistry B* **108**, 19467–19475 (2004).

468. M. L. Henle, C. D. Santangelo, D. M. Patel, P. A. Pincus, *Europhysics Letters* **66**, 284 (2004).

469. N. Adžić, R. Podgornik, *The European Physical Journal E* **37**, 49 (2014).

470. F. L. Barroso da Silva, M. Boström, C. Persson, *Langmuir* **30**, 4078–4083 (2014).

471. F. L. Barroso da Silva, P. Derreumaux, S. Pasquali, *Biochemical and Biophysical Research Communications*, Multiscale Modeling **498**, 264–273 (2018).

472. Y. Hong, D. G. Brown, *Langmuir* **24**, 5003–5009 (2008).

473. M. F. Perutz, *Science* **201**, 1187–1191 (1978).

474. M. Lund, B. Jönsson, *Quarterly Reviews of Biophysics* **46**, 265–281 (2013).

475. L. D. Landau, *Journal of Experimental and Theoretical Physics* **7**, 19–32 (1937).

476. E Justi, M Von Laue, *Zeitschrift für Technische Physik* **15**, 521 (1934).

477. H. E. Stanley, *Phase Transitions and Critical Phenomena* (Clarendon Press, Oxford, 1971).

478. R. Podgornik, *The Journal of Chemical Physics* **91**, 5840–5849 (1989).

479. R. Podgornik, V. A. Parsegian, *Chemical Physics* **154**, 477–483 (1991).

480. V. A. Parsegian, D. Gingell, *Biophysical Journal* **12**, 1192–1204 (1972).

481. A. Kornyshev, D. Kossakowski, S. Leikin, *Zeitschrift für Naturforschung A* **50**, 789–794 (1995).